On Non-Gaussian Beams and Optomechanical Parametric Instabilities in Interferometric Gravitational Wave Detectors

John Miller

M.Sci.

Submitted in fulfilment of the requirements for

for the Degree of Doctor of Philosophy

Department of Physics and Astronomy

Faculty of Physical Sciences

University of Glasgow

2010

(Deposited to Library May 2010)

"Interference phenomena permit us to refer determinations of length to a very small unit (of the order of ½ micron), the wavelength of a luminous radiation; for this reason the use of these phenomena it is at once suggested when it is a question of measuring very small thicknesses or very small changes or differences in thickness."

- A. Perot and C. Fabry (1899)

Abstract

Direct detection of gravitational radiation, predicted by Einstein's general theory of relativity, remains one of the most exciting challenges in experimental physics. Due to their relatively weak interaction with matter, gravitational waves promise to allow exploration of hitherto inaccessible objects and epochs. Unfortunately, this weak coupling also hinders detection with strain amplitudes at the Earth estimated to be of order 10^{-21}.

Due to their wide bandwidth and theoretical sensitivity, kilometre-scale Michelson style interferometers have become the preferred instrument with which to attempt ground based detection. A worldwide network of first generation instruments has been constructed and prodigious volumes of data recorded. Despite each instrument approaching or having reached its design sensitivity, a confirmed detection remains elusive.

Planned upgrades to these instruments aim to increase strain sensitivity by an order of magnitude, commencing the era of second generation detectors. Entry into this regime will be accompanied by an entirely new set of challenges, two of which are addressed in this work.

As advanced interferometers are commissioned, instrumental artifacts will give way to fundamental noise sources. In the region of peak sensitivity it is expected that thermal noise in the interferometers' dielectric mirror coatings will be the principal source of displacement noise. Theory suggests that increasing the spot size of laser light incident on these mirrors will reduce the measured thermal noise. In the first part of this work

we examine one method of realising larger spots.

By adopting non-spherical mirrors in the interferometers' arms it is possible to create resonators which support a wide, flat-topped field known as the mesa beam. This beam has been shown to theoretically reduce all forms of mirror thermal noise without being significantly more difficult to control. In this work we investigate these claims using a bespoke prototype mirror. The first results regarding a non-Gaussian beam created in a manner applicable to a gravitational wave interferometer are presented.

A common theme among all second generation interferometer designs is the desire to maximise circulating power. This increased power is partnered by commensurately increased thermal perturbations. Since the attractive properties of the mesa beam are produced by the fine structure of its supporting mirrors, it is important that we understand the effects absorption of stored optical power could have on mesa fields. In the second part of this work we report on numerical evaluations of measured thermal noise and mesa beam intensity profile as a function of absorbed power.

Increased optical power also has less obvious consequences. As a result of radiation pressure, there exists a pathway between optical energy stored in an interferometer's arms and mechanical energy stored in the acoustic modes of its test masses. Under appropriate conditions, this coupling can excite one or more test masses to such a degree that interferometer operation becomes impossible. In the final part of this work we determine whether it is possible to mitigate these parametric instabilities using electrostatic actuators originally designed to control the position and orientation of the test masses.

Contents

List of Tables

List of Figures

Preface

In **Chapter 1** we introduce the concept of the gravitational wave via linearised theory and examine what are thought to be the most promising sources for a ground based detection. Interferometric gravitational wave detectors are subsequently examined, together with the noise sources which limit their sensitivity. The properties of optical resonators are then reviewed, followed by the numerical techniques we have employed to model their behaviour.

In **Chapter 2** we commence study of the non-Gaussian mesa beam predicted to reduce measured thermal noise in interferometric gravitational wave detectors. After reviewing the theory underlying this alternative optical mode, we present our original contribution, an experimental study of the mesa beam. The design, construction and commissioning of a 7 m optical resonator supporting a mesa beam as its fundamental eigenmode are described, as is the manufacture of the unique, non-spherical, Mexican hat mirror. Experimentally measured intensity profiles are then compared to theoretical predictions, taking measured mirror imperfections into account. This investigation would not have been possible without the preliminary work undertaken by Marco Tarallo and Barbara Simoni.

Mesa beam interferometers are predicted to be moderately more sensitive to mirror tilts than the equivalent Gaussian instrument. In **Chapter 3** we experimentally investigate this prediction. A study of the mesa beam intensity profile as a function of mirror tilts is first made, before the possibility of closed loop alignment control is evaluated. The auto-alignment effort focuses on the extension of differential wavefront

sensing, a technique widely applied to Gaussian modes, to mesa beams. The analytical description of wavefront sensing with Gaussian beams is recounted before a new model to predict mesa beam alignment signals is developed. A comparison between modelled and experimentally measured alignment control signals is then made.

Chapter 4 presents results of a numerical investigation into thermal effects with mesa beams. In particular, it seeks to understand the consequences of absorption in the coatings of non-spherical mirrors. The chapter begins by summarising known methods for the analytical calculation of mirror thermal noise and the thermoelastic deformation resulting from absorbed optical power. The models developed for this work and used to obtain the steady state eigenmodes of a thermally perturbed cavity are then described. Using these techniques, the losses, intensity profiles and measured thermal noise, associated with both Gaussian and mesa beams, are given as a function of absorbed power. Thermal lensing and possible methods of thermal compensation with mesa beams are also considered.

In **Chapter 5** we discontinue the study of mesa beams to focus on mitigation of parametric instabilities. After reviewing techniques considered for this role in the past, we outline our proposal to damp acoustic modes of the test masses using the electrostatic actuators designed to control their position and angular orientation. Extensive finite element modelling was used to determine the frequencies and forms of the test mass eigenmodes and the force distribution of the electrostatic drive. Using this information, the force required to damp each acoustic mode to a safe level is determined. The predictions of this theoretical work are then tested experimentally using prototype Advanced LIGO hardware. This work was carried out in collaboration with Matthew Evans and Lisa Barsotti.

So that the results presented in this work might be verified or extended, the material parameters used in all calculations are tabulated in **Appendix A**.

In **Appendix B** we include technical drawings giving the dimensions of the electrostatic drive pattern used in our analysis of parametric instabilities.

Acknowledgments

I'd firstly like to express my gratitude to Jim Hough. It was Jim's lecture during my first year of undergraduate study at Glasgow which inspired me to enter the gravitational wave field. Since then he has always been there to offer advice and guidance; all of which proved to be correct, heeded or otherwise. Jim also gave me my first taste of research, working in his group with Harry Ward, Dave Robertson and Christian Killow. This was a great experience in a friendly, supportive atmosphere, which really encouraged me to continue in Physics. Thanks Jim.

My research supervisor Ken Strain deserves special thanks. Despite my often being on the other side of the world, Ken always seemed to know what I was doing, or more often should've been doing, better than I did. Without Ken's knowledge, insight and guidance I'd never have made it this far.

My second supervisor Norna Robertson was also a fantastic help during and after my stay at Caltech. Norna was always available, even at weekends, for a chat or to come down to the lab and look at the oscilloscope when I'd run out of steam. Norna provided support and assistance when I needed it most.

Riccardo DeSalvo also played a central role in the realisation of this thesis. Riccardo first took me in as a summer student in 2005. That period, working in his group with Marco, Juri and Chiara, showed me how much fun experimental physics could be and it is thanks to Riccardo that I was able to return to Caltech to resume working on mesa beams a year later. Riccardo's inimitable style and enthusiasm are infectious, he's been a constant source of advice and encouragement and his input made the mesa beam

experiment what it was. Riccardo, I will be forever grateful for all the opportunities you have given me.

At Caltech I also had the pleasure of working with Phil Willems. Phil taught me a tremendous amount about optics and even more about the right way to do an experiment. Phil spent an unreasonable amount of time helping to align the cavity and steering me toward the right path when I had wandered off into the weeds. Much of the experimental successes reported herein are a result of Phil's advice.

I'd like to thank Hiro Yamamoto for offering support when I was FFTired of FFTs, for all the trips to his whiteboard and, most of all, for being a friendly and approachable colleague on the third floor.

Thanks to Rana Adhikari for lunch, dinner, beer, for helping to get me across the line and for supporting my escape to the 40 m. Thanks also to Rob Ward and Sam Waldman for teaching me about interferometry while I was there.

Thanks to Eric Gustafson for always having an open door and being a great 'boss'; to Calum Torrie, for all the ANSYS; to Rich Abbott, for helping me every time I wandered into Wilson House looking like a lost toddler; to GariLynn Billingsley, for mapping my mirrors – *three times*; to Liyuan, for not hitting me when I insulted his newly upgraded scatterometer with a mirror one could barely see through.

Thanks to Alberto for the broccoli and for having such a lovely friend at MIT. To quote Brett Bochner, "...there really is a thesis out there for everybody."

Thanks to David Shoemaker and Peter Fritschel for hosting me at MIT and giving me a fascinating project to work on. Thanks to Rai Weiss for showing me what it means to be passionate about science. Thanks to Myron for all the help downstairs and for keeping me alive. Thanks to Brett for being great company in the high bay. Thanks to Matt Evans for being generally brilliant and answering all my questions. Someone should make this guy a professor. To Lisa, thanks for everything in and out of the lab and sorry about Mexico.

Lastly, to the loved ones in my life. To my mum, dad and sister, without you I wouldn't be where I am now. Thank you for your patience, love and support.

To Sharon, your contribution is beyond words. Let's get back to living life... until it's your turn.

For financial support throughout this work I am grateful to the Carnegie Trust for the Universities of Scotland.

Constants and variables

$\boldsymbol{A}$	Variously displacement amplitude of test mass eigenmode and optical power loss
$\boldsymbol{a}$	Test mass radius
$\boldsymbol{\alpha}$	Variously ESD force coupling constant i.e. $F = \alpha\Delta V^2$ and molecule polarisability
$\boldsymbol{\alpha_{\mathrm{th}}}$	Linear coefficient of thermal expansion
$\boldsymbol{A_{\mu\nu}}$	Gravitational wave polarisation tensor
$\boldsymbol{B}$	Measured ambient magnetic field
$\boldsymbol{\beta}$	Thermo-optic coefficient
$\boldsymbol{b_m}$	Force coupling between the ESD and test mass mechanical mode m
$\boldsymbol{B_{m,n}}$	Spatial overlap of test mass eigenmode m with optical mode n
$\boldsymbol{C}$	Variously specific heat capacity, clipping/loss matrix used in calculation of parametric gain and optical beam coupling coefficient
$\boldsymbol{c}$	Speed of light in vacuum, 2.998×10^8 ms^{-1}
$\boldsymbol{C_{\mathrm{elast}}}$	Elasticity matrix
$\boldsymbol{\chi}$	Variously reduced radiation constant and eigenvalue
$\boldsymbol{c_m}$	Geometric overlap of cavity mode with test mass mechanical mode m

$\boldsymbol{D}$	Variously electrical displacement and mesa beam integration disc
$\boldsymbol{d}$	Coating thickness
$\boldsymbol{\delta}$	Dirac delta function
$\boldsymbol{\Delta f_{\mathrm{FWHM}}}$	Cavity linewidth
$\boldsymbol{\Delta f_N}$	Higher order mode spacing
$\boldsymbol{\delta_{ij}}$	Kronecker's delta
$\boldsymbol{\Delta L_{\mathrm{FWHM}}}$	Cavity linewidth
$\boldsymbol{\Delta\psi}$	One way cavity Gouy phase
$\boldsymbol{\delta U}$	Linear elastic energy density
$\boldsymbol{\Delta V}$	Differential voltage between bias and control electrodes of ESD
$\boldsymbol{\Delta x}$	Translation of cavity optical axis due to mirror tilt
$\boldsymbol{ds}$	Proper distance
$\boldsymbol{E}$	Variously energy, electric field amplitude and strain tensor
$\boldsymbol{\vec{e}_i}$	i^{th} column of the identity matrix
$\boldsymbol{\epsilon}$	Coating absorption rate
$\boldsymbol{\varepsilon}$	Electrical permittivity
$\boldsymbol{\eta}$	Quantum efficiency
$\boldsymbol{\eta_{\mu\nu}}$	Minkowski tensor
$\boldsymbol{F}$	Variously force and heat flux
F	Digital signal representing force applied to ESD
$\boldsymbol{f}$	Variously linear frequency in Hz, spatial form factor and focal length
$\boldsymbol{F_{\mathrm{app},m}}$	ESD force effectively coupled into test mass mechanical mode m
$\boldsymbol{f_c}$	3 dB corner frequency

$\boldsymbol{F_{\mathrm{ESD}}}$	Peak-to-peak force from the electrostatic drive
$\boldsymbol{f_{\mathrm{ESD}}}$	Force density across rear surface of test mass
$\boldsymbol{\mathcal{F}}$	Cavity finesse
$\boldsymbol{f_{\mathrm{mod}}}$	Linear modulation frequency
$\boldsymbol{f_n}$	Spatial field distribution function of optical mode
$\boldsymbol{f_p}$	Corner frequency of filter pole
$\boldsymbol{F_{\mathrm{rad}}}$	Force due to radiation pressure
$\boldsymbol{f_{\mathrm{FSR}}}$	Free spectral range
$\boldsymbol{f_z}$	Corner frequency of filter zero
$\boldsymbol{G}$	Variously gain and Gouy phase
$\boldsymbol{g}$	Variously Fabry Perot cavity g factor and amplitude gain
$\boldsymbol{\Gamma}$	Phase modulation index
$\boldsymbol{g_{\mu\nu}}$	Metric tensor
$\boldsymbol{G_n^{\pm}}$	Closed loop optical gain of n^{th} higher order mode upper/lower scattering sideband
$\boldsymbol{H_{\mathrm{int}}}$	Interaction Hamiltonian
$\boldsymbol{H}$	Transfer coefficient from applied force to test mass displacement
$\boldsymbol{h}$	Variously Planck's constant and test mass thickness
$\boldsymbol{H_m(x)}$	Hermite polynomial of order m in x
$\boldsymbol{h_{\mu\nu}}$	Strain tensor
$\boldsymbol{h_0}$	Gravitational wave amplitude
$\boldsymbol{I}$	Variously identity matrix and current
$\boldsymbol{I_{00}}$	Intensity profile of fundamental cavity mode
$\boldsymbol{j}$	Complex unit

k	ESD force coupling coefficient in the digital realm
$\boldsymbol{k}$	Variously wavenumber and coupling coefficient between external magnetic fields and force applied to test mass
$\boldsymbol{\kappa}$	Variously thermal diffusivity and demodulation gain coefficient
$\boldsymbol{k_B}$	Boltzmann's constant, 1.381×10^{-23} $\mathrm{m^2kgs^{-2}K^{-1}}$
$\boldsymbol{K_m}$	Damping coefficient of test mass mechanical mode m
$\boldsymbol{k_m}$	Variously solution of $kaJ_1(ka) - \chi J_0(ka) = 0$ and stiffness of test mass mechanical mode m
$\boldsymbol{K_{\mathrm{th}}}$	Thermal conductivity
$\boldsymbol{L}$	Length
$\boldsymbol{\lambda}$	Variously wavelength and Lamé coefficient
$\boldsymbol{L_m^n(x)}$	Generalised Laguerre polynomial in x
$\boldsymbol{M}$	Variously mode matching efficiency and mirror matrix used in calculation of parametric gain
$\boldsymbol{m}$	Mass of test mass
$\boldsymbol{M_{\mathrm{loss}}}$	Mixer loss
$\boldsymbol{\mu}$	Lamé coefficient
$\boldsymbol{\mu_m}$	Modal mass of test mass eigenmode m
$\boldsymbol{\mu_{\mathrm{max}}}$	Maximum allowable single magnet dipole moment
$\boldsymbol{n}$	Refractive index
$\boldsymbol{\nu}$	Stress-temperature modulus
$\boldsymbol{\vec{n}}$	Outward pointing surface normal
$\boldsymbol{\Omega}$	Angular modulation frequency
$\boldsymbol{\omega}$	Variously angular frequency and spot size of a Gaussian beam

$\boldsymbol{\omega_g}$	Waist size of Gaussian beam optimally coupled to a particular mesa mode
$\boldsymbol{\omega_0}$	Waist size of a Gaussian beam
$\boldsymbol{\mathcal{O}_n}$	Order of n^{th} order higher order mode
$\boldsymbol{P}$	Variously power and pressure
$\boldsymbol{\Phi}$	Test mass loss angle
$\boldsymbol{\phi}$	Variously displacement of test mass normal mode along cavity direction and phase
$\boldsymbol{\Phi_G}$	Higher order mode Gouy phase e.g. $(m+n+1)G(z)$
$\boldsymbol{\Phi_n}$	Total propagation phase of optical field
$\boldsymbol{\Phi_0}$	Propagation phase of fundamental optical field
$\boldsymbol{P_L}$	Optical field propagator
$\boldsymbol{p_m}$	Dini expansion coefficient of optical intensity profile
$\boldsymbol{P_{\text{rad}}}$	Radiation pressure
$\boldsymbol{\Psi}$	Optical field
$\boldsymbol{P_0}$	Integrated laser power
$\boldsymbol{Q}$	Variously mechanical quality factor and quadrupole moment
$\boldsymbol{q}$	Complex beam parameter
$\boldsymbol{Q_m}$	Mechanical quality factor of test mass eigenmode m
$\boldsymbol{Q_p}$	Quality factor of filter pole
$\boldsymbol{Q_z}$	Quality factor of filter zero
$\boldsymbol{R}$	Variously mirror radius of curvature, transimpedance gain, wavefront curvature and scalar curvature
$\boldsymbol{r}$	Mirror/cavity amplitude reflectivity
$\boldsymbol{\rho}$	Variously mass density and number density
$\boldsymbol{\rho_{\text{E}}}$	Elastic energy density
$\boldsymbol{\rho_{\text{free}}}$	Free charge density

$\boldsymbol{\varrho_m}$	Dini expansion coefficient of optical intensity's form factor
$\boldsymbol{\mathcal{R}_m}$	Parametric gain associated with test mass eigenmode m
$\boldsymbol{R_{\mu\nu}}$	Ricci tensor
$\boldsymbol{S}$	Matrix of nodewise optical transfer coefficients
$\boldsymbol{\mathcal{S}}$	Surface of test mass normal to cavity direction
$\boldsymbol{S_\alpha}$	Fiducial surface of mesa/hyperboloidal modes
$\boldsymbol{S_{\mathrm{demod}}}$	Voltage output of mixer
$\boldsymbol{\sigma}$	Poisson's ratio
$\boldsymbol{\sigma'}$	Stefan-Boltzmann constant corrected for emissivity
$\boldsymbol{S_{\mathrm{pd}}}$	Photodiode voltage output
$\boldsymbol{\varsigma}$	Power density
$\boldsymbol{T_0}$	Ambient temperature, 300 K
$\boldsymbol{t}$	Variously time and mirror/cavity amplitude transmissivity
$\boldsymbol{\tau}$	Decay constant
$\boldsymbol{\tau_{\mathrm{sto}}}$	Cavity storage time
$\boldsymbol{\Theta}$	Stress tensor
$\boldsymbol{\theta}$	Variously general angles and angle of cavity mirror tilts
$\boldsymbol{\mathcal{T}}$	Temperature field
$\boldsymbol{T_{\mu\nu}}$	Energy-momentum tensor
$\boldsymbol{T}$	Variously difference between test mass temperature $\mathcal{T}$ and ambient temperature T_0 and mirror power transmissivity
$\boldsymbol{U}$	Elastic energy
$\boldsymbol{\vec{u}}$	Displacement vector
$\boldsymbol{\vec{u}_m}$	Displacement vector of test mass normal mode
$\boldsymbol{U_{mn}}$	Hermite-Gaussian transverse mode function
$\boldsymbol{\Upsilon}$	Maxwell stress tensor
$\boldsymbol{U_z}$	Displacement of test mass's reflective surface

$\boldsymbol{V}$	Electrical potential
$\boldsymbol{\mathcal{V}}$	Test mass volume
$\mathbf{V}$	Digital signal representing voltage applied to ESD electrode
$\boldsymbol{v_0}$	Most probable molecular speed
$\boldsymbol{W_{\mathrm{diss}}}$	Dissipated power
$\boldsymbol{x}$	Displacement
$\boldsymbol{x_0}$	Advanced LIGO technical displacement noise limit
$\boldsymbol{Y}$	Variously Young's modulus and mechanical admittance
$\boldsymbol{Z}$	Variously mechanical impedance and additional optical path introduced by thermal lens
$\hat{\boldsymbol{z}}$	Unit vector along cavity direction
$\boldsymbol{z_{\mathrm{HR}}}$	Phase profile of optical field in metres
$\boldsymbol{z_{\mathrm{R}}}$	Rayleigh range

Acronyms

ADC	Analogue to Digital Converter
AdvLIGO	Advanced LIGO
AMD	Acoustic Mode Damper
BHV	Bondu, Hello and Vinet
BSC	Basic Symmetric Chamber
CCD	Charge-Coupled Device
DAC	Digital to Analogue Converter
EOM	Electro-Optic Modulator
EPICS	Experimental Physics and Industrial Control System
ESD	Electrostatic Drive
ETM	End Test Mass
FDT	Fluctuation Dissipation Theorem
FEM	Finite Element Method
FFT	Fast Fourier Transform
FM	Folding Mirror
FPGA	Field Programmable Gate Array
FPM	Fabry-Perot Michelson

GAS	Geometric Anti-Spring
GW	Gravitational Wave
GWINC	Gravitational Wave Interferometer Noise Calculator
HAM	Horizontal Access Module
HEPI	Hydraulic External Pre-Isolator
HG	Hermite-Gauss
HOM	Higher Order Mode
HR	Highly Reflective
HVAC	Heating Ventilating and Air-Conditioning
IM	Input Mirror
ISI	Internal Seismic Isolation
ITM	Input Test Mass
LASTI	LIGO Advanced Systems Test Interferometer
LG	Laguerre-Gauss
LIGO	Laser Interferometer Gravitational wave Observatory
LMA	Laboratoire des Matériaux Avancés
LSC	LIGO Scientific Collaboration
LVDT	Linear Variable Differential Transformer
MEDM	Motif Editor and Display Manager
MH	Mexican Hat
MIT	Massachusetts Institute of Technology
NdFeB	Neodymium Iron Boron, $Nd_2Fe_{14}B$
NPRO	Non Planar Ring Oscillator
ODE	Ordinary Differential Equation

OMC	Output Mode Cleaner
PDE	Partial Differential Equation
PDH	Pound Drever Hall
PI	Parametric Instability
PR	Power Recycling
PZT	Piezoelectric Transducer
SIS	Stationary Interferometer Simulation
SmCo	Samarium Cobalt, $SmCo_5$ or Sm_2Co_{17}
SR	Signal Recycling
TNI	Thermal Noise Interferometer
WFS	Wavefront Sensing

Chapter 1

Introduction

Over the following pages we introduce those fundamental concepts required to fully understand the original part of this work. The level of discussion has been tailored to provide a basic working knowledge with adequate references provided for the more enthusiastic reader.

We begin in section 1.1 by introducing gravitational waves themselves, along with their putative sources. Considering only linearised theory, we show how interferometric detectors are ideally suited to detect this radiation. In section 1.2 we go on to examine the basic design of a contemporary gravitational wave detector, introducing more advanced material as appropriate in the coming chapters. In order to fully appreciate interferometer design and to understand later material, selected ideas in optics are also reviewed (see §1.5). After detailing the major noise sources that limit ground based gravitational wave interferometers in section §1.4, we conclude by discussing the simulation tools used in our work (see §1.6).

1.1 Gravitational radiation

In this section we describe the theory underlying the production of gravitational radiation. We could not hope to approach the expositions found in the many excellent textbooks covering the subject, instead we provide a readable treatment of the basic concepts and direct the reader to the literature for deeper insight [1, 2].

After introducing the idea of the gravitational wave, we discuss a selection of candidate sources for ground based interferometric detectors.

1.1.1 General relativity

Unlike Jansky's chance discovery of radio signals emanating from the centre of the Galaxy in the 1930s [3], the existence of gravitational radiation and the possibility of studying astrophysical objects in a new way has long been predicted [4].

One of the more exotic products of Einstein's general relativity [5], gravitational waves are small disturbances in the very fabric of space-time caused by accelerating aspherical mass distributions. Due to the relatively low strength of the gravitational interaction, matter does not impede gravitational waves in the same way as it does electromagnetic waves. Hence this radiation promises to reveal hitherto obscured information about the Universe.

1.1.1.1 Linear approximation

In Einstein's general theory, the four dimensional proper distance ds between points x^μ and $x^\mu + dx^\mu$ is given by

$$ds^2 = g_{\mu\nu} dx^\mu dx^\nu, \tag{1.1}$$

where $g_{\mu\nu}$ is the metric tensor. The nature of the metric is determined through the Einstein field equations

$$R_{\mu\nu} - \frac{1}{2} g_{\mu\nu} R = \frac{8\pi G}{c^4} T_{\mu\nu}, \tag{1.2}$$

where $R_{\mu\nu}$ is the Ricci tensor, $R = g^{\mu\nu} R_{\mu\nu}$ is the scalar curvature, G is the gravitational constant and $T_{\mu\nu}$ is the energy-momentum tensor.

It is often difficult, if not impossible, to solve (1.2) analytically, due to the inherent non-linearities involved. However when operating in a weak field, where space-time is nearly flat, the equations can be linearised.[1] Under these conditions, following [1, 6, 7], the metric may be written as the Minkowski metric $\eta_{\mu\nu}$ augmented by a small perturbation $h_{\mu\nu}$

$$g_{\mu\nu} \simeq \eta_{\mu\nu} + h_{\mu\nu}. \tag{1.3}$$

For a suitable gauge choice[2] the Einstein field equations in vacuum[3] then reduce to

$$\left(\nabla^2 - \frac{1}{c^2} \frac{\partial^2}{\partial t^2} \right) \overline{h}_{\mu\nu} = 0, \tag{1.4}$$

where we have introduced the trace reverse tensor[4] $\overline{h}_{\mu\nu}$. This equation clearly has wave-like solutions

$$\overline{h}_{\mu\nu} = h_0 A_{\mu\nu} \exp(i k_\mu x^\mu), \tag{1.5}$$

which under our gauge choice are transverse waves[5] propagating at the speed of light[6] – gravitational waves.

By operating in the transverse-traceless gauge,[7] $A_{\mu\nu}$ is tightly constrained. For a wave

[1] Fields may be considered 'weak' except in the close proximity of compact objects or cosmological singularities.

[2] Lorenz gauge condition $\overline{h}^{\mu\nu}{}_{,\nu} = 0$.

[3] i.e. $T_{\mu\nu} = 0$.

[4] $\overline{h}_{\mu\nu} = h_{\mu\nu} - 1/2 \eta_{\mu\nu} h$ where $h = h^\mu{}_\mu$.

[5] $A_{\mu\nu} k^\nu = 0$.

[6] $k_\nu k^\nu = 0$.

[7] Imposing additional constraints $A^\mu{}_\mu = 0$ and $A_{\mu\nu} U^\nu = 0$, where U^ν is any constant timelike unit vector.

travelling in the z direction we may write

$$\overline{h}^{\mathrm{TT}}_{\mu\nu} = h^{\mathrm{TT}}_{\mu\nu} = h_0 A^{\mathrm{TT}}_{\mu\nu} \exp(jk(ct - z)), \tag{1.6}$$

where

$$A^{\mathrm{TT}}_{\mu\nu} = \begin{pmatrix} 0 & 0 & 0 & 0 \\ 0 & h_+ & h_\times & 0 \\ 0 & h_\times & -h_+ & 0 \\ 0 & 0 & 0 & 0 \end{pmatrix}. \tag{1.7}$$

Here we have taken $k = k_0$, $A_{xx} = h_+$ and $A_{xy} = h_\times$. Since we have introduced the parameter h_0 to characterise the strength of the gravitational wave, we restrict the values of $A^{\mathrm{TT}}_{\mu\nu}$ to be 0 or 1.

To compute the effect of a gravitational wave on free masses, we consider the *proper* distance[8] between two particles, one located at the origin and the other located at $(x_0, 0, 0)$, both initially at rest. In this case, for $h_+ = 1$,

$$\Delta l = \int |ds^2|^{1/2} = \int_0^{x_0} |g_{xx}|^{1/2} \, \mathrm{d}x \simeq \left[1 + \frac{1}{2}h_0\right] x_0. \tag{1.8}$$

The effect of the gravitational wave is to produce a 'displacement', i.e. change in the proper distance, between the particles which is proportional to their initial separation. Since $h^{\mathrm{TT}}_{yy} = -h^{\mathrm{TT}}_{xx}$, an analogous argument shows that the proper distance between a particle at the origin and one at $(0, y_0, 0)$ is

$$\Delta l \simeq \left[1 - \frac{1}{2}h_0\right] y_0. \tag{1.9}$$

$A_{\mu\nu}$ has only two independent components, h_+ and $h_\times$, corresponding to two different polarisation states. The '+' state for $h_+ \neq 0$, $h_\times = 0$ and the '×' state for $h_\times \neq 0$, $h_+ = 0$. These states are termed *plus* and *cross* respectively. The effect of gravitational waves having each of these polarisations on a ring of free particles is shown in fig. 1.1.

[8] In the transverse-traceless gauge the coordinate distance between two particles is not changed by a gravitational wave.

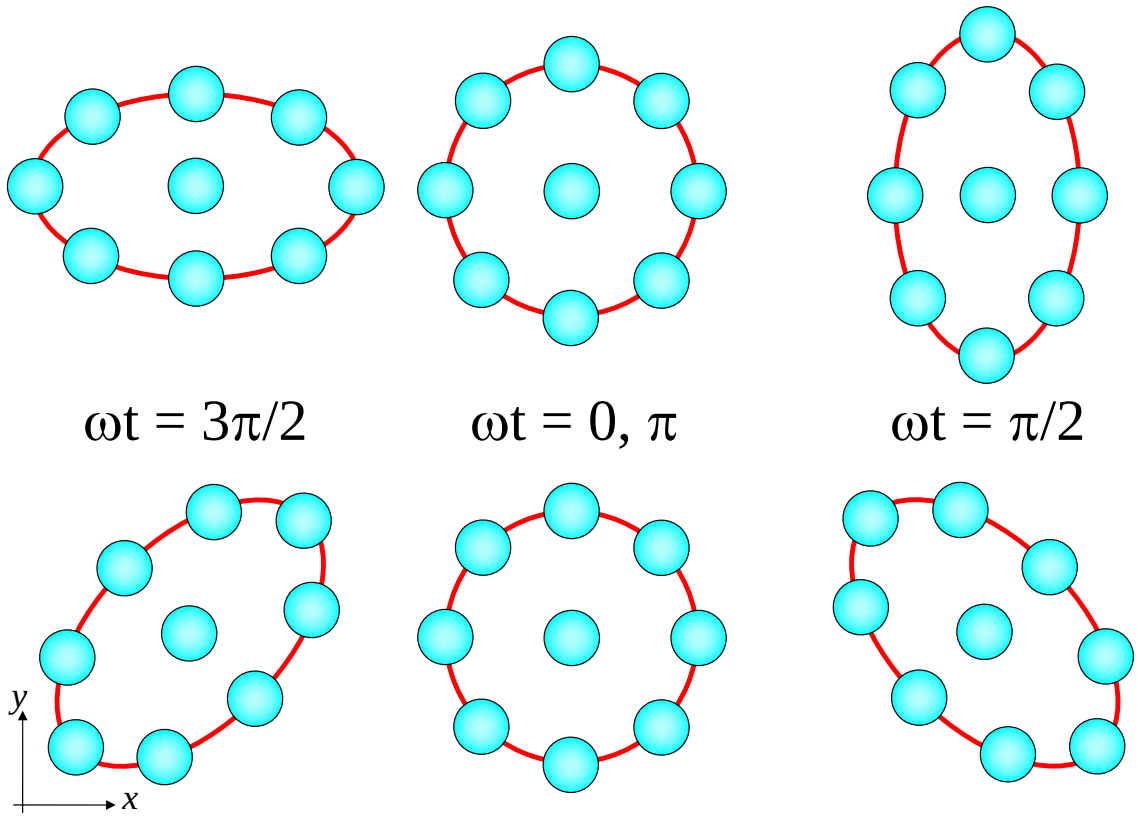

Figure 1.1: The effect of a gravitational wave with plus (top) and cross (bottom) polarisations on a ring of free particles in terms of proper distance from the central particle.

The effects of a gravitational wave may also be considered in a 'rigid' coordinate system which remains unaffected by the incident wave. In this case, for a '+' wave propagating in the z direction, our particle at $(x_0, 0, 0)$ will experience a displacement, in the commonly understood sense, of $\Delta x = (1/2)h_0 x_0$.

So in either representation the 'displacement' between the particles is proportional to their original separation. It is hence common to regard h as a strain.

1.1.2 Sources

Gravitational waves are produced by accelerating mass distributions. Due to mass-energy and momentum conservation, the lowest order multipole which can contribute to Gravitational Wave (GW) emission is the quadrupole moment Q.

Dimensional analysis gives that the magnitude of the strain produced by a gravitational wave is

$$h \sim \frac{G}{c^4}\frac{\ddot{Q}}{r} \sim \frac{G(E^{\rm ns}_{\rm kin}/c^2)}{c^2 r}, \tag{1.10}$$

where $E^{\rm ns}_{\rm kin}$ is the non-symmetric part of the kinetic energy. Setting $E^{\rm ns}_{\rm kin}/c^2 = M_\odot$ and considering sources in the Virgo cluster,[9] yields strains of order $h \lesssim 10^{-21}$.

We may thus conclude that only energetic astrophysical events produce terrestrially measurable GW signals. In the following section we summarise likely sources based on their time evolution. We do, of course, concede that the most interesting detected signals will likely be of unknown origin.

1.1.2.1 Burst

Supernovae in which initial conditions allow an asymmetric collapse are ideal GW candidates as they involve large masses and high accelerations [8]. Stellar collapses are typically short lived emitting broadband radiation down to a few Hz.

Compact binary coalescences, involving any combination of black holes and neutron stars, are another archetypal source of short-lived[10] GWs [9]. As the two massive bodies orbit one another they continually lose energy to gravitational radiation, reducing their orbital radius and period. In the final minutes of their lives the resulting GW signal enters the terrestrial detection band.[11] Moving ever closer, the efficiency of energy loss improves[12] and the signal rapidly increases in frequency and amplitude in what is known as a *chirp*. Eventually the bodies merge, form an excited state and decay to equilibrium.

Coalescent binaries are thought to be one of the most promising sources of gravitational wave signals for ground based detection as it is possible to predict the waveform of the

[9] $r \simeq 20$ Mpc.
[10] At least for ground based detectors.
[11] $\gtrsim 10$ Hz.
[12] A system separated by ∼100 km can lose all of its energy to gravitational radiation in a matter of seconds.

emitted signal to high accuracy and search for it in the detector output via matched filtering [10].

1.1.2.2 Periodic

A spinning neutron star with asymmetry[13] about its rotation axis should emit gravitational radiation at twice the rotation frequency. Known pulsars [11] thus provide an enticing target for gravitational wave searches.

To date more than one hundred such stars have been investigated. For the famous Crab pulsar it has been shown that the power radiated by gravitational waves does not exceed 2% of the available spin-down power [12].

1.1.2.3 Stochastic

One of the most exciting sources of gravitational waves is that due to density fluctuations immediately following the Big Bang.[14] Investigating radiation from this epoch would allow one to discriminate between various cosmological models and probe the early Universe, inaccessible by other means. Strain levels currently predicted by standard inflation models are likely beyond the capability of even second generation interferometers,[15] although correlating the output of multiple detectors does allow useful limits to be set [13].

1.1.3 PSR1913+16

At the time of writing the direct detection of gravitational radiation remains an outstanding goal. However strong evidence for their existence has been found in the

[13]Neutron stars cannot be perfectly axisymmetric. Mechanisms for creating such asymmetries include deformation by magnetic fields and accretion of matter from a nearby object.

[14]Similar to the cosmic microwave background.

[15]Alternative models suggest detectable signals.

behaviour of the binary neutron star system PSR1913+16 [14].

Since one of the stars in this system is a radio pulsar, the orbital parameters of the binary can be determined to high precision.[16] Recording these values as a function of time showed that the orbit was decaying[17] exactly as if it were radiating energy in the form of gravitational waves in accordance with general relativity [15] (see fig. 1.2).

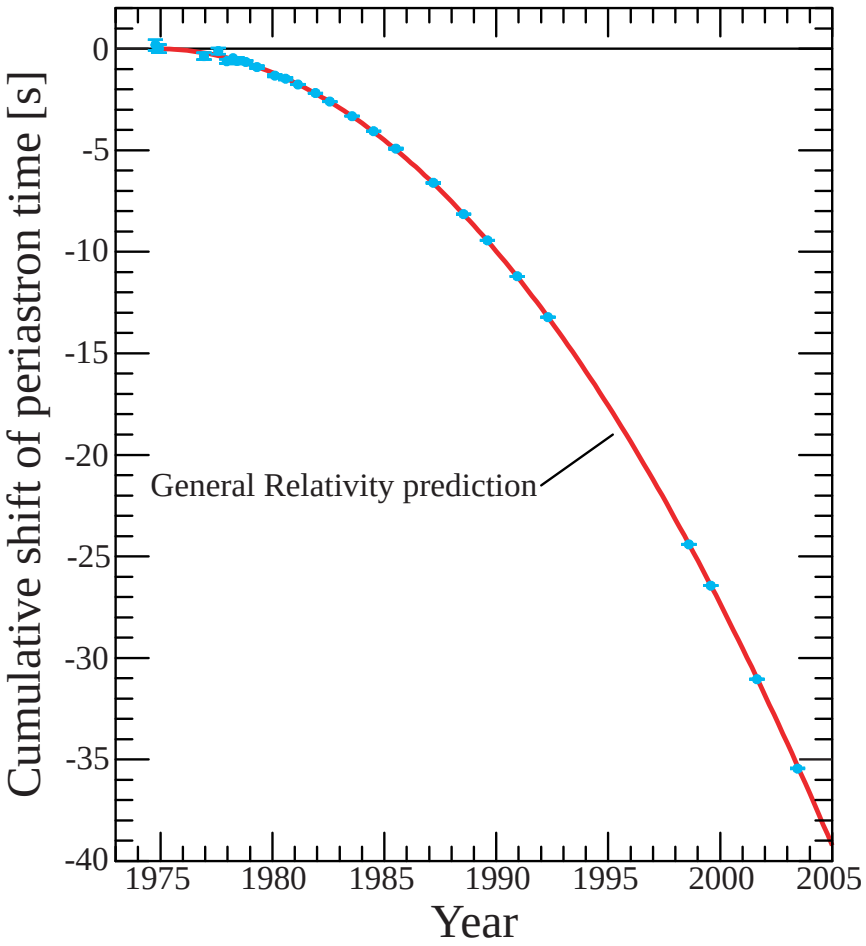

Figure 1.2: The orbit of the binary system PSR1913+16 decays exactly as if it is emitting energy in the form of gravitational waves at the level predicted by general relativity. Here the change in periastron epoch is shown as a function of time (blue) together with the general relativistic prediction (red). The orbital period of the system is ∼0.323 days. Adapted from [15].

[16] Better than one percent.
[17] By about 3 mm per cycle.

1.2 Interferometric gravitational wave detectors

In this section we describe the design of contemporary interferometric gravitational wave detectors. We start with the basic detection principle (§1.2.1) before moving on to describe more advanced light recycling techniques in sections 1.2.3 and 1.2.4. We finish our review by discussing future prospects for long baseline interferometers and introducing other detector types.

Although the existence of gravitational waves was predicted in 1916 [5] it was not until the 1960s that serious attempts to detect them began. This effort originated with Joseph Weber's room temperature acoustic detectors [16, 17]. Such instruments operate by measuring the effects a gravitational wave has on the fundamental resonant mode of a large aluminium bar [18, 19]. Following the lack of a confirmed detection, bar detectors operating at and below the boiling point of liquid helium with improved transducers were constructed. Work in this field continued, with modern resonant detectors achieving strain sensitivities of $h \sim 10^{-21}$ Hz$^{-1/2}$ over a few Hz bandwidth [20, 21, 22, 23]. Acoustic detectors have recently fallen out of favour but some interesting new projects have been funded (e.g. [24, 25]).[18]

The narrow detection bandwidth of resonant detectors is a severe constraint. A more promising design of gravitational wave detector, offering the possibility of high sensitivity over a wide frequency band, uses laser interferometry to interrogate the positions of widely separated test masses freely suspended as pendulums.

The study of ground based detectors of this type was pioneered in the 1970s by Forward, Weiss, Drever and Billing [26, 27, 28, 29]. Their work outlined the specifications which must be met in order for an interferometer to be astrophysically sensitive. These guidelines continue to shape the design of gravitational wave interferometers today. We now sketch the conceptual design of such detectors, introducing limiting fundamental noise sources and resulting modifications to the ideal detector in §1.4 below.

[18] These acoustic detectors use spherical, rather than bar-shaped, resonators. Appropriately instrumented, this construction allows both the direction and polarisation of incident gravitational waves to be determined using a single detector.

1.2.1 Michelson

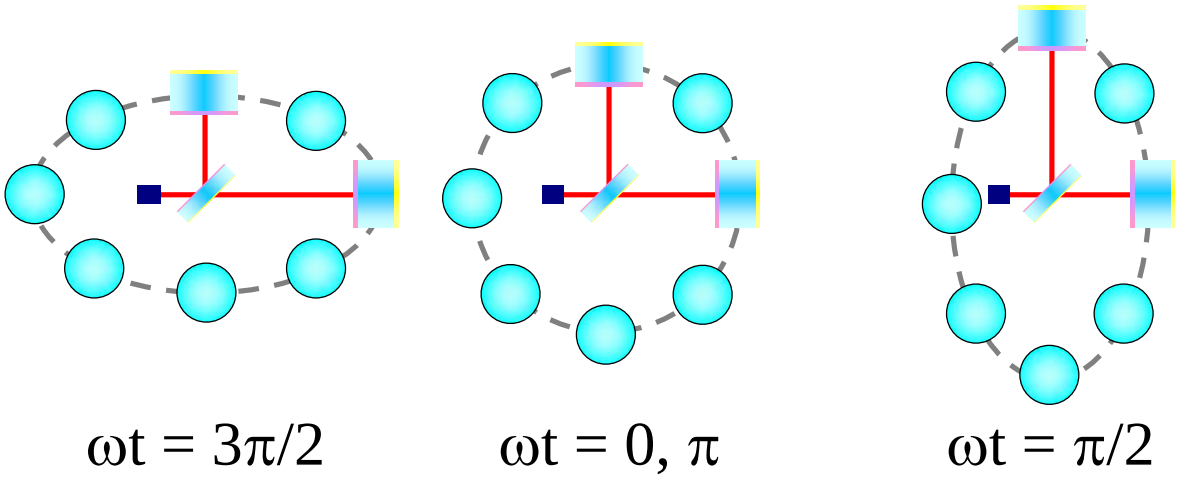

Figure 1.3: The effect of a plus-polarised gravitational wave on a Michelson interferometer with suspended mirrors.

The quadrupolar nature of gravitational waves makes a Michelson interferometer an ideal device with which to attempt detection. Imagine replacing two of the ring of free particles shown in fig. 1.1 with mirrors and the central particle with a beamsplitter (see fig. 1.3).

If the mirrors are suspended from pendulums they will respond just as the free particles in fig. 1.1 and an appropriately polarised gravitational wave will alternately stretch and contract the space separating the mirrors of each arm. This 'displacement' will impart a phase shift on the injected laser light, evidenced by a changing interference pattern at the output of the interferometer.

Consider a low frequency, plus-polarised gravitational wave. As we saw in §1.1, this radiation will, for one particular phase, cause displacements of $\Delta x = (1/2)hL_{\rm arm}$ and $\Delta y = -(1/2)hL_{\rm arm}$ in the x and y arms respectively. Thus the total path length change in each arm is $hL_{\rm arm}$ and the total phase difference of the interfering beams is $\Delta\phi_{\rm GW} = 2khL_{\rm arm}$, where k is the wavenumber.

For mirrors with a reflectivity of unity and a beamsplitter which is perfectly 50-50, the power output at the anti-symmetric port of a Michelson interferometer may be written

as

$$P_{\rm out} = \frac{1}{2} P_{\rm BS}[1 + \cos(\Delta\phi)], \tag{1.11}$$

where $\Delta\phi$ is the differential phase between the beams returning from each arm and $P_{\rm BS}$ is the power on the beamsplitter.[19] Thus the response to our gravitational wave signal is

$$P_{\rm out} = \frac{1}{2} P_{\rm BS}[1 + \cos(\Delta\phi + 2khL_{\rm arm})]. \tag{1.12}$$

1.2.2 Arm cavities

From (1.12) we see that the sensitivity to gravitational wave signals improves with arm length. The frequency dependent peak response is achieved when $L_{\rm arm} = c/4f_{\rm GW}$. For signals with a frequency of 1 kHz this optimal length is around 75 km.

Realising an interferometer with 75 km arms poses significant technical challenges, mainly due to the large beam spots which result and the curvature of the surface of the Earth. A number of alternative solutions, which increase the phase shift effected by a gravitational wave without changing the physical length of the arm, have been found.

The first involves repeatedly bouncing the light back and forth between two mirrors, forming what is known as a *delay line* [30]. In this configuration the effective phase shift is increased by a factor approximately equal to the number of bounces.

A second, currently more popular, approach is to allow the multiple beams of a delay line to converge, forming a Fabry-Perot resonator (see §1.5.2). Including Fabry-Perot cavities in the arms increases their effective length by a factor of $2\mathcal{F}/\pi$, where $\mathcal{F}$ is the arm cavity finesse. Fig. 1.4 shows a Michelson interferometer with Fabry-Perot arms (circled).

[19] The port of the Michelson where the laser light is injected is known as the symmetric port; the port where the photodiode resides is known as the anti-symmetric port.

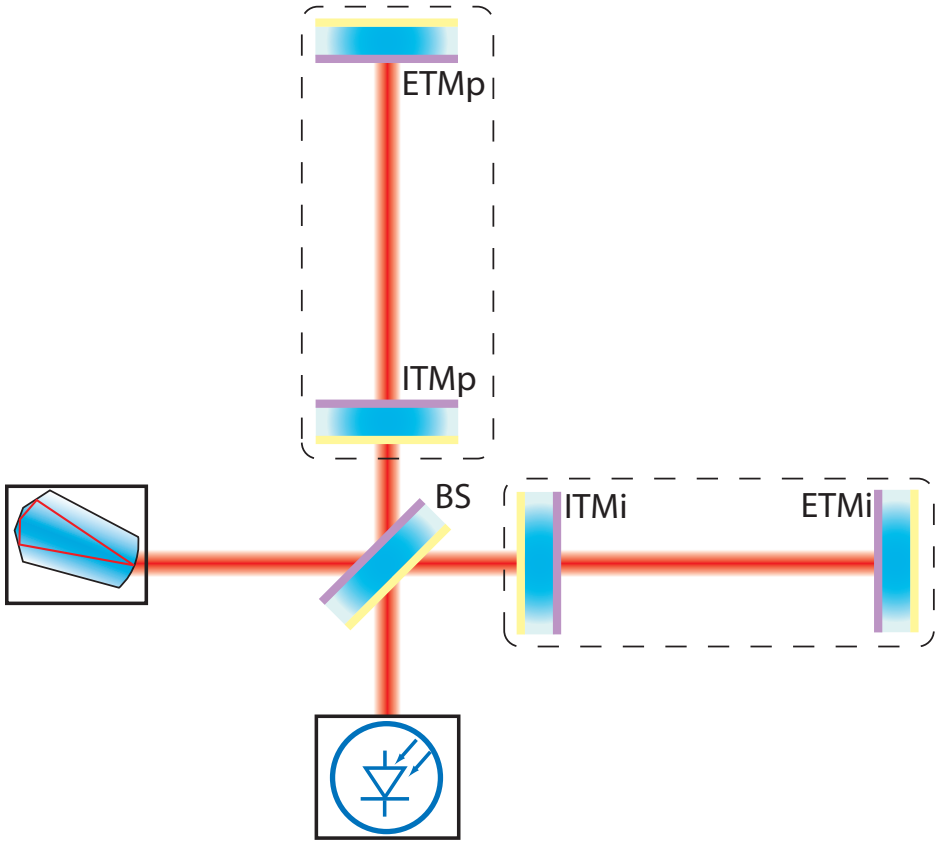

Figure 1.4: A Fabry-Perot Michelson interferometer - input laser, beam splitter (BS), input mirrors (ITMi and ITMp), end mirrors (ETMi and ETMp) and readout photodiode. Suffixes i and p denote the in-line and perpendicular cavities respectively.

1.2.3 Power recycling

In order to reduce shot noise[20] (see §1.4) the output of the Michelson interferometer is generally held at a dark fringe.[21] In this condition the majority of the incident laser power[22] is reflected back toward the laser. By appropriately positioning a partially transmissive *power recycling* mirror between the interferometer and the laser source, the reflected light can be made to interfere constructively with the incoming field, resonantly enhancing input power [31].

The analysis of a power-recycled system can be treated similarly to that of a two mirror Fabry-Perot resonator, where the role of the input mirror is played by the

[20]Which scales with the square root of incident power.
[21]Light returning from both arms toward the anti-symmetric port interferes destructively.
[22]In a lossless interferometer this would be all of the incident power.

Power Recycling (PR) mirror and the end mirror is assigned the complex reflectivity of the Fabry-Perot Michelson (FPM). Working in this way, one finds that the maximum power recycling gain[23] is inversely proportional to the total loss A_{FPM} in the FPM

$$G_{\mathrm{PR}} \simeq \frac{1}{A_{\mathrm{FPM}}}. \tag{1.13}$$

In addition to increasing the effective laser power, the introduction of a power recycling mirror also reduces the interferometer bandwidth for common mode signals. This reduction in linewidth provides an additional level of filtration for noise in the carrier light without affecting differential signals, i.e. gravitational waves, which are not recycled.

Power recycling is currently utilised in all operating detectors, with gain factors ranging from about 30 to ∼2000.

1.2.4 Signal recycling

Just as the power recycling mirror is able to return reflected laser light into the interferometer, so it is also possible to control light exiting the anti-symmetric port of the interferometer with the addition of a *signal recycling* mirror.

In an ideal interferometer, the only field exiting the anti-symmetric port is due to differential arm motion. Thus the addition of a signal recycling mirror between the beamsplitter and detection optics (see fig. 1.5) modifies the response of the instrument to gravitational waves [32, 33]. Considering the cavity formed by the FPM and the Signal Recycling (SR) mirror, the detuning from resonance[24] determines the frequency of gravitational wave sideband which is enhanced and the reflectivity of the SR mirror determines the bandwidth and enhancement factor.

Currently the only long-baseline detector employing signal recycling is GEO600 [34].

[23] i.e. the maximum enhancement of the input laser power.
[24] Controlled by the microscopic position of the SR mirror (see §1.5.2).

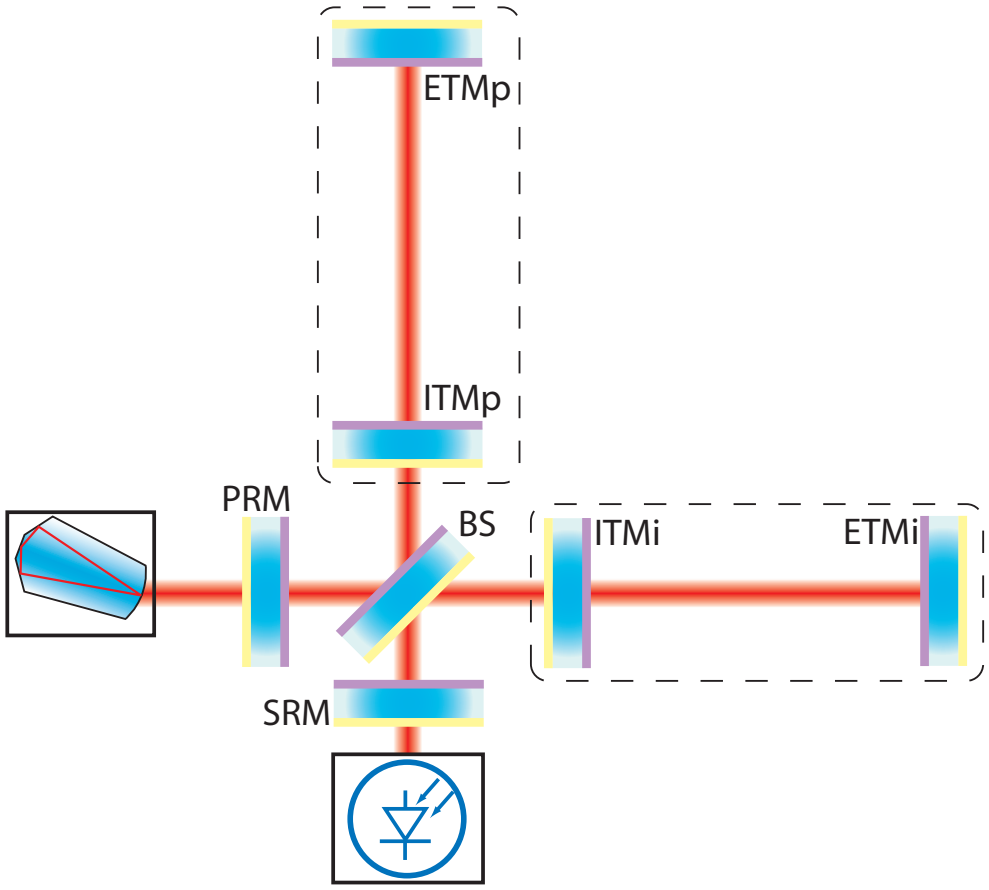

Figure 1.5: A dual-recycled Fabry-Perot Michelson interferometer. The additional vertex optics are necessary for the advanced techniques of power (PRM) and signal (SRM) recycling.

However, in future upgrades other detectors such as LIGO [35] and VIRGO [36] will adopt this advanced technique.

1.2.5 Detector projects

Around the world the effort to detect gravitational waves via interferometric means continues apace.

The British-German GEO600 collaboration operates a 600 m detector near Hannover [37]. GEO600 has pioneered the use of many technologies which will be implemented by other detectors in coming upgrades, such as monolithic suspensions and signal

recycling. In the future GEO600 will increase its input power and incorporate squeezed light [38] to focus on high frequency sensitivity [39].

In contrast, the 3 km French-Italian VIRGO detector [36], located near Pisa, has achieved greater sensitivity than any other instrument at low frequencies thanks to its multi-stage vibration isolation systems which filter seismic noise [40].

The LIGO project, overseen jointly by Caltech and MIT, consists of three detectors[25] distributed over two sites and has led the way in producing astrophysically relevant data. The LIGO interferometers are the most sensitive of the currently operating detectors [35].

Although currently operating the 300 m TAMA detector [41], the thrust of research in Japan is toward the proposed cryogenic detector LCGT [42]. To this end, a prototype low temperature detector, CLIO [43], has been constructed underground in the Kamioka mine to demonstrate the reduction of mirror thermal noise through cooling.

Both LIGO and VIRGO are preparing for major upgrades to become second generation instruments, Advanced LIGO and Advanced VIRGO respectively. These upgrades involve comprehensive modifications of almost every interferometer subsystem.

Input power will be increased from ∼10 W to ∼100 W. Beam spots on the optics will grow by factor of ∼2 to around 6 cm. The test masses themselves will increase in mass from 10 kg or 20 kg to approximately 40 kg. Signal recycling and DC readout [44, 45] will be adopted. Suspension systems will abandon metal wires to suspend fused silica masses from fused silica fibres in a quasi-monolithic fashion. In the case of LIGO, passive seismic isolation stacks will be replaced by actively damped platforms and the place of simple wire-loop suspensions will be taken by multi-stage pendulums with suspended actuators.

With these changes it is hoped that mid-band strain sensitivity will improve by an order of magnitude. Both detectors performed intermediate upgrades, Enhanced LIGO and

[25] Two 4 km in length and one 2 km.

Virgo+, as a stepping stone toward Advanced status [46, 36].

Although the construction of Advanced LIGO is expected to continue until ∼2015, a design study of third generation detectors is currently being made [47]. Funded by the European Union, the goal of this project is to provide an interferometer design which offers 100 times better sensitivity than current detectors. No firm results have been published but it seems likely that the resulting design will incorporate some of the following ideas: longer arms, ∼ 10 km; increased input laser power, ∼ 500 W; squeezing [38], ∼10 dB at all frequencies; larger beams,[26] $\omega \sim 10$ cm; cryogenic temperatures; underground construction; complex multi-stage seismic isolation and larger test masses, ∼100 kg.

Given the work of this thesis, we naturally focus on ground based interferometric gravitational wave detectors. However there exist a number of other detection methods currently being researched. Examples include the space-borne interferometer project LISA [48], pulsar timing [49], spacecraft Doppler tracking [50] and atom interferometry [51].

1.3 Test masses

Central to the operation of an interferometer are the test masses which form its arms, either as the end mirrors of a Michelson or as the boundaries of resonant cavities.[27] Suspended so that they are freely falling, the test masses respond to the passage of gravitational waves; the highly reflective coatings deposited on their surfaces allow one to measure this response. In this section we briefly describe the design of a test mass appropriate for Advanced LIGO (AdvLIGO) as a way of introducing features common to the test masses of all second generation interferometers.

[26] Gaussian or otherwise

[27] The two mirrors of the Fabry-Perot arm cavities are usually called the Input Test Mass (ITM) and End Test Mass (ETM).

1.3.1 Substrate

The test mass substrate is constructed from a cylinder of high quality fused silica,[28] chosen for its mechanical and optical properties.[29] The substrate has a diameter of 34 cm and a thickness of 20 cm, its plane faces have an angle of $\sim 0.1^\circ$ between them and all corners have a 2 mm, 45° chamfer. The size of the substrate is chosen considering the capabilities of the suspension system and future manufacturing processes. In general the substrate should be as large as possible.

A flat surface is machined on either side of the substrate at a distance of ∼163 mm from the optic's centre line. Silica 'ears' are hydroxy-catalysis bonded [53] onto each flat to provide an attachment point for the fused silica fibres which suspend the optic (see fig. 1.6).[30] More information on the AdvLIGO suspension system is given in section 5.3.1.1.

All surfaces of the optic are polished to a five micrometre grit finish. Further attention is paid to the optical surfaces and to the regions where ears will be bonded. For the front surface of the optic, the allowable radius of curvature error is of order 10 m or 0.5%.

In addition to the ears, other items may be attached to the test masses. If the orientation and position of the masses is to be controlled using coil-magnet actuators, four small magnets will be fixed their rear surfaces. AdvLIGO will instead use electrostatic drives (see §5.1.5). To mitigate parametric instabilities, lossy materials or dampers can be attached to the barrels of the masses. AdvLIGO will likely employ acoustic mode dampers (see §5.1.4.4).

[28] Low temperature experiments currently favour sapphire [42] and in the future may adopt silicon [52].

[29] Quantities such as mechanical loss, the coefficient of thermal expansion, the thermo-optic coefficient $\mathrm{d}n/\mathrm{d}T$ and optical absorption are key drivers.

[30] For more traditional wire suspensions, stand-offs or clamps will be attached in similar positions using e.g. epoxy.

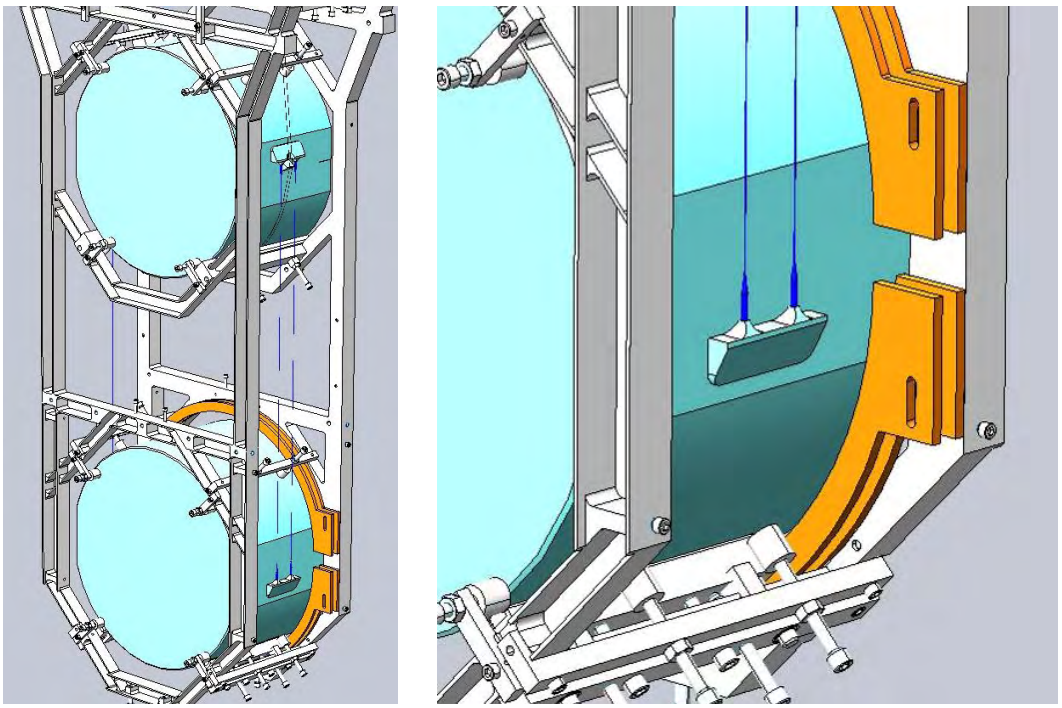

Figure 1.6: Left: Image of the penultimate mass and test mass hanging in the lower suspension structure. Right: Test mass flat and bonded ear. Adapted from [54].

1.3.2 Optical coatings

Since the laser light in the interferometer contains a very narrow range of frequencies, the high reflectivity required of the test masses can be realised by depositing a Bragg mirror on the surface of the substrate. A Bragg mirror consists of a series of thin layers of dielectric material with varying refractive indices. At each interface between materials, part of the incident light undergoes Fresnel reflection. By controlling the thickness of each layer the reflected beams can be made to interfere constructively, resulting in a strong reflection.

One common configuration utilises alternating layers of two materials, one high index, one low (see fig. 1.7). For a given number of layers optimal reflectivity is obtained when the thickness of each layer is $\lambda/4$.[31] As the number of layers increases, so does the reflectivity.

[31] These are the wavelengths *in the medium*. Such a configuration is often called a quarter wave stack.

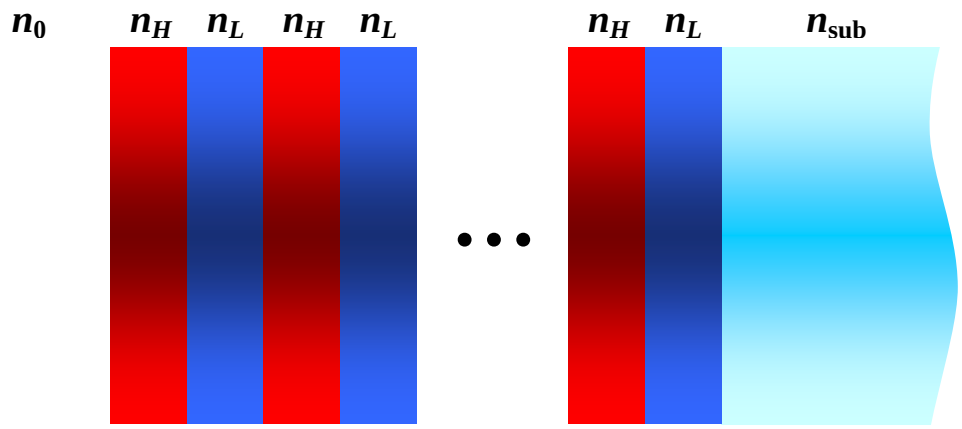

Figure 1.7: The optimal reflectivity Bragg mirror consists of alternating layers of high (n_H) and low (n_L) refractive index material where each layer has a thickness of $\lambda/4$. The refractive indices of the substrate and surroundings are denoted by n_{sub} and n_0 respectively.

The reflectivity of such mirrors may easily be calculated [55]. For each layer we construct a *transfer matrix* given by

$$M_i = \begin{pmatrix} \cos(k_i l_i) & -\frac{j}{n_i}\sin(k_i l_i) \\ -jn_i \sin(k_i l_i) & \cos(k_i l_i) \end{pmatrix}, \tag{1.14}$$

where n_i is the refractive index of layer i, $k_i = 2\pi/\lambda_i = 2\pi n_i/\lambda_0$ is its wavenumber and l_i is its thickness. Normal incidence is assumed. The transfer matrix of the entire stack is got by matrix multiplication

$$M_{\text{stack}} = M_1 M_2 \cdots M_N = \begin{pmatrix} A & B \\ C & D \end{pmatrix}. \tag{1.15}$$

Writing the matrix of the system in this way, the amplitude reflectivity and transmissivity of the mirror are

$$r = \frac{An_0 + Bn_0 n_{\text{sub}} - C - Dn_{\text{sub}}}{An_0 + Bn_0 n_{\text{sub}} + C + Dn_{\text{sub}}}, \tag{1.16}$$

$$t = \frac{2n_0}{An_0 + Bn_0 n_{\text{sub}} + C + Dn_{\text{sub}}}, \tag{1.17}$$

where n_0 and n_{sub} are the refractive indices of the surroundings and mirror substrate

respectively.[32] The power reflectivity of mirrors with 16 and 32 layers are plotted, as a function of wavelength, in fig. 1.8.

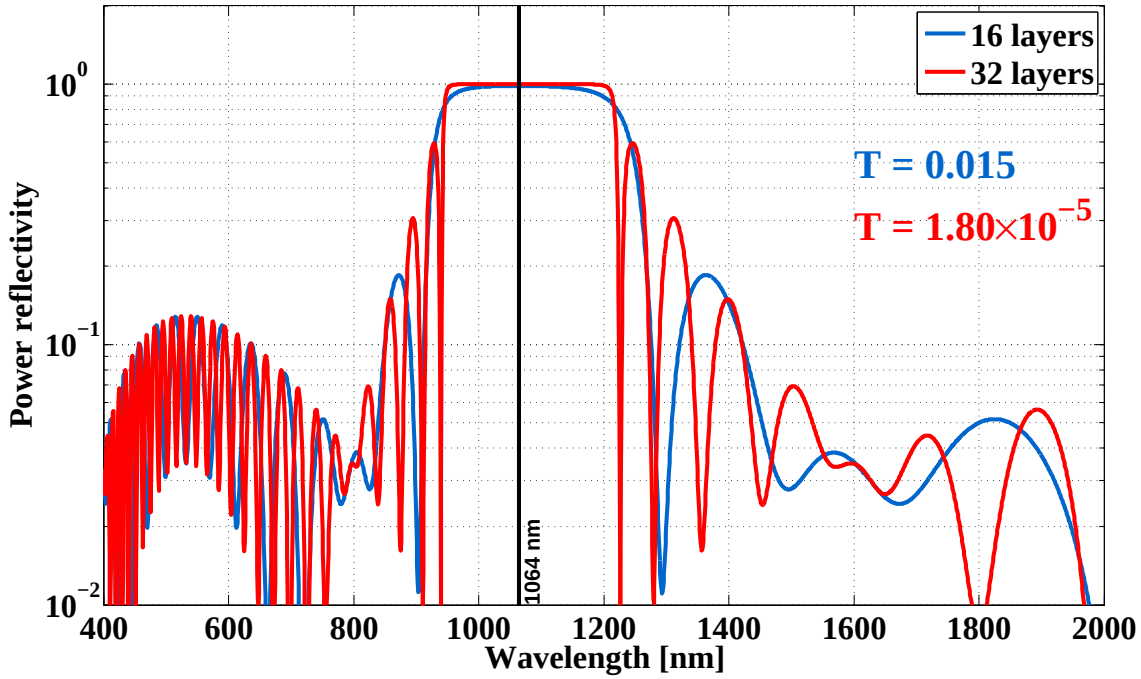

Figure 1.8: Power reflectivity of multilayer dielectric mirrors with 15 and 31 $\lambda/4$ layers and a $\lambda/2$ low index cap layer ($n_H = 2.12,\ n_L = 1.46$). T denotes power transmission.

For AdvLIGO the end mirror transmission is to be below 20 ppm, for the input mirror the current design value is 1.4%. However these are not the only constraints. Other qualities such as absorption, scattering and thermal noise also influence the coating design.

1.3.2.1 Optimised coatings

In future gravitational wave detectors Brownian thermal noise in the test masses' highly reflective coatings is expected to be a significant source of displacement noise (see §4.2.6). Realisation that this thermal noise contribution is dominated by the high

[32] All of the above applies equally to the anti-reflective coatings applied to the rear faces of the test masses. In this case the optimal layer thickness is $\lambda/2$.

index material[33] prompted investigations into the structure of the coating.

Numerical optimisation revealed that by deviating from the standard quarter wave stack thermal noise could be reduced by approximately 20% [57]. The final design used high-low index pairs with a total thickness of $\lambda/2$ as before but instead of two $\lambda/4$ layers the high index layer was made thinner, reducing the total amount of the noisy material. The specified reflectivity of the coating was maintained by adding more layers.

By moving away from quarter wave stacks it is also possible to achieve good reflectivity at more than one wavelength. Such coatings will be used to accommodate deterministic locking schemes employing multiple laser frequencies [58].[34]

1.4 Noise

In this section we present some of the major limiting noise sources which have guided interferometer design or impacted detector operations. We focus mainly on *fundamental* noise sources,[35] introducing *technical* noise sources[36] only as applicable to our work. We consider arms of length 4 km and assume no correlation between the noise observed at opposite ends of each arm.

Since interferometers are designed to detect gravitational wave strain amplitudes, it is often convenient to discuss noise sources in terms of *equivalent strain noise*, i.e. the amplitude of gravitational wave strain which would produce the same measured signal at the output of the interferometer. This idea is utilised even when the noise source

[33]The high and low index materials favoured by the Laser Interferometer Gravitational wave Observatory (LIGO) collaboration are silica and titania-doped tantala [56].

[34]The requirements at the second wavelength are not as stringent as those for the main interferometer beam.

[35] Fundamental noise sources are driven by the underlying laws of physics and cannot be removed. We can however, by clever design of our instruments reduce the impact of these effects. Thermal noise would be a good example of this type of noise.

[36]Technical noise arises due to 'real-world' effects, the kind that are never discussed in the classroom. A good example of technical noise would be RF oscillator phase noise. Identifying and controlling technical noise occupies much of the detector commissioning time.

under consideration is in no sense a strain e.g. mirror thermal noise (see fig. 1.9).

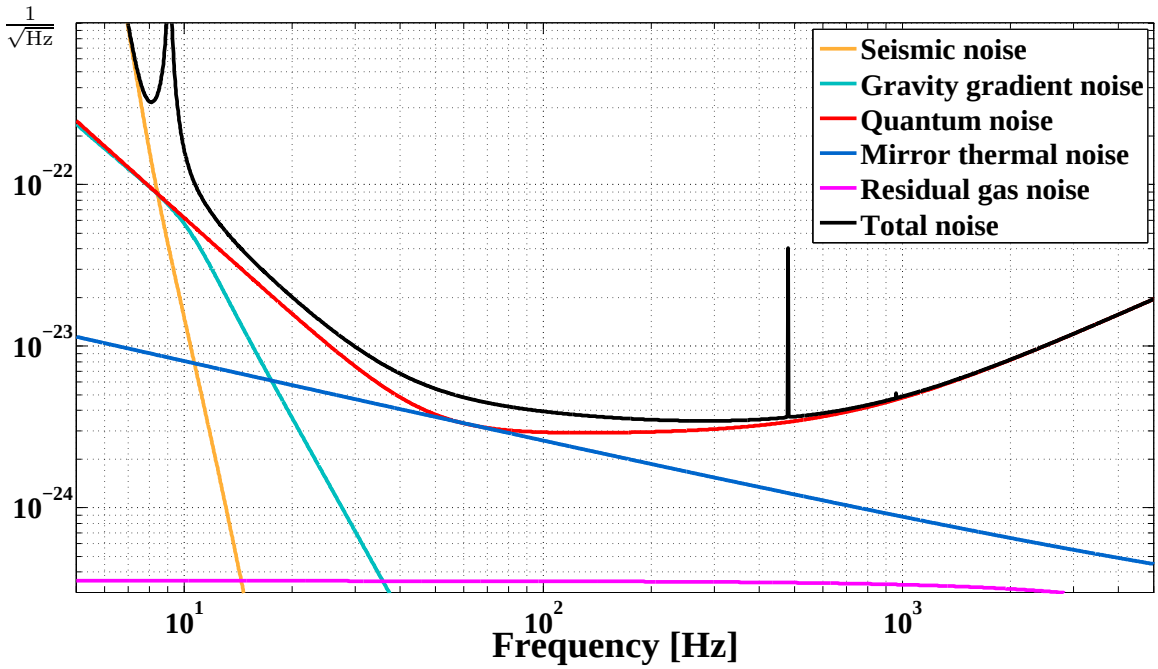

Figure 1.9: Noise from selected sources described in terms of equivalent strain noise. Quantum noise encompasses both radiation pressure noise and shot noise.

1.4.1 Seismic noise

For terrestrial gravitational wave detectors one of the principal limits to low frequency sensitivity is imposed by seismic motion. This noise comes from a variety of sources – ocean waves, human activity and all the pumps, fans and air conditioning equipment necessary at any large scale laboratory.

This noise is strongly site dependent but even at the quietest of locations the motion is several orders of magnitude greater than that expected from gravitational waves. For frequencies above ∼1 Hz

$$h_{\text{seismic}}(f) \sim \frac{10^{-8}}{f^2} \quad \left[\frac{1}{\sqrt{\text{Hz}}}\right]. \tag{1.18}$$

In order to isolate the interferometer's mirrors from ground motion multi-stage iso-

lation systems are used.[37] For a discussion of the solutions employed by the Laser Interferometer Gravitational wave Observatory (LIGO) collaboration see §5.3.1.1.

1.4.1.1 Gravity gradient noise

Newtonian or gravity gradient noise (see e.g. [59]) is a related noise source which cannot be isolated against by traditional methods. This noise emerges when fluctuations in the local gravitational field act on the test masses to produce a measurable displacement. Such fluctuations can arise due to passing seismic waves changing the local density of the earth [60] or by anthropogenic means [61].

The transfer function $T(f)$ from the spectrum of rms seismic displacements averaged over horizontal and vertical directions $W(f)$ to the spectrum of differential test mass motion $x(f)$ has form

$$T(f) = \frac{x(f)}{W(f)} = \frac{4\pi G\rho}{\sqrt{(\omega-\omega_0)^2+\omega^2/\tau^2}}\beta(f), \tag{1.19}$$

where G is the gravitational constant, ρ is the density of the earth near the test mass, ω is the angular frequency of the seismic waves[38] and ω_0 and τ are the resonant frequency and damping time of the test mass pendulums. The parameter $\beta(f)$ is a model dependent dimensionless parameter in the range ∼0.1-1 (see [59, 60]). One estimate of the resulting strain noise is approximately

$$h(f) \sim \frac{5\times10^{-23}}{\sqrt{\text{Hz}}} \times \begin{cases} \left(\dfrac{10\text{ Hz}}{f}\right)^2 & : \quad 3\text{ Hz} \lesssim f < 10\text{ Hz} \\ \left(\dfrac{10\text{ Hz}}{f}\right)^4 & : \quad 10\text{ Hz} < f \lesssim 30\text{ Hz} \end{cases} \tag{1.20}$$

This noise is not of an immediately concerning level but it could be meaningful in second generation instruments around 10 Hz.

Strategies for mitigating gravity gradient noise include active correction using seis-

[37] Pendulums, mass-spring stacks, active hydraulic platforms etc.
[38] And the resulting fluctuating forces.

mometer arrays and underground operation with the test masses housed in spherical caverns [62].

1.4.2 Radiation pressure noise

In order to reduce shot noise (see §1.4.4) scientists continually strive to increase the circulating power in their interferometers. One of the undesirable consequences of this increased power is radiation pressure noise due to fluctuations in the vacuum field entering the anti-symmetric port of the interferometer [63]. The amplitude spectral density of displacement noise arising from these fluctuations is given by [64]

$$\delta x(f) = \sqrt{\frac{P_{\mathrm{circ}} h}{2m^2\pi^4 f^4 c\lambda}} \quad \left[\frac{\mathrm{m}}{\sqrt{\mathrm{Hz}}}\right], \tag{1.21}$$

where m is the mass of an interferometer optic.

This displacement noise may prove troublesome at low frequencies in future interferometers. It may be suppressed either by using more massive optics or by sacrificing high frequency sensitivity through a reduction in laser power.

1.4.3 Test mass thermal noise

One of the principal goals of this work is to investigate the feasibility of using a non-Gaussian optical field in long baseline interferometers. This new mode is of interest as it is predicted to reduce measured test mass thermal noise. Appropriately, a thorough introduction to the principal forms of thermal noise, including an indication of how to quantify their magnitudes, is presented later in §4.2. In this section we provide a concise summary.

The different forms of thermal noise are generally associated with some form of dissipation via the Fluctuation Dissipation Theorem (FDT) (see §4.2). Before discussing

each of these different mechanisms it is important to understand that modern methods of calculating thermal noise, which allow for inhomogeneous loss, have revealed that the physical distribution of dissipation throughout the test mass is important [65, 66]. Loss located closest to the incident laser beam which probes the test mass's position is most important. Hence dissipation mechanisms active in the test masses' dielectric coatings are the leading sources of interferometer displacement noise.

1.4.3.1 Brownian thermal noise

Brownian thermal noise may be thought of as a variation in the position of the mirror's surface due to fluctuations induced by internal friction [67].

Brownian noise is quantified by the introduction of a complex elastic modulus, $Y \rightarrow Y(1 + j\phi)$, the imaginary part of which is known as the *loss angle* [68]. The loss angle is a function of the material in use and is related to its quality factor by $Q = 1/\phi$. The magnitude of Brownian thermal noise is directly related to this material loss. Continuing efforts to measure ϕ (e.g. [69, 70, 71, 72]) have revealed that the dominant contribution to thermal noise comes from the high index layer[39] in the mirror's dielectric coating.

1.4.3.2 Thermoelastic noise

Despite being in equilibrium with an external reservoir, the test mass continually exchanges energy with its surroundings. Although not strictly correct, it is convenient to regard these energy fluctuations as fluctuations in temperature. For test mass materials with non-negligible coefficients of thermal expansion these fluctuations will give rise to motion.

Alternatively, one can view thermoelastic noise as a result of a thermoelastic damping process. Braginsky et al. [73] showed that the application of a periodic pressure to the

[39] Ta_2O_5.

surface of the test mass induces heat flux and therefore energy dissipation.

Concern regarding thermoelastic noise originally motivated the switch to non-Gaussian beams. In current interferometer designs thermoelastic noise is no longer the chief concern but it may be important in future interferometers employing test mass substrate materials such as sapphire.

1.4.3.3 Thermorefractive noise

Just as non-null coefficients of thermal expansion give rise to measured displacement noise, so too do non-null thermo-optic coefficients,[40] through changes in the phase of the reflected light. This noise is particularly important in transmissive optics [74] and in the highly reflective coatings applied to the test masses, as materials in thin film form can have much larger values of β [75, 76].

Recent research efforts [77] have shown that, since they are driven by the same temperature fluctuations, thermoelastic and thermorefractive noises in dielectric coatings may be treated as a single *thermo-optic* noise. This coherent treatment revealed that the two mechanisms appear with a relative *negative* sign so that their combined contribution has previously been overestimated. Including the cancellation effect, this noise becomes insignificant in comparison to coating Brownian noise and should not be considered a key driving force in coating design for second generation interferometers.

Direct measurement of test mass thermal noise is an extremely difficult task requiring highly specialised apparatus. One such setup, known as the Thermal Noise Interferometer (TNI), has been constructed at the California Institute of Technology [78, 79, 80]. This device, modelled after the initial LIGO interferometers, is used to test the properties of mirrors destined for full scale detectors.

Methods being explored for the reduction of test mass thermal noise include operation at cryogenic temperatures [43, 42], modifications to the optical modes used in the

[40] $\beta = \mathrm{d}n/\mathrm{d}T$.

interferometer (see §2.1) and implementation of improved materials.

Prospects for the first two methods seem bright. Although experimentally challenging, there exist known pathways toward reduced thermal noise. However, the search for improved materials is a more difficult task as the mechanisms which give rise to mechanical loss, and therefore thermal noise, are just beginning to be understood.

1.4.4 Shot noise

A fundamental limit to the sensitivity of optical readout in gravitational wave interferometers is set by shot noise in the detected light power. The detection process is assumed to obey Poisson statistics, so that the amplitude spectral density of noise associated with P_{dc} watts of detected power is

$$\delta P(f) = \sqrt{\frac{2P_{\mathrm{dc}}hf}{\eta}} \quad \left[\frac{\mathrm{W}}{\sqrt{\mathrm{Hz}}}\right], \tag{1.22}$$

where η is the quantum efficiency of the photodiode and h is Planck's constant.

The equivalent strain noise introduced by photon shot noise is dependent on both the optical configuration of the interferometer and the particular scheme used to read out differential arm motion.

Consider the case of a Michelson interferometer (see §1.2.1) operating at half-fringe, the point where differential arm motion produces the largest response. In this configuration $\Delta\phi = \pi/2$ (see (1.11)). Detecting signals at both the symmetric and anti-symmetric ports, the total dc power recorded and $\mathrm{d}P_{\mathrm{dc}}/\mathrm{d}\Delta\phi$ are both equal to P_{BS}. The resulting shot noise limited phase sensitivity is

$$\delta\phi(f) = \left.\frac{\mathrm{d}\Delta\phi}{\mathrm{d}P_{\mathrm{dc}}}\right|_{\Delta\phi=\pi/2} \delta P_{\mathrm{dc}}(f) = \sqrt{\frac{2hf}{P_{\mathrm{BS}}\eta}} \quad \left[\frac{\mathrm{rad}}{\sqrt{\mathrm{Hz}}}\right], \tag{1.23}$$

or in terms of strain

$$\delta h(f) = \left.\frac{\mathrm{d}h}{\mathrm{d}P_{\mathrm{dc}}}\right|_{\Delta\phi=\pi/2} \delta P_{\mathrm{dc}}(f) = \frac{1}{\pi L}\sqrt{\frac{h\lambda c}{8P_{\mathrm{BS}}\eta}} \quad \left[\frac{1}{\sqrt{\mathrm{Hz}}}\right]. \tag{1.24}$$

In reality, due to power recycling, long baseline gravitational wave interferometers do not operate at half fringe. Maximising the signal to shot noise ratio in a power recycled interferometer, one finds that the optimal working point is in fact just a small offset from the dark fringe. In such instruments shot noise is usually the dominant noise source above a few hundred Hz.

1.4.5 Residual gas noise

The sensitivity of modern interferometers is such that even statistical fluctuations in the density of residual gas in the vacuum enclosure is of concern. These effects were a strong influence on the design and cost of first generation interferometer facilities. Taking account of the variation in spot size $\omega(z)$ along the length of the arm, one model [81] predicts the power spectral density of optical path length variation to be

$$S_L(f) = \frac{4\rho(2\pi\alpha)^2}{v_0} \int_0^{L_{\mathrm{arm}}} \frac{\exp[-2\pi f\omega(z)/v_0]}{\omega(z)}\,\mathrm{d}z \tag{1.25}$$

for a particular molecule with number density ρ, most probable speed v_0 and polarisability α. The amplitude spectral density of differential arm length variations will be $\sqrt{2S_L(f)}$.

Formulae such as this provide maximum allowable pressures for each type of gas and inform the design of vacuum systems. For example, the LIGO detector does not allow residual gas phase noise above the $h \sim 10^{-24}$ level at 100 Hz. For hydrogen this limits the pressure to a maximum of 10^{-6} torr throughout a 20,000 m^3 envelope. Such specifications have been met but as we progress toward third generation detectors facility limits will likely be tested.

The direct interaction of residual gas with the interferometer's suspended test masses can also introduce measurable noise. This noise source has recently become an issue of concern for the AdvLIGO detectors. In these instruments a second cylinder of fused silica is suspended directly behind each test mass at a nominal separation of 5 mm (see fig. 5.12). This *reaction mass* accommodates actuators which control the position and orientation of the test mass (see §5.1.5). Recent findings indicate that the narrow gap between the two masses will lead to enhanced gas damping, even when pressures are low enough such that collisions between the gas molecules themselves may be ignored [82].

Estimates of the displacement noise resulting from gas damping are a strong function of the gas pressure achieved in the vacuum system. Current estimates suggest that gas damping noise will be comparable to radiation pressure noise at low frequencies[41] [83, 84, 85], making it one of the principal components of the interferometer noise budget.

Possible methods of reducing gas damping noise include: increasing the separation between the two masses, modifying the reaction mass so that gas flow is less constrained[42] or working to reduce the residual gas pressure. Whichever scheme is chosen many practical issues remain to be overcome [83] and any modifications may be implemented as a retrofit after AdvLIGO has already commenced operation.

1.4.6 Laser frequency noise

For a single Fabry-Perot cavity, fluctuations in laser frequency are indistinguishable from cavity length variations. The spectral density of fundamental frequency noise[43] is given by [86]

$$f_{\text{noise}} = \Delta f_{\text{FWHM}} \sqrt{\frac{2hf}{P_{\text{laser}}}} \quad \left[\frac{\text{Hz}}{\sqrt{\text{Hz}}}\right], \tag{1.26}$$

[41] $\sim$ 10 Hz to $\sim$ 40 Hz.
[42] For example machining channels in its surface.
[43] The Schawlow-Townes limit.

where Δf_{FWHM} is the cold laser cavity linewidth. This noise level is independent of frequency and is due to perturbations of the carrier field via spontaneous emission and linear losses in the laser resonator.

The output frequency noise of real lasers is more usually dominated by other noise sources which vary the path length in the laser resonator. These effects give the spectral density of noise a $1/f^n$ dependence, particularly at low frequencies.

Gravitational wave detectors go to great lengths to stabilise the frequency of their laser light, locking it to a series of stable resonators and finally to the common mode of the interferometer itself (see e.g. §5.1.4 of [87]).

1.5 Optics

Below we introduce the key ideas in optics necessary to understand both the design of gravitational wave detectors and the results of the coming sections. We begin by introducing the Gaussian beam and describing its properties before moving on to optical resonators.

1.5.1 Gaussian beams

Our work concerns the interaction of coherent, monochromatic laser light with structures far larger than the laser wavelength. Under these conditions Maxwell's equations for beam propagation can be replaced with the Helmholtz equation

$$(\nabla^2 + k^2)\Psi(x, y, z) = 0, \tag{1.27}$$

where $k = 2\pi/\lambda$ is the wavenumber and $\Psi(x, y, z)$ is the complex electric field. For a beam propagating in the z direction, with only slow variation in the transverse dimensions, we write $\Psi(x, y, z) = \psi(x, y, z)\exp(-jkz)$, where $\psi(x, y, z)$ is a slowly

varying complex function which describes the differences between a laser beam and a plane wave. We then assume paraxial behaviour $\partial^2\psi/\partial z^2 \simeq 0$ so that (1.27) becomes

$$\left(\frac{\partial^2}{\partial x^2} + \frac{\partial^2}{\partial y^2} - 2jk\frac{\partial}{\partial z}\right)\psi = 0, \tag{1.28}$$

the paraxial wave equation.

The paraxial wave equation supports an infinite number of solutions, one of which is the Gaussian beam. Use of this particular solution is widespread as it is an eigenmode of free space,[44] it remains Gaussian upon propagation through optical systems,[45] it is the lowest order resonant mode in spherical mirror cavities and the output mode of most laser systems is Gaussian. This mode may be expressed as

$$\Psi(x,y,z) = \sqrt{\frac{2}{\pi\omega^2(z)}}\exp\left[-\frac{x^2+y^2}{\omega^2(z)} - \frac{jk(x^2+y^2)}{2R(z)} - j(kz - G(z))\right]. \tag{1.29}$$

The Gaussian beam can be characterised at all points along its propagation axis by two parameters – the radius of curvature of its wavefront $R(z)$ and the radius $\omega(z)$ at which the beam intensity drops to $I_{\max}/e^2$, often called the *spot size*. The minimum value of the spot size,[46] known as the *waist*, is denoted by ω_0. Defining a characteristic length scale z_{R} known as the *Rayleigh range*

$$z_{\mathrm{R}} = \frac{\pi\omega_0^2}{\lambda}, \tag{1.30}$$

$R(z)$ and $\omega(z)$ are given by

$$R(z) = z\left[1 + \left(\frac{z_{\mathrm{R}}}{z}\right)^2\right] \quad \text{and} \quad \omega(z) = \omega_0\sqrt{1 + \left(\frac{z}{z_{\mathrm{R}}}\right)^2}. \tag{1.31}$$

The behaviour of these quantities on propagation is shown in figures 1.10 and 1.11. At the waist the Gaussian beam wavefront is flat; at $z = z_{\mathrm{R}}$ it achieves its minimum

[44] As it propagates a Gaussian beam remains Gaussian, only the beam width varies.
[45] Ideal lenses, mirrors etc.
[46] Which must be large in comparison to λ under the paraxial approximation.

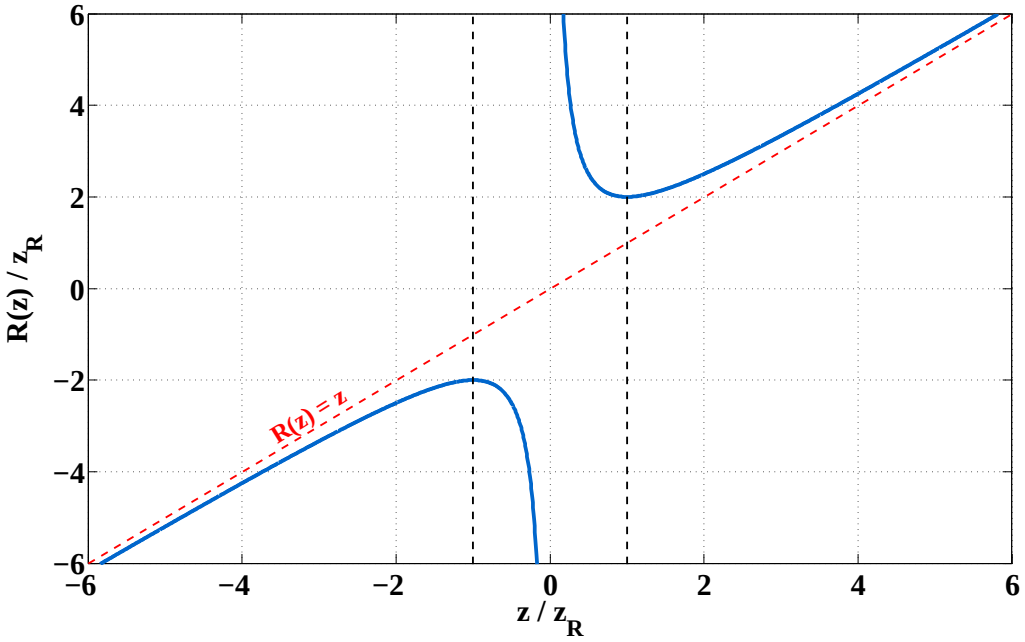

Figure 1.10: Wavefront curvature of a Gaussian beam upon propagation.

radius of $2z_{\mathrm{R}}$. On propagation beyond the Rayleigh range the wavefront curvature approximates that of a spherical wave $R(z) \simeq z$. Propagating from the waist to z_{R} the beam's spot size grows by a factor of $\sqrt{2}$ in radius and 2 in area. Thereafter growth is quasi-linear with $\omega(z) \simeq \omega_0 z/z_{\mathrm{R}}$.

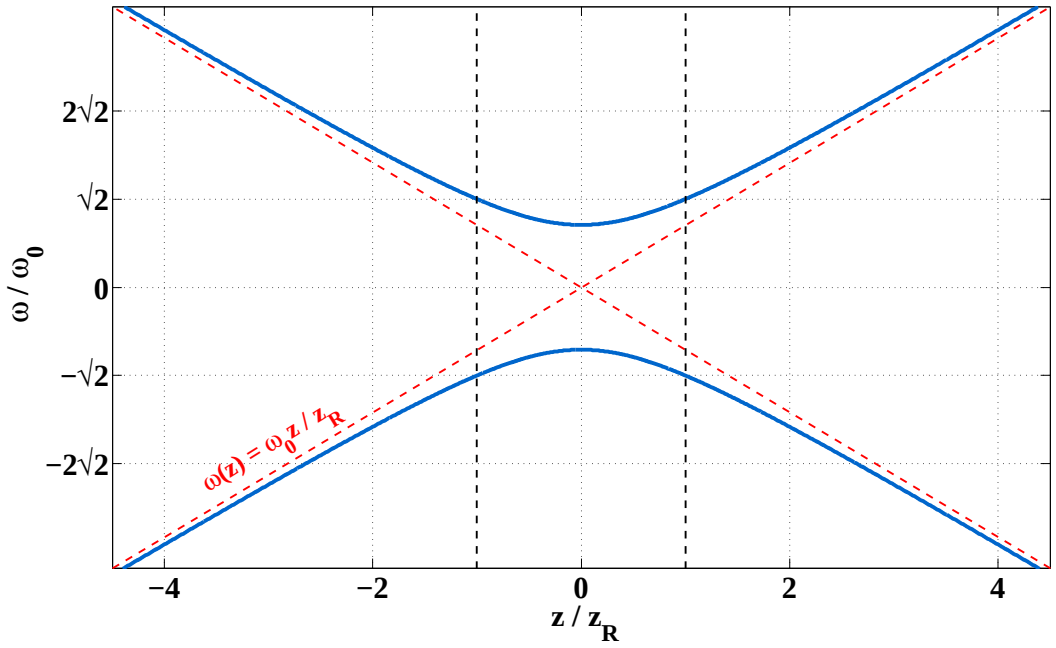

Figure 1.11: Spot size of a Gaussian beam upon propagation.

The term $G(z)$ is known as the Gouy phase and represents the retardation of our Gaussian beam solution relative to an equivalent plane wave [88]. This phase may be written

$$G(z) = \arctan\left(\frac{z}{z_{\mathrm{R}}}\right). \tag{1.32}$$

The overall Gouy phase shift propagating from far field to far field through a focus is π (see fig. 1.12). This additional phase breaks the degeneracy of optical resonators (see §1.5.2) and plays a crucial role in the separation of differential wavefront sensing signals (see §3.2.1.1).

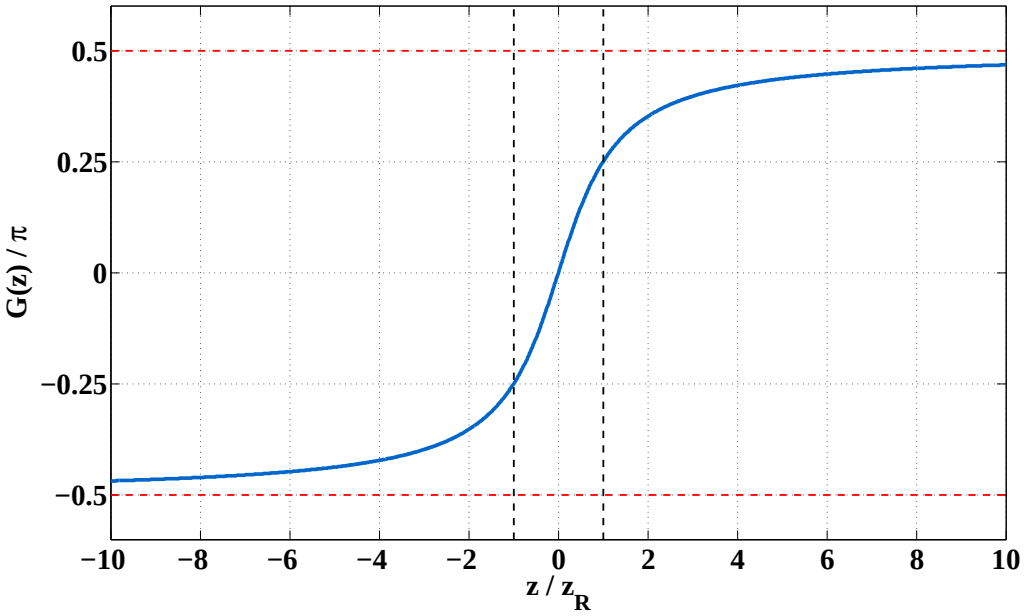

Figure 1.12: Gouy phase of a Gaussian beam upon propagation.

1.5.1.1 Higher order modes

The Gaussian beam is only one solution of the paraxial wave equation (1.28) with special properties. In this section we address two solution families, called *modes of propagation*, which form complete sets of basis functions Ψ_{mn}. Any optical mode can be expressed as a linear combination of these modes $\Psi' = \sum_{m,n} c_{mn}\Psi_{mn}$.

Hermite-Gaussian modes In standard Cartesian coordinates the propagation modes may be written

$$\begin{aligned}\Psi_{mn}(x,y,z) =& \sqrt{\frac{2}{2^{m+n}m!n!\pi\omega^2(z)}} H_m\left(\frac{\sqrt{2}x}{\omega(s)}\right) H_n\left(\frac{\sqrt{2}y}{\omega(s)}\right) \\ & \times \exp\left[-\frac{x^2+y^2}{\omega^2(z)} - \frac{jk(x^2+y^2)}{2R(z)} - j(kz-(m+n+1)G(z))\right],\end{aligned} \tag{1.33}$$

where $H_i(x)$ denotes a Hermite polynomial of order i in x and all other parameters are as before.

The first few Hermite polynomials are

$$\begin{aligned} H_0(x) &= 1, \\ H_1(x) &= 2x, \\ H_2(x) &= 4x^2 - 2. \end{aligned} \tag{1.34}$$

The intensity profiles of the lowest order Hermite-Gaussian modes are plotted in fig. 1.13. Notice that the mode Ψ_{mn} has m nodes in the x direction and n nodes in the y direction. Also note that Ψ_{00} is nothing other than the standard Gaussian beam described above. For this reason, the Gaussian beam is often called the fundamental or lowest order mode. Modal expansions in the Hermite-Gauss (HG) basis are often used when modelling spherical mirror resonators. These modes are particularly adept in describing beams propagating along an axis which is tilted or translated with respect to the fiducial frame (see §3.2.1.1).

Laguerre-Gaussian modes The propagation modes may also be expressed in cylindrical coordinates (r,ϕ,z) as

$$\begin{aligned}\Psi_{mn}(r,\phi,z) =& \sqrt{\frac{4}{(1+\delta_{n0})\pi\omega^2(z)}\frac{m!}{(m+n)!}} \left(\frac{\sqrt{2}r}{\omega(z)}\right)^n L_m^n\left(\frac{2r^2}{\omega^2(z)}\right)\cos(n\phi) \\ & \times \exp\left[-\frac{r^2}{\omega^2(z)} - \frac{jkr^2}{2R(z)} - j(kz-(2m+n+1)G(z))\right],\end{aligned} \tag{1.35}$$

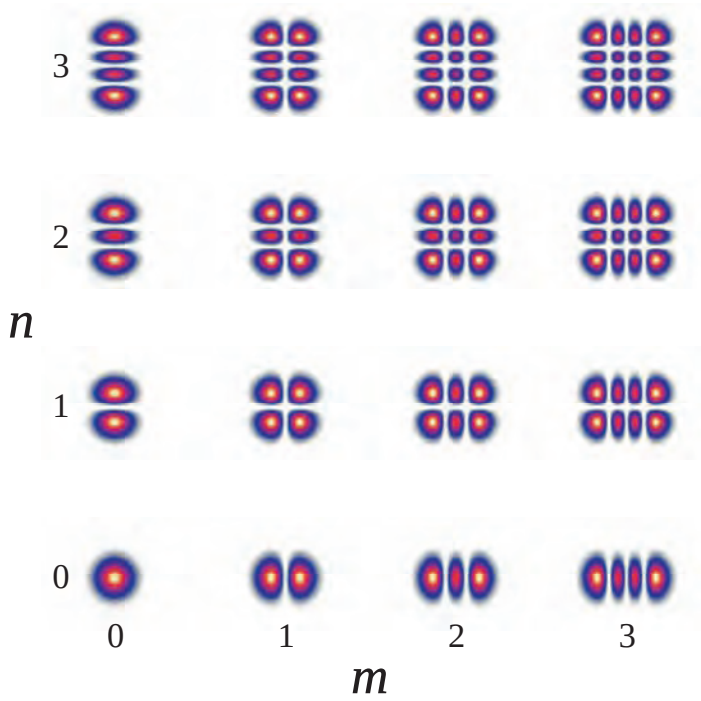

Figure 1.13: The intensity profiles of low order Hermite-Gaussian modes. The Ψ_{mn} mode has m nodes in the x direction and n in the y direction.

where $L_m^n(x)$ are the generalised Laguerre polynomials

$$L_m^n(x) = \frac{e^x}{m!x^n}\left(\frac{d}{dx}\right)^m (x^{n+m}e^{-x}). \tag{1.36}$$

The definition of angle is arbitrary, we may replace the $\cos(n\phi)$ term with $\sin(n\phi)$, preserving a solution. We may also replace it with $\exp(jn\phi)$ to obtain modes exhibiting an axially symmetric intensity profile. Such modes are known as a *helical* Laguerre-Gauss (LG) modes due to the shape of their phasefronts. Helical LG modes can be written

$$\begin{aligned}\Psi_{mn}(r,\phi,z) =& \sqrt{\frac{2}{\pi\omega^2(z)}\frac{m!}{(m+n)!}}\left(\frac{\sqrt{2}r}{\omega(z)}\right)^n L_m^n\left(\frac{2r^2}{\omega^2(z)}\right)\exp(jn\phi) \\ &\times \exp\left[-\frac{r^2}{\omega^2(z)} - \frac{jkr^2}{2R(z)} - j(kz-(2m+n+1)G(z))\right].\end{aligned} \tag{1.37}$$

This axial symmetry is particularly useful when working with symmetric models during thermal noise or thermal deformation calculations. Modal expansions in the LG basis

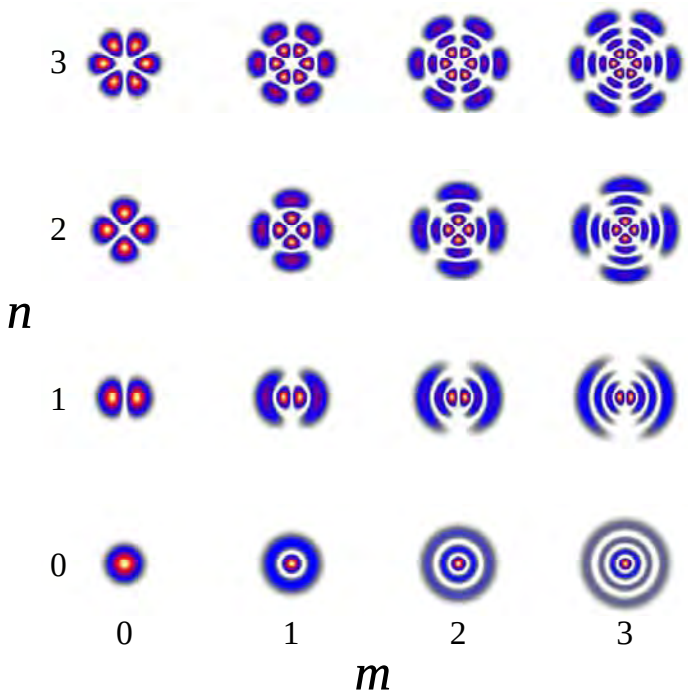

Figure 1.14: Intensity profiles of low order sinusoidal Laguerre-Gaussian modes. The Ψ_{mn} mode has m nodes in the radial direction and n in the azimuthal direction.

are often used in describing mode mismatches between beams due to incorrect waist sizes or positions. The intensity profiles of low order helical and sinusoidal LG modes are shown in figures 1.14 and 1.15. Notice again that Ψ_{00} is a standard Gaussian mode.

1.5.2 Resonators

In gravitational wave interferometers optical resonators are used to filter amplitude and frequency noise, to remove spurious higher order modes and to enhance the phase response to differential arm motion.[47] Optical resonators were also used extensively in our experimental work. In this section we outline the properties of these devices, examining resonator modes, stability and frequency response. In §1.5.2.5 we describe the standard technique used to lock a laser source to an optical resonator – Pound-Drever-Hall reflection locking. For concreteness we limit our discussion to a simple two

[47] i.e to increase the effective arm length as discussed in §1.2.2.

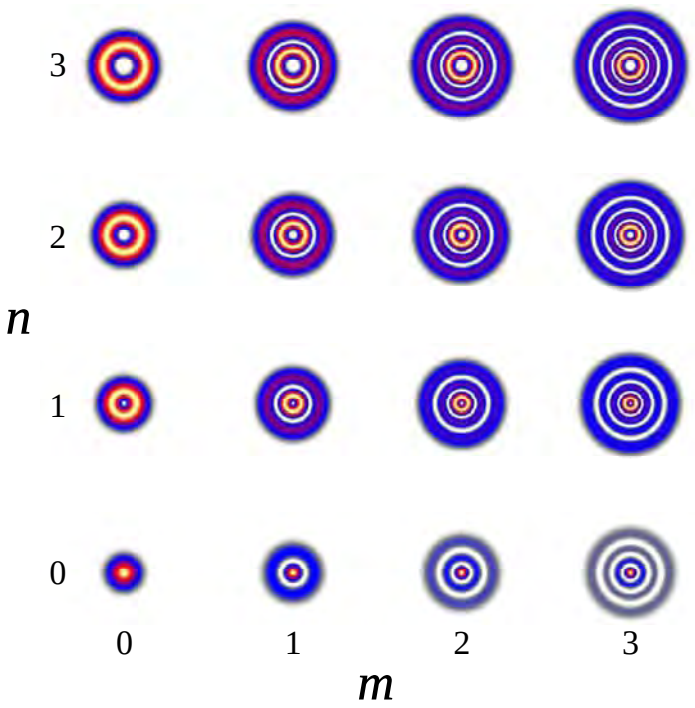

Figure 1.15: Intensity profiles of low order helical Laguerre-Gaussian modes. These modes exhibit useful radial symmetry.

mirror resonator in vacuum. Throughout this section and the rest of this document the terms resonator, cavity and (Fabry-Perot) interferometer are used interchangeably.

1.5.2.1 Modes

In the form applicable to gravitational wave interferometers, the optical resonator, first investigated at the end of the 19$^{\text{th}}$ century by Fabry and Perot [89, 90], usually consists of a pair of partially reflective spherical[48] mirrors arranged such that light bouncing back and forth between them may form a standing wave. In this configuration, only a field pattern which reproduces itself upon each cavity round trip has the chance to be resonantly enhanced. Such fields are called resonator modes.

In a spherical mirror cavity the resonator modes must have wavefront curvatures at each mirror position which match that mirror's figure. For a cavity of length L, formed

[48]Including the limit of infinite radius of curvature.

by mirrors with radii of curvature R_1 and R_2, the waist of such a mode is given by

$$\omega_0^2 = \frac{L\lambda}{\pi}\sqrt{\frac{g_1 g_2(1-g_1 g_2)}{(g_1+g_2-2g_1 g_2)^2}}, \tag{1.38}$$

where

$$g_1 = 1 - \frac{L}{R_1} \quad \text{and} \quad g_2 = 1 - \frac{L}{R_2} \tag{1.39}$$

are the cavity *g factors*. The positions of each mirror relative to this waist, taken to be at $z = 0$, are

$$z_1 = \frac{g_2(1-g_1)}{g_1+g_2-2g_1 g_2}L \quad \text{and} \quad z_2 = \frac{g_1(1-g_2)}{g_1+g_2-2g_1 g_2}L. \tag{1.40}$$

A cavity is said to be *mode matched* if the waist size and position of the input light field match those of the cavity mode.

The bulk of this thesis is concerned with the relationship between mirror shapes and cavity modes. Specifically, we seek to create a non-spherical cavity whose fundamental mode has a predominantly flat topped intensity distribution (see §2.1).

1.5.2.2 Resonant frequencies

For a resonator with spherical mirrors every member of the HG and LG families (see §1.5.1) is a cavity mode. However they are not all resonant simultaneously. In order for a cavity mode to be resonantly enhanced the intracavity field must interfere constructively with the input field. This condition corresponds to the cavity round trip phase ϕ_{rt} being an integer multiple of 2π. For a HG mode we have

$$\phi_{\mathrm{rt}} = 2\left(\frac{2\pi f}{c}L - (m+n+1)[G(z_2)-G(z_1)]\right) = a2\pi, \quad a \in \mathbb{Z}. \tag{1.41}$$

Using equations (1.38) and (1.40), $[G(z_2)-G(z_1)]$ may be replaced by $\arccos[\pm\sqrt{g_1 g_2}]$, where the plus sign is taken for $g_1, g_2 > 0$ and the negative for $g_1, g_2 < 0$. Solving for

f gives an expression for the resonant frequencies of HG modes

$$f_{mn}^{\mathrm{HG}} = \frac{c}{2L}\left(a - (m+n+1)\frac{\arccos[\pm\sqrt{g_1 g_2}]}{\pi}\right). \tag{1.42}$$

In the same way an equivalent expression for LG modes may be found

$$f_{mn}^{\mathrm{LG}} = \frac{c}{2L}\left(a - (2m+n+1)\frac{\arccos[\pm\sqrt{g_1 g_2}]}{\pi}\right). \tag{1.43}$$

Thus by choosing the cavity geometry carefully the degeneracy of the higher order modes may be controlled. This is crucial in gravitational wave interferometers where it is important that only a single cavity mode is resonant.[49] In §2.3.2 we study the resonant frequencies of higher order modes in a non-Gaussian resonator.

The cavity geometry also influences the spot size on each of the cavity mirrors. This has a direct effect on the measured thermal noise. Since the End Test Mass (ETM) has more coating layers than the Input Test Mass (ITM), thermal noise is minimised by having a bigger spot on the ETM and the cavity waist slightly closer to the ITM. This has the added benefit of reducing the beam's spot size in the recycling cavities.

1.5.2.3 Stability

Not all cavity geometries are useful. In order for a cavity to be stable its optics must periodically focus paraxial rays. This occurs when the cavity g factors satisfy the following criterion

$$0 \leqslant g_1 g_2 \leqslant 1. \tag{1.44}$$

This idea may be represented graphically on a *cavity stability diagram* (see fig. 1.16). All cavity configurations falling within the shaded area are said to be stable.

We now discuss certain special cavity types and nomenclature used in our work. These cavity configurations are marked on fig. 1.16.

[49] For alignment purposes the resonant properties of higher order modes are also important [91].

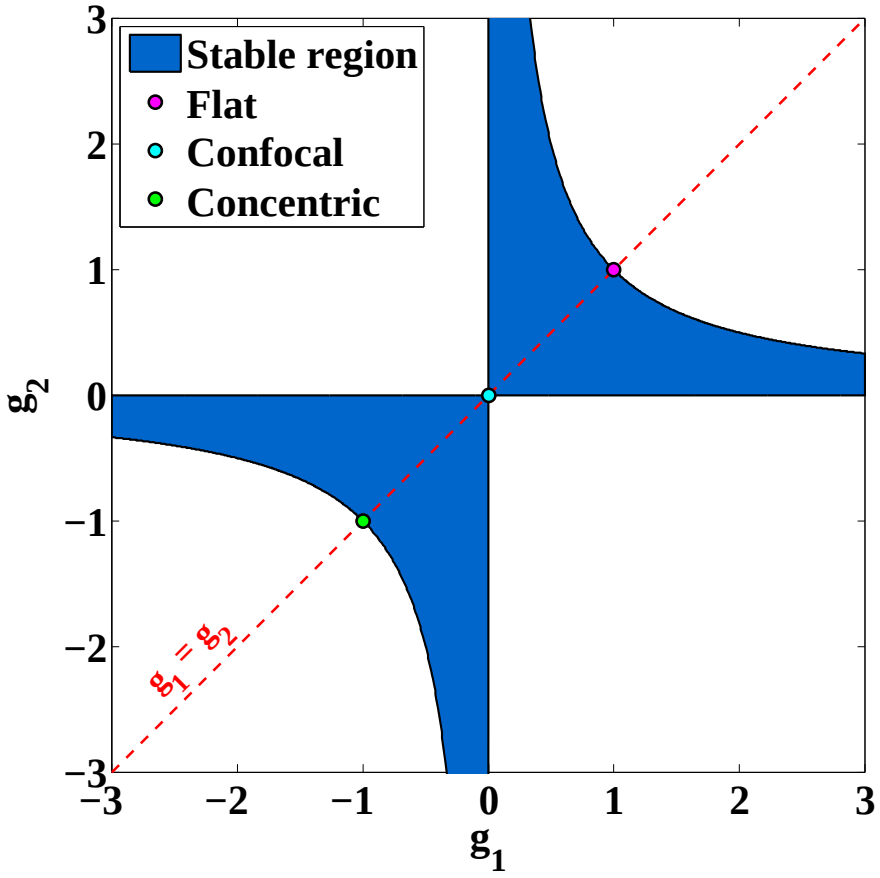

Figure 1.16: Cavity stability diagram.

A *symmetric* resonator is one with $g_1 = g_2$. These cavities lie along the dashed red line in fig. 1.16. A *half-symmetric* resonator has one plane mirror and one curved mirror. Such a resonator is equivalent to half of a symmetric system which is twice as long.[50]

A *confocal* resonator has $R_1 = R_2 = L$ and therefore $g_1 = g_2 = 0$. The confocal resonator has the smallest *average* spot size along its length of any stable configuration. The degeneracy of confocal resonators is useful in the construction of devices such as optical spectrum analysers.

Nearly flat resonators have $R_1 \simeq R_2 \simeq \infty$ and $g_1 \simeq g_2 \simeq 1$. Thus they are on the edge of stability and are very difficult to align. Our experimental non-Gaussian cavity falls into this category (see §2.2).

[50] Our experimental mesa beam cavity utilised this property to limit its length to a reasonable value.

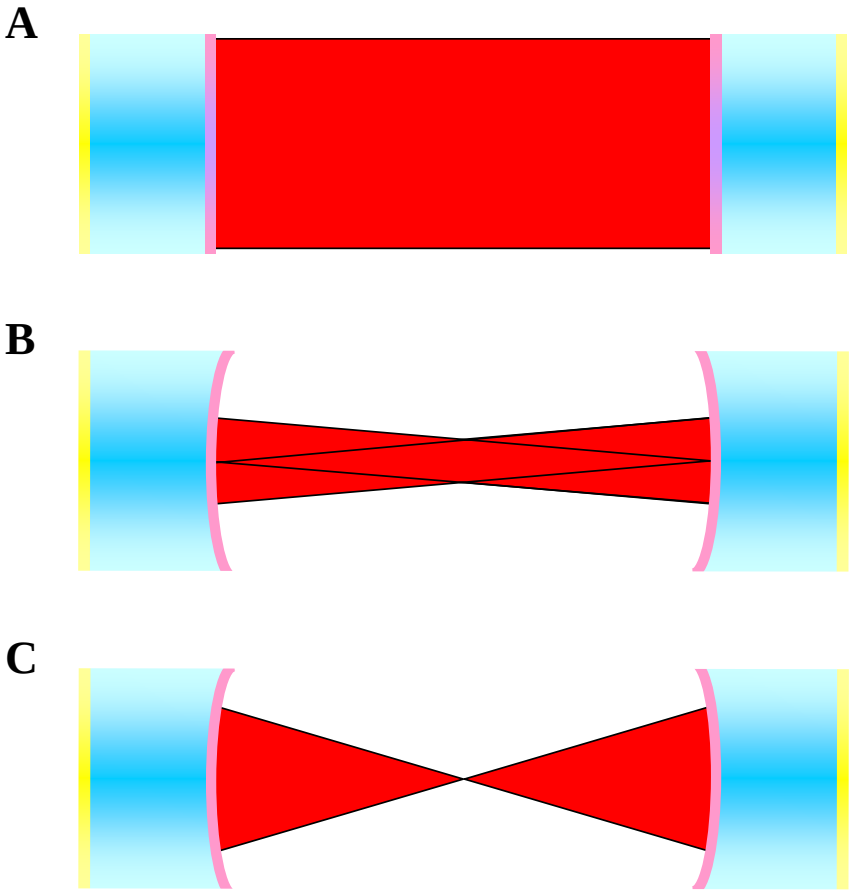

Figure 1.17: Radiation pattern of special cavity types. A - Flat, B - Confocal, C - Concentric.

Nearly concentric resonators are also marginally stable, having $R_1 \simeq R_2 \simeq L/2$ and $g_1 \simeq g_2 \simeq -1$. The cavities of AdvLIGO and AdvVIRGO are expected to be of nearly concentric construction to increase the spot size on the cavity mirrors.

Fig. 1.17 presents the radiation pattern inside each of these cavity types.

1.5.2.4 Longitudinal response

We now investigate the response of the cavity fields to longitudinal mirror motions.[51] For clarity we assume that the input laser field consists of a fundamental Gaussian mode, perfectly matched to a lossless cavity. Under these assumptions our analysis is

[51] In all studies of Fabry-Perot cavities there is an equivalence between cavity length changes and laser frequency modulations.

similar to that of a plane wave incident on a plane-plane cavity.

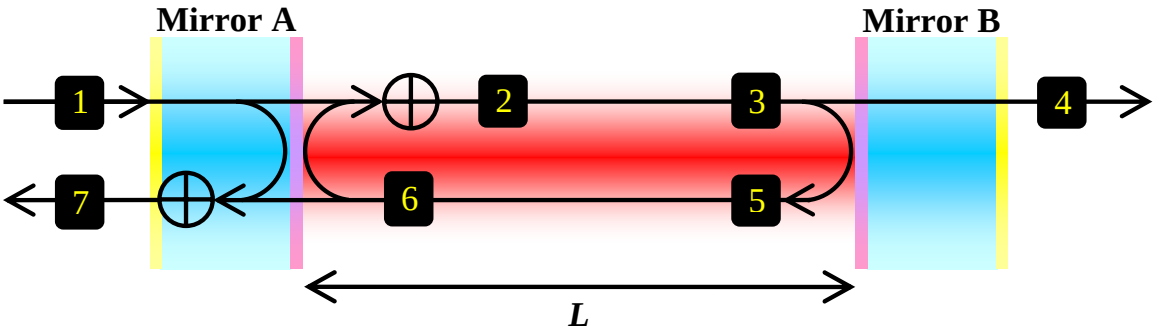

Figure 1.18: Enumeration of cavity fields for the calculation of longitudinal response.

With reference to fig. 1.18, the cavity fields are

$$\begin{aligned}
\Psi_2 &= jt_\mathrm{A}\Psi_1 + r_\mathrm{A}\Psi_6, \\
\Psi_3 &= \Psi_2 \exp(-j\phi), \\
\Psi_4 &= jt_\mathrm{B}\Psi_3, \\
\Psi_5 &= r_\mathrm{B}\Psi_3, \\
\Psi_6 &= \Psi_5 \exp(-j\phi). \\
\Psi_7 &= r_\mathrm{A}\Psi_1 + jt_\mathrm{A}\Psi_6.
\end{aligned} \tag{1.45}$$

where r_A, r_B and t_A, t_B are the amplitude reflectivities and transmissivities of mirrors A and B, $\phi = kL$ is the one way cavity phase and we have adopted the sign convention that a beam transmitted by a mirror acquires a phase shift of $\pi/2$.

Solving (1.45) the complex amplitude reflectivity, transmissivity and gain of the cavity are found:

$$r(\phi) = \frac{\Psi_7}{\Psi_1} = r_\mathrm{A} - \frac{t_\mathrm{A}^2 r_\mathrm{B} \exp(-j2\phi)}{1 - r_\mathrm{A} r_\mathrm{B} \exp(-j2\phi)}, \tag{1.46}$$

$$t(\phi) = \frac{\Psi_4}{\Psi_1} = -\frac{t_\mathrm{A} t_\mathrm{B} \exp(-j\phi)}{1 - r_\mathrm{A} r_\mathrm{B} \exp(-j2\phi)}, \tag{1.47}$$

$$g(\phi) = \frac{\Psi_2}{\Psi_1} = \frac{jt_\mathrm{A}}{1 - r_\mathrm{A} r_\mathrm{B} \exp(-j2\phi)}. \tag{1.48}$$

We say that the cavity is resonant when $\phi = a\pi$; $a \in \mathbb{Z}$. In this state both the

circulating and transmitted powers are maximised.

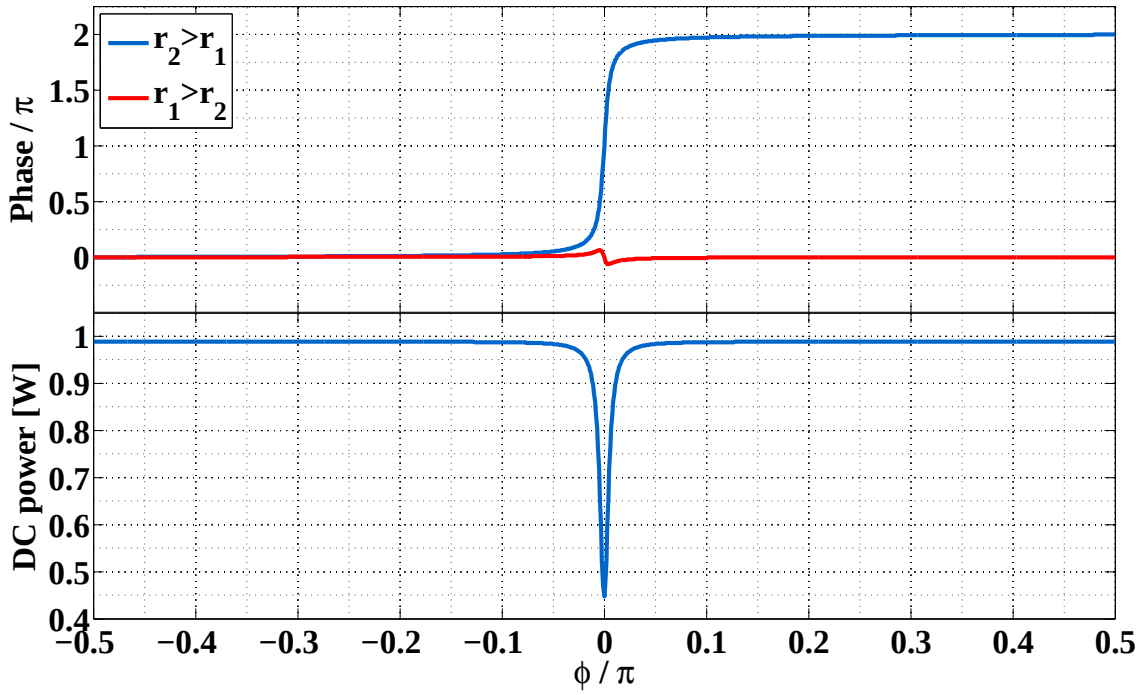

Figure 1.19: The phase and power in the field reflected from a Fabry-Perot cavity with $r_A^2 = 0.95$, $r_B^2 = 0.99$ and no losses. Mirrors A and B are swapped to investigate undercoupled cavities.

Figures 1.19 and 1.20 plot the power and phase of the reflected and transmitted cavity fields as a function of ϕ. Notice that the phase of the reflected field depends on the mirror reflectivities. For $r_1 < r_2$ the field reflected at resonance is π out of phase with the incoming field, whereas for $r_2 < r_1$ there is no phase shift. This is due to the relative strengths of the field promptly reflected by the input mirror and the field leaking out of the cavity.[52]

When $r_1 < r_2$ the reflected field is dominated by cavity leakage. In this case the cavity is called *overcoupled*. Conversely, when $r_2 < r_1$, the promptly reflected field dominates and the cavity is said to be *undercoupled*. *Optimal coupling* occurs when $r_1 = r_2$. An optimally coupled cavity transmits all light incident upon it.[53]

Notice also that the reflected phase is extremely sensitive to small changes in cavity

[52]The first and second terms of (1.46) respectively.

[53]In reality the losses also play a role in determining the cavity coupling but these have been neglected here.

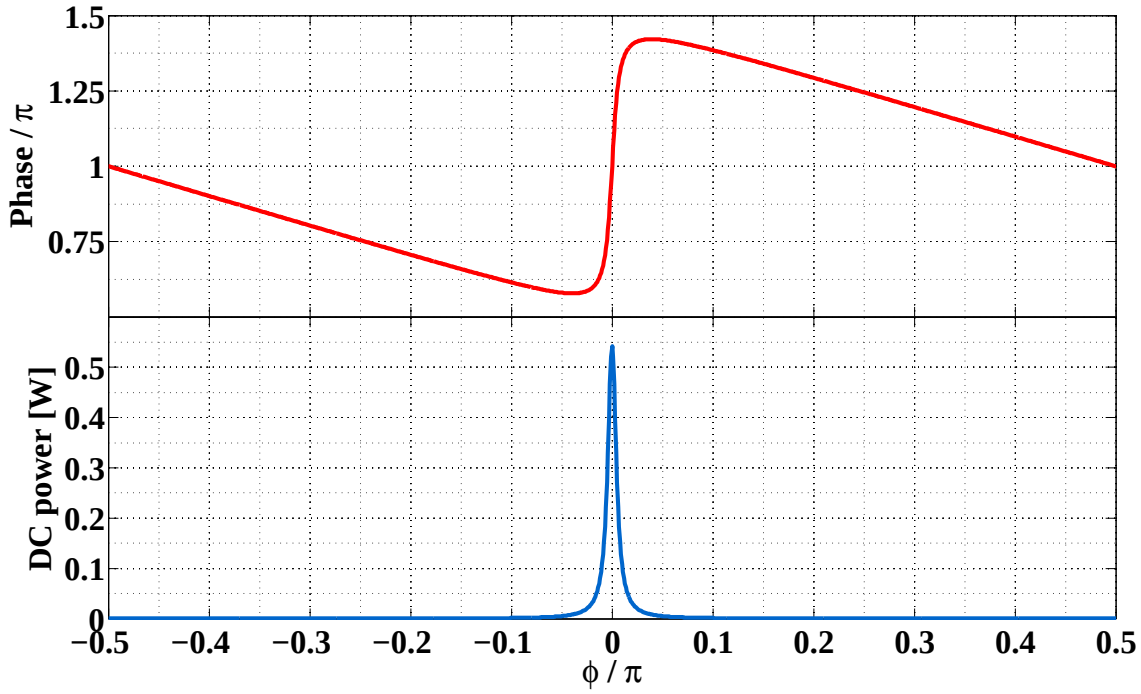

Figure 1.20: The phase and power in the field transmitted by a Fabry-Perot cavity with $r_A^2 = 0.95$, $r_B^2 = 0.99$ and no losses.

tuning about resonance, explaining why resonant cavities are used in the arms of most gravitational wave interferometers.

Writing the intracavity power P_{circ} as

$$P_{\text{circ}} = |\Psi_2|^2 = \frac{t_{\text{A}}^2}{(1 - r_{\text{A}} r_{\text{B}})^2} \frac{1}{\frac{4 r_A r_B}{(1 - r_{\text{A}} r_{\text{B}})^2} \sin^2(\phi)} P_1 \tag{1.49}$$

we see that it is a periodic function of ϕ with period π. In terms of frequency this period is known as the *free spectral range* and is given by

$$f_{\text{FSR}} = \frac{c}{2L}. \tag{1.50}$$

The free spectral range is the inverse of the cavity round trip propagation time.

From (1.49) the full width at half maximum of the resonance peak is found to be

$$\Delta f_{\text{FWHM}} = f_{\text{FSR}} \frac{1 - r_{\text{A}} r_{\text{B}}}{\pi \sqrt{r_A r_B}}. \tag{1.51}$$

The sharpness of the peak is given by the ratio of the free spectral range to the linewidth. Let us introduce the *finesse* $\mathcal{F}$ to describe this quantity:

$$\mathcal{F} = \frac{f_{\mathrm{FSR}}}{\Delta f_{\mathrm{FWHM}}} = \frac{\pi\sqrt{r_A r_B}}{1 - r_A r_B}. \tag{1.52}$$

Using our new parameters (1.49) may be expressed in a more compact form

$$P_{\mathrm{circ}} = \frac{G P_1}{(2\mathcal{F}/\pi)^2 \sin^2(2\pi f L/c)}, \tag{1.53}$$

where $G = g^2$ is the power gain of the cavity.

Due to interference effects within it, a cavity filters low[54] frequency modulations of its length or input laser frequency like a single pole low pass filter. This filter, known as the *cavity pole*, has 3 dB frequency

$$f_c = \frac{1}{2\pi\tau_{\mathrm{sto}}} = \frac{f_{\mathrm{FSR}}}{2\mathcal{F}}. \tag{1.54}$$

Here $\tau_{\mathrm{sto}} = \mathcal{F}/(\pi f_{\mathrm{FSR}})$ is the average storage time of light in the cavity, from which the average number of bounces is easily derived:

$$N_{\mathrm{bounce}} = \frac{c\tau_{\mathrm{sto}}}{L} = \frac{2\mathcal{F}}{\pi}. \tag{1.55}$$

1.5.2.5 Pound-Drever-Hall reflection locking

In order to take advantage of the Fabry-Perot cavity's sharp phase response it must be held on resonance, either by stabilising a laser source to the resonator length or vice versa.[55] This is most often achieved using one of the most elegant techniques in the gravitational wave field – Pound-Drever-Hall reflection locking [92]. This scheme exploits the change in phase experienced by reflected light as the cavity passes through resonance to derive a signal which is linearly proportional to the detuning from resonance.

[54] $f < f_{\mathrm{FSR}}$.

[55] Sometimes both techniques are used simultaneously in different frequency bands.

In order to measure the phase of the reflected light a stable reference is required. Phase modulating[56] the input laser light produces radio frequency sidebands about the main carrier frequency. Near the carrier resonance these sidebands are not affected by the state of the cavity[57] and thus are a suitable phase reference. In the remainder of this section we show how the phase difference between these spectral components is measured and converted into a useful correction signal.

For small modulation indices Γ, the field incident on the cavity[58] may be written as [94]

$$E_1 = E_{\rm inc}(J_0(\Gamma) + jJ_1(\Gamma)\exp(j\Omega t) + jJ_1(\Gamma)\exp(-j\Omega t)), \tag{1.56}$$

where Ω is our modulation frequency. The output of an RF photodiode in reflection will be proportional to

$$S_{\rm pd} = |E_0|^2 + |E_+|^2 + |E_-|^2 + 2\Re[(E_-^* E_0 + E_0^* E_+)\exp(j\Omega t)] + 2\Re[(E_-^* E_+)\exp(j2\Omega t)], \tag{1.57}$$

where $E_0 = r(0)J_0(\Gamma)E_{\rm inc}$, $E_\pm = r(\pm\Omega)jJ_1(\Gamma)E_{\rm inc}$ and $r(f)$ is the complex cavity reflectivity.

Three frequency components are apparent in the detected power – one at DC, one at Ω and one at 2Ω. The component which carries the information we seek is that at Ω. This signal is due to the beat between the carrier and sidebands and thus contains information about the phase difference between them.[59] We extract the component at Ω via coherent demodulation[60] as follows:

$$\begin{aligned} S_{\rm demod} &= \frac{1}{t1 - t0}\int_{t0}^{t1} S_{\rm pd}\cos(\Omega t' + \phi_{\rm demod})\mathrm{d}t' \\ &= \Re[(E_-^* E_0 + E_0^* E_+)e^{-i\phi_{\rm demod}}], \end{aligned} \tag{1.58}$$

[56] Other schemes exist which rely on amplitude or complex modulation [93].

[57] This is only strictly true if the modulation frequency is outside of the cavity bandwidth. At lower modulation frequencies the cavity has a differential effect on the sidebands and carrier. The technique is still applicable but produces weaker signals.

[58] Omitting spatial dependence and the overall $\exp(j\omega t)$ term.

[59] The component at 2Ω is due to the beat between the two sidebands.

[60] i.e. mixing and low pass filtering.

where we have assumed that $T = t1 - t0 \gg 1/\Omega$ so that only the lowest frequency terms survive integration. Notice that the size of the signal has been halved. This is due to equal amounts of signal being upconverted and downconverted by Ω.

In fig. 1.21 we plot the in phase and quadrature components of S_{demod} along with the cavity transmission. About resonance, the in phase signal is linear with cavity detuning and is therefore a good error signal for close loop control.

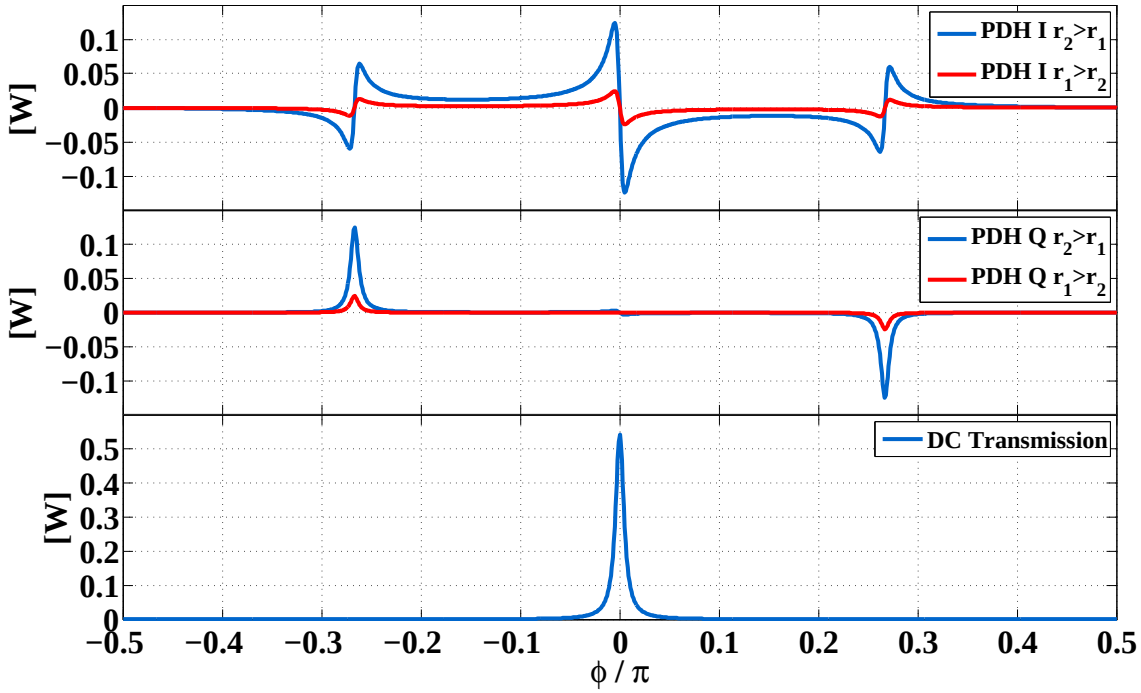

Figure 1.21: Pound Drever Hall reflection locking. Top: In phase demodulated error signal for over and undercoupled cavities. Middle: Quadrature phase error signals. Bottom: DC cavity transmission. As desired the PDH error signal is linear and bipolar about resonance. The secondary features at $\sim \pm 0.25\pi$ arise when the sidebands themselves become resonant and the carrier acts as the phase reference.

1.6 SIS – Static Interferometer Simulation

In the numerical study of optical systems two techniques are prevalent – modal analysis (e.g. [95]) and Fast Fourier Transform (FFT) based methods. Modal analysis operates by describing fields in a complete basis of optical modes, for example the HG or LG

families (see §1.5.1.1). The properties of these modes are well-known and any interaction, such as reflection from a mirror, may be characterised by its mode-mode coupling coefficients [96]. System output is obtained through summation over all basis functions.

Modal analysis is well-suited to the study of spherical mirror interferometers. Unperturbed, such instruments support fundamental Gaussian beams which may be described by a single term in a modal expansion and for small perturbations only scattering into the first few excited modes is significant (see e.g. §3.2.1.1). Hence the behaviour of these systems can be accurately captured by a series containing few terms, making modal approaches very efficient.

However, if one desires to investigate non-Gaussian beams or realistically flawed optics, modal analysis quickly becomes computationally expensive, requiring many modes if it is able to be used at all. In these cases FFT based approaches are more suitable.

1.6.1 The FFT method

In this section we outline the theory behind FFT based simulation methods, examining how the propagation of an optical field can be reduced to a pair of two dimensional Fourier transforms. We subsequently show how the FFT approach can be used to study complex interferometer configurations with imperfect optics. For a more comprehensive treatment see e.g. [97] from where much of the present discussion was derived.

Under the paraxial approximation propagation of an arbitrary optical field can be performed using the following three steps:

a) The input light field $\Psi(x, y, 0)$ is first transformed into the spatial frequency domain via a two dimensional Fourier transform

$$\tilde{\Psi}(k_x, k_y, 0) = \iint_{\mathbb{R}^2} \Psi(x, y, 0) \exp(j(k_x x + k_y y)) \, \mathrm{d}x \, \mathrm{d}y, \tag{1.59}$$

where k_i is the wave number in the i direction and $k^2 = k_x^2 + k_y^2 + k_z^2$. This step

may be thought of as decomposing the field into a superposition of plane waves.

b) Each of these plane waves is then propagated in the positive z direction. Under the paraxial approximation $k_x^2 + k_y^2 \ll k^2$ so that

$$\begin{aligned} k_z &= \sqrt{k^2 - (k_x^2 + k_y^2)} \\ &\simeq k - \frac{k_x^2 + k_y^2}{2k}. \end{aligned} \tag{1.60}$$

Propagation over distance L is thus equivalent to a phase shift in k-space

$$\tilde{\Psi}(k_x, k_y, L) = \tilde{\Psi}(k_x, k_y, 0) \exp\left[-j\left(k - \frac{k_x^2 + k_y^2}{2k}\right)L\right]. \tag{1.61}$$

c) Finally the propagated field in position space is recovered via a second Fourier transform

$$\Psi(x, y, L) = \left(\frac{1}{2\pi}\right)^2 \iint\limits_{\mathbb{R}^2} \tilde{\Psi}(k_x, k_y, L) \exp(-j(k_x x + k_y y))\, \mathrm{d}k_x\, \mathrm{d}k_y. \tag{1.62}$$

In order to extend the FFT approach beyond simple propagation we must also include optical elements. Vinet showed that mirrors suitable for use in gravitational wave interferometers may be described by reflection and transmission operators in coordinate space [98]. With reference to fig. 1.22, these operators are

$$t_{\mathrm{op}}(x, y) = jte^{jkD} e^{jk(n-1)f(x,y)} a(x, y) \tag{1.63}$$

for transmission from $z = 0$ to $z = D$,

$$r^{\mathrm{l}}_{\mathrm{op}}(x, y) = re^{2jknf(x,y)} a(x, y) \tag{1.64}$$

for a beam starting from $z = 0$ and returning to $z = 0$ via reflection at $z = f(x, y)$ and

$$r^{\mathrm{r}}_{\mathrm{op}}(x, y) = re^{2jkD} e^{-2jkf(x,y)} a(x, y) \tag{1.65}$$

for a beam starting at $z = D$ and returning to $z = D$ via reflection at $z = f(x, y)$.

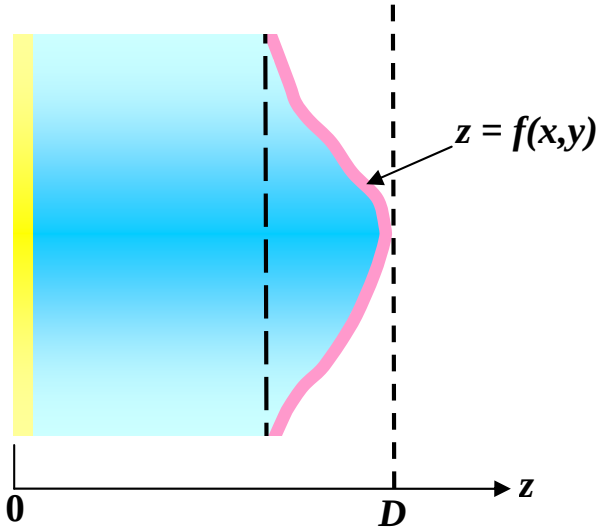

Figure 1.22: FFT based simulation methods are able to include mirrors having complicated profiles $z = f(x, y)$.

Here n is the refractive index of the substrate, r and t are the amplitude reflectivity and transmissivity of the coating and $a(x, y)$ is an aperture function, taking value 1 inside the mirror radius and 0 outside. Using the above examples as a guide, operators treating other optical components, such as beamsplitters, may be formed.

The true utility of the FFT approach lies in its ability to incorporate almost arbitrary mirror profiles by appropriately defining $f(x, y)$. These definitions may simply describe the shape of the mirror's surface[61] or be expanded to include tilts, surface roughness, perturbations due to absorption of optical power etc. Spatial variation in other parameters such as reflectivity or transmission is also easily included.

In practice all of the operations described above are carried out using a computer and therefore all quantities must be described by a finite set of values. This is generally achieved by sampling over a uniform two dimensional grid normal to the beam's propagation direction. In the interests of computational efficiency this grid is usually square and of dimension $2^n \times 2^n$ for some $n \in \mathbb{N}$. Each grid square is known as a *pixel*.

Using discrete grids the above integrals become finite sums and the transforms necessary for propagation may be carried out using fast Fourier transform algorithms,

[61] Spherical or otherwise.

reducing computation time by orders of magnitude.[62] The application of phase factors, during propagation and on interaction with a mirror, amount to pixel by pixel multiplication.

Care must be taken to choose both the physical extent and resolution of the grid appropriately. The overall size of the grid should be large enough so that

- all of the optical power is captured,
- sufficient resolution is available in k-space and
- large angle scattering from adjacent Fourier cells does not introduce spurious optical power [97].

In all our work the total width of the grid was equal to twice the mirror diameter.

The resolution of the grid must be

- appropriately matched to the physical scale of interest,
- high enough to avoid aliasing and
- such that the optical path difference between neighbouring pixels is strictly less than $\lambda/2$.[63]

The minimum number of grid squares used in our work was 128×128.

Having dealt with propagation and interaction with mirrors it is easy to see how interferometer configurations may be constructed. For example, denoting the three-stage propagation described above as p_{op}, we may write the equation for the steady state circulating field Ψ_{ss} in a Fabry-Perot cavity as

$$\Psi_{\mathrm{ss}} = t_{\mathrm{op,itm}}\Psi_{\mathrm{input}} + r^{\mathrm{r}}_{\mathrm{op,itm}} p_{\mathrm{op}} r^{\mathrm{l}}_{\mathrm{op,etm}} p_{\mathrm{op}} e^{j\varphi}\Psi_{\mathrm{ss}}, \tag{1.66}$$

[62] The speed of the FFT approach goes as $N_{\mathrm{pixels}}\log(N_{\mathrm{pixels}})$ as opposed to N^2_{pixels} for standard techniques.

[63] This path difference gives rise to a phase of 2π on reflection which cannot be observed. For our mesa cavity this limits us to tilts below 1.5 mrad.

where φ represents a tuning phase which can be modified to maximise the circulating power.[64] Iteratively solving this equation (see e.g. [97]) the steady state field distribution in the cavity may be found. This process remains the same regardless of whether we are considering a basic spherical mirror or the measured phase map of an exotic profile supporting non-Gaussian beams.

As a result of their wide-ranging capabilities and ease of use, FFT simulations were used extensively throughout this work. The particular program employed is discussed in the following section.

1.6.2 Description of SIS

Static Interferometer Simulation or SIS [99] is a program developed at Caltech's LIGO Laboratory[65] in order to study, in detail, the optical aspects of the Advanced LIGO interferometer. SIS operates via the principles described in the preceding section, using an iterative procedure to find the stationary fields for a given optical configuration and input field spectrum. The mirrors' positions can be 'locked' to the appropriate fraction of an optical fringe by applying error signals which approximate those of standard heterodyne techniques. SIS is capable of calculating the signal sidebands induced by small mirror motions and can include surface deformations due to thermal absorption,[66] measured aberrations, randomly generated figure error and micro-roughness.

At the time of writing SIS cannot simulate a full interferometer and does not incorporate phase modulation, quantum effects or radiation pressure. Despite these shortcomings SIS is an extremely versatile and accurate tool which has proven indispensable in this work.

[64] Mirror imperfections may shift the resonance frequency of a spherical mirror cavity; for non-spherical cavities the resonance frequency may not be known.
[65] In an effort led by Hiroaki Yamamoto.
[66] Using the Hello-Vinet approximation [100].

Chapter 2

Mesa beams

It is anticipated that the second generation of earthbound gravitational wave detectors will be limited in their most sensitive region by mirror thermal noise. The impact of this noise may be reduced by switching from standard optical modes to non-Gaussian mesa beams. In this chapter we present a theoretical description of the mesa beam and its competitors before documenting results of experimental work.

We begin by discussing the motivation and conceptual ideas behind the mesa beam prior to introducing its mathematical construction. With a solid theoretical foundation we continue by describing, in detail, the design of apparatus constructed to verify the properties of this beam.

The second portion of the chapter describes the investigations made with this apparatus, culminating in the first ever experimental realisation of a flat-topped non-Gaussian mode in a manner applicable to interferometric gravitational wave detectors.

2.1 Theory

In advance of recounting the experimental work that is the main focus of this thesis we present an overview of the non-Gaussian beams considered for use in kilometre scale detectors, paying particular attention to the mesa beam.

2.1.1 Motivation

The majority of interferometric gravitational wave detectors operate by measuring the variations in phase between light beams resonating in two perpendicular optical cavities caused by the passage of gravitational waves. Any physical displacement of the mirrors forming these cavities also creates phase variations and thus contributes noise to the measurement. In particular, random displacements of the test masses' reflective surfaces due to thermodynamical fluctuations are expected to be a major source of noise in future interferometers.

As in currently operating detectors, it is anticipated that the optical mode used to probe mirror positions in future interferometers will be Gaussian. Gaussian beams which meet strict diffraction loss requirements are narrow and have steeply sloping intensity profiles. Such beams perform a poor spatial average of thermodynamic fluctuations leading to a high level of measured thermal noise.

It is possible to significantly reduce the measured test mass thermal noise by using modified cavity optics which reshape the incident Gaussian mode into a beam with a more uniform intensity profile. Heuristically, the ideal mode for mitigating the effects of thermal noise should have equal intensity across the entire mirror[1] - a *top hat* beam. Unfortunately such ideal beams are not physically realisable.

In 2003 O'Shaughnessy and Thorne conceived a more realistic mode with the following reasoning [101]. The top hat beam may be considered as a superposition of Dirac

[1]To provide the best spatial average of thermodynamical fluctuations.

δ functions or, equivalently, infinitely narrow Gaussian beams. Upon propagation these narrow beams quickly diverge, giving rise to large diffraction losses. Increasing the width of each constituent Gaussian moderates diffraction loss at the expense of intensity profile uniformity (see fig. 2.1). Balancing the competing demands of thermal noise mitigation and diffraction loss defines the optimal width of component Gaussian and thus our new mode.

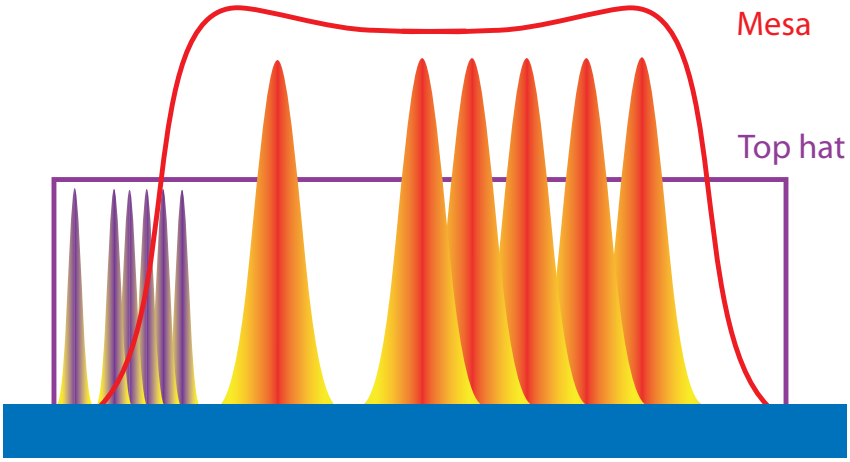

Figure 2.1: Heuristically the ideal mode for mitigating the effects of thermal noise would be a top hat beam (purple). This mode can be considered as a superposition of infinitely narrow Gaussian beams. The mesa beam (orange) is a physically realisable approximation to this mode created by broadening each constituent Gaussian.

2.1.2 Intensity/Mirror profiles

In this subsection we define the optimal width of a component Gaussian and present the mathematical formulae describing the mesa beam fields and mirror profiles. We also explain the origins of the terms *mesa* and *Mexican hat*.

2.1.2.1 Flat mesa beams

The Gaussian beams which sum to form the mesa mode are known as *minimal* Gaussians and are, for a given wavelength λ and cavity length L, the fundamental Gaussian

mode with the smallest possible spot size on the cavity mirrors. A minimal Gaussian has a waist[2] given by

$$\omega_0 = \sqrt{\frac{L\lambda}{2\pi}} \tag{2.1}$$

and a Rayleigh range z_{R} of $L/2$, so that the beam width at the mirror position is $\sqrt{2}\,\omega_0$.

In its original form,[3] the mesa beam consists of a superposition of minimal Gaussians whose optical axes are parallel to the cavity axis and distributed uniformly over a disc of radius D centred on it (see fig. 2.7). In the literature D is typically taken to be four times the waist of the minimal Gaussian, $D = 4\omega_0$. For such a construction the unnormalised field at the mirror position is given by

$$\begin{aligned}\Psi_{\mathrm{FM}}(r, L/2) &\propto \int\limits_{\vec{r}\,'\leq D} \exp\left[-\frac{(\vec{r}-\vec{r}\,')^2(1-j)}{2\omega_0^2}\right]\mathrm{d}^2\vec{r}\,', \\ &= 2\pi\int\limits_0^D \exp\left[-\frac{(r^2+r'^2)(1-j)}{2\omega_0^2}\right] I_0\left(\frac{rr'(1-j)}{\omega_0^2}\right) r'\mathrm{d}r', \end{aligned} \tag{2.2}$$

where $I_0(x)$ is a zeroth order modified Bessel function of the first kind.

In order for this field to be a cavity eigenmode, the shapes of the cavity mirrors must match the phase fronts of the beam. Therefore the mirrors must have profiles given by $z = \pm L/2 \mp z_{\mathrm{HR}}$ where

$$z_{\mathrm{HR}}(r) = \frac{\mathrm{Arg}[\Psi_{\mathrm{FM}}(r, L/2)] - \mathrm{Arg}[\Psi_{\mathrm{FM}}(0, L/2)]}{k} \tag{2.3}$$

is the height of the mirror's Highly Reflective (HR) surface[4] and $k = 2\pi/\lambda$ is the wavenumber.[5]

[2] We define the waist size as the *radius* at which the beam intensity falls to $1/e^2$ times its peak value.

[3] i.e. for nearly flat cavities.

[4] Later the same notation will be used to denote the height of the mirror's HR profile above the fiducial surface.

[5] Strictly speaking this mirror does not have the *exact* profile we desire as we have calculated its shape from the field at $z = L/2$ whilst the mirror's surface sits at $z = L/2 - z_{\mathrm{HR}}$. The effect of this error is negligible, the difference being a phase $\sim kz_{\mathrm{HR}}$. Thus we assume the intensity on the mirror to be equal to that at $z = L/2$. Similar arguments apply in the concentric and hyperboloidal cases below.

Although (2.2) clearly demonstrates how the mesa beam was devised and assists in determining the appropriate mirror figure, it is not the most useful form of the mesa beam field. Thanks to Agresti and Vinet [102, 103] a more general expression exists, giving the normalised mesa field as a function of propagation distance z from the waist:

$$\Psi_{\mathrm{FM}}(r,z) = N \int_0^{D/\omega} \exp[-Z(\rho-\rho_0)^2] \exp(-2Z\rho\rho_0) I_0(2Z\rho\rho_0)\rho_0 \,\mathrm{d}\rho_0, \tag{2.4}$$

$$\text{where} \quad N(z) = \frac{2\omega}{D\omega_0\sqrt{\pi\aleph}},$$

$$\text{and} \qquad \aleph = 1 - \exp(-D^2/\omega_0^2)[I_0(D^2/\omega_0^2) + I_1(D^2/\omega_0^2)].$$

Here $\omega(z)$ is the spot size of the minimal Gaussians $\omega(z) = \omega_0\sqrt{1+(z/z_{\mathrm{R}})^2}$, $\rho(z) = r/\omega(z)$ and $Z(z) = 1 - jz/z_{\mathrm{R}}$. N is a normalisation factor found in the Fourier domain via Hankel transforms.

Fig. 2.2 illustrates how the mesa intensity and mirror profiles vary as a function of beam parameters. Choosing D and w_0 without restriction, a good approximation to a top hat beam may be achieved. However the corresponding mirrors are unphysical. With sensible parameter choices a reasonable, physically realisable solution may be found.

Using minimal Gaussians, our only free parameter is D. The standard $D = 4\omega_0$ value was chosen to comply with the 10 ppm per bounce diffraction loss requirement in the AdvLIGO design of the time. This design has naturally evolved and currently permits a loss of only 1ppm, i.e. diffraction loss should be negligible by design. With this in mind and in the interests of a fair comparison, we reduce the radius of the disc over which we integrate to be $D = 3.55\omega_0$. This choice gives a simulated[7] round trip diffraction loss in the AdvLIGO arm cavity of approximately 0.5 ppm, equal to that of the equivalent Gaussian cavity. The resulting intensity profile on the mirror is predominantly flat topped, providing a good spatial average of thermal fluctuations, with an edge that

[6] Eschewing the more obvious and less captivating *Sombrero mirror*.

[7] The analytical clipping approximation was not used as this generally underestimates diffraction loss.

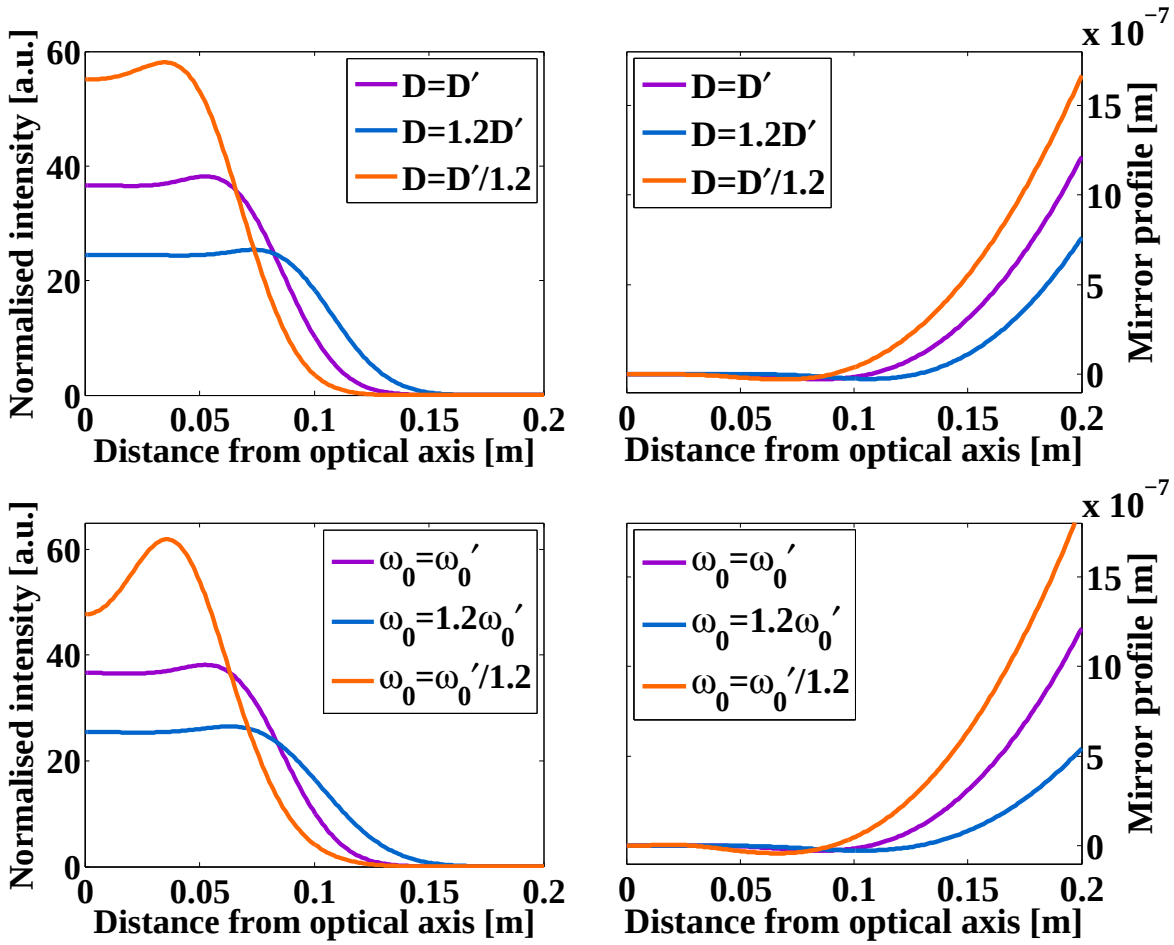

Figure 2.2: The mesa beam as a function of its parameters. In this figure primed variables denoted standard values. Upper plots: Mirror and intensity profiles (at mirror position) as a function of D for fixed ω_0. Lower plots: Mirror and intensity profiles (at mirror position) as a function of ω_0 for fixed D. Studying the nominal intensity profile one understands why Willems coined the term *mesa beam* in reference to the landform of the same name common in the southwestern United States. Owing to their unique shape, the mesa beam mirrors have earned their own moniker. With their steep outer brim and central crown they are known as *Mexican hat* mirrors.[6]

falls off like a Gaussian with waist ω_0.

2.1.2.2 Concentric mesa beams

Mesa beams realised in the manner described above shall be known here and henceforth as *flat* mesa beams, since the mirrors which support them are but a small perturbation from flat optics. These beams were extensively studied both theoretically [104, 105, 106] and experimentally [107] before a possible problem was uncovered.

Angular test mass motions cause the arm cavity's optical axis to deviate from its nominal centred position. With the beam spots no longer symmetric about the centres of the test masses, radiation pressure can exert non-negligible torques on the cavity optics. In 2006 Sidles and Sigg showed that, in future high power interferometers, such optically-generated torques could drive angular mirror motions to become unstable [108]. Furthermore, their geometric approach revealed that the severity of such *tilt instabilities* for Gaussian beams is proportional to the spot size on the mirrors raised to the fourth power, a worrying prospect for the wide mesa beam.

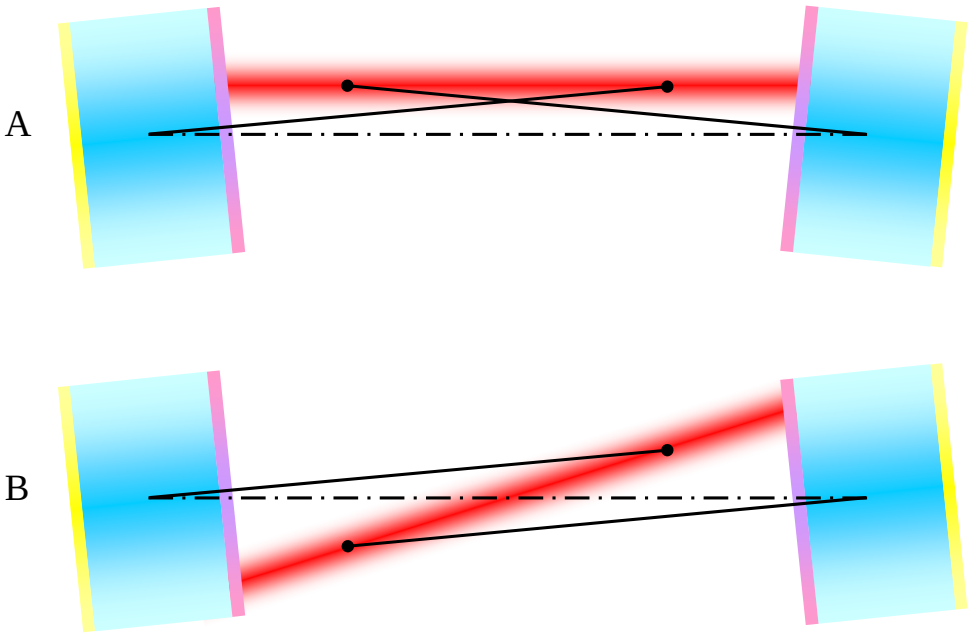

Figure 2.3: A: Lateral displacement of the optical axis gives rise to a statically unstable configuration. B: A configuration with a tilted optical axis is statically stable. The broken line represents the nominal cavity axis. The mirrors' centres of curvature are marked with filled circles.

Sidles and Sigg concluded that switching from nearly flat to nearly concentric cavities should mitigate the instability for Gaussian beams. Although both cavities are very sensitive to misalignment, their response to mirror tilts differs in a useful way. In the nearly flat case the optic axis predominantly shifts whereas in the nearly concentric case it tilts. A simple geometric picture reveals a cavity with a tilted optical axis to be more robust (see fig. 2.3 or §3.2.1.1 for a more mathematical approach). On the strength of this work the fiducial AdvLIGO cavity geometry was modified from a nearly

flat to nearly concentric configuration.

Our standard mesa beam is supported by a nearly flat cavity and should therefore be equally susceptible to tilt instabilities at high power, if not more so due to its greater width. This realisation motivated Bondarescu and Thorne to devise nearly concentric mirrors supporting mesa beams [109].

Recall that our flat mesa beam was generated as a superposition of minimal Gaussians with optical axes parallel to the cavity axis and uniformly distributed throughout a cylinder of radius D centred on it. Taking inspiration from geometric optics, we suppose that the equivalent nearly concentric beam may be constructed as a superposition of minimal Gaussians whose optical axes all pass through the centre of the cavity and are uniformly distributed inside a right circular cone centred on the cavity axis with aperture angle $4D/L$ (see fig. 2.7).

Evaluating the superposition of minimal Gaussians on the concentric sphere $z = S = \sqrt{(L/2)^2 - r^2} \simeq L/2 - r^2/L$ we find the concentric mesa field to be

$$\begin{aligned}\Psi_{\mathrm{CM}}(r) &\propto \int\limits_{\vec{r}\,'\leq D} \exp\left[-\frac{(\vec{r}-\vec{r}\,')^2(1+j)}{2\omega_0^2}\right]\mathrm{d}^2\vec{r}\,', \\ &= 2\pi\int\limits_0^D \exp\left[-\frac{(r^2+r'^2)(1+j)}{2\omega_0^2}\right] I_0\left(\frac{rr'(1+j)}{\omega_0^2}\right) r'\mathrm{d}r'. \qquad (2.5)\end{aligned}$$

The above is simply the complex conjugate of the flat mesa field, one demonstration of the more general duality relation discovered by Agresti [110]. As a result of this similarity we know that the intensity profile of the concentric mode will be equal to that of the flat mesa beam and will thus possess the same properties desirable from a thermal noise standpoint. We can also state that the phase front of the concentric beam will simply be $-z_{\mathrm{HR}}$ (see (2.3)) and the mirror profiles will be given by $z = \pm S \pm z_{\mathrm{HR}}$.

Again a more useful expression exists for the normalised field as a function of propa-

gation distance [102]:

$$\Psi_{\mathrm{CM}}(r,z) = \frac{jke^{-jkz}}{z\sqrt{\pi\aleph}} \int_0^\infty \exp\left[-\frac{\rho_0^2}{\omega_0^2} - \frac{jk}{2z}(\rho_0^2 + r^2)\right] J_1\left(\frac{2\rho_0 D}{\omega_0^2}\right) J_0\left(\frac{k\rho_0 r}{z}\right) \mathrm{d}\rho_0. \quad (2.6)$$

Subsequent analysis of this new mode by Savov and Vyatchanin confirmed expectations [111]. The flat mesa beam was indeed more susceptible to tilt instabilities than the flat Gaussian due to the mesa beam's greater width and concentric cavities were in general more stable. This work also revealed that the concentric mesa cavity has a weaker tilt instability than any other configuration. Table 2.1 presents a quantitative comparison of optical torques in the various cavities.

Table 2.1: Quantitative comparison of optical torques for various cavity configurations. Values are normalised such that the torque in the currently favoured concentric Gaussian cavity is unity.

	Nearly flat cavity	Nearly concentric cavity
Gaussian beam	26.2	1
Mesa beam	96	0.91

Figure 2.4 compares the mirror and intensity profiles of the concentric mesa beam to those of comparable Gaussian and flat mesa modes.

2.1.3 Expected gains

Mesa beams were originally conceived to combat the problem of thermoelastic noise in second generation interferometers employing sapphire test masses. As time progressed most collaborations made the decision to retain fused silica as the material of choice for future optics (see e.g. [112]). With this change the most worrisome form of thermal disturbance became coating Brownian thermal noise [113]. In this section we compare the thermal noise measured by Gaussian and mesa beams, showing that the mesa beam remains effective in improving detector sensitivity. We then provide context by explaining how this reduced thermal noise impacts some well-known metrics of interferometer performance.

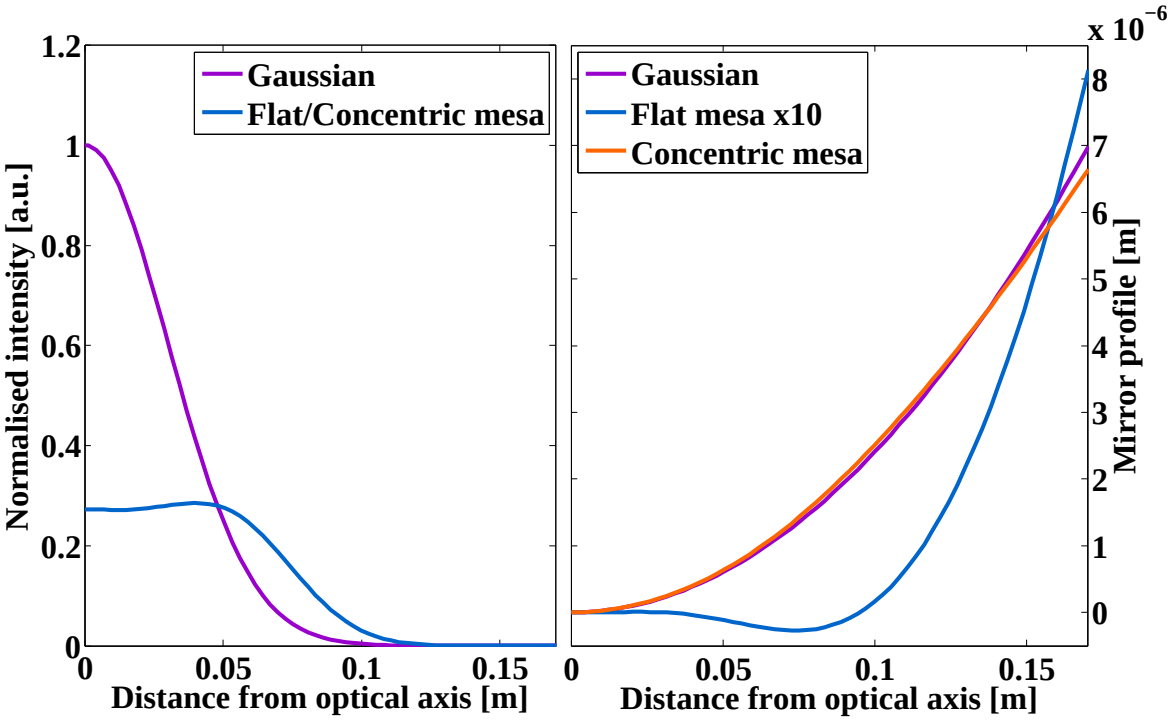

Figure 2.4: A comparison of mesa and Gaussian beams and the mirrors which support them. Left: Intensity profiles normalised to have equal power. The spot size of the Gaussian beam (the radius at which the intensity falls by $1/e^2$) is 6 cm, while that of the mesa beam is $\simeq$ 12 cm; i.e. at FWHM the Gaussian beam samples $\sim$4% of the mirror's surface whereas the mesa beam samples over 27%. Right: Nominal mirror figures for a symmetric 4 km cavity. The flat mesa beam mirror profile has been expanded by a factor of ten to better show its structure. The concentric mesa mirror profile is realised by subtracting the flat mesa profile from a concentric sphere with $R = L_{\rm cavity}/2$. The abscissa extends to 0.17 m, the baseline mirror radius for AdvLIGO.

Table 2.2 presents the reductions in thermal noise expected on switching to mesa beams. The ratio of total interferometer strain noise considering all mechanisms is 0.64. These

Table 2.2: Thermal displacement noise of mesa beams relative to equivalent Gaussians for a single test mass. The ratio of total interferometer strain noise considering all mechanisms is 0.64. All quantities are evaluated at 100 Hz.

	Brownian	Thermoelastic
Coating	0.62	0.62
Substrate	0.70	0.54

values were calculated using intensity profiles obtained from FFT based simulations. Hence we are using a mesa mode affected by finite mirror effects (see §2.1.6 below) and diffraction losses. We believe this approach yields a more realistic estimate of the

gains which may be realised experimentally than would be obtained using a theoretical profile. For details of the thermal noise calculations and material parameters used please see §4.2 and Appendix A.

While these gains are smaller than those quoted in the past, due to the change in substrate material,[8] their astrophysical significance is still great. Using the Gravitational Wave Interferometer Noise Calculator (GWINC) tool [114] developed by the LIGO Scientific Collaboration (LSC) the impact of the reduced thermal noise associated with mesa beams was estimated.[9] Fig. 2.5 shows the strain sensitivity of AdvLIGO one might obtain on switching to mesa beams.[10] This improvement results in:

- An increase in binary neutron star inspiral range [115] from 198 Mpc to 238 Mpc
- An increase in binary black hole inspiral range [115] from 1690 Mpc to 2022 Mpc
- An improvement in the sensitivity to the stochastic gravitational wave background [13] from $\Omega_{\mathrm{GW}} = 2 \times 10^{-9}$ to $\Omega_{\mathrm{GW}} = 1.7 \times 10^{-9}$
- An event rate[11] increased by a factor of 1.7

There are of course numerous caveats associated with these values, perhaps foremost among these is the non-ideal coupling between Gaussian and mesa beams.

2.1.4 Coupling to Gaussian beams

We envisage that mesa beams will be created by injecting a Gaussian mode into a cavity formed by Mexican hat mirrors.[12] One popular scheme involves modifying the arm cavities to support mesa beams while the other interferometer optics remain spherical.

[8] And to a lesser extent the more stringent diffraction loss requirements.

[9] Values were obtained by appropriately modifying the thermal noise source terms in the GWINC code. The interferometer parameters were optimised for NS-NS binary inspirals. Hence the numbers quoted for black holes and the stochastic background can be improved upon.

[10] Similar improvements are expected for other second generation interferometers.

[11] Assuming event rate scales as the cube of NS-NS binary inspiral range.

[12] This cavity could be internal to the laser system, a preliminary mode cleaner or the arm cavities themselves.

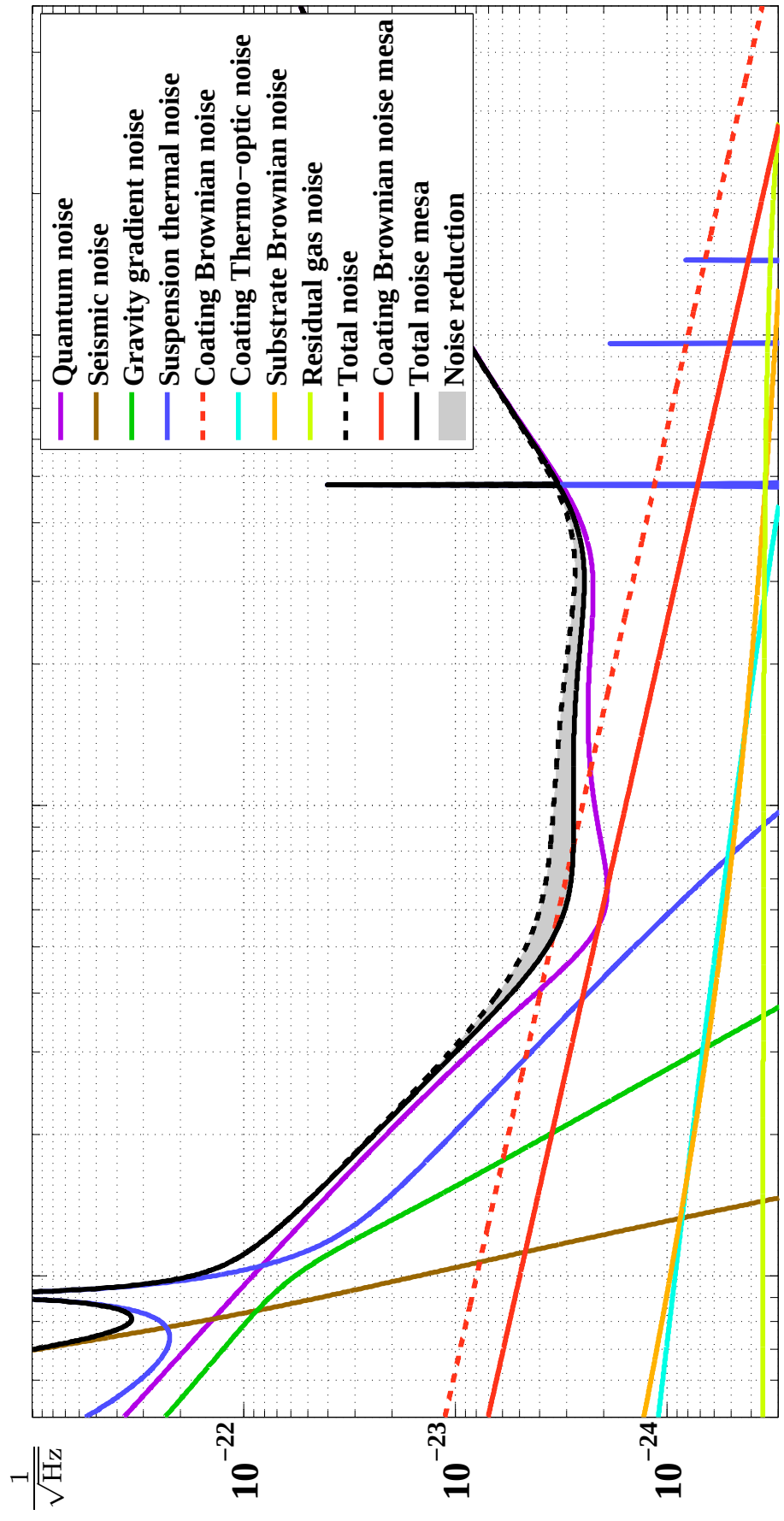

Figure 2.5: Interferometer noise curve for mesa beams with the instrument optimised for NS-NS binary inspirals.

In this case the Gaussian-mesa coupling has ramifications for RF reflection locking schemes and optical gain in the recycling cavities.

Regardless of the exact interferometer design, it is crucial to identify the Gaussian beam with the strongest coupling to any mesa cavity. The quantity we seek may easily be found from the inner product of normalised Gaussian and mesa fields

$$C = \langle \Psi_{\text{gauss}} | \Psi_{\text{mesa}} \rangle. \tag{2.7}$$

For flat mesa beams we have

$$C_{\text{FM}} = \frac{\omega_{\text{g}}}{D}\sqrt{\frac{2}{\aleph}}\left(1 - \exp\left[-\frac{D^2}{\omega_0^2 + \omega_{\text{g}}^2}\right]\right). \tag{2.8}$$

Maximising this function we are able to find an equation for the waist of the optimally coupled Gaussian beam ω_{g} [106, 102],

$$1 - \exp\left[-\frac{D^2}{\omega_0^2 + \omega_{\text{g}}^2}\right]\left(1 + \frac{2\omega_{\text{g}}^2}{\omega_0^2 + \omega_{\text{g}}^2}\frac{D^2}{\omega_0^2 + \omega_{\text{g}}^2}\right) = 0. \tag{2.9}$$

The corresponding coupling for concentric mesa beams is

$$C_{\text{CM}} = \frac{\omega_0^2}{\omega_{\text{g}} D}\sqrt{\frac{2}{\aleph}}\left(1 - \exp\left[-\frac{\omega_{\text{g}}^2}{\omega_0^2}\frac{D^2}{\omega_0^2 + \omega_{\text{g}}^2}\right]\right) \tag{2.10}$$

which is greatest for the Gaussian beam with waist ω_{g} solving

$$1 - \exp\left[-\frac{\omega_{\text{g}}^2}{\omega_0^2}\frac{D^2}{\omega_0^2 + \omega_{\text{g}}^2}\right]\left(1 + \frac{2\omega_{\text{g}}^2}{\omega_0^2 + \omega_{\text{g}}^2}\frac{D^2}{\omega_0^2 + \omega_{\text{g}}^2}\right) = 0. \tag{2.11}$$

For both beam configurations $\aleph$ is as defined in (2.4).

These relationships are represented graphically in fig. 2.6. In both cases the optimal power coupling is around 95%. Such a strong overlap indicates that any additional shot noise due to reduced circulating power should be negligible.[13] However, the 5% of light rejected by each arm cavity may lead to elevated readout noise as inevitable

[13] Shot noise scales as the square root of power.

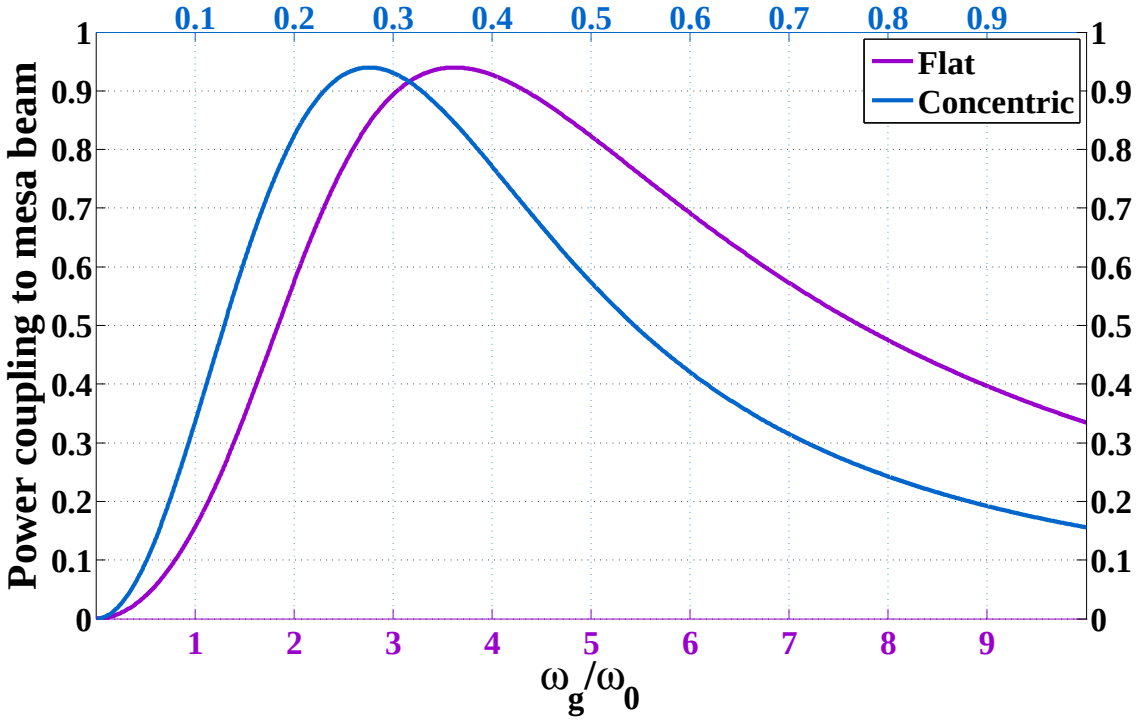

Figure 2.6: Power coupling $|C|^2$ between Gaussian and mesa beams as a function of Gaussian waist size ω_g. The mesa beams are formed from minimal Gaussians of waist ω_0. The optimal coupling occurs when $\omega_g \simeq 3.6\omega_0$ for flat mesa beams and when $\omega_g \simeq 0.28\omega_0$ for concentric modes.

differences between the arms will prevent it interfering perfectly at the beam splitter.

2.1.5 Possible alternatives

Although this thesis focuses on the mesa beam, several other modes aiming to reduce measured test mass thermal noise have been proposed. In this section we introduce these alternatives.

2.1.5.1 Hyperboloidal beams

As an extension of their work on concentric mesa beams, Bondarescu and Thorne also devised an entire continuum of modes spanning nearly flat to nearly concentric configurations [109]. These beams appear particularly promising once finite mirror

effects are taken into account (see §2.1.6).

Flat mesa beams are created by superposing minimal Gaussians whose optical axes form a cylinder; for the concentric beam these axes instead form a cone. The generators of a cylinder of height L radius r are the lines joining the points $(r, \phi, -L/2)$ to the points $(r, \phi, L/2)$. The generators of a cone of height L and radius r are the lines joining the points $(r, \phi, -L/2)$ to points $(r, \phi + \pi, L/2)$. A smooth interpolation from the cylinder to the cone is given by the set of hyperboloids generated by lines joining the points $(r, \phi, -L/2)$ to the points $(r, \phi + \alpha, L/2)$.[14] Minimal Gaussians distributed with axes along these lines superpose to form a new family of beams ranging from nearly flat to nearly concentric.

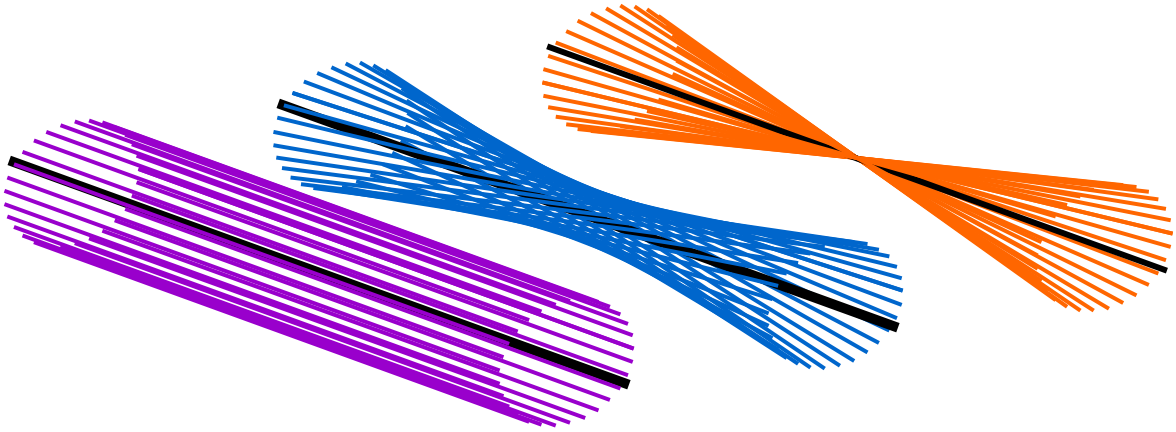

Figure 2.7: Construction of mesa and hyperboloidal modes. The optical axes of selected minimal Gaussians are shown to illustrate the differences between flat, concentric and hyperboloidal mesa beams. The minimal Gaussians of the flat mesa beam are spread uniformly over a cylinder of radius D (purple) whereas those of the concentric mesa beam form a cone with aperture angle $4D/L_{\text{cavity}}$ (orange). Exploiting a smooth mapping between these shapes one is able to generate a family of hyperboloidal beams spanning the space from flat, through Gaussian, to concentric mesa beams (blue).

The mirror figures which support mesa beams were obtained through evaluation of the appropriate optical field over flat and concentric fiducial surfaces. These surfaces were found by truncating the axis of each minimal Gaussian after it had propagated a

[14] With $\alpha = 0$ giving the cylinder and $\alpha = \pi$ the cone (see fig. 2.7).

distance $L/2$. For our new beams the surface formed is given by

$$z = S_\alpha(r) = \sqrt{(L/2)^2 - r^2 \sin^2(\alpha/2)} \simeq \frac{L}{2} - \frac{r^2 \sin^2(\alpha/2)}{L}. \tag{2.12}$$

Evaluating the field on this surface we find

$$\Psi_\alpha(r, \alpha, D) = \int_0^D \int_0^{2\pi} \exp\left[j \frac{r r_0}{\omega_0^2} \sin\phi_0 \sin\alpha - \frac{r^2 + r_0^2 - 2 r r_0 \cos\phi_0}{2\omega_0^2} (1 - j\cos\alpha) \right] r_0 \, \mathrm{d}\phi_0 \mathrm{d}r_0. \tag{2.13}$$

As before, adding the phase front of Ψ_α at $z = L/2$ to our fiducial surface S_α we obtain the complete mirror figure $z = \pm S_\alpha \mp z_{\mathrm{HR}}(\alpha)$. Selected hyperboloidal mirrors and intensity profiles are shown in fig. 2.8. The full range of modes is explored for $\alpha \in [0, \pi]$.[15]

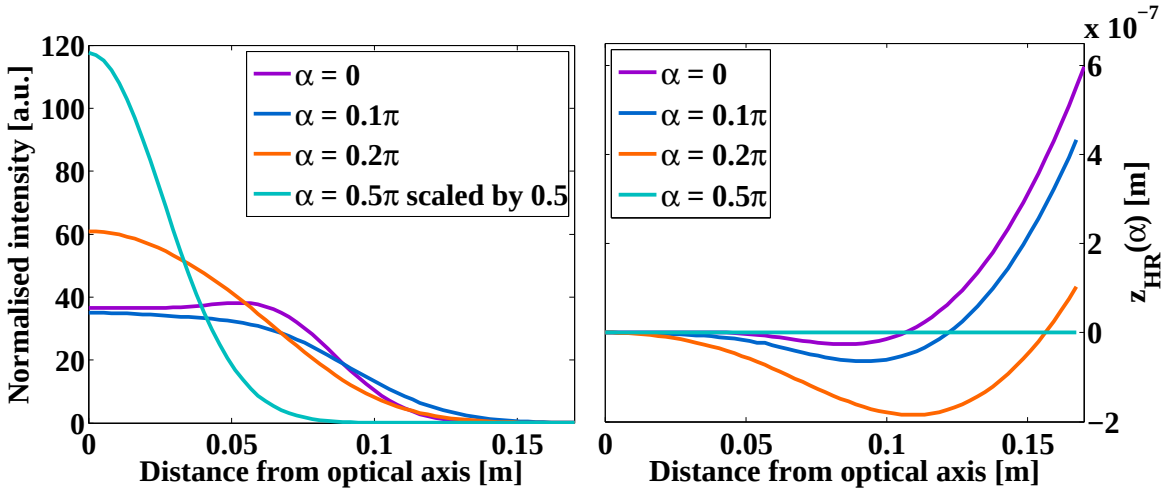

Figure 2.8: Left: Normalised intensity profiles of various hyperboloidal modes. The Gaussian $\alpha = 0.5\pi$ mode has been reduced by a factor of two for ease of comparison. Right: The correction to the fiducial surface for each of the intensity profiles. Notice that the correction for the $\alpha = 0.5\pi$ mode is null i.e. the mirror is spherical.

In addition to the flat and concentric configurations given by $\alpha = 0$ and π, one other twist angle has special properties. In the $\alpha = \pi/2$ case S becomes a spherical surface with $R = L$ and the resulting cavity eigenmode is our minimal Gaussian.[16]

[15] Or over half this interval if use is made of the duality relations [110].

[16] Also, in the limit $D \to \infty$ all hyperboloidal beams become Gaussian [116].

Compared to standard mesa modes, hyperboloidal beams provide another degree of freedom α, allowing better optimisation of cavity design to meet diffraction and tilt instability requirements while still reducing the measured thermal noise.

2.1.5.2 Higher order LG beams

All of the non-Gaussian beams discussed above demand specially made phase-graded optics. Concerns over the production of these mirrors[17] and the control of non-Gaussian modes has led to another proposal.

It has been shown that high order LG modes (see fig. 2.9 and §1.5.1.1) are able to produce reductions in substrate Brownian noise comparable to those seen with mesa beams while allowing standard spherical optics to be retained [117]. More recent work at the University of Birmingham concluded that, in all aspects of interferometer control, the behaviour of high order LG modes[18] is similar if not preferable to the standard LG_{00} [118]. The idea of LG modes therefore seems promising and experimental investigations are now in progress.

As with mesa beams, a number of issues must be resolved before high order LG modes can be considered a credible alternative to the standard Gaussian. Foremost amongst these is the initial creation of the mode. Solutions involving spatial light modulators and diffractive optics have great potential, as do approaches based on bespoke optical fibres. Such fibres could be used to drive mode cleaner cavities or as mode cleaners themselves. Of course, efficiency and noise implications will ultimately distinguish the best technique.

There are also a number of other concerns surrounding these modes. The nodes of LG beams impose large thermal gradients near the surface of the test mass, elevating thermoelastic noise levels above those of even the LG_{00}. Although overall noise is reduced this effect should be borne in mind where absorption is unknown or alternative

[17] Although the required technology has been proven (see §2.2.2.2).
[18] They specifically studied LG_{33} modes.

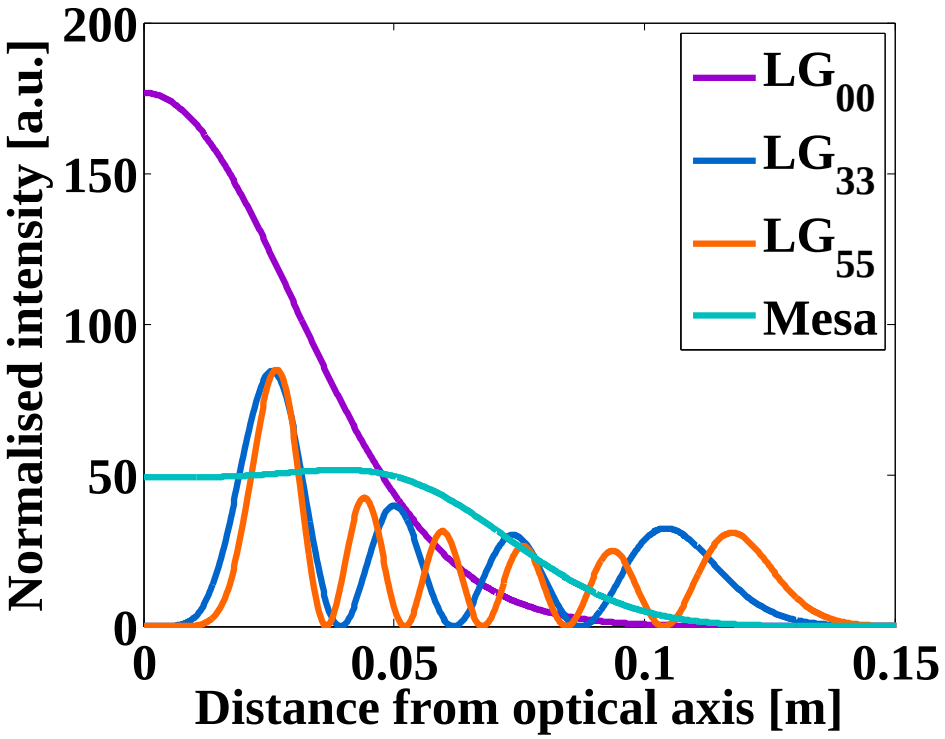

Figure 2.9: Comparison of LG and mesa modes of equal diffraction loss.

substrate materials are used.

Perhaps the key benefit of high order LG beams is their ability to resonate in spherical mirror cavities, allowing one to exploit all the manufacturing nous obtained to date. However, one must always remain mindful that, where one Higher Order Mode (HOM) is resonant, all modes of the same order are also resonant – a degeneracy not exhibited by the other candidate modes.

Another troublesome issue associated with the proposed helical LG modes is the 180° phase shift experienced by the cavity-plane field distribution in resonators with an odd number of reflections. Such resonators are widely used as mode cleaners in gravitational wave interferometers. Switching to bow-tie cavities or sinusoidal LG modes eliminates this problem at the expense of increased development time and thermal noise respectively.

2.1.5.3 Optimal beams

The variety of modes discussed above leads one to wonder what the optimal beam shape for reducing thermal noise would be. Efforts in this direction were greatly expedited by two publications. The first by Lovelace [119] developed scaling laws for four principal sources of thermal noise in the infinite test mass limit. Significantly, these laws are applicable to arbitrary beam shapes. The second key development was led by Galdi and collaborators [120] who found a computationally efficient parameterisation of arbitrary beam profiles and their supporting mirrors in terms of rapidly converging LG expansions. Building on this work it was finally possible to begin defining a minimisation function and investigating whether physical solutions were available, subject to the given constraints.

Galdi et al. continued their work in this field, contributing several interesting results [121]. Ignoring diffraction loss, it was discovered that the ideal beam for mitigating coating thermal noise is indeed the top hat mode discussed above. This conclusion confirmed the intuitive approach which led to the creation of the mesa beam. However, approximations to the optimal beam which included diffraction loss revealed that beams with large ripples in their radial profiles could outperform flat topped mesa modes. Overall it was estimated that optimised beams might surpass mesa beams by a factor of $\sim$2.5.

Unbeknownst to Galdi, Caltech's Bondarescu and Chen were simultaneously creating their own algorithms built on the same foundations. Optimising for coating noise alone they were able to extract a mode shape and mirror profile promising significant noise benefits over Gaussian *and* mesa beams [122]. This work provided an independent corroboration of Galdi's results, with Bondarescu's optimised conical beam (see fig. 2.10) yielding an improvement factor of 2.32 over mesa beams, approaching the predicted value of 2.5. This beam also exhibited the large scale ripples in its intensity profile which Galdi had anticipated.

Bondarescu also studied the practical performance of his new mode revealing it to

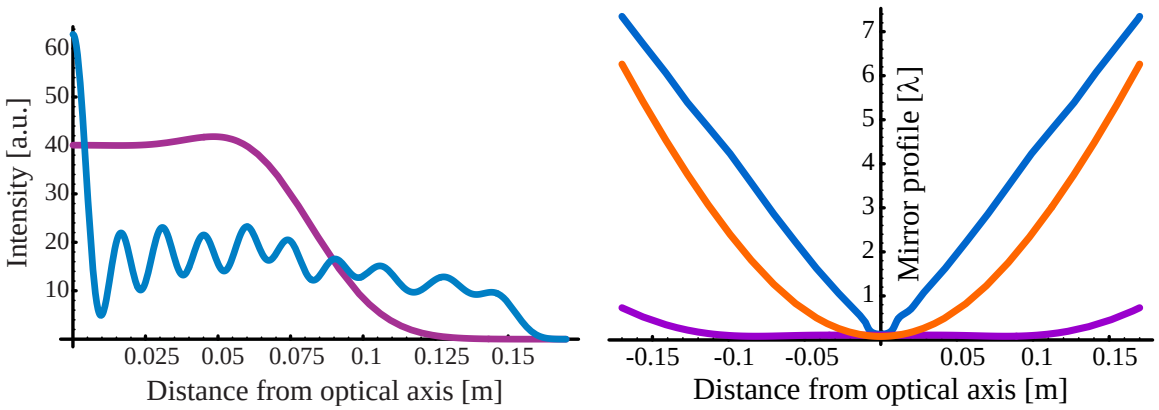

Figure 2.10: Bondarescu's conical beam. Left: Intensity of conical (blue) and mesa (purple) modes. Right: Mirror profiles in units of λ for the conical beam (blue), flat mesa beam (purple) and concentric mesa beam (orange). Plots adapted from [122].

be significantly more sensitive to all perturbations (mirror figure errors, tilts, transverse translations) than the equivalent mesa beam and to have almost no coupling to Gaussian fields. Although these issues will likely prohibit the use of such beams in future detectors, we hope that this seminal result will stimulate work toward a full optimisation including all noise sources and finite mirror effects simultaneously.

2.1.6 Finite mirror effects

Above we saw how mesa and hyperboloidal mirrors were constructed by truncating the phase front of the infinite theoretical field at the mirror radius. In reality the cavity mode is finite and the phase front of this finite beam fails to match the mirror surface leading to increased loss. Lundgren et al. came to the same realisation and began investigating finite mirror effects numerically [116].

They discovered that diffraction loss is not a monotonic function of beam radius. For beam sizes comparable to the mirror dimension local minima exist. Exploiting this new understanding, larger beams giving greater reductions in measured thermal noise can be used without breaching the 1 ppm diffraction loss limit. Limiting study to the family of hyperboloidal beams (§2.1.5.1), which includes flat and concentric mesa beams, it was found that a reduction in coating thermal noise of 12% was available

using an $\alpha = 0.91\pi$ beam broadened such that $D = 4.2\omega_0$.

Further reductions are available if one iteratively shapes the mirror surface so that its profile matches the phase front of the finite eigenmode. In this case the optimal starting point is a concentric mesa beam with $D = 4.36\omega_0$.[19] The resulting mirror and intensity profiles remain very close to their non-optimised counterparts but provide a reduction in coating thermal noise of 28%. The corrections applied to the optimised mirror do not present any manufacturing difficulties beyond those imposed by standard mesa modes.

These gains strengthen the argument for further investigation of mesa beams and suggest another effect which must be included if truly optimal beams are to be found.

2.1.7 Summary

In this section we have presented a basic introduction to the mesa beam. Theoretical expressions for its fields and mirror profiles have been given while more realistic modes from numerical simulation were used to estimate thermal noise reductions and their astrophysical significance. Competing non-Gaussian modes currently under investigation and the state of efforts to find optimal beams have also been discussed.

When searching for an alternative to the fundamental Gaussian beam, with a view to reducing measured thermal noise, it is important to remember that candidate modes must be suitable for use in a real interferometer.[20] At the time of writing, the mode accompanied by the most mature theoretical study and thought most likely to operate successfully in an kilometre-scale detector was the mesa beam. Hence this was the mode preferred for our experimental investigations.

[19] Recall that we are using $D = 3.55\omega_0$ to match the diffraction loss of the Gaussian beam.

[20] i.e. the mode can be excited by a Gaussian beam, techniques are available which can realise the appropriate mirror profiles, sensitivity to mirror figure errors and angular perturbations is not prohibitive etc.

2.2 Apparatus

With the theoretical benefits of switching to mesa beams well established, complementary experimental work began. This effort was intended to investigate practical aspects of the mesa beam's control rather than measure thermal noise suppression directly.[21] In this section we describe the apparatus which was built with this goal in mind.

2.2.1 Non-spherical optics

We begin by detailing the construction of our Mexican hat mirror, it is the unique feature of our experiment and its properties drove the design of our entire apparatus.

Prior to the realisation that tilt instabilities would be a major problem in future interferometers (see §2.1.2.2) only nearly flat cavity configurations were discussed in the context of mesa beams. Thus we desired to construct a mirror profile similar to those shown in fig. 2.2.

Due to the unusual profile of this mirror it was not possible to utilise standard polishing techniques. To circumvent this problem collaborators at Laboratoire des Matériaux Avancés (LMA) [123] developed an innovative two-step deposition process to shape the mirror substrate. Upon its completion highly reflective mirror coatings were applied in the usual way.

2.2.1.1 Deposition process

Starting from a micro-polished substrate, the initial deposition is effected through a large mask with the substrate in rotation (see fig. 2.11). The mask aperture is shaped to deposit the gross features of the desired profile, accounting for the angular velocity of the substrate (see fig. 2.12). This first stage has a precision of ∼60 nm and is able

[21] It was thought to manufacture a Mexican hat optic for Caltech's TNI. However, as discussed in §2.2.1.1, such small optics (the TNI cavities are ∼1 cm long) are extremely difficult to realise.

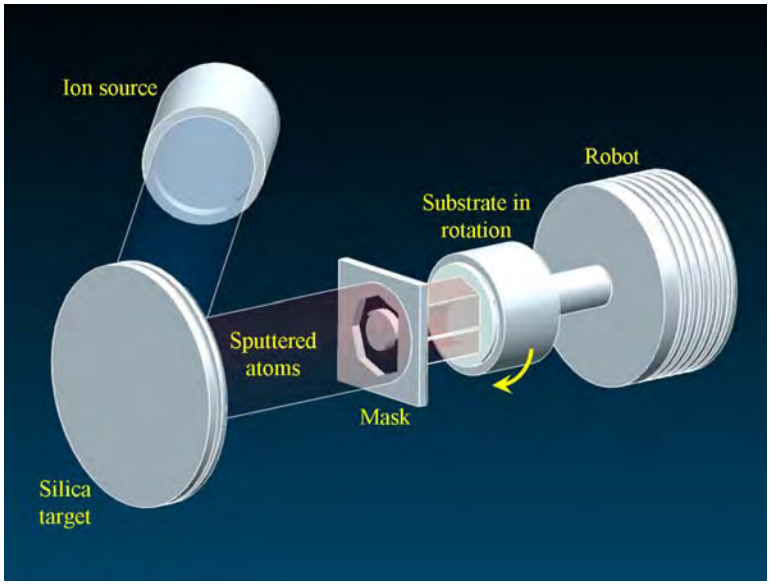

Figure 2.11: The first step in the manufacture of a MH mirror. Using a specially tapered mask (fig. 2.12) the gross features of the mirror profile are deposited with the substrate in rotation.

Figure 2.12: The mask used in the first step of MH mirror construction is specially tapered to account for the mirror's angular velocity.

to deposit a coating with a thickness of order 1 µm. Upon completion, the achieved figure is evaluated using a Fizeau interferometer and compared to the ideal profile. This process creates a correction map which is used as input for the second deposition step.

For the second deposition stage the large aperture mask is replaced with a small pinhole (see fig. 2.13). Using data from the correction map, the mirror substrate is translated across the narrow sputtered beam to add small amounts of material where necessary (see fig. 2.14). The fine structure of the mirror profile is created by adjusting the dwell

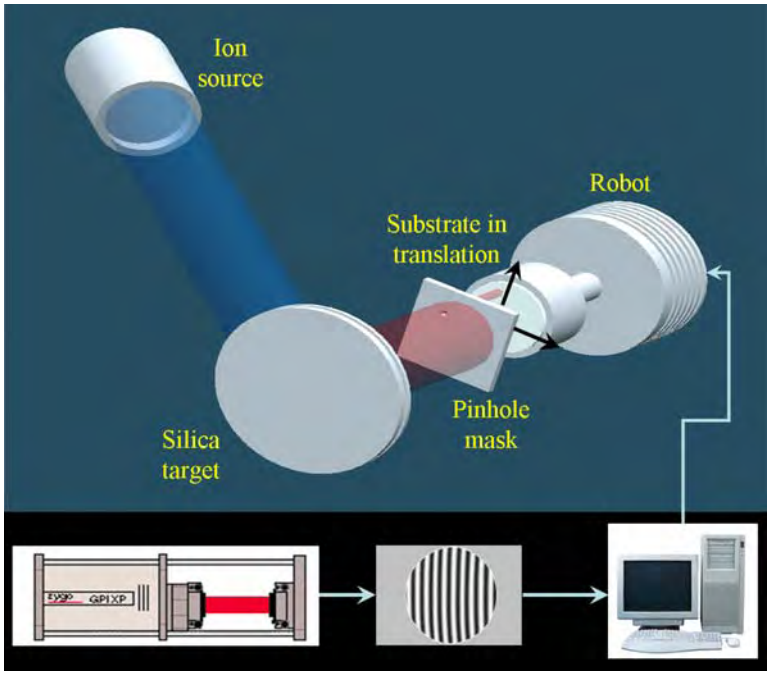

Figure 2.13: The second stage of MH mirror construction. With the substrate in translation a narrow atomic beam deposits a corrective coating to realise the fine features of the profile .

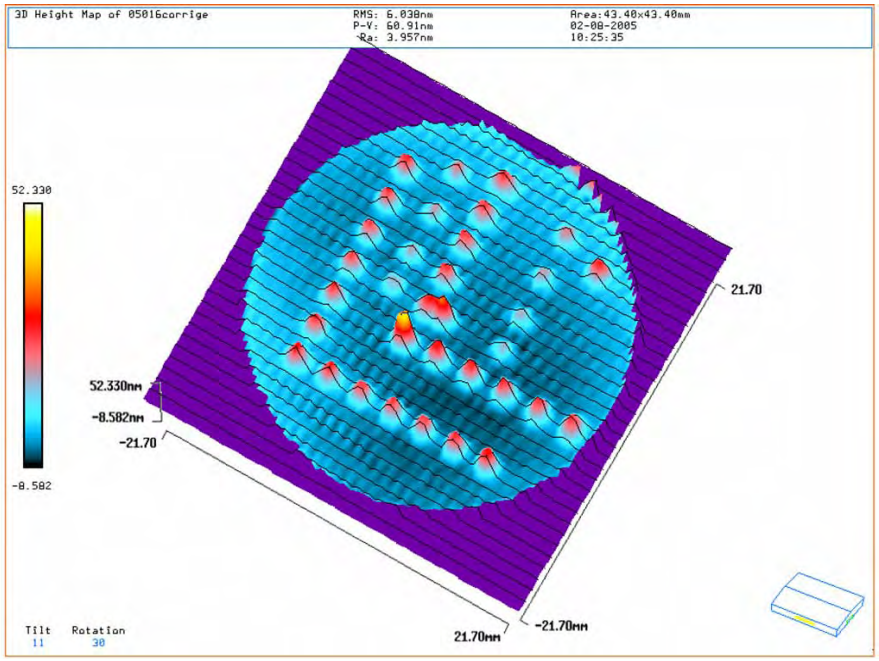

Figure 2.14: Calibration measurements for the second stage of mirror construction. Small amounts of material are deposited at regular intervals to allow characterisation of the robotic arm and corrective beam. Substrate diameter is 50 mm, the same as our experimental optic.

time of the beam in each location. The precision of this technique is around 2 nm. Due to the slow rate of material deposition it is impractical to deposit layers more than 100 nm thick.

Factors limiting the accuracy of this technique include the precision of the robotic arm used to manoeuvre the substrate (0.2 mm) and the sharpness of the atomic beam passed by the pinhole. However the principal constraint is imposed by the transverse resolution of the interferometric correction map (0.35 mm).

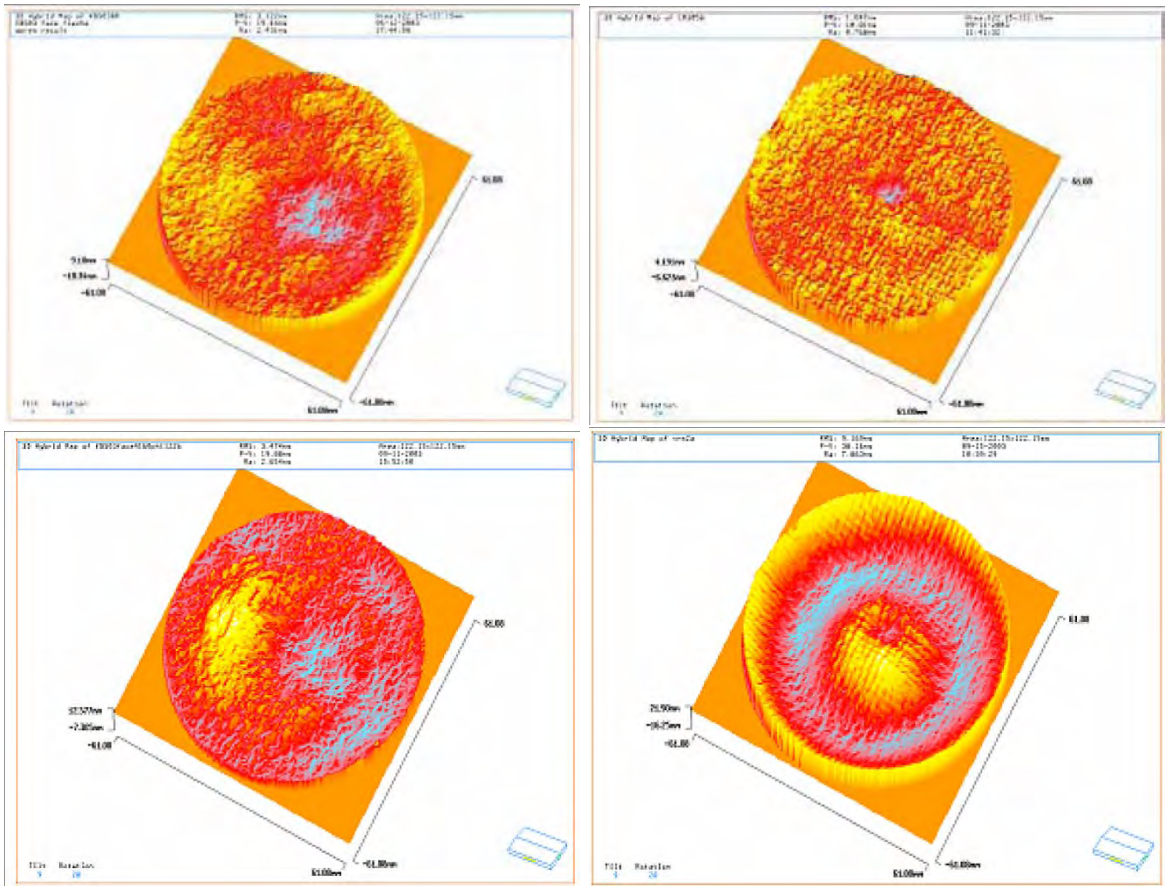

Figure 2.15: The first tests of the new deposition technique were made on opposite sides of the same substrate. Flat (upper) and MH (lower) profiles were attempted. The left hand column shows the profiles after the first deposition stage while the right shows the same surfaces after corrective coating. Both tests were successful. The small defects near the centres of both mirrors were caused by a known problem with the computer controlled translation stage. This problem was fixed before production mirrors were attempted.

Initial tests of this technique were made on opposite sides of the same 156 mm ⌀×

100 mm tk. substrate.[22] Both spherical and Mexican Hat (MH) profiles were deposited successfully (see fig. 2.15) and the decision to proceed with production was made.

2.2.2 Our mirror

2.2.2.1 Cavity length

It was originally envisioned that the practical investigation of mesa beams would entail a 'table top' experiment with a cavity length of around 1 m. Unfortunately such a compact setup proved unfeasible.

For standard mesa modes, beam size is related to cavity length through

$$D = 4\omega_0 = 4 \times \sqrt{\frac{\lambda L}{2\pi}}. \tag{2.14}$$

Consider now the case of fixed diffraction loss. Under this assumption the mirror radius is proportional to the square root of the cavity length[23] and, for mesa beams, the *height* of the mirror profile is independent of cavity length. Hence shorter cavities demand smaller mirrors with larger gradients in their figures.

The interferometric measurement performed between the two deposition stages detailed above was able to resolve a maximum slope of 500 nm/mm. Moving to shorter cavities one quickly becomes metrology limited. This limit defined the smallest mirror which we were able to construct with confidence and thus the shortest feasible cavity length. Allowing a reasonable margin this shortest length was 16 m.

Unable to accommodate such a long resonator in our laboratory, the decision was made to build a folded half-symmetric cavity. By placing one flat mirror at what would have been the mid point of the full cavity and a second internal to the new cavity, the total length of the mechanical structure could be reduced to a more manageable 4 m (see

[22] The aspect ratio of the optic must be small as coating stresses can lead to deformations of the substrate beyond our allowed tolerances.

[23] Ignoring the finite mirror effects discussed above.

fig. 2.21).

Aiming for a 4 m structure we began sourcing equipment. Working in the United States, many materials were only available in imperial lengths. In particular the rods chosen to form our cavity (see §2.2.3) could only be sourced in lengths of 12 feet or 3.658 m. Thus was defined the length of our cavity.

Taking $L = 4L_{\mathrm{INVAR}} = 14.632$ m in (2.1),[24] gives mesa beam parameters $\omega_0 = 1.57$ mm and $D = 6.30$ mm. Allowing 1 ppm diffraction losses then fixes the mirror radius at 13 mm.[25] With the desired MH profile now fully defined the design was relayed to LMA.

Unfortunately, when calculating the mirror profile, the true cavity construction was not accounted for. The cavity length is not given by $2L_{\mathrm{INVAR}}$. Including the separation of the input and MH mirrors (60 mm) and the distance each HR surface encroaches into the cavity structure ($\gtrsim$30 mm), the true cavity length is 7.195 m not 7.315 m as assumed. This error was not appreciated in time to correct the profile given to LMA resulting in a subtle mismatch between the received MH mirror and our experimental apparatus. The effects of this misunderstanding are tacitly accounted for in each of the following analyses.

2.2.2.2 Construction

Before construction of our MH mirror could commence a substrate had to be chosen. Development work with thin substrates had revealed that warping due to coating stresses had the potential to ruin the figure of our mirror. Hence the final article was deposited on a stout 50 mm ⌀× 30 mm tk. substrate, despite our mirror having a diameter of just 26 mm.

Initially there was some indecision regarding the polish which should be applied to this

[24] To account for the folded, half symmetric construction of our resonator.

[25] The maximum slope of our MH mirror is thus ∼460nm/mm, safely below the 500nm/mm metrology limit.

substrate. A flat polish would require the deposition of more than 1 µm of material to achieve the MH profile; for a substrate having a commercial spherical polish[26] this number could almost be halved (see fig. 2.16). Ultimately a flat polish was chosen. This approach was thought more conservative as it limits the amount of additional material applied in the mirror's central region where defects are most problematic.

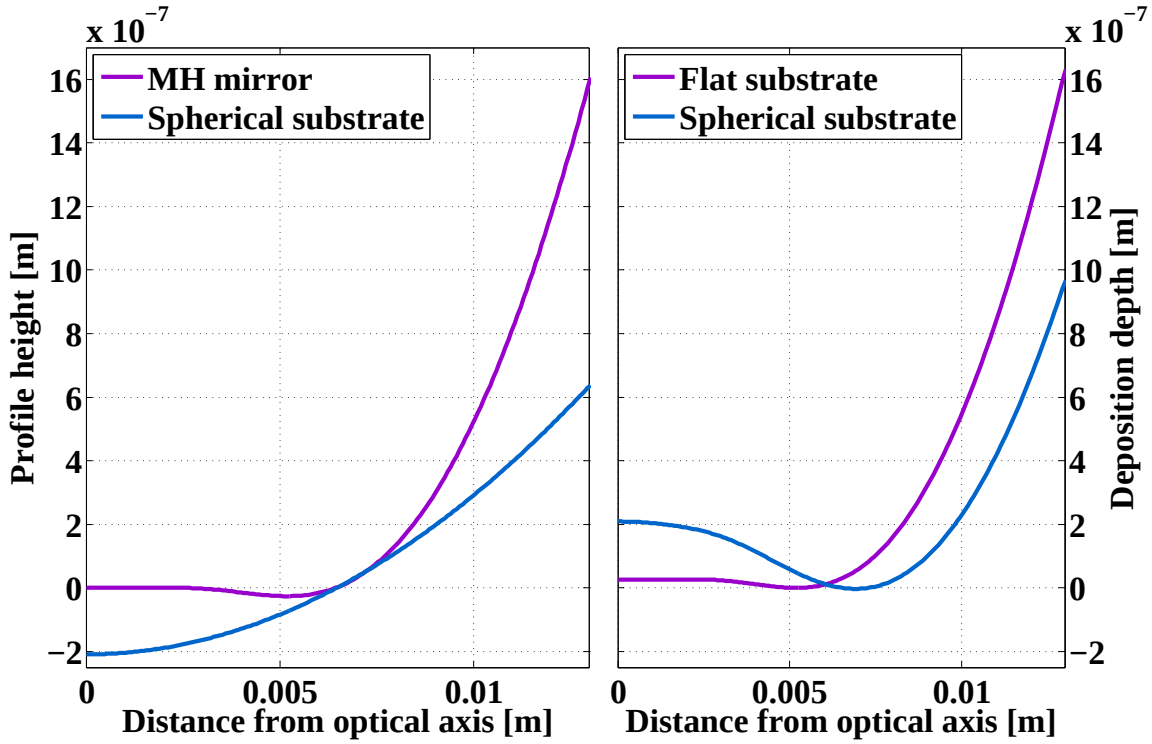

Figure 2.16: A spherical polish was considered for the MH substrate as it could reduce the volume of deposited material. The left hand axes display the profiles of the MH mirror and the optimal spherical polish. The right hand axes show the depth of deposited material required to produce our mirror starting from flat and spherical substrates.

Despite prototyping, the challenging nature of producing Mexican hat optics for lab-scale experiments resulted in the realisation of a mirror with significant figure error. Fig. 2.17 compares the achieved profile with its theoretical counterpart.

Deviations from the specified profile are clearly apparent, with the errors in the mirror's central region most concerning. In addition to random anomalies of amplitude ∼5 nm, there exists a global tilt of the central bump with respect the mirror's fiducial plane

[26]For our purposes R≃100 m.

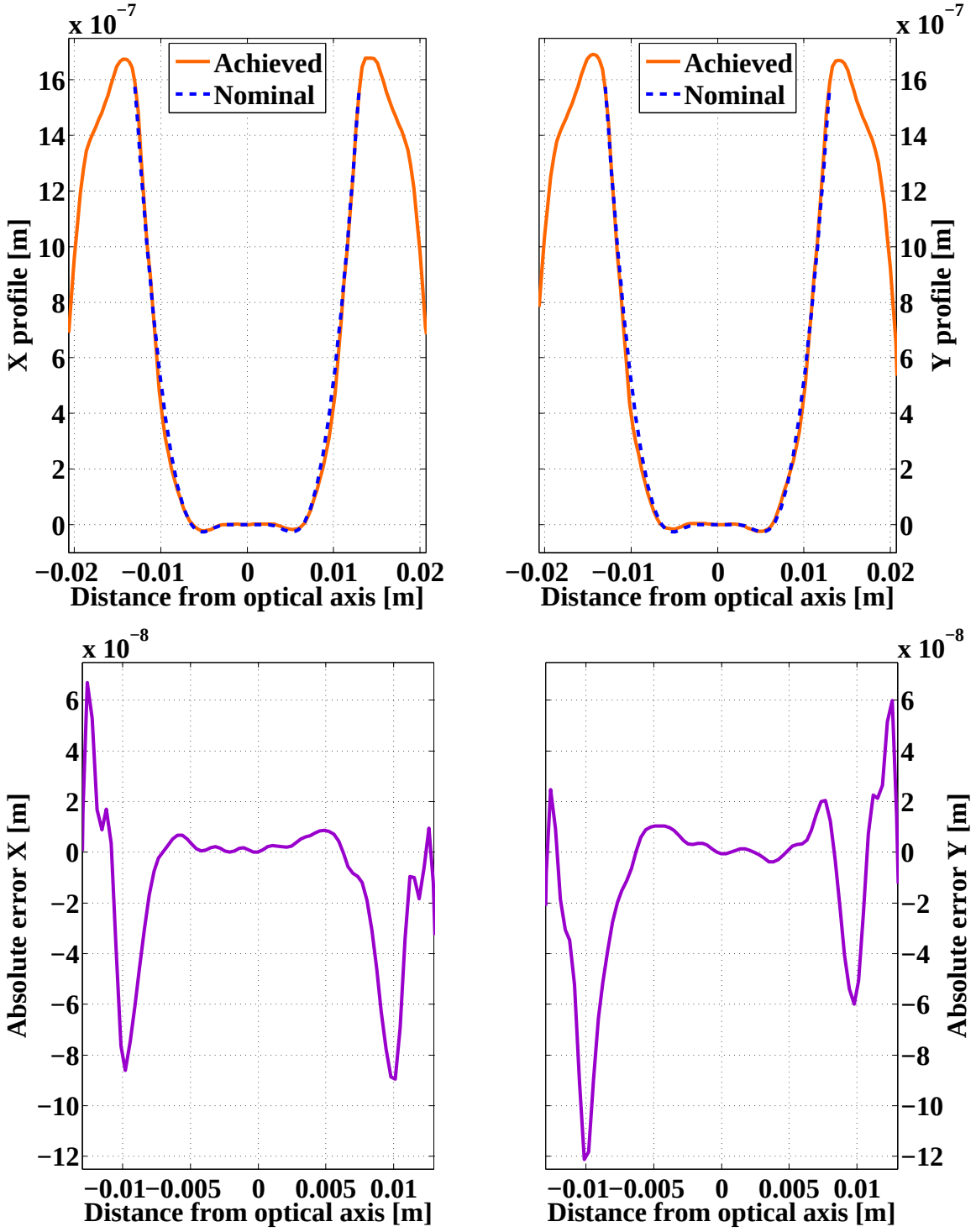

Figure 2.17: Comparison between experimental and theoretical mirrors across orthogonal profiles.

(see fig. 2.18).

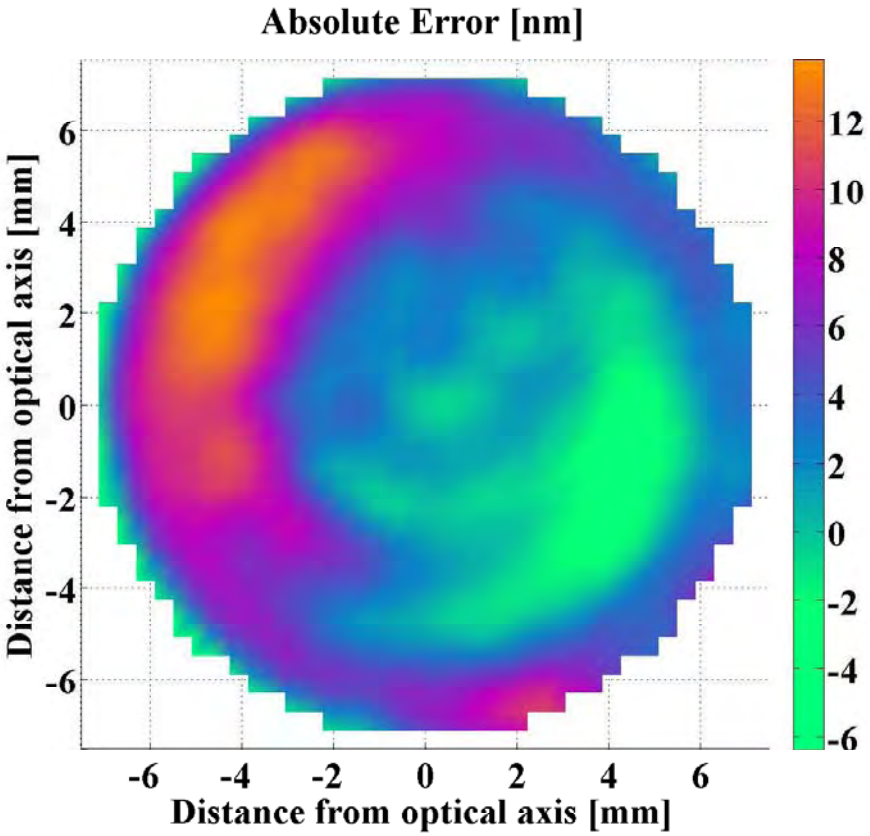

Figure 2.18: The central bump of the experimental MH mirror is tilted ≤1 µrad with respect to the steep brim.

In order to determine whether the achieved profile was acceptable for our work it was implemented in the numerical simulation of a Fabry-Perot resonator. A malformed eigenmode resulted. However, it was quickly found that a reasonable mode shape could be recovered by applying a compensating tilt of order 0.9 µrad (see fig. 2.19). Adjusting our expectations and goals accordingly we proceeded.

2.2.2.3 Optical properties

Curious to understand the optical properties of a mirror generated by the new deposition technique a suite of measurements was made.

The prototype mirrors were found to exhibit large scattering losses (∼150 ppm). This

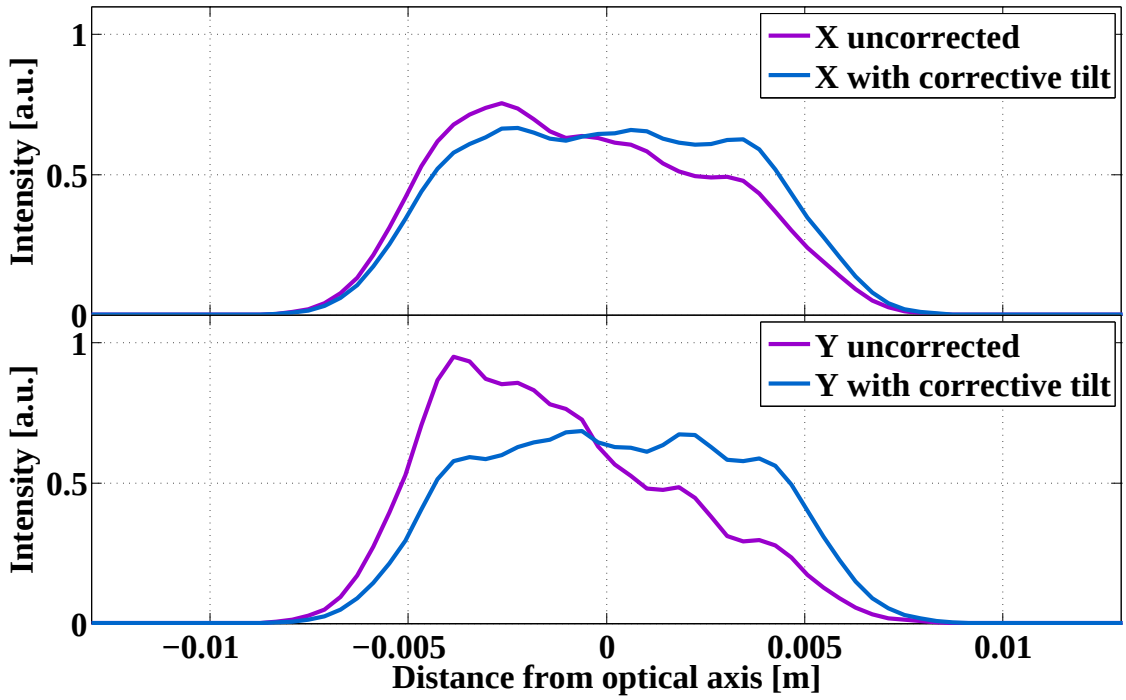

Figure 2.19: Applying a corrective tilt of order 0.9 µrad mitigated manufacturing errors which left the central area of the MH optic tilted with respect to the mirror's fiducial plane (see fig. 2.18).

problem is believed to be due to nucleation centres created through the transfer of mask material to the substrate by the deposition beam. It is expected that this issue could be resolved by pre-coating the edges of the mask with silica before use. Unfortunately resources were not available to investigate this effect at the time our mirrors were being manufactured.

The absorption of the prototype mirrors was also anomalously high at ∼5 ppm. This excess was traced to the quality of fused silica deposited in pre-production runs. The absorption of the delivered MH mirror was below 0.5 ppm.

The average transmission of the final MH mirror was found to be in good agreement with the desired specification. However, on mapping this quantity as a function of position, spatial inhomogeneity was significant. The measured transmission was found to vary by 700 ppm over the central region of the mirror with a form parallelling the mirror's figure error (see fig. 2.20). The mechanism behind this error remains unknown.

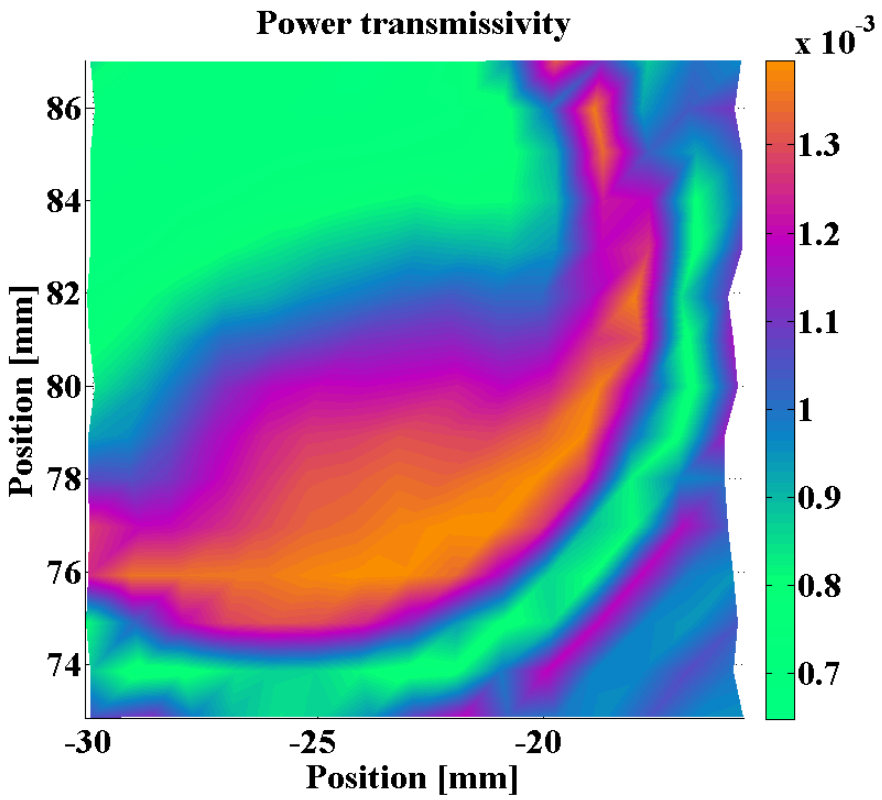

Figure 2.20: Transmission map of production MH mirror's central region. Average transmission is 996 ppm.

2.2.2.4 Summary

Taking into account all known defects, the production MH mirror was adjudged adequate for our purposes, noting that producing a perfect mesa beam was no longer an achievable goal.

The difficulties experienced during the production of our MH mirror may all be traced to the small size and intricate features of our optic. Such problems should not arise in the construction of full size mirrors as the height of the Mexican hat profile is independent of cavity length. Further, the relative transverse resolution of the interferometric map, atomic correction beam and robotic arm will be greater and will thus introduce correspondingly smaller errors.

The preceding discussions assume that any MH mirror will be constructed using the deposition process described in §2.2.1.1. Other possible options include diamond machin-

ing of aluminium substrates and magnetorheological finishing [124]. Neither process is immediately preferable. The magnetorheological technique suffers from metrology limits similar to those highlighted above, meaning small optics are still beyond reach. Diamond machining should allow smaller mirrors to be produced but only if one is willing to forgo transmission of light through the substrate, perhaps a manageable impediment in our work but entirely unfeasible in a full size gravitational wave detector.

2.2.3 Mechanical structure

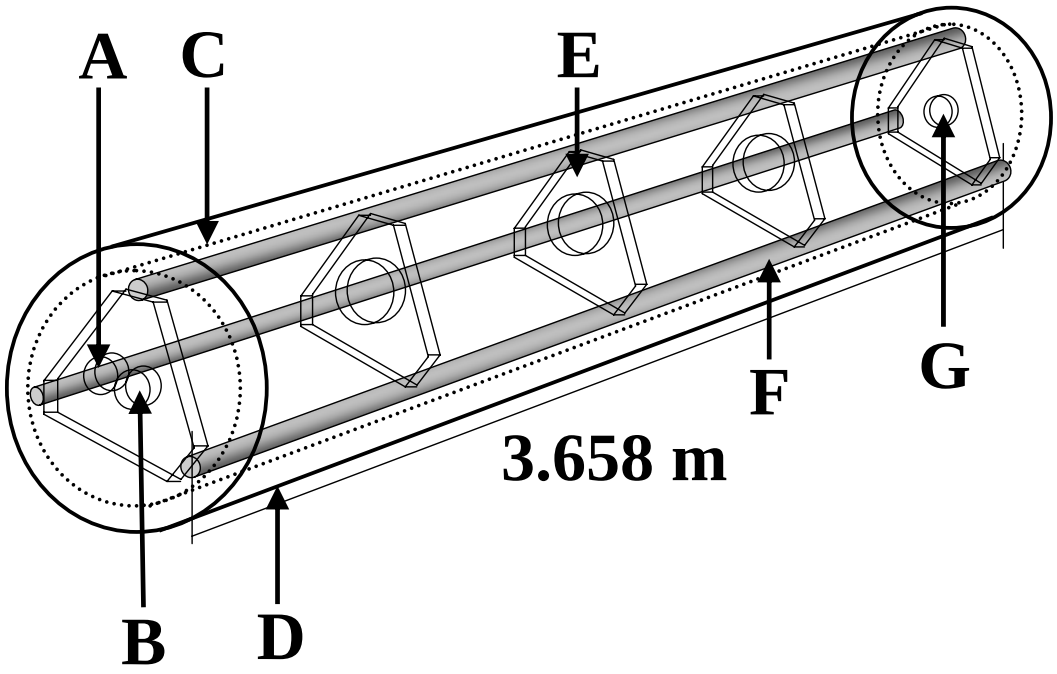

Figure 2.21: A Schematic of the prototype cavity. The entire rigid system is suspended inside a vacuum tank from four pairs of geometric anti-springs to provide environmental isolation. A - Flat input mirror, B - Mexican hat mirror, C - Heat shield, D - Vacuum tank, E - Spacer plate, F - INVAR rod, G - Flat folding mirror. The alignment of each mirror is controlled by a triplet of PZTs mounted at 120^o intervals around the periphery of the mirror. Each PZT is mounted in series with a micrometric screw to allow coarse adjustment. Items A, B and G correspond to U, W and V in fig. 2.30.

2.2.3.1 Cavity and vacuum tank

In the interests of simplicity, a rigid cavity structure was selected over a more complicated independently suspended design. This structure was formed from three solid metal rods 31.75 mm in diameter and 3.658 m in length fixed together by five triangular bracing plates, each 25 mm thick. The cavity optics were mounted on the bracing plates at the extremities of this structure (see fig. 2.21).

Longitudinal stability is of key importance to any resonator. In order for a cavity to remain passively locked its length must be stabilised to around one linewidth $\Delta L_{\mathrm{FWHM}} = \lambda/2\mathcal{F}$. For our cavity this corresponds to[27] $\sim$2.7 nm. Achieving such length stability in a 4 m structure would be unlikely.

Low thermal expansion material was sought for the cavity construction. ULE ($\alpha_{\mathrm{th}} = 3 \times 10^{-9}$ K^{-1}) and Zerodur (1×10^{-7}) were considered but available lengths, ease of machining, lead time and cost forced the use of INVAR. An iron-nickel alloy, INVAR has a specified linear coefficient of thermal expansion of $\alpha_{\mathrm{th}} = 1.2\times10^{-6}$ K^{-1}. Experimental measurements of the delivered material came acceptably close to this value at $\alpha_{\mathrm{th}} = 1.9\times10^{-6}$ K^{-1}. Achieving the required length stability with INVAR thus demands that temperature fluctuations not exceed 3×10^{-4} K. Knowing that thermal drifts would be problematic the cavity was encased in an aluminium heat shield.

In addition to longitudinal stability, the structure was also designed to have high mechanical impedance, obviating the need for an active alignment system and confining any resonances to high frequency. This effort was stymied by the immutable cavity length requirement. An approximate finite element analysis revealed several low frequency eigenmodes (see table 2.3). These resonances were detected experimentally[28] but did not significantly hinder progress.

To allow for vacuum operation the entire cavity structure and thermal shield were

[27] Remembering an extra factor of two in the denominator to account for our folded construction of the cavity.

[28] Particularly the torsional mode at $\sim$60 Hz (see §2.2.4.4).

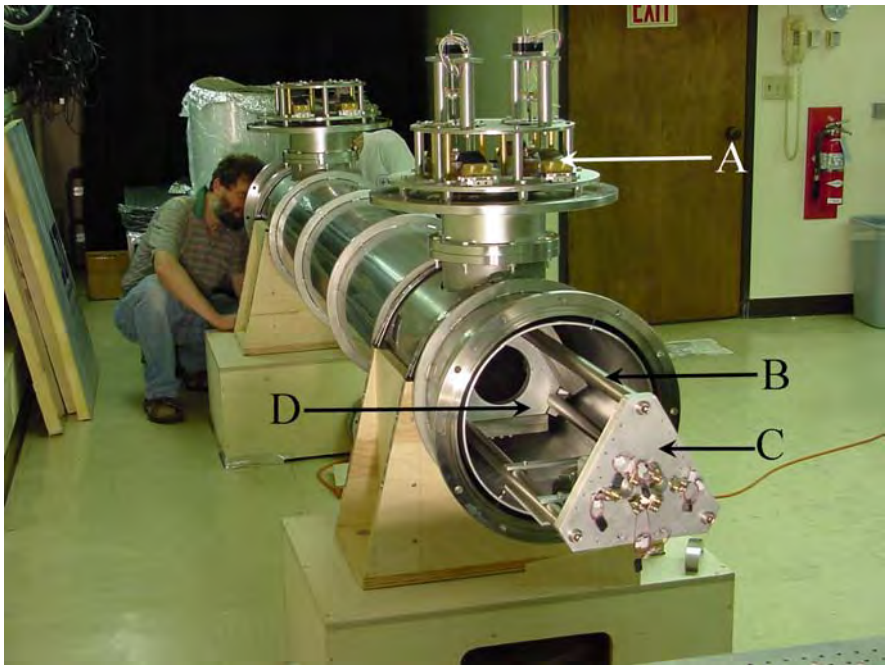

Figure 2.22: Image of cavity structure during construction. A - Suspension system, B - INVAR rods, C - Cavity end plate housing input and MH mirrors, D - Intracavity bracing plate.

Table 2.3: Mechanical resonances of the cavity's supporting structure from finite element analysis.

Frequency [Hz]	Description
0.1272	See saw
2.2027	Yaw
21.707	Snake - 1st bending mode
31.872	Torsion about third bracing plate
32.045	Snake - 2nd bending mode
41.042	Snake - 3rd bending mode
60.358	Torsional about second and fourth bracing plates
84.04	Second torsional about third bracing plate
93.74	INVAR rods
93.812	INVAR rods
96.503	INVAR rods
99.222	INVAR rods
99.31	INVAR rods
100.71	INVAR rods
105.36	INVAR rods
105.45	INVAR rods

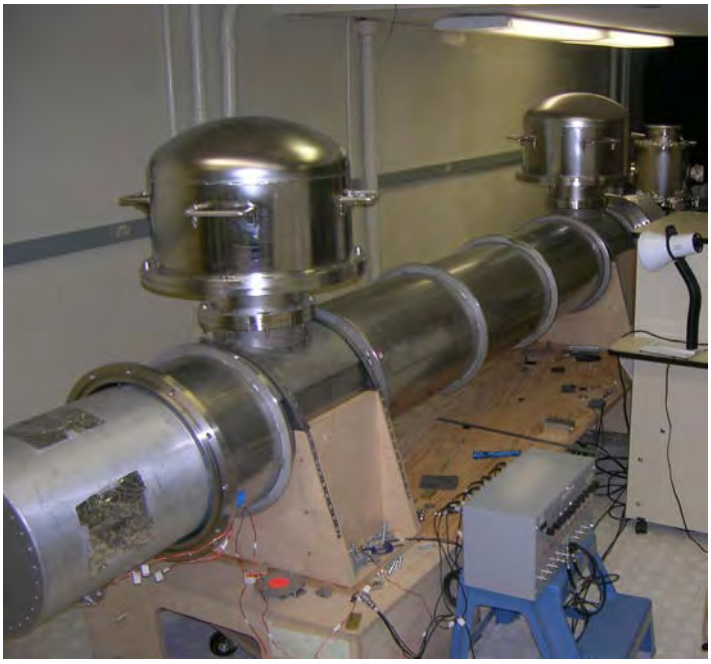

Figure 2.23: Image of cavity apparatus during operation. The thermal shield can be seen protruding from the main vacuum tank.

mounted inside a pressure vessel. This feature was never employed. Figures 2.22 and 2.23 present images of our apparatus during construction and operation.

2.2.3.2 Suspension

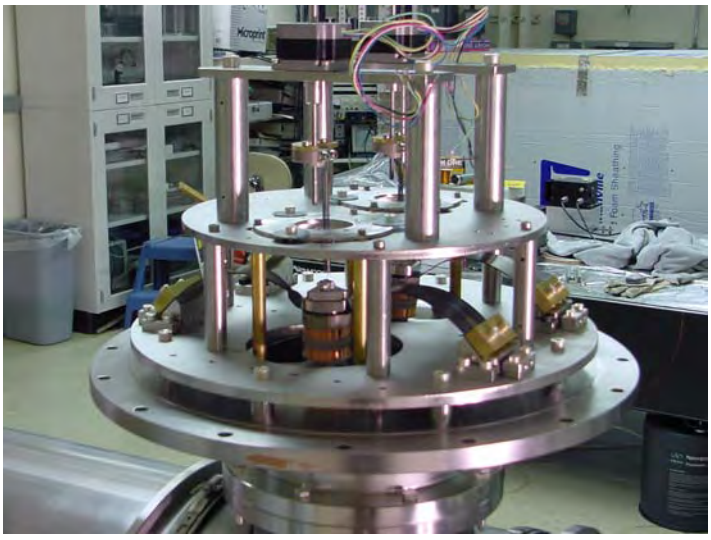

Figure 2.24: The entire cavity assembly weighing 80 kg was suspended from four pairs of geometric anti-springs (two shown). The horizontal and vertical resonant frequencies were 400 and 500 mHz respectively.

To further isolate the mesa beam cavity from environmental disturbances it was suspended from two pairs of Geometric Anti-Springs (GASs) [125]. The simplest GAS consists of two opposing cantilever blades with their suspension points fixed to a common keystone. Unstressed, these blades are flat; in the GAS, under radial compression with an inclined launch angle, they become bowed. The radial compression of the blades generates a force opposing that due to the suspended load, lowering the effective stiffness and therefore resonant frequency of the spring. Through careful tuning one can produce an extremely soft spring capable of suspending large loads.

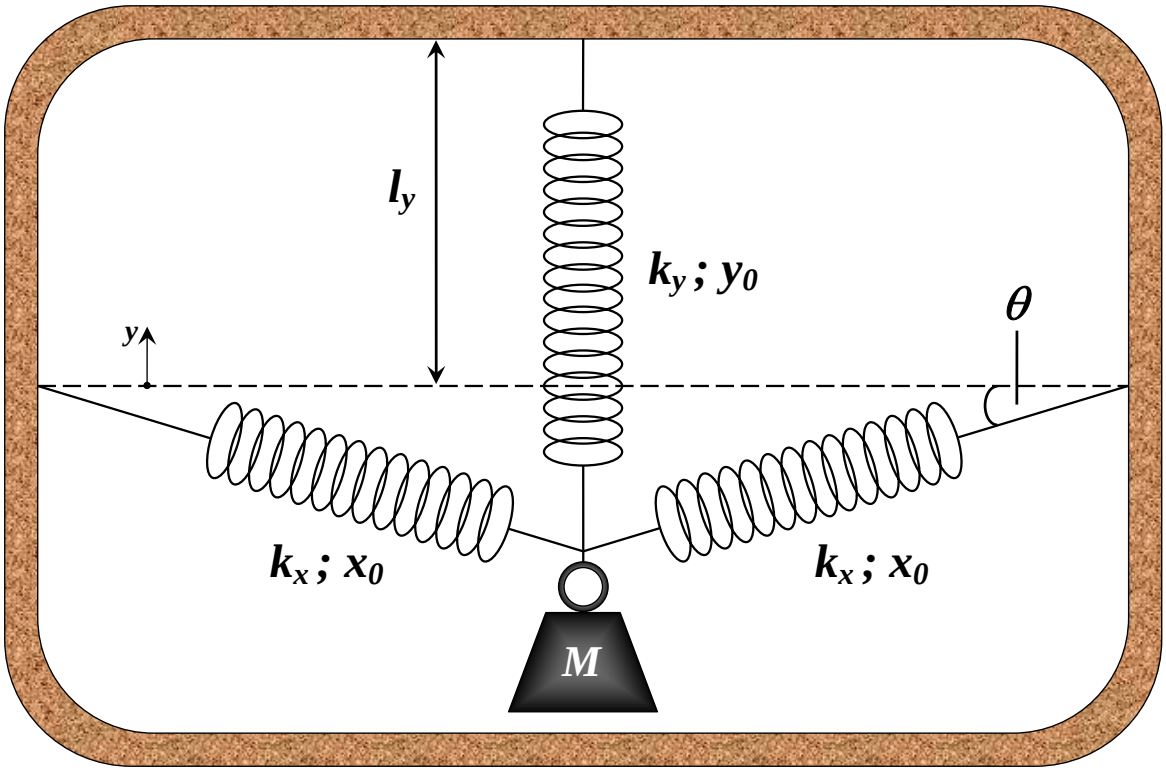

Figure 2.25: Toy model of a GAS.

This concept is demonstrated in the following simple model [126]. A mass M is suspended by one vertical spring and two radial springs, all massless (see fig. 2.25). The vertical spring has spring constant k_y and unstressed length y_0. The radial springs have identical spring constants and lengths k_x and x_0 respectively. The angle the radial springs make with the horizontal is denoted θ. With the mass suspended at equilibrium, $\theta = 0$, the vertical spring has length l_y and each radial spring has length

l_x. The equation of motion of this system is

$$M\ddot{y} = k_y(l_y - y - y_0) + 2k_x\left(\sqrt{y^2 + l_x^2} - x_0\right)\sin\theta - Mg. \tag{2.15}$$

Assuming small departures from equilibrium, so that $\sin\theta \simeq \tan\theta = -y/l_x$ and terms quadratic in y may be neglected, we find

$$\begin{aligned} M\ddot{y} &= k_y(l_y - y - y_0) - 2k_x\left(1 - \frac{x_0}{l_x}\right)y - Mg, \\ &= -k_{\text{eff}}y + k_y(l_y - y_0) - Mg, \qquad (2.16) \\ \text{where} \quad k_{\text{eff}} &= k_y + 2k_x - \frac{2k_x x_0}{l_x}, \qquad (2.17) \end{aligned}$$

the equation of an harmonic oscillator with effective spring constant k_{eff}. The third term of k_{eff} has opposite sign and is known as the *anti-spring* term. This expression clearly shows how adjusting the radial compression of the GAS modifies the stiffness and resonant frequency of the system. A more complete model is discussed in [127].

Our system was slightly more complicated, involving two pairs of springs operating in parallel, with suspension wires attaching to the 2$^{\text{nd}}$ and 4$^{\text{th}}$ intracavity bracing plates (see figures 2.24 and 2.26). Other novel features were also included. A LVDT-stepper motor pair were connected to the suspension point of each GAS allowing the equilibrium height of the keystone to be sensed and altered. This capability allowed one to compensate thermal drifts and finely adjust the resonant frequency of the system.

The vertical resonances of the blades were generally tuned to ∼800 mHz to avoid bi-stability although resonances as low as 400 mHz were achieved. Horizontal attenuation was provided by the long cavity suspension wires. This pendulum had a ∼500 mHz resonance. The entire suspension system was controlled using six eddy current dampers. Both the GASs and suspension wires were manufactured using maraging steel for its high Young's modulus, temperature stability and yield strength. The total suspended mass was greater than 80 kg.[29]

[29] Approximately 79 kg for the cavity structure plus the ballast mass used in tuning the working point of the system.

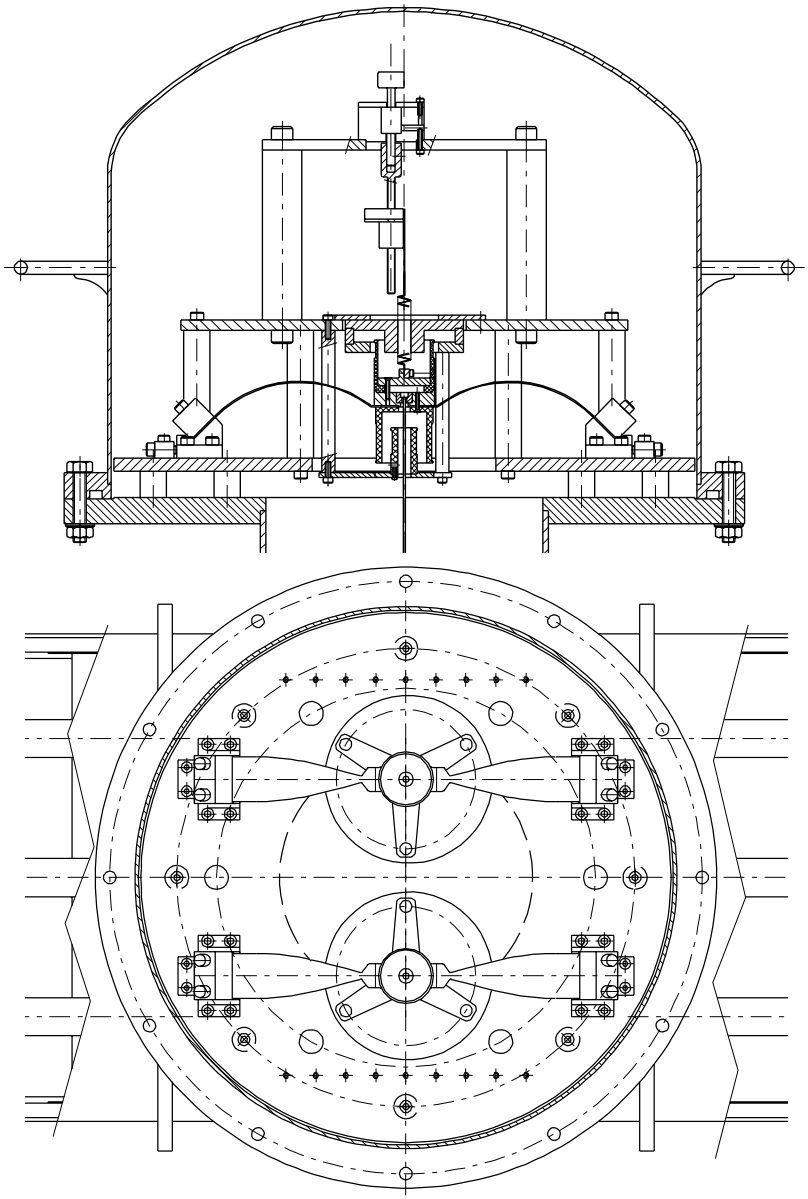

Figure 2.26: Schematic of the cavity suspension system viewed along orthogonal axes.

2.2.3.3 Mirror mounts and actuators

The three mirrors forming our resonator were fixed to the cavity support in two mounts, one on each of the triangular cavity end plates. The input and MH mirrors shared the same mounting with the folding mirror at the opposite end of the structure (see fig. 2.21). Fig. 2.27 show two aspects of the plate housing the input and MH mirrors; the plate supporting the folding mirror was simply a reduced version of this design.

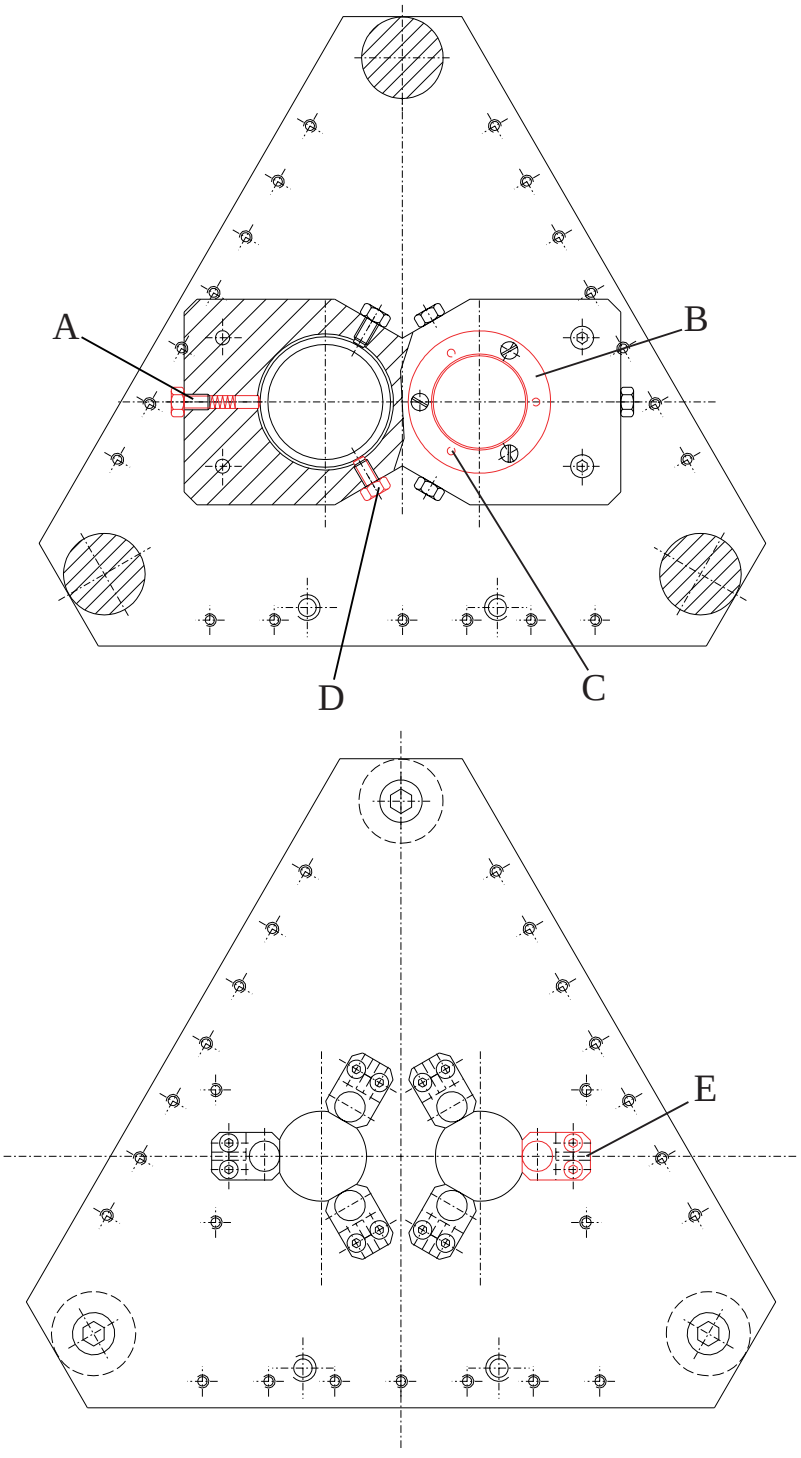

Figure 2.27: The input and MH mirrors were housed in a single mount on the first triangular bracing plate. Here we present schematics showing the cavity (upper) and external (lower) sides of this structure. A - Side spring, pin and compression screw, B - Annular copper beryllium spring, C - Return pin, D - Vertical locating screw , E - Mounting for micrometric screw.

The mirrors were constrained in the plane transverse to the cavity by means of three screws positioned at 120° intervals around the barrel of each optic. One screw per optic was arranged in series with a coil spring and metal pin (A in fig. 2.27, C in fig. 2.28).

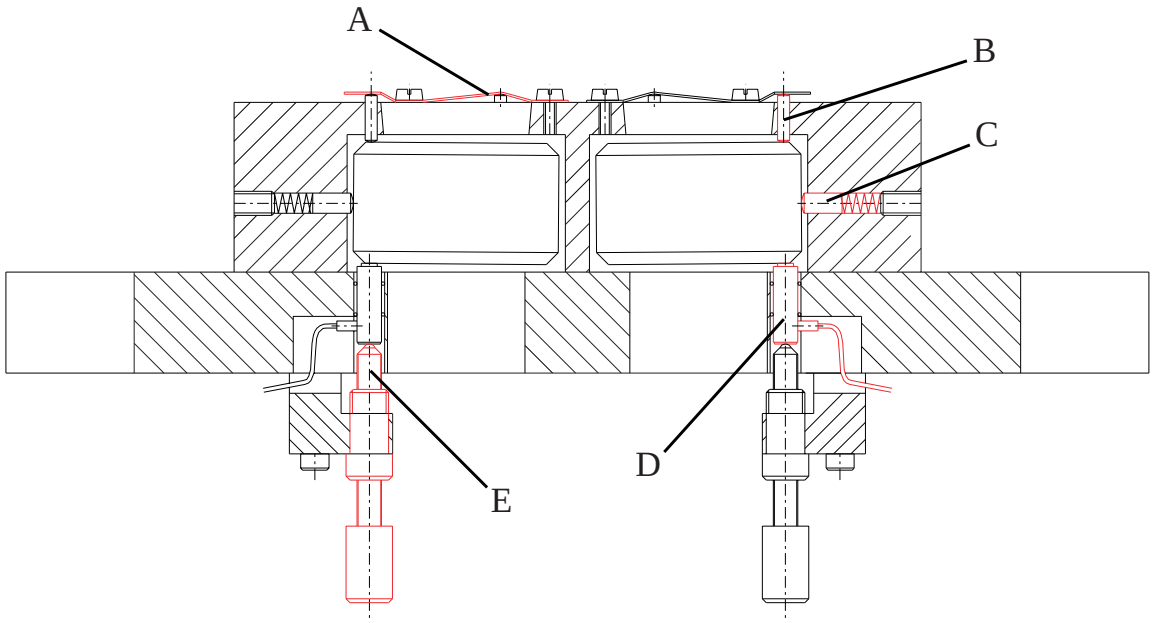

Figure 2.28: Schematic of mirror mounts and actuators. A - Annular copper beryllium spring, B - Return pin, C - Side spring and pin, D - PZT actuator, E - Micrometric screw. Each optic was endowed with three return pins, PZTs and micrometric screws. For clarity only one of each is shown.

Longitudinal and angular control was provided by a triplet of PZTs, equidistant from one another around the periphery of the optic. Opposing these PZTs were three metal pins, one coaxial with each PZT, acted upon by a single copper beryllium spring (B & C fig. 2.27; A & B fig. 2.28).

The PZTs were driven by a ten channel,[30] dual stage amplifier. This amplifier performed two functions: It provided a finely adjustable DC bias, enabling bi-polar actuation and precise control of the PZTs. It also accepted low voltage AC signals which were amplified and superimposed onto the DC level. This facility was used to modulate the angular and longitudinal positions of the mirrors for alignment purposes or when making transfer function measurements. The low gain summing stage was constructed around basic OP27s [128] while the high gain stage used the APEX PA 82 [129]. The

[30]Three channels per mirror plus one spare.

maximum gain and output of the circuit were tailored to match the range of the PZTs.

The PZT used was a PI-810.10 [130], providing a verified displacement of 150 nm/V up to a maximum of 15 µm. This PZT has a resolution <0.2 nm and its first resonance at 22 kHz.[31] The PZTs were connected to the driver electronics via vacuum compatible, kapton coated, twisted pairs. Fine wires were used to avoid seismic shorts. As with all PZTs, our units exhibited noticeable hysteresis and push/pull imbalance. These effects hampered many of our measurements but were ultimately unimportant. Transfer function measurements from PZT drive to angular mirror motion revealed that all channels exhibited uniform response below ∼1 kHz with their first resonances around 2 kHz.

In order to preserve the dynamic range of the PZTs and permit the large manual adjustments necessary to align the cavity, micrometric screws with a pitch of 254 µm [131] were placed in series with each PZT (E in fig. 2.28).

2.2.4 Optics

2.2.4.1 Other mirrors and cavity

Having written at length about the construction and attributes of the MH mirror in §2.2.2, this section is devoted to the remaining mirrors and resulting cavity properties.

The Input Mirror (IM) is positioned at the cavity waist (see §2.2.2) while the Folding Mirror's (FM's) role is simply to relay the cavity beam. Hence both mirrors were flat i.e. $R = \infty$ and no deposition process was applied after the initial polish. The substrates of all three cavity mirrors were identical, their properties are listed in table 2.4.

[31] This resonant frequency is for an unloaded PZT, the first resonance of the combined PZT, mirror and mount is far below this.

Table 2.4: All three mirror substrates display the following properties. An image of one substrate is shown in fig. 2.29. A scratch/dig specification of 10-5 means that the maximum permissible scratch width is 10 µm and the maximum permissible dig diameter is 50 µm.

Property	Value
Material	7980 Fused silica (Corning)
Overall dimension	50 mm ⌀× 30 mm tk.
Chamfer	3 mm × 3 mm @ 45°
Roughness	<1 Å rms
Flatness	1/10 wave @ 6328 Å
Scratch/Dig	10-5

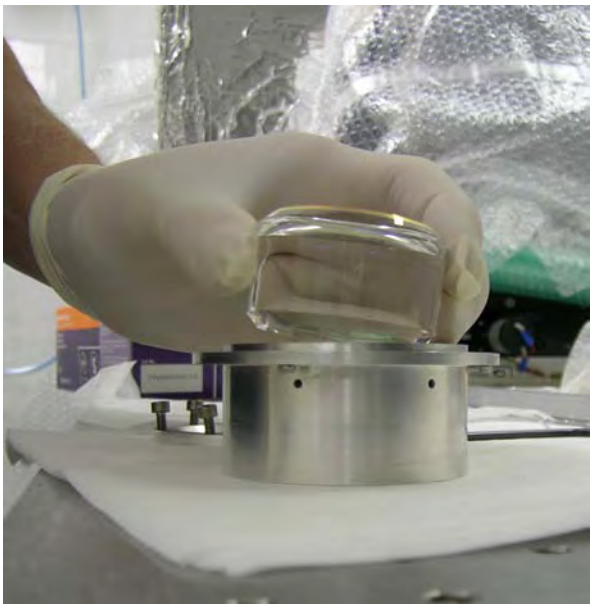

Figure 2.29: All three cavity optics had identical substrates.

For a three mirror cavity in our configuration the finesse is given by

$$\mathcal{F} = \frac{\pi\sqrt{r_{\mathrm{IM}} r_{\mathrm{MH}} r_{\mathrm{FM}}^2}}{1 - r_{\mathrm{IM}} r_{\mathrm{MH}} r_{\mathrm{FM}}^2}. \tag{2.18}$$

With mirror profiles selected this finesse had to be determined.

Our cavity may be thought of as a mode cleaner, accepting a Gaussian input and transforming it into a flat topped mesa beam. This description argues in favour of high finesse. However we had to remain mindful that this was a prototype interferometer and cavity control could be an issue, suggesting the use of a lower reflectivities.

Numerical simulations revealed that for $\mathcal{F} \gtrsim 100$ the remnant Gaussian field circulating in the cavity was negligible. Such a finesse was also acceptable from a lock acquisition viewpoint. The coating transmission specifications were thus set to give a finesse of ∼110 (see table 2.5).

Table 2.5: Measured optical properties of cavity mirrors. Power loss due to various mechanisms in parts per million. Blank entries denote unmeasured quantities.

Optic	Specified Transmission	Transmission	Scatter†	Absorption	AR reflectivity
IM	50000	49400	5.343	0.60	28
FM	3000	3068	5.190	0.55	24
MH	1000	996	1350	—	—

† Integrated over $1.5° \leq \theta \leq 78°$.

Including measured losses the theoretical finesse was ∼103, with experimental measurements coming exquisitely close to this value. The unusually high transmission of the folding mirror was chosen to provide an extra port for our control and readout system. With limited experience of non-Gaussian interferometry it was thought prudent to maximise the flexibility of our apparatus.

2.2.4.2 Laser table

The following sections describe the optical layout of our experiment, fig. 2.30 provides a pictorial companion.

The cavity is driven by a 1064 nm NPRO with a maximum output power of 800 mW [132]. Following the beam path from the laser (A) we have: B - an iris to remove pump light, C - a $\lambda/4$ plate to linearise the polarisation, D - a Faraday isolator to protect the laser and mitigate instabilities caused by retro reflected light, E - a $\lambda/2$ plate to rotate the polarisation, F - a pair of cylindrical lenses to remove astigmatism from the beam, G - a resonant electro-optic modulator to imprint the laser light with phase sidebands, I - a $\lambda/4$ plate to create circular polarisation, J,K,M - steering mirrors to align the input beam to the cavity axis and L - a mode matching lens.

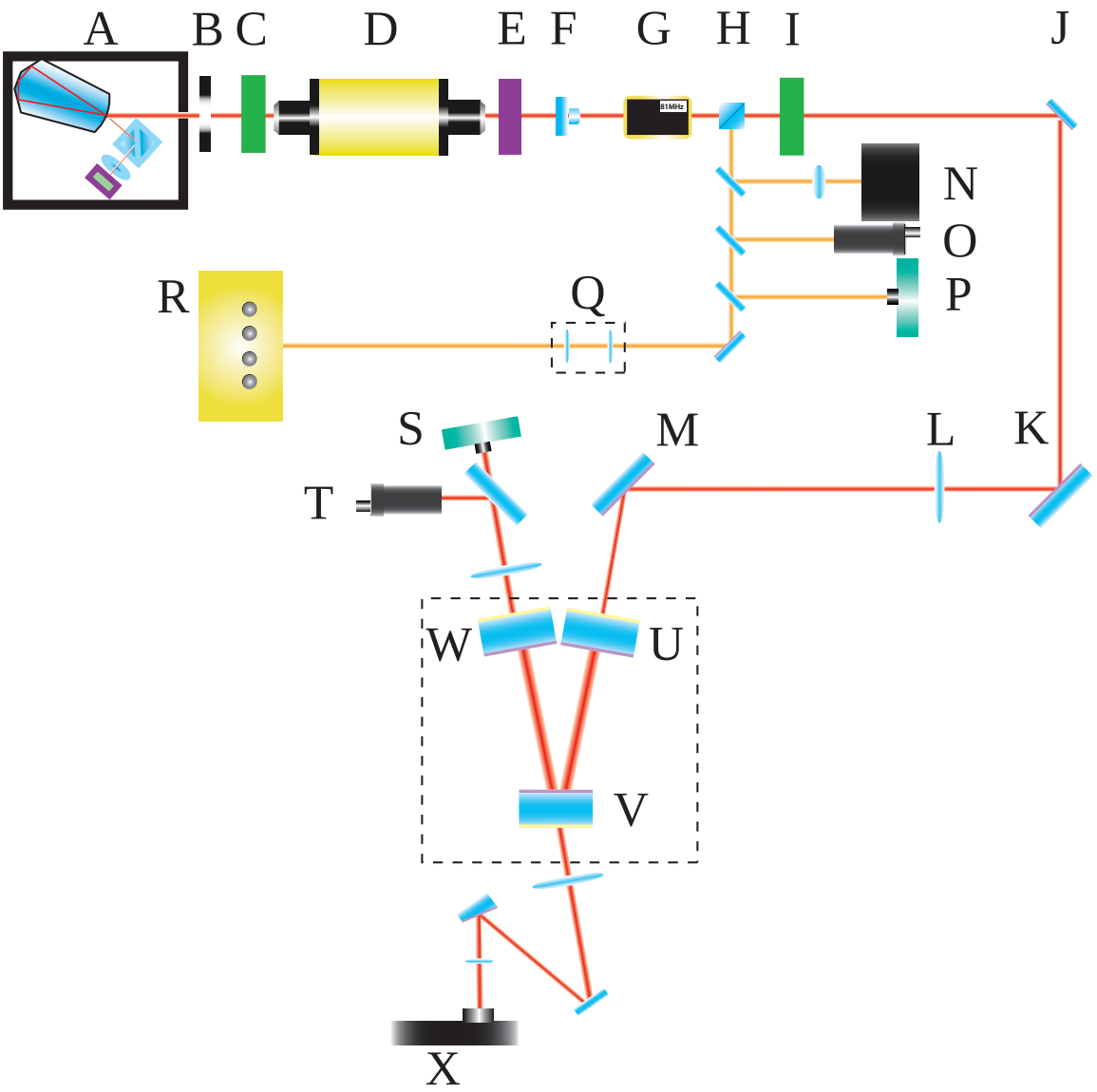

Figure 2.30: The mesa beam experiment optical layout. A - 800 mW 1064 nm NPRO, B - Iris, C - $\lambda/4$ plate, D - Faraday isolator, E - $\lambda/2$ plate, F - Cylindrical lenses, G - Electro-optic modulator, H - Polarising beam splitter, I - $\lambda/4$ plate, J - Steering mirror, K - Steering mirror, L - Mode matching lens, M - Steering mirror, N - Radio frequency photodiode, O - Reflected DC photodiode, P - Reflected beam camera, Q - Gouy phase telescope, R - Wavefront sensor head, S - Transmitted beam camera, T - Transmitted DC photodiode, U - Input mirror (IM), V - Folding mirror (FM), W - Mexican hat (MH) mirror, X - CCD camera.

The light returning from the cavity is selected by a polarising beamsplitter (H) and split between: N - an RF photodiode used for Pound Drever Hall (PDH) reflection locking, O - a DC photodiode, P - a CCD camera and Q,R - a Gouy phase telescope and differential wavefront sensor.

Light transmitted by the cavity is sampled by a CCD camera (S) and DC photodiode (T) while the radiation leaking through the folding mirror is attenuated and passed through a telescope before being sampled by a high-resolution CCD camera (X).

The folded cavity is formed by the three mirrors U,V,W.

One of the attributes which distinguishes the mesa beam from competing modes is its strong coupling to Gaussian fields. In order to realise this coupling experimentally, great care was taken over mode matching the Gaussian input beam to the cavity.[32]

According to (2.9) the optimal cavity input beam has a waist of size $\omega_{\mathrm{g}} \simeq 3.62\omega_0 = 5.70$ mm located on the surface of the IM (see fig. 2.31). Using this information our mode matching problem is no different to that of a standard Gaussian cavity, the only possible peculiarity of our setup being the large ratio of waist sizes.[33]

Having fully characterised the laser's output mode and surveyed the applicable constraints, the first matching design investigated was a simple one lens solution. Two waists ω_1 and ω_2 may be appropriately matched by a single lens of focal length f if the distances from each waist to the lens (d_1, d_2) are arranged according to

$$(d_1, d_2) = \left(f \pm \frac{\omega_1}{\omega_2}\sqrt{f^2 - f_0^2}, f \pm \frac{\omega_2}{\omega_1}\sqrt{f^2 - f_0^2} \right) \tag{2.19}$$

and f is strictly greater than the characteristic focal length of the system $f_0 = \pi\omega_1\omega_2/\lambda$ [134]. Selecting the most suitable focal length from readily available lenses, we found for our parameters that $(d_1, d_2) \simeq (2, 36)$ m, not an entirely feasible solution.

Given the layout of our apparatus the maximum practicable telescope length was

[32]For a summary of the possible mismatches see [133].
[33]The laser waist is some 50 times smaller than that of the cavity.

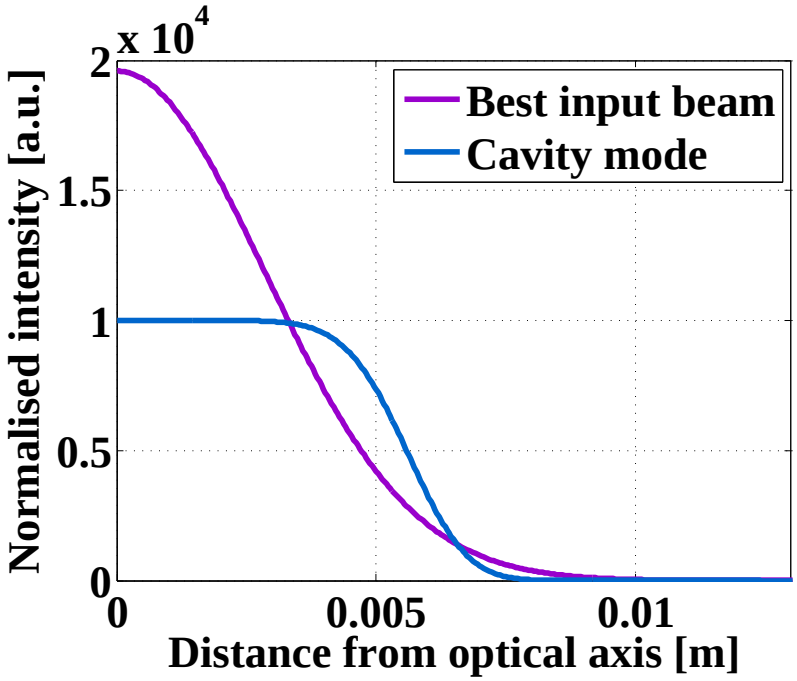

Figure 2.31: Normalised intensity profiles of the ideal Gaussian injection beam and mesa cavity eigenmode at the input mirror.

around 3 m. Exploring single lens solutions with this limitation an interesting configuration was found. Using our chosen lens to 'collimate' the beam i.e. setting $d_1 = f$ a good approximation to the exact solution could be achieved. The resulting beam parameters at the input mirror were $\omega_{\mathrm{IM}} \simeq 6.1$ mm and $|R_{\mathrm{IM}}| \simeq 2.9$ km.

Investigating this solution analytically, the discrepancy in coupled power with respect to the ideal beam was found to be $\lesssim 1\%$. This result was confirmed in numerical simulations incorporating the phase profile of the real MH mirror. These simulations also satisfied us that this solution would not cause unforeseen excitation of Higher Order Modes (HOMs).

As anticipated, subsequent investigations of multiple lens telescopes revealed that more efficient solutions were available. However using standard commercial optics these arrangements were dramatically more sensitive to variations in focal length and lens placement. Hence the one lens solution was chosen for initial commissioning of the experiment and was eventually retained throughout.[34] A peak mode matching effi-

[34]Two lens solutions were implemented later in the life of the experiment but never offered significant advantages over the simpler one lens design.

ciency of 88.4% was recorded.[35] This number should be compared to the theoretical maximum of ∼94% and the predicited matching with our solution of ∼93%. A typical transverse mode spectrum is shown in fig. 2.32.

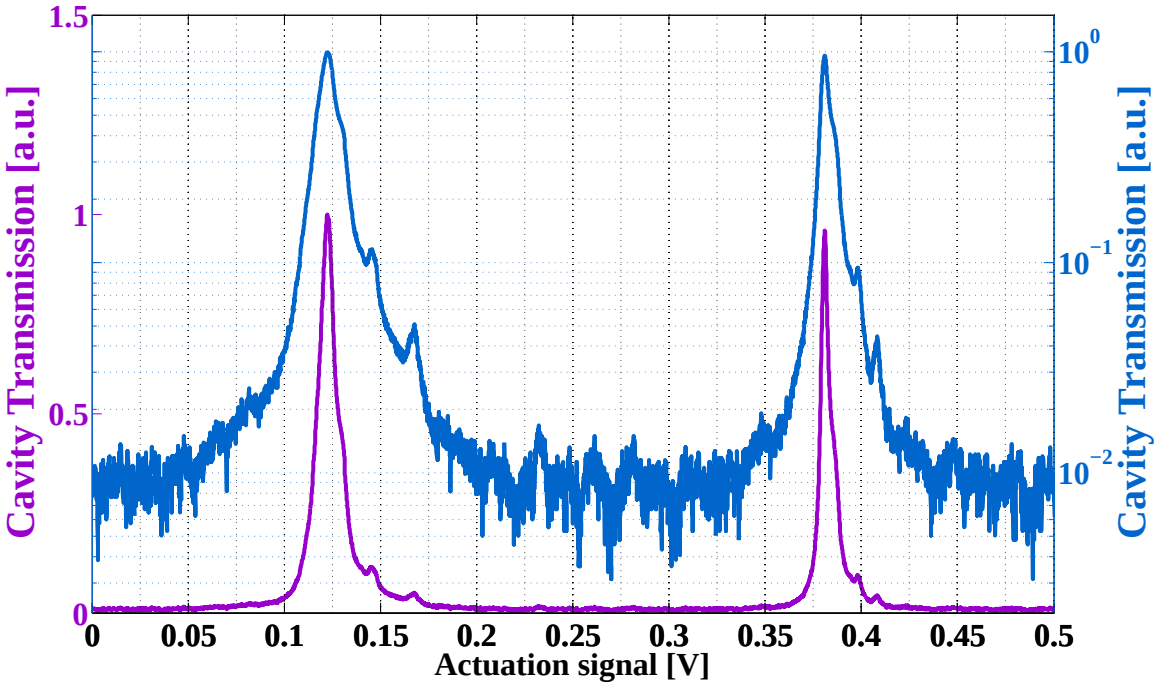

Figure 2.32: Experimentally measured mesa beam transverse mode spectrum. Cavity transmission is shown on both linear (purple) and logarithmic (blue) axes as a function of the actuation signal controlling the input laser's frequency.

2.2.4.3 Beam capture

The main goal of our work was to test whether non-Gaussian mesa beams were experimentally realisable. It was thus essential to have an accurate means of recording the transverse intensity distribution of the cavity field. This was achieved with the help of a high resolution CCD camera.

The chosen camera was a Coherent LaserCam IIID 1/2 in. [135]. This device has an active area of approximately 4.1 × 4.7 mm^2 with a pixel size of 17.05 × 19.69 µm. It possesses a dynamic range greater than 900 to 1, may be locally or externally triggered

[35]Based on the relative intensities of peaks in the transverse mode spectrum (see fig. 2.32). More typical mode matching efficiency was around 85%

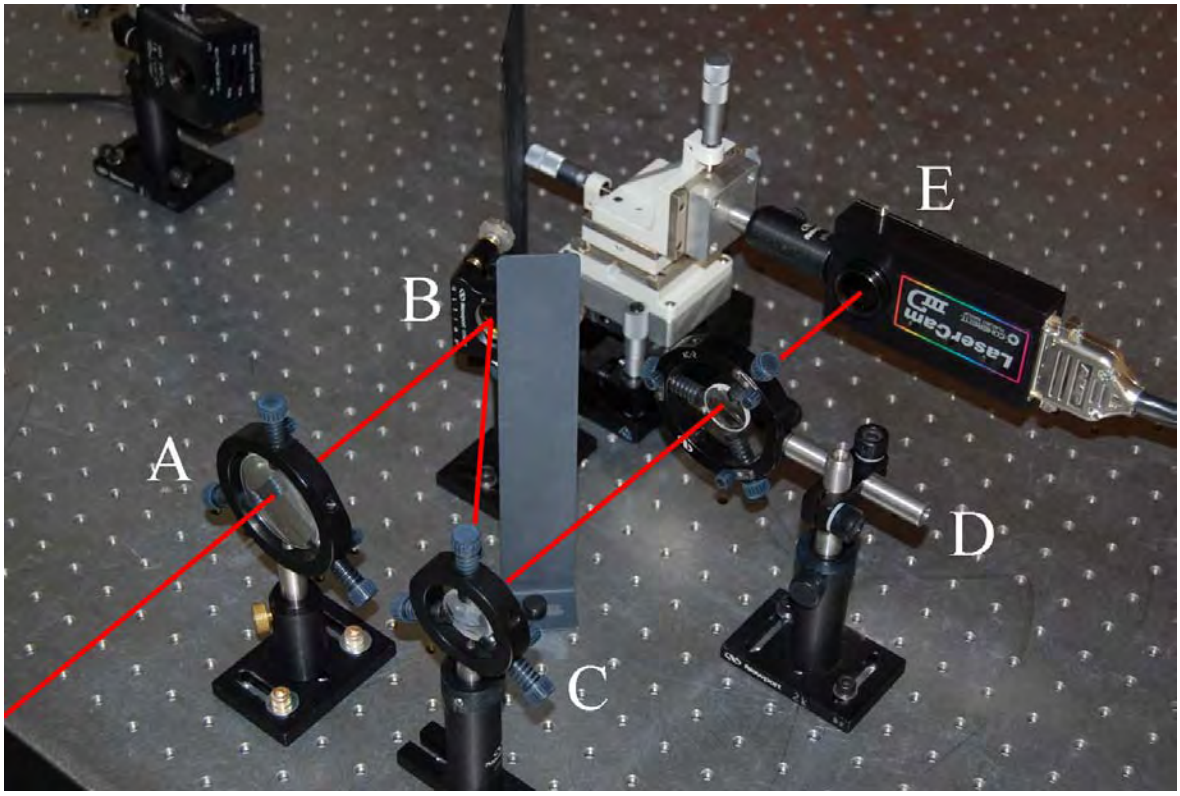

Figure 2.33: Optical layout of components used to condition and capture the mesa beam profile. A - Lens, B - steering mirror, C - Wedge, D - Lens, E - High resolution CCD camera.

and has a saturation level of 0.8 mW/cm^2. Preliminary characterisation of the CCD and acquisition electronics found the gain uniformity to be better than 1.5%.

The camera was positioned at the opposite end of the cavity from the input and MH mirrors, utilising the high transmission of the folding mirror to observe the profile of the resonating mode. Before capture, the beam was pre-conditioned by attenuators and a two lens telescope. Reflective attenuation was used to avoid creation of spurious interference patterns and to mitigate thermal distortion during long lock stretches. Here and throughout the experiment large optics were used where appropriate to avoid vignetting and spherical aberration. Fig. 2.33 shows an image of the profile readout bench.

2.2.4.4 Commissioning and control

In this section we describe how the cavity was brought to a state in which meaningful data could be recorded.

Alignment of the cavity consisted of three basic steps: preparatory work with a visible laser, alignment of the injection beam using steering mirrors on the input bench (J,K,M in fig. 2.30) and final cavity alignment, using first the micrometric screws and later the PZTs.

This terse summary disguises what proved to be the most challenging aspect of our experimental work.

- The physical size of our apparatus meant that it was, prior to resonance, impossible to observe the effect of any alignment changes while making them, forcing one to continuously shuttle between actuator and beam spot.

- The heat shield enshrouded the mirrors, limiting both physical and visual access, making it difficult to centre beam spots on the mirror substrates.

- Several PZTs could produce the same effect on the cavity mode often leading to false maxima in the circulating power and sub-optimal cavity alignment.

- Due to mode matching constraints a lens was interposed between our steering mirrors, hampering translation of the input beam.

These issues were compounded by the optical properties of the mesa beam resonator. In a spherical mirror cavity small tilts of the optics merely shift the optical axis so that it remains perpendicular the mirror surfaces; the phase front presented to the beam remains spherical and the eigenmode remains Gaussian. By contrast a tilted MH mirror[36] presents a radically altered figure to the cavity with strong consequences for the resonant field.

[36]Or analogously a perturbed optical axis.

With experience and subtle additions to the apparatus[37] our endeavours ultimately prevailed. What initially took two people several hours to achieve with variable success could be accomplished alone in less than one. With the cavity in a well aligned state attention was diverted to longitudinal control.

After preliminary work with offset and dither locking schemes, PDH reflection locking was investigated (see §1.5.2.5). Use of this technique is so widespread in gravitational wave interferometers that its failure with mesa beams would likely prohibit their use.

Proceeding as for a spherical mirror cavity, an Electro-Optic Modulator (EOM), optical diode, RF photodiode and appropriate demodulation electronics were prepared. The EOM [136] impressed 81 MHz phase sidebands[38] with a modulation index of $\Gamma = 0.33$ upon the carrier light. This modulation frequency encouraged the use of a small, low capacitance photodiode with an active area of just 1 mm^2 [138]. Controlling the spot size on and alignment to this diode was crucial in removing spurious offsets from the longitudinal control loop. Sweeping the system about resonance, the dispersion-like error signals characteristic of the PDH technique were witnessed (see fig. 2.34).

For small deviations Δf about resonance, the signal voltage at the output of a PDH mixer V_{PDH} is given by [139]

$$V_{\mathrm{PDH}} = \frac{\Delta f}{f_{\mathrm{FSR}}} \frac{8\mathcal{F}^2 T_1}{\pi r_1 r_2} M J_0(\Gamma) J_1(\Gamma) G I_{\max}, \tag{2.20}$$

where f_{FSR} is the cavity free spectral range, M is the fraction of incident light coupled into the cavity's fundamental mode, Γ is the sideband modulation index, G is the net gain of the detection photodiode and mixer in Volts per Ampere and $I_{\max}$ is the DC photocurrent recorded far from resonance.

Calibrating our demodulation chain using a well characterised AM laser and adapting (2.20) to a three mirror resonator, the measured PDH discriminant was found to be in

[37] 'Targets' mounted to the cavity end plates (internal and external to the cavity) were greatly beneficial to initial alignment. The addition of a projector made diagnostic signals visible throughout the lab.

[38] The choice of such a high modulation frequency was motivated by available equipment (perhaps originally purchased by Mason [137, 94]) rather than optical constraints.

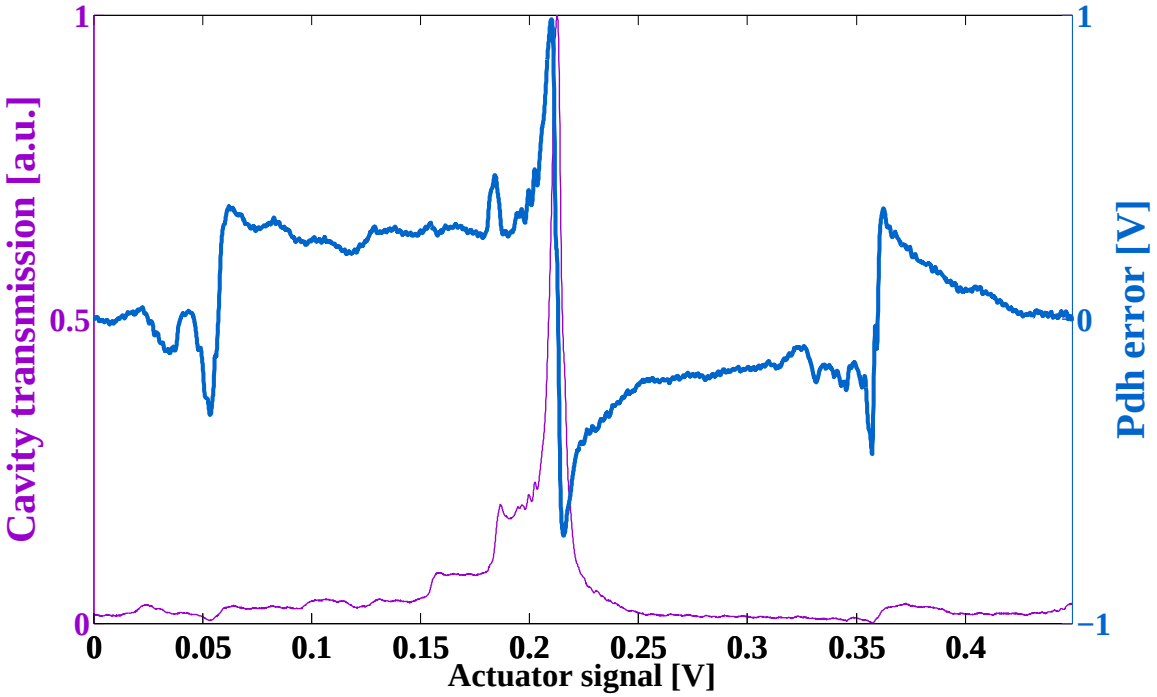

Figure 2.34: Experimental PDH signals with the mesa beam.

excellent agreement with the expected value

$$\left(\frac{V_{\mathrm{PDH}}}{\Delta f}\right)_{\mathrm{meas}} = 3.07 \pm 0.34 \times 10^{-5}\ \mathrm{VHz}^{-1},$$
$$\left(\frac{V_{\mathrm{PDH}}}{\Delta f}\right)_{\mathrm{theory}} = 3.02 \times 10^{-5}\ \mathrm{VHz}^{-1}.$$

Once it had been demonstrated that the novel feature of our cavity would cause no control issues, a simple servo was designed around the measured error signal.

Due to stiction in their mountings and non-uniform gain it was time consuming to extract purely longitudinal mirror motion from our PZT triplets. The decision was made to actuate instead on the laser frequency.

A blended loop driving the laser's PZT [39] above ~ 0.1 Hz and its temperature controller below was commissioned, latterly achieving a unity gain of 7 kHz with a 40° phase margin. Fig. 2.35 show the residual length noise of our system.

[39] Early in the experiment a laser without a PZT was used. During these times high frequency corrections were applied to the diode pump current [140, 141].

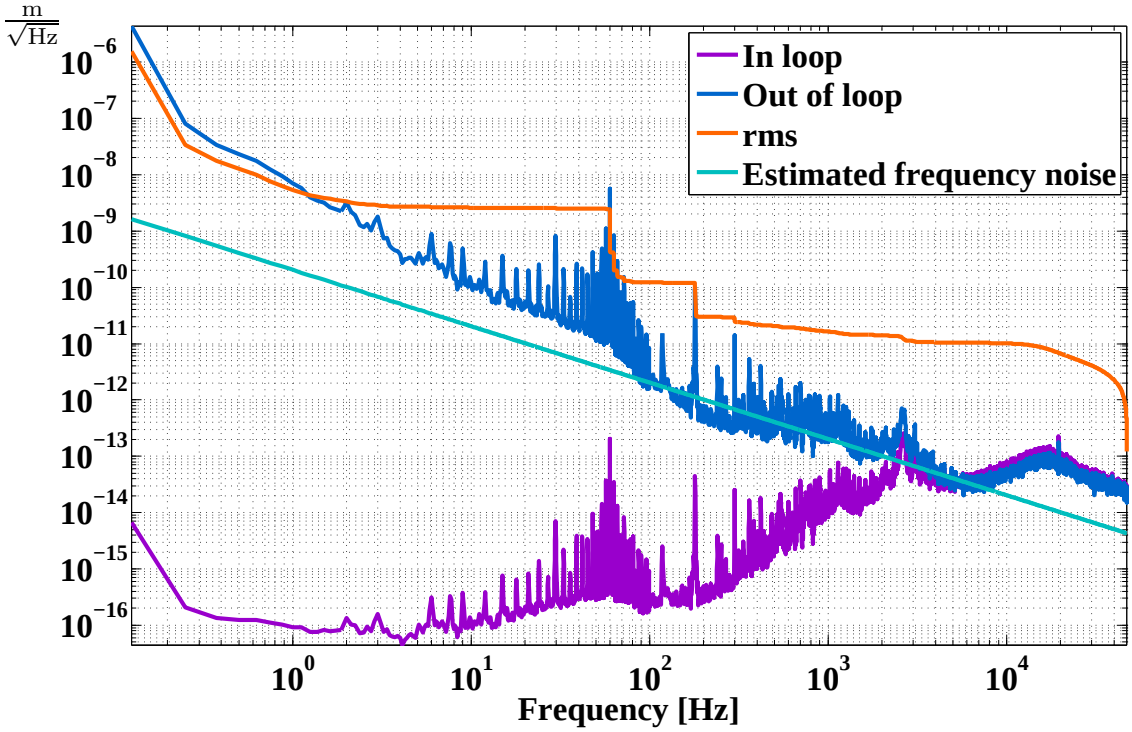

Figure 2.35: Residual length noise in mesa beam cavity. The total rms displacement is 1.55×10^{-6} m.

The rms residual motion is dominated by a strong feature at 60 Hz. This is not standard power line coupling[40] but the nefarious interaction of ambient noise with a mechanical mode of our cavity structure.

During the lifetime of our experiment a new HVAC system serving our group's laboratories was installed.[41] The chiller itself was placed in the room adjacent to ours, routing all ducts through our workspace. This led to increased acoustic noise and vibration, particularly at the ∼59.5 Hz fan frequency. Unfortunately our cavity structure had a low Q resonance at around 60 Hz – a torsional mode about the 2$^{\text{nd}}$ and 4$^{\text{th}}$ intracavity bracing plates (see §2.2.3.1 and fig. 2.21) – which became excited by this acoustic noise. Shaping the loop to provide greater low frequency gain[42] compensated for this coupling and robust locking resumed.

[40] Experimental work on the mesa beam cavity was carried out in the United States where the line frequency is 60 Hz rather than 50 Hz.

[41] Closing our laboratory for 12 months.

[42] Two low frequency gain boosts were implemented - simple pole zero pairs at $f_p = 30, 150$ Hz, $f_z = 1.5, 1.5$ kHz. In general these boosts were not used in tandem.

In its final state the PDH based longitudinal control loop was able to preserve the cavity in a resonant state for several hours at a time. This stability allowed the results of long series of measurements to be safely compared and combined. Further it allowed alignment and mode matching to be slowly optimised leading to vastly improved visibility.

2.3 Results

2.3.1 The fundamental mode

With good alignment, efficient mode matching and robust laser frequency control it was possible to stably lock the cavity to its fundamental mode. While recorded intensity profiles showed the resonant field to be clearly non-Gaussian and of considerable width, the mesa beam's characteristic flat top was absent (see Fig. 2.36).

We had been previously alerted to this possibility by FFT based simulations including measured defects of the MH mirror. This numerical work produced similarly perturbed mode shapes even after the application of corrective tilts (see §2.2.2.2). Fig. 2.37 superimposes the intensity profiles of one such simulated field with those of an experimental mode. To ensure fair comparison the simulated beam was propagated from the MH mirror to the image plane of our readout telescope.

The agreement between numerical and experimental modes is striking, indicating that deviations from the theoretical profile are likely dominated by mirror defects rather than misalignments or other effects omitted from our simulations.

Having confirmed the observed mode to be consistent with the best achievable given our apparatus, we measured it against the nominal mesa beam by means of a least squares fit (see fig. 2.38). One will notice that the fit function differs from previously shown mesa beams. The readout optics were designed to image the folding mirror of the cavity, hence our fit function was evaluated at this point and thus lacks the central

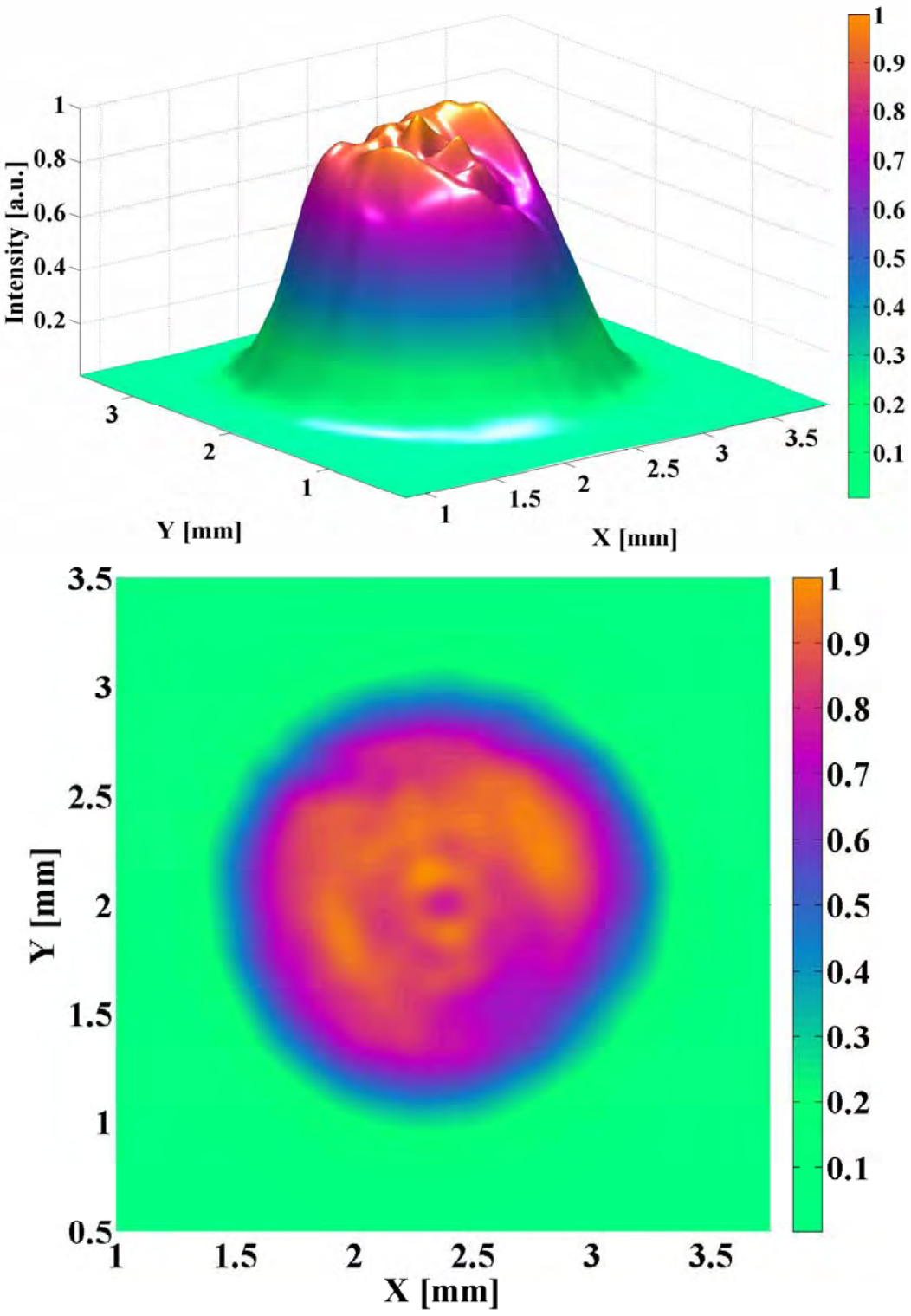

Figure 2.36: Intensity profile of a typical mesa mode realised in our prototype cavity.

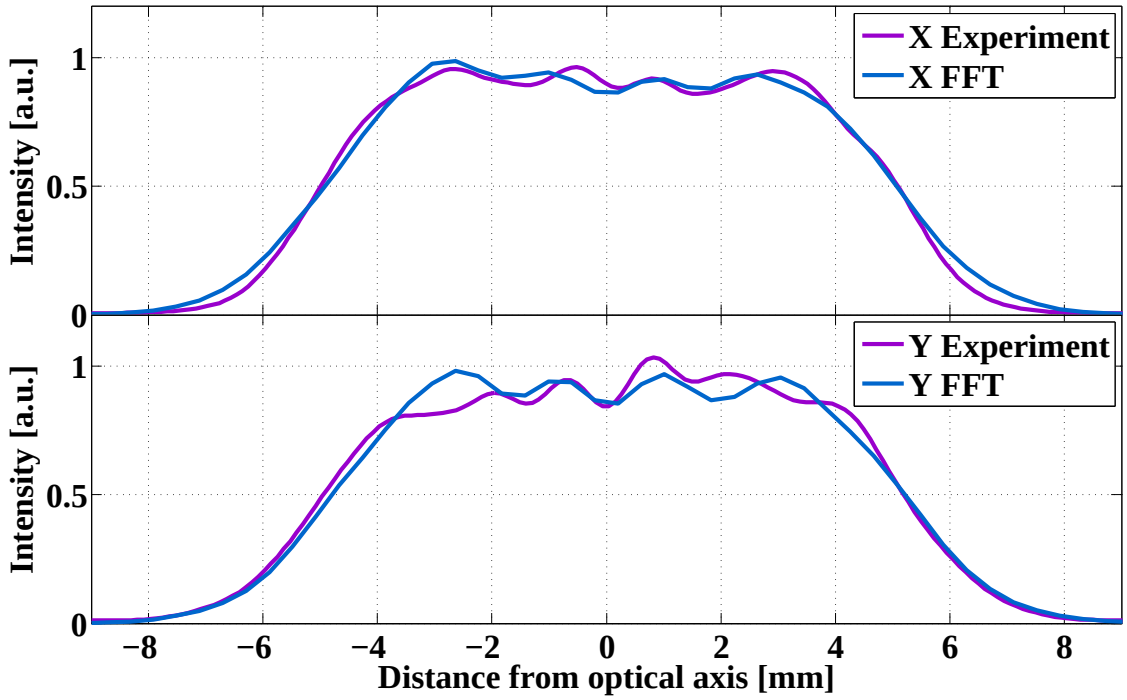

Figure 2.37: Comparison between a typical experimental mesa beam and a mode obtained through an FFT simulation taking account of measured mirror imperfections.

'dip' in its intensity profile which one finds in mesa beams at the MH mirror position.

Assuming $D = 4\omega_0$ our only fit parameter was ω_0, the width of the minimal Gaussian. So that we might extract useful beam parameters, the theoretical magnification of the readout telescope was applied to the experimental mode prior to fitting. Unfortunately uncertainties in lens positions and focal lengths placed an error of 12% on this parameter, an uncertainty which must be applied directly to our estimated beam widths. The extracted values were $\omega_0^x = 1.52$ mm and $\omega_0^y = 1.61$ mm with an average of $\omega_0 = 1.57$ mm, in exact agreement with theory.

The observed ellipticity may have arisen through poor beam alignment in the readout telescope or in the cavity itself. Early work revealed that the design of our mirror mounts, with forces applied directly to the substrate, had a tendency to induce astigmatism in the cavity optics, a realisation which forced us to use identical thick substrates for all mirrors.[43] This modification was thought to have eliminated any warping but

[43]The MH substrate was initially the only thick optic (to mitigate coating stresses).

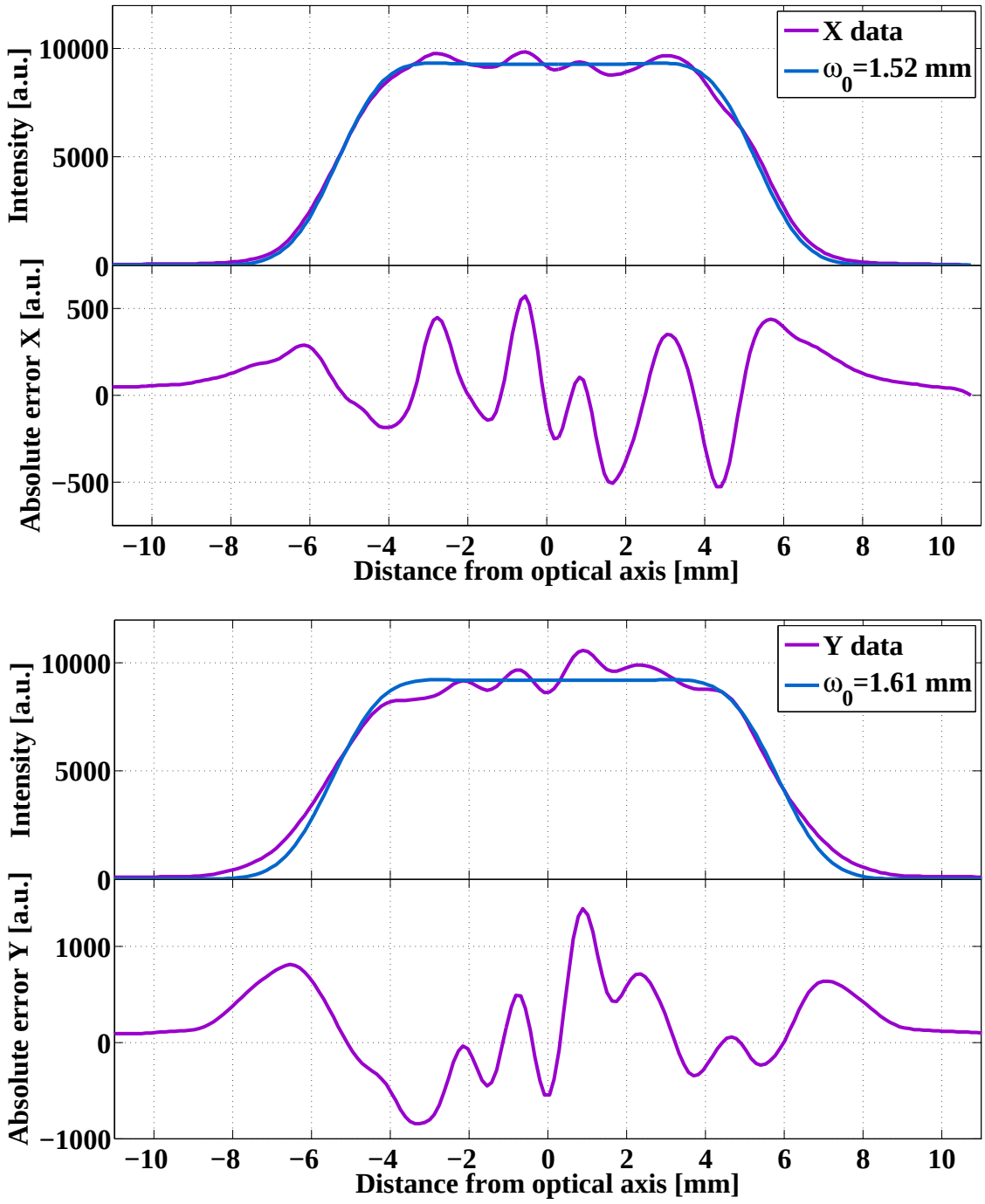

Figure 2.38: Least squares fit of theoretical mesa beam profile to experimental data.

imperceptible deformations of the new optics could explain the observed ellipticity.

The average deviations from flat and the power not fitted by the mesa mode are both around 10%.

2.3.2 Higher order mode spectrum

During characterisation of the fundamental mesa beam a brief investigation was made into its excited transverse modes (see fig. 2.39). These modes bear a superficial re-

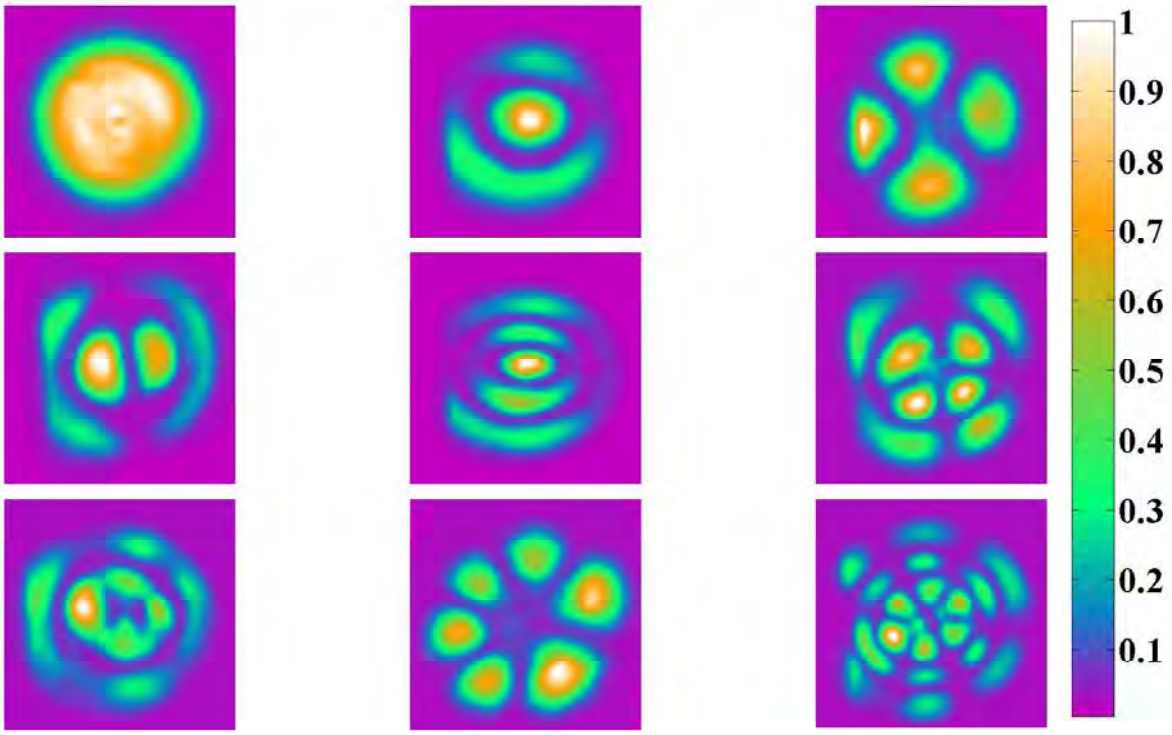

Figure 2.39: A selection of mesa beam transverse modes. These images were taken opportunistically during a period of poor input mode coupling efficiency. A complete catalogue of well formed higher order modes does not exist as efforts in this direction directly conflicted with our primary goal of maintaining good mode matching and alignment for the fundamental beam.

semblance to the excited modes of a spherical mirror resonator, however quantitative investigation reveals notable differences [107].

With cavity alignment and mode matching purposely degraded, the laser's frequency

was slowly modulated, tracing out the mesa beam cavity's HOM spectrum. The equivalent operation was subsequently performed in FFT simulation, first for a spherical mirror cavity, to verify that HOMs were found in the expected positions with the correct intensity distributions, then for a mesa beam cavity using the phase map of the experimental mirror. In this instance no corrective tilt was applied in hopes of increasing the coupling to HOMs. Fig. 2.40 presents the results of this work. Notice that the mesa beam HOMs are no longer regularly spaced as they are in Gaussian resonators (see §1.5.2.2).

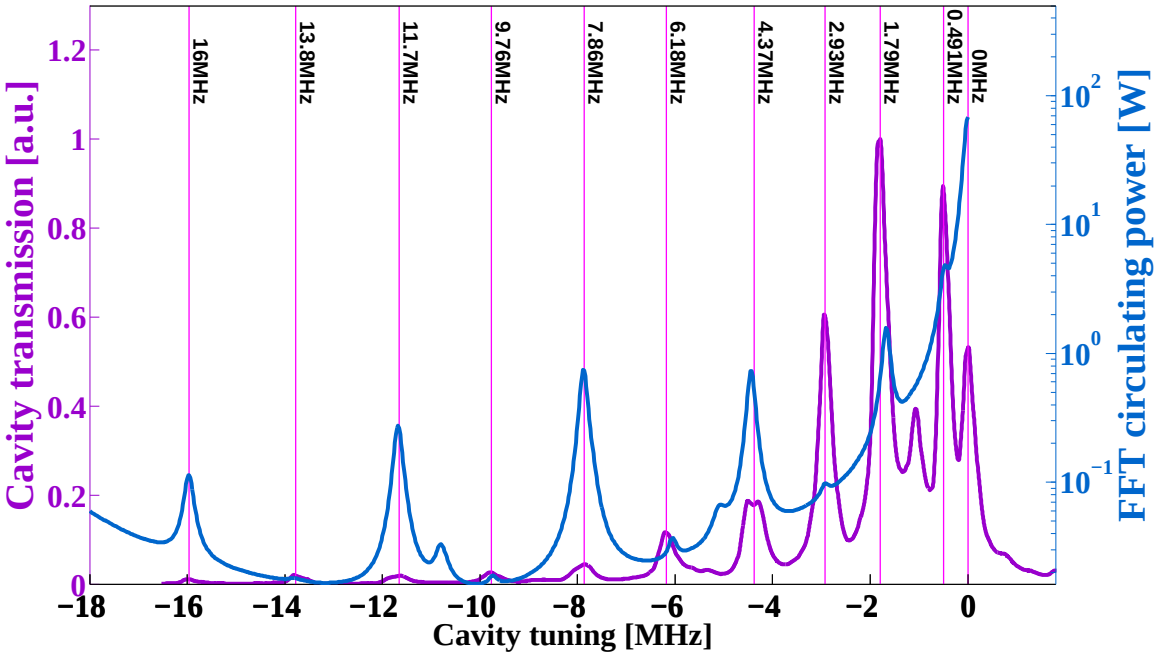

Figure 2.40: Comparison of experimental and numerical mesa beam transverse mode spectra. Notice that HOMs are not regularly spaced as with Gaussian resonators. The mesa spectrum can be compared to that shown in fig. 2.32 taken during a period of good alignment and input matching.

The intensity of each mode is a function of the particular cavity mismatch. Hence the relative amplitude of each peak is not expected to agree between spectra and some modes are not excited at all. Nevertheless the accord between experimental and numerical data is impressive. For modes observed in both spectra the average difference in frequency is just 46 kHz or 0.2% of a free spectral range.

2.3.3 Summary

Above we have demonstrated, for the first time, creation of a non-Gaussian flat topped beam in a manner applicable to gravitational wave interferometers. This mode is of particular interest as it is predicted to reduce measured thermal noise. Experimental results closely followed theoretical predictions with departures from the ideal intensity distribution well explained by known mirror imperfections.

These imperfections are the result of manufacturing constraints imposed by our experimental infrastructure and are of little consequence for future work. Large optics suitable for astrophysically sensitive interferometers should be easier to produce.

Our investigations have further illustrated the utility and accuracy of FFT based simulations, suggesting that these techniques may be used with confidence to study mesa beams in more complex interferometer topologies.

Chapter 3

Angular alignment

Mesa beam cavities are expected to be more sensitive to angular misalignments of their optics than equivalent spherical mirror resonators. In this chapter we explore two issues related to this prediction.

We first examine how the fundamental resonant mode of a mesa beam cavity is perturbed by errors in angular alignment. This is of crucial importance as the advantages offered by mesa beams are due to their unique shape. If small mirror misalignments were to destroy the uniformity of the mesa beam's intensity profile it would likely prevent their use in future interferometric gravitational wave detectors.

We subsequently consider methods of controlling the alignment of a mesa beam cavity, focusing heavily on the extension of differential wavefront sensing to non-Gaussian modes.

Prior to commencing we must stress that the work discussed in this chapter was motivated by theoretical work concerning the flat mesa beam. Nearly concentric mesa cavities were devised several years later and hence remain to be studied in depth. Since our apparatus is of nearly flat construction and thus allows us to test predictions for flat beams by experiment, we limit our discussion to these modes.

3.1 Tilt sensitivity

Following the initial proposal of mesa beams, experimentalists became concerned that the flatness of the MH mirror in its central region, where optical intensity is greatest, would make mesa beam interferometers substantially more sensitive to errors in the positions, figures and orientations of their mirrors.

Subsequent theoretical investigation did not confirm these suspicions, concluding that mesa beam interferometers offer significant advantages over Gaussian beam designs[1] without being substantially more sensitive to mirror errors [104, 106, 105]. In particular, it was found that the mesa beam interferometer was, at most, a factor of 4 more sensitive to mirror tilts than the equivalent Gaussian.[2] Further, the absolute alignment sensitivity required with mesa beams[3] was similar to that already achieved in the first generation of detectors [142].

Having already witnessed the effects of mirror misalignment in our own apparatus, we decided to conduct a more quantitative investigation to validate the numerical methods used in the literature.

3.1.1 Experiment

In order to verify the tools which predicted the properties of mesa beams in a full interferometer we would apply them to our cavity, recording the intensity profile of the fundamental mesa mode as a function of MH mirror tilt and comparing the results to numerical data.

In our prototype cavity, just as in a long baseline interferometer, the fundamental cavity mode was strongly perturbed by even the smallest mirror tilts. Accurately measuring the magnitude of these tilts was the most challenging aspect of this investigation.

[1] These works compared nearly flat mesa beam cavities to equivalent nearly flat Gaussian cavities.
[2] The metric used in these analyses was the coupling of light into parasitic modes.
[3] This sensitivity was driven by the properties of the marginally stable recycling cavities. With the switch to stable cavities this requirement can likely be relaxed.

Nonlinearities and variability in the mirror actuators obliged us to measure mirror tilt directly, rather than inferring it from applied signals. Fig. 3.1 shows how this was achieved.

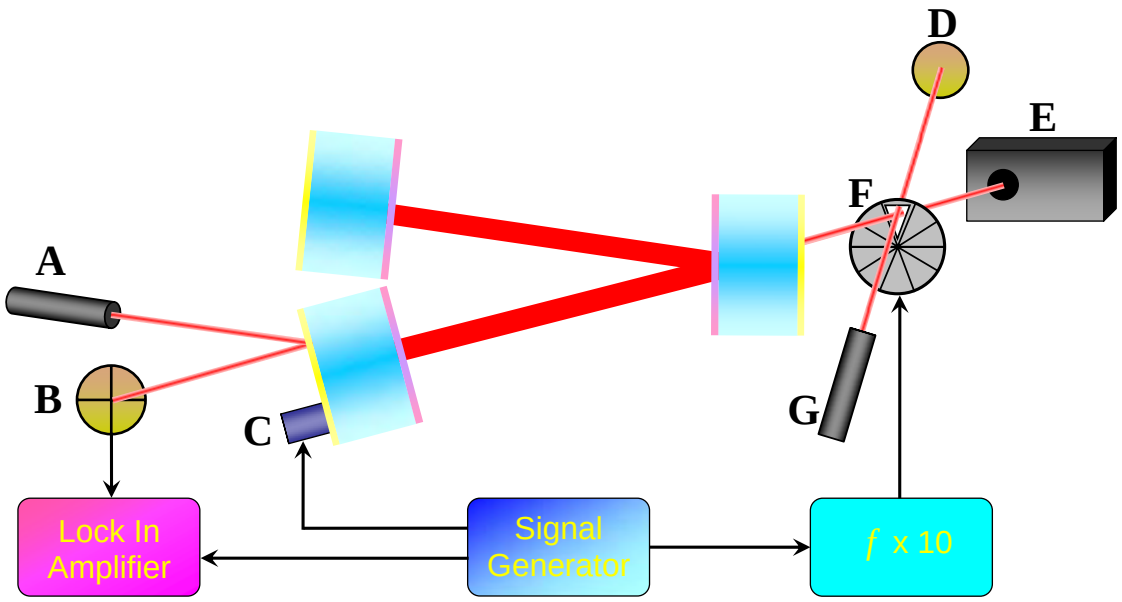

Figure 3.1: Apparatus used to measure the tilt sensitivity of the mesa beam cavity. A - He-Ne optical lever laser, B - Quadrant photodiode, C - PZT, D - DC photodiode, E - High resolution CCD camera, F - Optical chopper, G - He-Ne laser.

Applying a sinusoidal excitation to the MH mirror alignment PZTs, the resultant mirror motion was recorded using a well calibrated optical lever. The output of the optical lever was subsequently relayed to a lock-in detector where the beam motion and thus mirror tilt at the excitation frequency were calculated. This approach was adopted to mitigate low frequency beam jitter in the optical lever which had contaminated previous measurements. The resulting precision of our angle measurement is estimated to be 0.05 µrad.

The oscillating alignment of the MH mirror meant it was important to have an accurate means of recording the intensity profile of the cavity mode with the mirror at its maximum angular deviation. This was accomplished by interposing an optical chopper wheel between the cavity leakage beam and the CCD camera, triggering beam capture only when the CCD camera was exposed. The phase of the chopper wheel was measured using a second additional laser and diode as shown in fig. 3.1.

3.1.2 Results

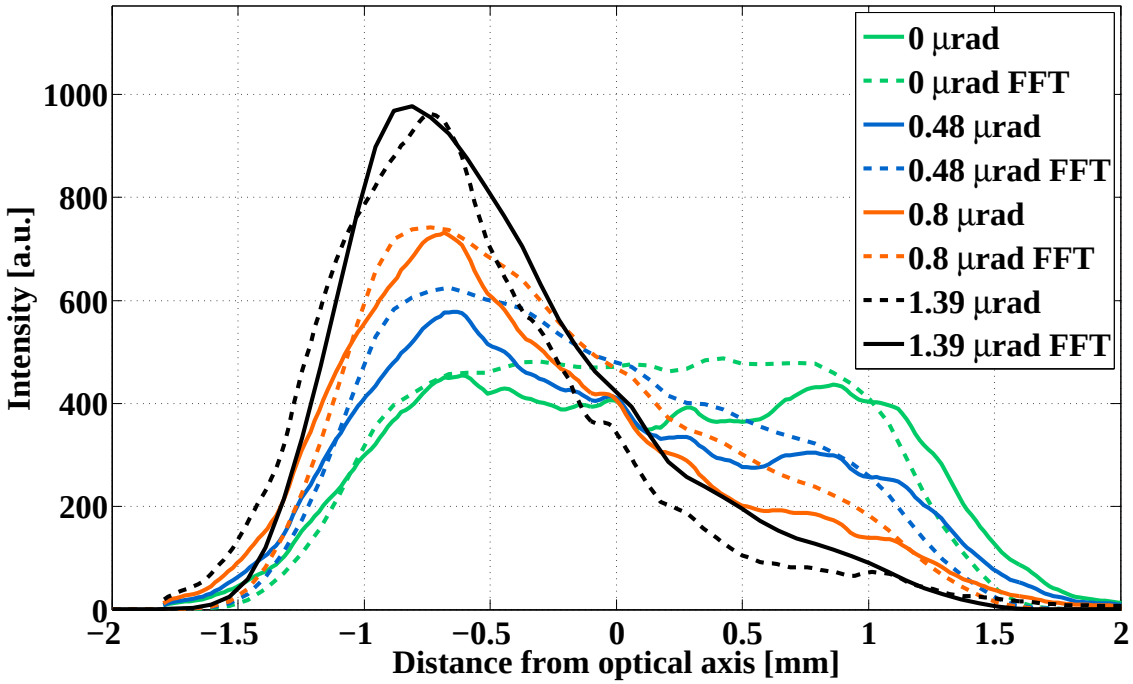

Figure 3.2: Mesa beam intensity profiles as a function of MH mirror tilt. Comparison between experimental results (solid lines) and numerical simulation (dashed lines).

After the tilt at which each profile was recorded had been calculated, FFT simulations incorporating the same perturbations were carried out.[4] The scale factors, in both width and integrated power, which best matched the unperturbed beams of the numerical and experimental data were found. The same factors were then applied to all numerical modes. Fig. 3.2 compares the two data sets.

3.1.3 Discussion

The sensitivity of the fundamental mesa beam's intensity profile to mirror tilt is in qualitative agreement with numerical predictions, supporting the conclusion that mesa beam interferometers will not be significantly more sensitive to tilt errors. However this assertion does not mean that mesa beam interferometers will not be significantly more difficult to *control*.

[4]These measured tilts were added to the baseline corrective tilt of the real MH mirror phase map.

Experience in the first generation of gravitational wave detectors has shown that alignment of the cavity optics can be controlled to a level acceptable for mesa beams using differential wavefront sensing [142]. This technique remained untested with mesa beams although theoretical work [104, 106] suggested that since the field excited by small mirror tilts has the same geometrical asymmetry about the rotation axis of the tilted mirror, the physical principles and control system that work for Gaussian beams should also work well for the mesa beam. In the remainder of this chapter we explore this idea, examining differential wavefront sensing with mesa beams.

3.2 Differential wavefront sensing

PDH techniques are well proven in controlling cavity lengths (see §1.5.2.5) but they have no effect on *angular* stability. If a resonator is misaligned, even by small amounts, the optical gain of the cavity is diminished and the shot noise of the gravitational wave readout channel is increased. Consider that just to have the beam reflecting from a mirror 4 km away return within one spot diameter requires a pointing precision of $\sim 10^{-5}$ radians. If we impose the constraint that angular alignment should not significantly degrade the sensitivity of the instrument to gravitational waves[5] then we must maintain alignment at the $\sim 10^{-8}$ radian level [143].

For Gaussian resonators, an extension of PDH locking to angular control known as differential wavefront sensing [144, 145] can help us maintain alignment within these stringent bounds. This technique relies on the detection of higher order modes which are excited by cavity misalignments [146, 133]. In the following sections we consider whether similar techniques can be usefully applied to mesa beam resonators, our investigations culminating in an experimental test.

[5] $<$ 5% effect.

3.2.1 WFS with Gaussian beams

Before discussing Wavefront Sensing (WFS) schemes as applied to mesa beams, we first describe how such a system operates with well-understood Gaussian modes. We show how cavity misalignments scatter light into HOMs (Higher Order Modes), how these HOMs are detected and how clever manipulation of Gouy phase allows one to distinguish between misalignment of the front and rear cavity mirrors. Although WFS schemes can also detect mode matching errors [147] we assume perfect matching and limit ourselves to angular misalignments.

Rather than presenting a general formalism for the calculation of WFS signals in arbitrary topologies [148], we instead develop a single instructive example illustrating the key physical principles of the scheme. Following the approaches of Heinzel and Matone [149, 150], we derive an analytical expression for the WFS error signal in a simple and easily understood Fabry-Perot cavity.

3.2.1.1 Scattering into HOMs

To demonstrate how misalignments result in the excitation of higher order modes we shall consider the concrete example of a single Fabry-Perot resonator. In order to efficiently discuss misalignment in this context we introduce two bases and coordinate systems: the unprimed system of the perfectly aligned input beam and the primed system which follows the cavity axis as the mirrors tilt (see fig. 3.3). In the absence of any perturbation these two systems overlap and the input beam is perfectly matched to the cavity. Equivalently, any error in the orientation of the cavity optics will displace the cavity axis from its nominal position and excite higher order modes.

We demonstrate this idea using a plano-spherical cavity as it is the most basic non-trivial example and because it is the configuration closest to that of our mesa beam resonator. In our arguments we shall assume that all departures from the ideal alignment are small, so that only quantities up to first order in tilt need be retained.

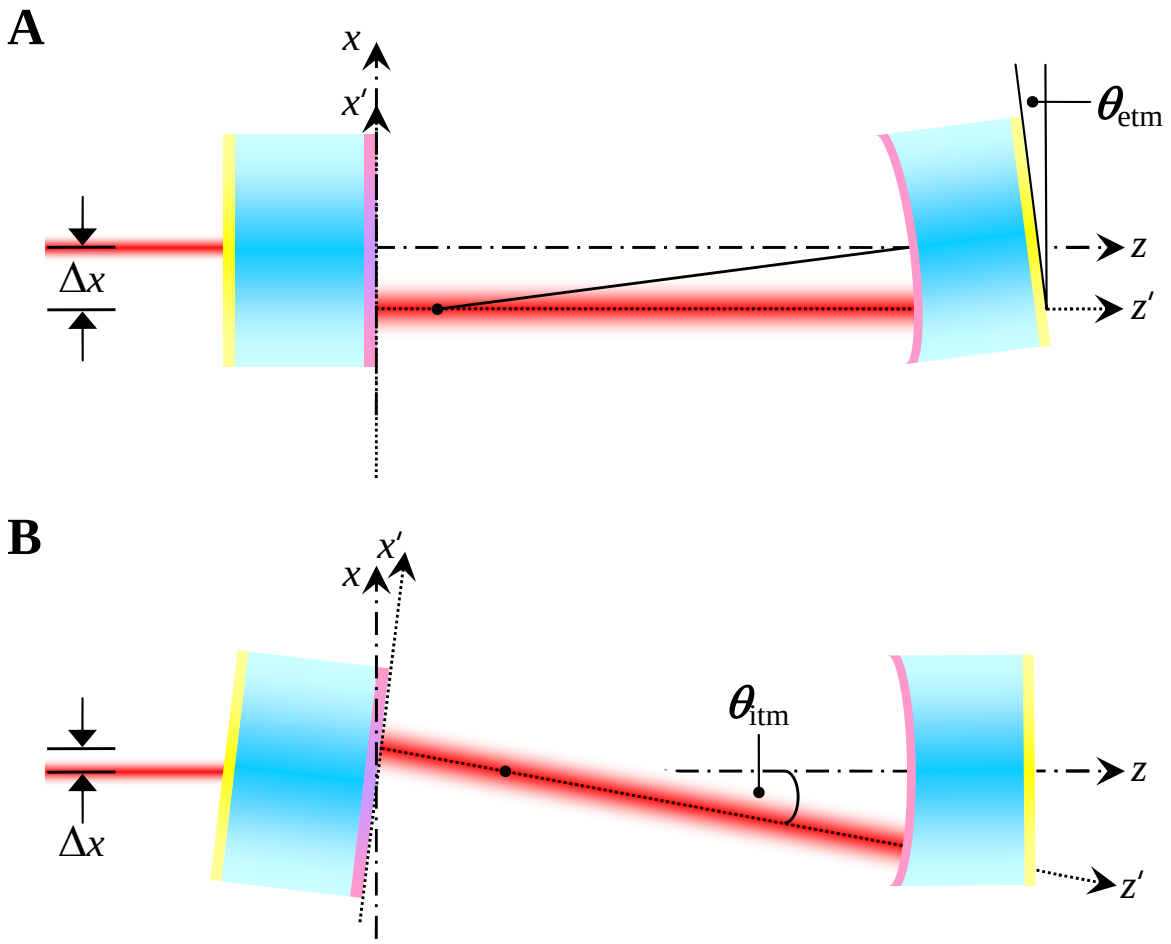

Figure 3.3: Motion of the cavity axis with mirror tilts. The unprimed system represents ideal alignment whilst the primed system follows the cavity axis as mirrors tilt. A - Tilts of the spherical mirror translate the cavity axis, B - Tilts of the plane mirror give rise to tilts and translations.

Tilts of the spherical mirror are most easily analysed (see fig. 3.3). Since the cavity axis must pass through the centre of curvature of this optic, any tilt results in a simple translation Δx of the cavity axis in direct proportion to the applied tilt θ_{etm}

$$\Delta x_{\text{etm}} \simeq R_{\text{etm}} \theta_{\text{etm}}. \tag{3.1}$$

Geometric arguments also assist our consideration of the flat mirror. The cavity axis must always be normal to this optic, so that mirror tilts introduce an equivalent rotation[6] in the cavity axis $\theta_{\text{axis}} = \theta_{\text{itm}}$. In addition there is a small translation given

[6]In this work we use 'rotation' to refer to angular movements of the cavity axis whereas 'tilt' refers to angular movements of mirrors.

by

$$\Delta x_{\rm itm} \simeq (R_{\rm etm} - L_{\rm cav})\theta_{\rm itm}. \tag{3.2}$$

Both tilts also change the cavity length by a small amount. However this length change is of order θ^2 and can thus be ignored in our analysis. Moreover, any cavity control loop should have ample gain at frequencies where angular motion is seismically excited to quash such length noise.

We now show how this motion of the cavity axis results in excitation of HOMs, using the completeness of the HG basis (see §1.5.1.1) to express the input beam in the basis of cavity modes.

The electric field of a Gaussian beam propagating in the z direction may be written as (see §1.5.1)

$$\begin{aligned}\Psi_{mn}(x,y,z) &= E_0 \frac{\omega_0}{\omega(z)} U_m(x,z) U_n(y,z) \\ &\quad \times \exp\left(j(\omega t - kz) + j(m+n+1)G(z) - jk\frac{x^2+y^2}{2R(z)}\right), \\ &= E_0 e^{j\omega t} U_m U_n A_{mn}.\end{aligned} \tag{3.3}$$

The most lucid explanation of the scattering process is provided by considering only a single transverse dimension and focusing attention on the transverse mode functions[7]

$$U_0(x,z) = \left(\frac{2}{\pi}\right)^{1/4}\left(\frac{1}{\omega(z)}\right)^{1/2}\exp\left(\frac{-x^2}{\omega^2(z)}\right), \tag{3.4}$$

$$U_1(x,z) = \left(\frac{2}{\pi}\right)^{1/4}\left(\frac{1}{\omega(z)}\right)^{1/2}\left(\frac{2x}{\omega(z)}\right)\exp\left(\frac{-x^2}{\omega^2(z)}\right). \tag{3.5}$$

For small misalignments only scattering into the first excited mode is relevant.

We have seen that mirror tilts give rise to two classes of perturbation of the cavity axis, rotations and translations. We now consider each case separately starting with pure translation by Δx. Our arguments may be adapted to any longitudinal position

[7]Of the many permissible normalisations we have chosen to impose that $\int_{-\infty}^{\infty} |U_i(x,z)|^2 {\rm d}x = 1$.

[149] but for clarity we work at the waist.

In the unprimed frame the input beam is simply

$$\Psi_{\text{input}}(x,0) = \Psi_0(x,0) = E_0 e^{j\omega t} U_0(x,0). \tag{3.6}$$

In the primed cavity axis frame this mode is

$$\begin{aligned}
\Psi_{\text{input}}(x',0) &= \Psi_0(x'-\Delta x,0),\\
&= E_0 e^{j\omega t} U_0(x'-\Delta x,0),\\
&= E_0 e^{j\omega t}\left(\frac{2}{\pi}\right)^{1/4}\left(\frac{1}{\omega_0}\right)^{1/2}\exp\left(\frac{-(x'-\Delta x)^2}{\omega_0^2}\right),\\
&= E_0 e^{j\omega t}\left(\frac{2}{\pi}\right)^{1/4}\left(\frac{1}{\omega_0}\right)^{1/2}\exp\left(\frac{-x'^2}{\omega_0^2}\right)\exp\left(\frac{2x'\Delta x}{\omega_0^2}\right)\exp\left(\frac{-\Delta x^2}{\omega_0^2}\right).
\end{aligned} \tag{3.7}$$

Under our assumption of small tilts we may neglect the term in Δx^2 and expand the second exponential to first order. We find that translations of the cavity axis scatter light into the Ψ_1 mode in phase with a coupling coefficient $\Delta x/\omega_0$

$$\begin{aligned}
\Psi_{\text{input}}(x',0) &\simeq E_0 e^{j\omega t}\left(\frac{2}{\pi}\right)^{1/4}\left(\frac{1}{\omega_0}\right)^{1/2}\exp\left(\frac{-x'^2}{\omega_0^2}\right)\left[1+\frac{2x'\Delta x}{\omega_0^2}\right],\\
&= E_0 e^{j\omega t}\left[U_0(x',0)+\frac{\Delta x}{\omega_0}U_1(x',0)\right],\\
&= \Psi_0(x',0)+\frac{\Delta x}{\omega_0}\Psi_1(x',0).
\end{aligned} \tag{3.8}$$

We now examine a pure rotation of the optical axis by angle θ. In this case the input beam (3.6) in the cavity frame acquires an extra phase[8] given by $\phi(x') = kx'\sin\theta \simeq$

[8] In general one also needs to consider the projection of amplitude onto the new transverse cavity plane. This second order effect is ignored in our analysis.

$kx'\theta$. Hence

$$\begin{aligned}
\Psi_{\text{input}}(x',0) &= \Psi_0(x',0)\exp(jkx'\theta),\\
&= E_0 e^{j\omega t}U_0(x',0)\exp(jkx'\theta),\\
&\simeq E_0 e^{j\omega t}U_0(x',0)\left[1+jkx'\theta\right],\\
&= E_0 e^{j\omega t}U_0(x',0)\left[1+j\theta\frac{\pi\omega_0}{\lambda}\frac{2x'}{\omega_0}\right],\\
&= E_0 e^{j\omega t}\left[U_0(x',0)+j\theta\frac{\pi\omega_0}{\lambda}U_1(x',0)\right],\\
&= \Psi_0(x',0)+j\theta\frac{\pi\omega_0}{\lambda}\Psi_1(x',0).
\end{aligned} \tag{3.9}$$

Rotations of the cavity axis scatter light into the Ψ_1 mode in quadrature with coupling coefficient $\theta\pi\omega_0/\lambda$.

General misalignments entail both transverse displacements and rotations of the cavity axis. At the waist this combination can be written as

$$\Psi_{\text{input}}(x',0) \simeq \Psi_0(x',0)+\left(\frac{\Delta x}{\omega_0}+j\frac{\theta}{\lambda/(\pi\omega_0)}\right)\Psi_1(x',0). \tag{3.10}$$

3.2.1.2 Detection of misalignments

Cavity misalignments may be detected in reflection [144] or transmission [133], each style having its own merits. We describe the case of signal extraction in reflection as this is the technique employed in the mesa beam experiment and the majority of long baseline interferometers.

Consider a phase modulated input beam of form

$$\Psi_{\text{input}}(x,z) = E_0 A_0 e^{j\omega t}U_0(J_0(\Gamma)+jJ_1(\Gamma)e^{j\Omega t}+jJ_1(\Gamma)e^{-j\Omega t}), \tag{3.11}$$

where Ω is the modulation frequency and Γ the modulation index.[9] For compactness we

[9]Notice that this is the same input beam as was discussed in §1.5.2.5. When signals are detected in reflection the same phase sidebands may be used for both longitudinal and angular control.

shall henceforth suppress the A_0 phase term, reintroducing its constituents as necessary. For the same reason we also omit function arguments, $J_i(\Gamma)$ becoming J_i for example.

With this notation the input beam in the cavity frame may be described at its waist position by

$$\begin{aligned}\Psi'_{\text{input}} &= E_0 e^{j\omega t}(U'_0 + CU'_1)(J_0 + jJ_1 e^{j\Omega t} + jJ_1 e^{-j\Omega t}),\\ &= E_0 e^{j\omega t}\Big[J_0(U'_0 + CU'_1) + jJ_1 e^{j\Omega t}(U'_0 + CU'_1) + jJ_1 e^{-j\Omega t}(U'_0 + CU'_1)\Big],\end{aligned} \quad (3.12)$$

where $C = \Re(C) + j\Im(C) = \Delta x/\omega_0 + j\theta\pi\omega_0/\lambda$.

To find the reflected field we must apply the complex reflectivity of the cavity

$$r^{mn}_{\text{cpt}}(f) = r_1 - \frac{t_1^2 r_2 \exp(-j2\pi f 2L/c)}{1 - r_1 r_2 \exp(-j2\pi f 2L/c)} \quad (3.13)$$

where f is the detuning in Hz from resonance, mn are mode indices and cpt represents a spectral component, e.g. CR or $SB+$ for carrier or upper sideband respectively.

The reflected field in the primed cavity frame is thus

$$\begin{aligned}\Psi'_{\text{refl}} = E_0\Big[&J_0(r^{00}_{CR}U'_0 + r^{10}_{CR}CU'_1)e^{j\omega t}\\ &+ jJ_1((r^{00}_{SB+}U'_0 + r^{10}_{SB+}CU'_1)e^{j(\omega+\Omega)t})\\ &+ jJ_1((r^{00}_{SB-}U'_0 + r^{10}_{SB-}CU'_1)e^{j(\omega-\Omega)t})\Big].\end{aligned} \quad (3.14)$$

To convert back to the input frame for detection we must recognise that the U'_0 mode will be affected by a misalignment $-\Re(C) + j\Im(C) = -C^*$ so that

$$\begin{aligned}\Psi_{\text{refl}} = E_0\Big[&J_0\Big(r^{00}_{CR}(U_0 - C^*U_1) + r^{10}_{CR}CU_1\Big)e^{j\omega t}\\ &+ jJ_1\Big((r^{00}_{SB+}(U_0 - C^*U_1) + r^{10}_{SB+}CU_1)e^{j(\omega+\Omega)t}\Big)\\ &+ jJ_1\Big((r^{00}_{SB-}(U_0 - C^*U_1) + r^{10}_{SB-}CU_1)e^{j(\omega-\Omega)t}\Big)\Big].\end{aligned} \quad (3.15)$$

Let us separate this field into spectral components by expressing it as $\Psi_{\text{refl}} = e^{j\omega t}(a_0 + a_1 e^{j\Omega t} + a_{-1} e^{-j\Omega t})$ where

$$\begin{aligned} a_0 &= E_0 J_0 \left(r_{CR}^{00}(U_0 - C^* U_1 e^{jG}) + r_{CR}^{10} C U_1 e^{jG} \right), \\ a_1 &= j E_0 J_1 \left(r_{SB+}^{00}(U_0 - C^* U_1 e^{jG}) + r_{SB+}^{10} C U_1 e^{jG} \right), \\ a_{-1} &= j E_0 J_1 \left(r_{SB-}^{00}(U_0 - C^* U_1 e^{jG}) + r_{SB-}^{10} C U_1 e^{jG} \right). \end{aligned} \tag{3.16}$$

Here we have also reintroduced the additional Gouy phase G which the U_1 mode will acquire with respect to the fundamental upon any propagation away from the waist. This Gouy phase will prove crucial in identifying misalignments of specific optical components (see §3.2.1.3).

This representation allows us to easily compute the voltage signal S_{pd} from any photodetector in reflection

$$\begin{aligned} S_{\text{pd}} &= G_{\text{pd}} R_{\text{pd}} |(a_0 + a_1 e^{j\Omega t} + a_{-1} e^{-j\Omega t}) e^{j\omega t}|^2, \\ &= G_{\text{pd}} R_{\text{pd}} \Bigg[\underbrace{|a_0|^2 + |a_1|^2 + |a_{-1}|^2}_{\text{dc components}} + \underbrace{2\Re[(a_{-1}^* a_0 + a_0^* a_1) e^{j\Omega t}]}_{\text{components at } \Omega} + \underbrace{\mathcal{O}(2\Omega)}_{\text{components at } 2\Omega} \Bigg], \end{aligned} \tag{3.17}$$

where R_{pd} is the responsivity of the photodiode in amperes per watt and G_{pd} is the transimpedance gain in volts per ampere.

We have seen above that mirror tilts are evidenced by the excitation of higher order modes. In order to detect the presence of the U_1 mode the orthogonality of the basis functions ($\int_{-\infty}^{\infty} U_0(x,z) U_1(x,z)\, \mathrm{d}x = 0$) demands that we employ a split photodetector, subtracting its outputs.[10] Hence the true signal of interest is

$$S_{\text{pd}}^{\text{split}} = \int_0^{\infty} S_{\text{pd}}\, \mathrm{d}x - \int_{-\infty}^{0} S_{\text{pd}}\, \mathrm{d}x. \tag{3.18}$$

[10] In practice, when dealing with two transverse dimensions a quadrant detector is used.

We may simplify the calculation of our error signal by noting that

$$\int_0^\infty U_0(x,z)U_0(x,z)\,\mathrm{d}x - \int_{-\infty}^0 U_0(x,z)U_0(x,z)\,\mathrm{d}x = 0 \tag{3.19}$$

$$\text{and } \int_0^\infty U_0(x,z)U_1(x,z)\,\mathrm{d}x - \int_{-\infty}^0 U_0(x,z)U_1(x,z)\,\mathrm{d}x = \sqrt{\frac{2}{\pi}}. \tag{3.20}$$

With this information we may proceed under the assumption of an infinite, single element detector[11] and make the following substitutions in our final answer

$$\begin{aligned} U_0U_0 &\to 0, \\ U_0U_1 &\to \sqrt{2/\pi}. \end{aligned} \tag{3.21}$$

The most useful component of S_{pd} is that at the modulation frequency Ω. This signal is extracted via coherent demodulation (see §1.5.2.5)

$$S_{\mathrm{demod}} = \kappa\Re[(a_{-1}^* a_0 + a_0^* a_1)e^{-j\phi_{\mathrm{demod}}}], \tag{3.22}$$

where the term $\kappa = M_{\mathrm{loss}}G_{\mathrm{pd}}R_{\mathrm{pd}}$ includes the responsivity and transimpedance of the photodiode and any mixer loss M_{loss}. Notice that the size of the signal has been halved with respect to (3.17), this is due to equal amounts of signal being upconverted and downconverted by Ω.

Using the a_j values given in (3.16) and applying the replacement rules (3.21) to account

[11] Here we have assumed the beams to be perfectly aligned on the photodetector, a non-trivial issue.

for diode geometry, the resulting in-phase WFS error signal is

$$\begin{aligned} S_{\text{demod}} = \kappa\sqrt{\frac{2}{\pi}}\Bigg(&\Im\Big[e^{-jG}E_0^2 J_0 J_1 \Re(C)(r^{00}_{SB-}r^{00*}_{CR} - r^{00}_{CR}r^{00}_{SB+} \\ &+ e^{2jG}((r^{00}_{SB-} - r^{10}_{SB-})r^{00*}_{CR} + (r^{10}_{CR} - r^{00}_{CR})r^{00*}_{SB+}) - r^{00}_{SB-}r^{10*}_{CR} + r^{00}_{CR}r^{10*}_{SB+})\Big] \\ &- \Re\Big[e^{-jG}E_0^2 \Im(C) J_0 J_1 (r^{00}_{CR}r^{00*}_{SB+} - r^{00}_{SB-}r^{00*}_{CR} \\ &+ e^{2jG}((r^{00}_{SB-} + r^{10}_{SB-})r^{00*}_{CR} - (r^{00}_{CR} + r^{10}_{CR})r^{00*}_{SB+}) - r^{00}_{SB-}r^{10*}_{CR} + r^{00}_{CR}r^{10*}_{SB+})\Big]\Bigg). \end{aligned}$$

Assuming that all fields are perfectly reflected, with the carrier in anti-phase, this expression can be simplified to

$$S_{\text{demod}} = 4\kappa E_0^2 J_0 J_1 \sqrt{\frac{2}{\pi}}(\Re(C)\sin(G) + \Im(C)\cos(G)). \tag{3.23}$$

Further, if we utilise the properties of our plano-spherical cavity we can write the error signal in terms of mirror misalignments as

$$\begin{aligned} S_{\text{demod}} = 4\kappa E_0^2 J_0 J_1 \sqrt{\frac{2}{\pi}}\Bigg[&\left(\frac{R_{\text{ETM}}}{w_0}\sin(G)\right)\theta_{\text{ETM}} \\ &+\left(\frac{\pi w_0}{\lambda}\cos(G) - \frac{R_{\text{ETM}} - L_{\text{cav}}}{w_0}\sin(G)\right)\theta_{\text{ITM}}\Bigg]. \end{aligned} \tag{3.24}$$

3.2.1.3 Isolating individual components

Perhaps the most useful feature of the WFS scheme is its ability to distinguish simultaneous misalignments of the two cavity optics through clever manipulation of Gouy phase. We demonstrate this point using the above example.

Equation (3.24) shows that when $G = n\pi$, $n \in \mathbb{Z}$ the signal due to the end mirror is null and we are purely sensitive to tilts of the input mirror. To similarly null input mirror signals and detect only tilts of the end mirror, algebraic manipulation shows that we require

$$G = \text{atan}\left[\frac{\pi w_0^2}{\lambda(R_{\text{ETM}} - L_{\text{cav}})}\right]. \tag{3.25}$$

Thus by positioning two split photodetectors at these Gouy phases one can construct a diagonal alignment control system.

The apposite Gouy phase advance may be introduced by simple propagation but is more often realised using a system of lenses known as a Gouy phase telescope. This approach is preferred as it also allows the spot size at the diode position to be controlled. If the beam spot is too large it will be apertured; too small and beam centring on the WFS diode will be difficult.

To calculate the Gouy phase at the detector position after propagation through the telescope it is useful to introduce the complex beam parameter

$$q = z + jz_{\mathrm{R}}, \tag{3.26}$$

where z and z_{R} are the propagation distance from the waist and Rayleigh range respectively. The spot size of the Gaussian beam and its Gouy phase[12] are found from q as

$$\begin{aligned} \omega(z) &= \sqrt{\frac{\lambda \Im(q)}{\pi}\left[1 + \left(\frac{\Re(q)}{\Im(q)}\right)^2\right]} \\ \text{and } G(z) &= \operatorname{atan}\left[\frac{\Re(q)}{\Im(q)}\right], \end{aligned} \tag{3.27}$$

adaptations of the more familiar (1.31) and (1.32).

The transformation of q on propagation through any telescope may be found using using ray transfer matrices [146]. The action of the matrix

$$\begin{pmatrix} A & B \\ C & D \end{pmatrix}$$

being

$$q_{\mathrm{out}} = \frac{Aq_{\mathrm{in}} + B}{Cq_{\mathrm{in}} + D}. \tag{3.28}$$

[12]Which is equal to the Gouy phase difference between the fundamental and first excited modes.

The transfer matrices for propagation over distance d through material with refractive index n and for a thin lens of focal length f are[13]

$$\begin{pmatrix} A & B \\ C & D \end{pmatrix}_{\text{prop}} = \begin{pmatrix} 1 & L/n \\ 0 & 1 \end{pmatrix}, \tag{3.29}$$

$$\text{and} \quad \begin{pmatrix} A & B \\ C & D \end{pmatrix}_{\text{lens}} = \begin{pmatrix} 1 & 0 \\ -1/f & 1 \end{pmatrix}. \tag{3.30}$$

In general the great utility of matrix methods is that, through multiplication, they allow a complex system to be represented by a single matrix. Using the matrix representation of a Gouy phase telescope for example, the spot size at the detector position is easily found from the properties of the input beam without having to evaluate beam parameters at any intermediate stage (see also §1.3.2). Unfortunately such an approach is not applicable in calculating the Gouy phase itself.

The expression for Gouy phase (3.27) gives the phase gained on propagation from the beam's waist position. Passing through any focusing element creates a field with a new waist position so that blind application of the above formulae results in unphysical discontinuities in Gouy phase across a lens.

To calculate the true Gouy phase at the output of our telescope we adopt the following approach. For propagation up to the first lens $G(z)$ is calculated as normal. Then for each additional propagation, from z_m to $z_m + d$ say, we add to $G(z)$ only the Gouy phase accumulated propagating over distance d i.e. $G(z_m + d) - G(z_m)$, taking care to use the correct beam parameter for each distinct propagation section. In this way Gouy phase is continuous throughout any telescope and the advance of the first excited mode with respect to the fundamental is accurately determined.

Real Gouy phase telescopes typically consist of a converging and diverging lens separated by $d \simeq f_1 + f_2$. When a Gaussian beam passes through its waist it acquires an additional 180° of Gouy phase (see fig. 1.12). By positioning the second lens near the focal plane of the first, the desired Gouy phase at the detector position may be

[13]The transformation due to propagation may also be found trivially by addition (see (3.26)).

extracted. Since the second lens is near a focus it is usually strongly diverging, expanding the beam to the required size. Good control of the separation between the lenses is essential when using this telescope configuration[14] while the resultant Gouy phase is more robust with respect to the positioning of the first lens and detector.

Telescope layouts are usually found via numerical optimisation routines to minimise sensitivity to variation in focal lengths and lens positioning. A typical design is shown in fig. 3.4.

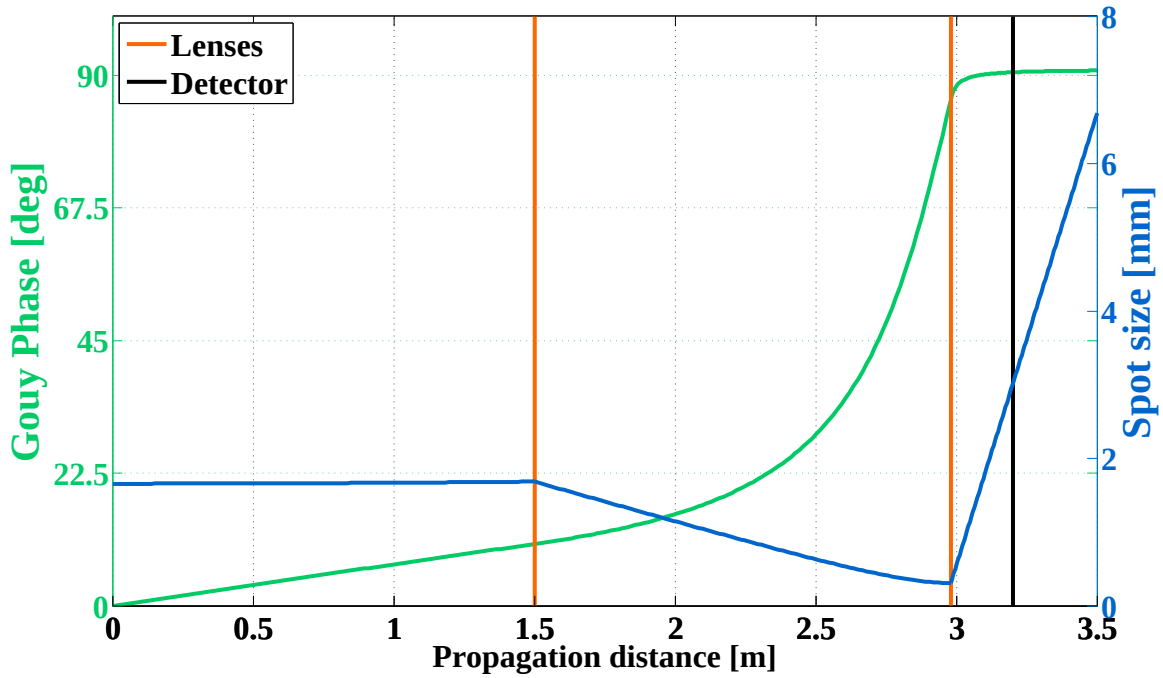

Figure 3.4: Gouy phase telescopes allow phase and spot size at the detector position to be controlled simultaneously. Here we show a design providing approximately 90° of Gouy phase and a spot size of 3 mm. The lens separation is 1480 mm, $\omega_0 = 1.66$ mm, $f_1 = 1500$ mm and $f_2 = -25$ mm.

In practice it can be difficult to achieve perfect signal separation for a number of reasons. For example, if a cavity is close to degenerate there will be appreciable mixing of the signals from each optic unless those due to misalignments of one mirror are perfectly nulled; if the cavity is degenerate uncontaminated signals cannot be produced.[15]

[14] Although experimentally challenging this sensitivity to lens separation allows the Gouy phase at the WFS to be tuned over a wide range.

[15] However, in the normal application of wavefront sensing within servo loops, all the signals are driven to zero, so unless the cross terms actually dominate over the diagonal terms the servos should

Further, it is often not necessary to create independent error signals for each mirror optically. So long as angular motions of one mirror can be well distinguished, electronic subtraction can be used to obtain uncorrupted information about the other optic [145].

3.3 WFS with mesa beams

Similarly to PDH reflection locking (see sections 1.5.2.5 and 2.2.4.4), differential wavefront sensing has become an indispensable technique in the control of gravitational wave interferometers employing Gaussian beams. Hence it is important that WFS translate effectively to non-Gaussian mesa beams if they are to be considered a serious option for future detectors.

An analytical expression for the excited modes of a mesa beam resonator remains to be found, making it difficult to investigate WFS with mesa beams theoretically. However, work by D'Ambrosio [104] and O'Shaughnessy [106], based around FFT simulation and perturbation of an integral eigenequation [105] respectively, has shown that WFS is likely to operate successfully with mesa beams. Their work investigated the field resonating in a misaligned mesa cavity, showing that tilts of the MH mirror through angle θ excite an odd mode in proportion to θ and an even mode in proportion to θ^2 – exactly the behaviour exhibited by a spherical cavity.[16] Fig. 3.5 shows the odd contribution.

This result suggests that useful error signals for the angular control of a mesa beam resonator can be produced via a differential wavefront sensing scheme analogous to that of a Gaussian cavity.

find the correct alignment.

[16] Although the mode shapes are quite different.

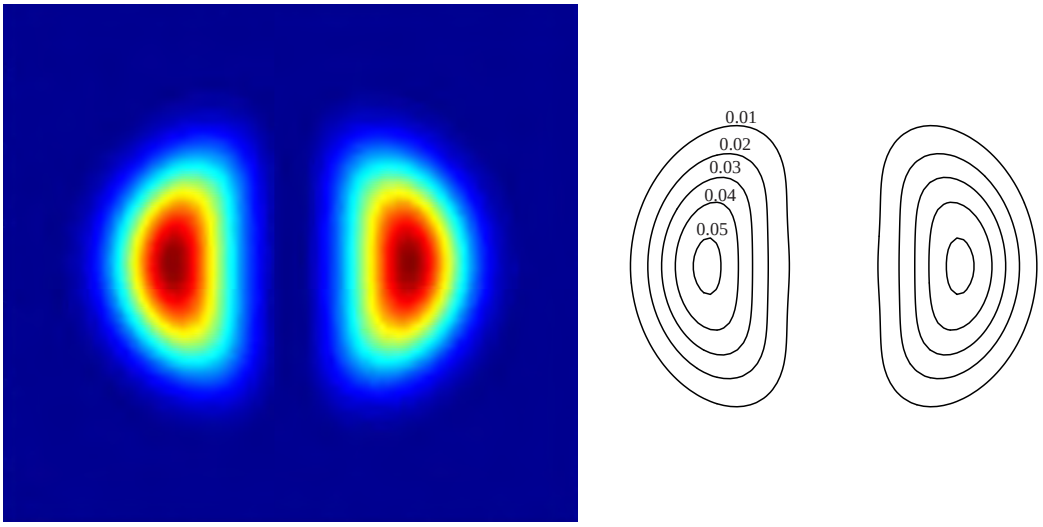

Figure 3.5: Tilts of the Mexican hat mirror in a Fabry-Perot cavity excite an odd mode in proportion to the applied tilt. Here we show the intensity distribution of this mode found via FFT simulation (left) and perturbation theory (right). Figures adapted from the work of D'Ambrosio and O'Shaughnessy [104, 106].

3.3.1 Modelling

Since analytical arguments similar to those presented for Gaussian beams in §3.2.1.1 were not able to be developed, an accurate model capable of predicting mesa beam WFS signals was required. Problems such as this are often tackled using modal expansion [148] since for Gaussian beams only the first few excited modes need be considered. Unfortunately, working with mesa beams, this approach becomes computationally expensive, as even the description of a perfectly aligned cavity demands ∼20 terms.[17] [120] Again an FFT based simulation was the obvious choice.

Having already developed a comprehensive model of our prototype cavity in SIS (see 1.6.2), only slight modifications were required to generate the cavity fields as a function of mirror tilt. In our simulations, Gouy phase was controlled by simple propagation i.e. no Gouy phase telescopes were considered. This propagation was performed external to SIS using an FFT tool developed in *Matlab* [151].

[17] Compared to 1 for the Gaussian case.

3.3.2 Calculation of error signals

Since SIS does not incorporate phase modulation, the sidebands (SB) and carrier (CR) were derived from the available fields as

$$CR = J_0(m) \cdot \text{Total reflected field}; \qquad SB = jJ_1(m) \cdot \text{Promptly reflected field}.$$

With this notation the WFS error signals in watts were then calculated as

$$\text{WFS} = \Delta_x \Delta_y \sum_{1}^{N_x/2} \sum_{1}^{N_y} \text{Err} - \Delta_x \Delta_y \sum_{N_x/2+1}^{N_x} \sum_{1}^{N_y} \text{Err}, \tag{3.31}$$

$$\text{where Err} = \Re[CR(SB \exp(j\phi) + SB \exp(-j\phi))^*].$$

Here ϕ is the demodulation phase and Δ_i is the size of one of the N_i FFT grid squares in the i direction. In the mesa beam calculations done here, the grid was 128×128 pixels on a 5.2 cm square.

3.3.3 Verification of model

To test the accuracy of our FFT methods, we simulated a well understood Gaussian cavity, comparing output to the theory of section 3.2.1.1 and the extensively tested Finesse program developed by Freise [95].

The first investigation studied error signals as a function of mirror tilt at two fixed Gouy phases (see fig. 3.6). Aside from comparing our simulation techniques to other methods, this work also confirmed that signals were linear and became null at the predicted Gouy phases. We subsequently verified that our propagation of the reflected cavity fields was accurate by considering the WFS error signals as a function of Gouy phase for fixed mirror tilts (see fig. 3.7).

Extremely strong agreement between all three methods is observed, both in the magnitude of the signals and in their behaviour as a function of Gouy phase. The results

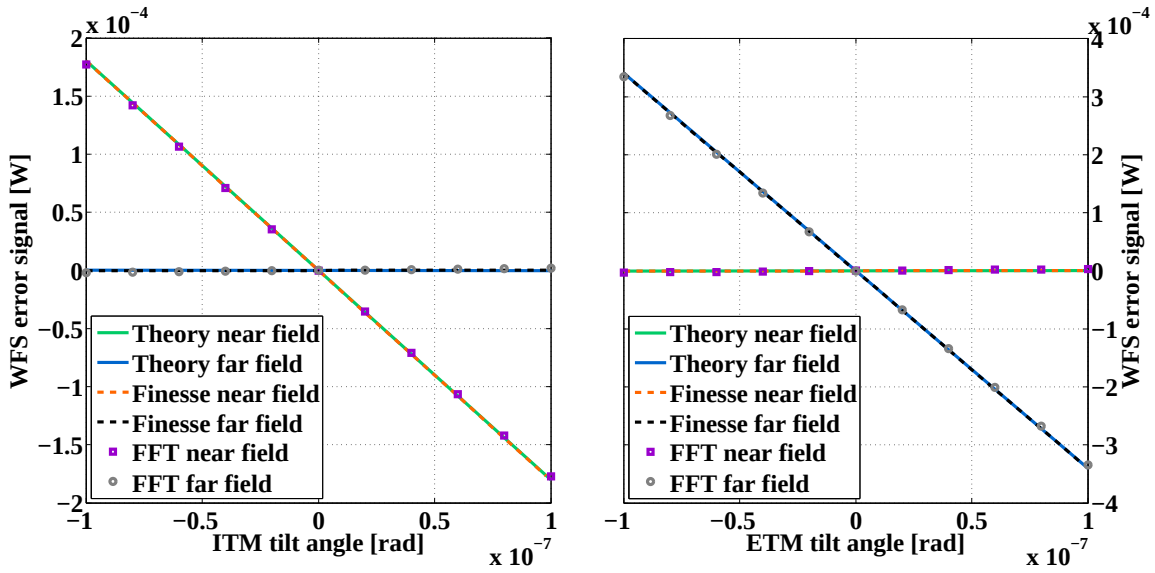

Figure 3.6: WFS error signals as a function of mirror tilt calculated in three different ways – analytically, using Finesse and via the FFT methods which we hope to extend to mesa beams. Near field and far field detector positions are those calculated to null the end and input mirror respectively.

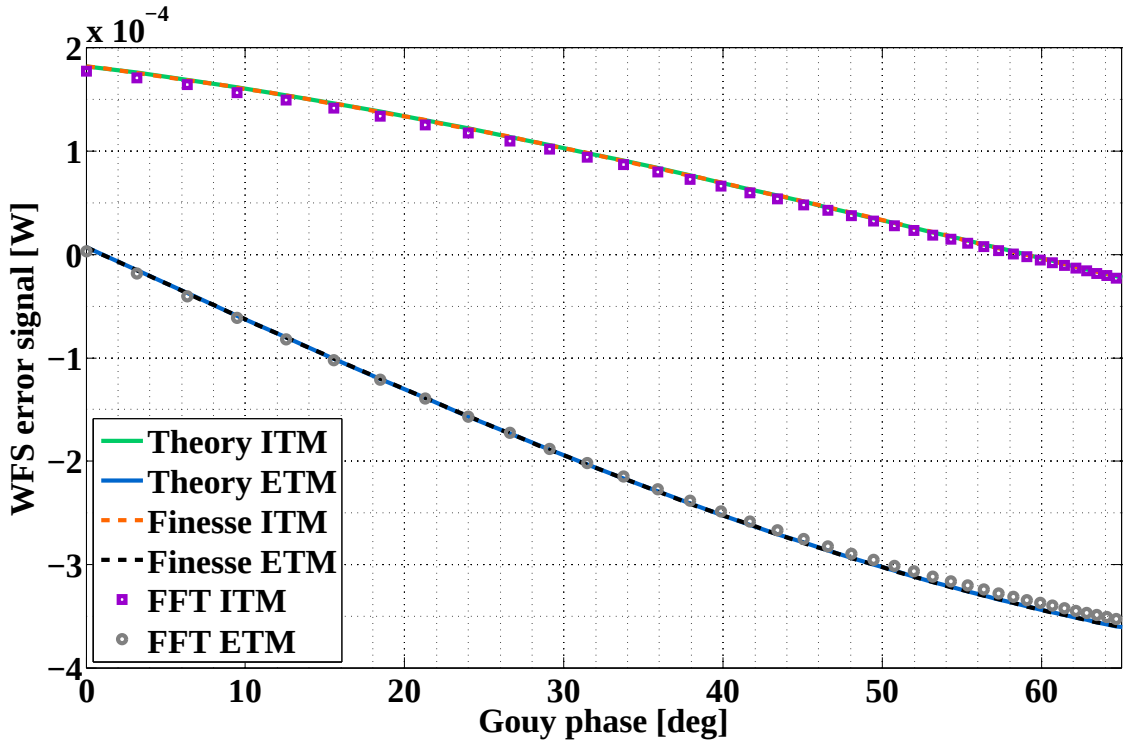

Figure 3.7: WFS error signals as a function of Gouy phase for fixed mirror tilts.

from Finesse and theory are in perfect agreement while those from FFT simulation differ slightly. These differences can be attributed to finite mirror effects and diffraction losses which are not included in the other models.

3.3.4 Predictions for mesa beams

Confident that our simulation technique was sound, we began to investigate the differential wavefront sensing signals expected from our mesa beam cavity.

WFS error signals arising from tilts of each mirror were first calculated as a function of Gouy phase in order to determine where they vanished (see fig. 3.8). It was found

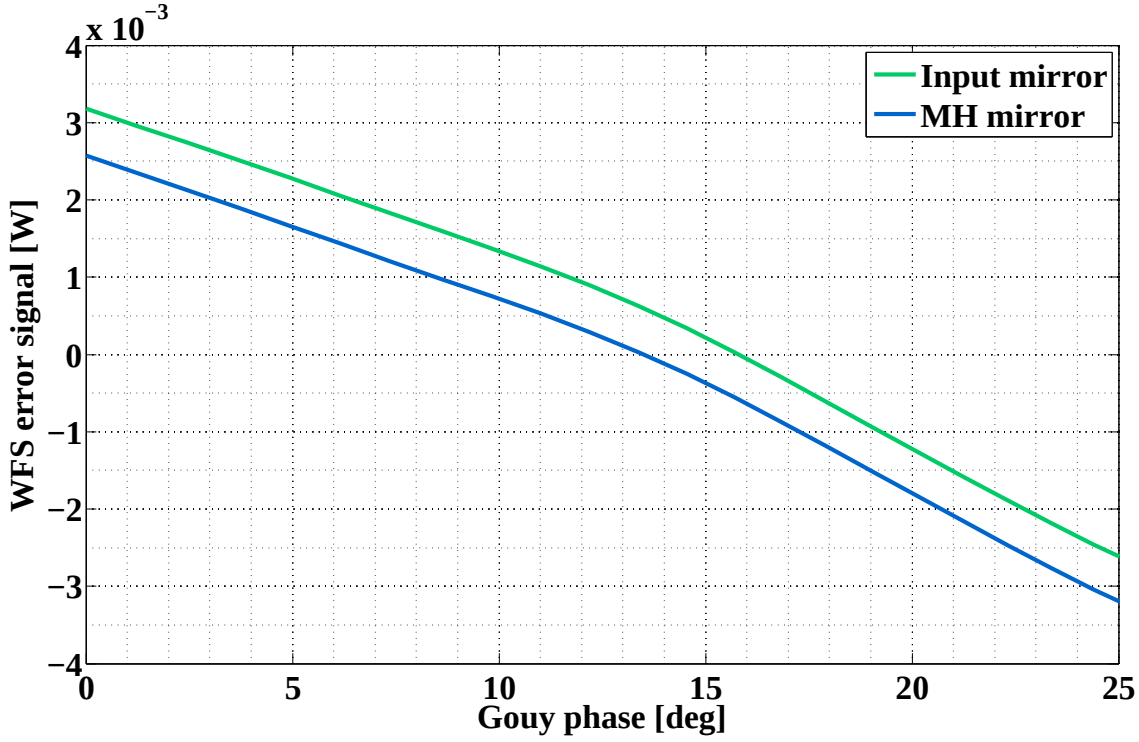

Figure 3.8: Simulated WFS error signals for our prototype cavity as a function of Gouy phase.

that the optimal detector positions were separated by just 2.3°. This suggested that the fundamental and first excited modes of our cavity were near degenerate and that separation of signals due to input and end mirror tilts would be extremely taxing.

Fig. 3.9 shows signals as a function of mirror tilt at the cavity waist (near field) and at the position where input mirror tilts remain undetected (far field). Although it is

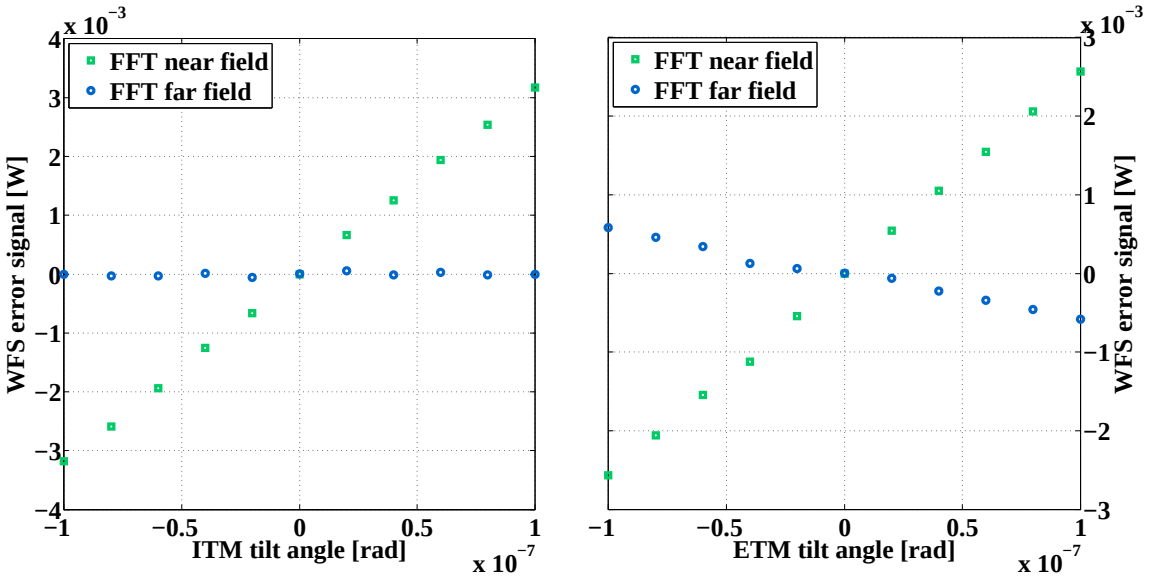

Figure 3.9: Predicted WFS error signals in our prototype cavity as a function of mirror tilt. The near field detector is located at the cavity waist whilst the far field diode is positioned to null input mirror signals.

of course possible to achieve independent sensing, as was done for the spherical mirror cavity, we studied signals at these positions to emphasise the differences between our plano-Mexican hat resonator and the plano-spherical cavity investigated in the previous section.[18]

Using the predictions of simulation to guide design, experimental work commenced.

3.4 Experiment

In this section we detail the approach and findings of an experimental investigation into differential wavefront sensing with mesa beams carried out using our prototype cavity. The principal goals of this work were to validate our modelling tools[19] and to study the error signals themselves rather than develop a functional auto-alignment

[18] In a plano-spherical cavity ETM signals are null at the cavity waist.

[19] So that they might be applied to future gravitational wave interferometer designs utilising mesa beams.

system. This strategy was adopted as the true vagaries of designing a robust alignment control scheme are related to dynamical thermal and radiation pressure effects which could not be recreated in our low power apparatus.

3.4.1 Apparatus and method

A comprehensive discussion of the prototype mesa beam cavity was presented in §2.2. In this section we discuss only those elements unique to the WFS experiment, beginning with the split photodetector.

The wavefront sensor itself was constructed from an EG&G YAG-444-4A quadrant photodiode.[20] The properties of this diode are listed in table 3.1.

Table 3.1: Attributes of wavefront sensor quadrant photodiode.

Property	Value
Diameter	11.4 mm
Optimal spot size	∼3 mm
Reverse bias	100 V
Responsivity	0.4 A/W
Capacitance per quadrant	9 pF
Forward resistance	100 Ω
Interchannel cross coupling	-25 dB
Dark current	∼100 nA

A tunable inductor was placed in parallel with each quadrant to form a circuit resonant at the modulation frequency. To suppress harmonics of the modulation frequency two notch filters were also included. In operation the output of each diode quadrant was divided into AC and DC components, with the DC outputs being used to centre the incident beam. No active beam steering servo was employed.

The RF photodiode signals were demodulated individually and appropriately combined using analogue electronics to construct the WFS error signals. The unique demodula-

[20]The diode was oriented like this $\bigoplus$ as opposed to this $\bigotimes$. The relative merits of each configuration are discussed in [152].

tion phase of each quadrant was set by introducing the electronic delay which minimised evidence of a high frequency cavity length excitation in the Q quadrature.

The WFS head[21] was positioned as shown in fig. 2.30. Using the results of our simulation work, a flexible two lens Gouy telescope of the type discussed in §3.2.1.3 was designed. The detector and each lens were mounted atop high-performance linear translation stages so that their location could be accurately determined and controlled. By carefully tuning the lens spacing and the position of the WFS head, the Gouy phase at the detector position could be varied over a large range whilst preserving an acceptable spot size.

Great care was taken to ensure that our design encompassed the phases where signals due to tilts of the input and Mexican hat mirrors were predicted to be null, at 15.8° and 13.5° respectively. With this setup we hoped to create an experimental analogue of fig. 3.8.

Measurements were made at AC using the following procedure. The cavity was locked using PDH techniques and aligned to simultaneously maximise transmitted power and minimise evidence of angular excitations in the PDH error signal. The cavity was left in this state for some time to allow thermal transients, particularly in the laser, to subside. After this period, if necessary, alignment was once more optimised.

A study of the cavity's residual length fluctuations was then made to select a low noise band, where the longitudinal loop also had high gain,[22] in which to operate. The region around 100 Hz was found to be suitable.

Due to the layout of the PZT actuators (see §2.2.3.3) analogue electronics were required to convert applied excitations into pitch and yaw motion. This circuit also allowed the relative gains of each PZT channel to be adjusted by hand, using audio feedback,[23] to eliminate any angle to length coupling. Previous checks had confirmed that the first

[21]The quadrant photodiode and associated electronics (filters, gain stages) were packaged as a single unit known as the WFS 'head'.

[22]To suppress any residual angle to length couplings.

[23]Cordless headphones monitoring the cavity's longitudinal error signal.

angular resonance of the PZT-mirror mount combination was well out of band.

Modulating the angular orientations of the input and end mirrors at distinct frequencies across the 100 Hz octave, the transfer function between applied excitation and the appropriate WFS error signal was then measured. The magnitude of the applied excitations was varied but always chosen to ensure operation in the linear regime (see fig. 3.10). For clarity pitch and yaw were studied separately.

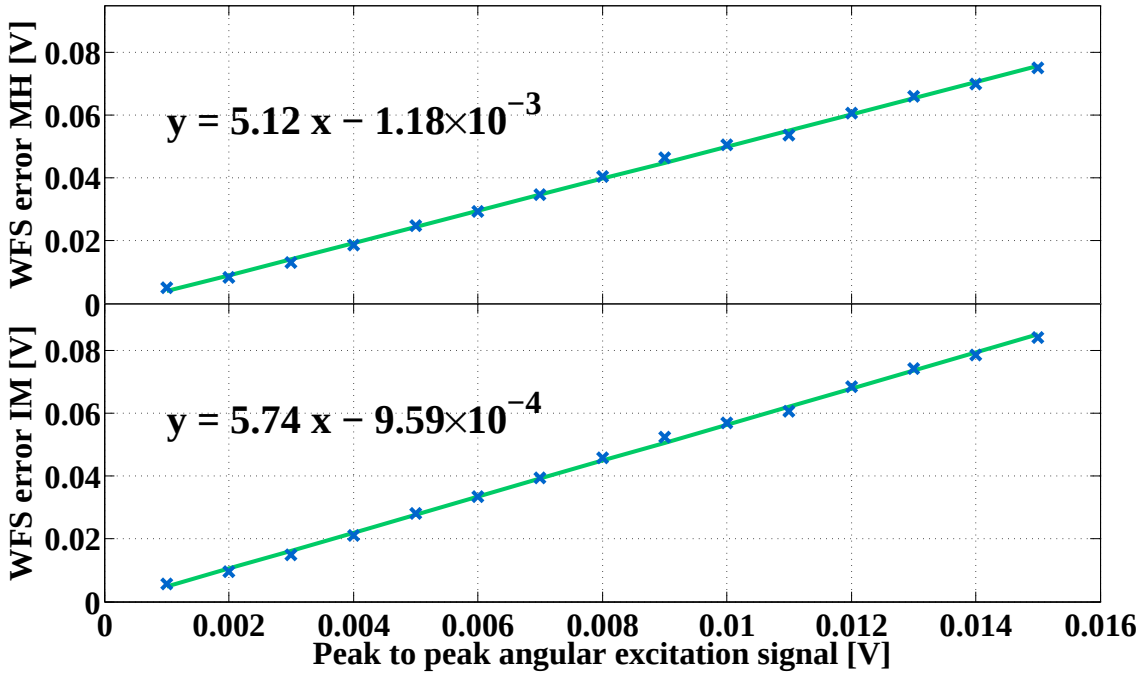

Figure 3.10: The magnitudes of angular excitations applied to the mesa beam cavity were chosen to ensure linear operation. Applied voltages were strictly below 0.01 Vpp.

This process was repeated a number of times for each telescope configuration to test consistency of results over time, between locks and as a function of tilt. A sketch of the experimental set up is shown in fig. 3.11.

3.4.2 Calibration

In order to express experimental data in useful units and facilitate comparison with simulation a thorough calibration was performed.

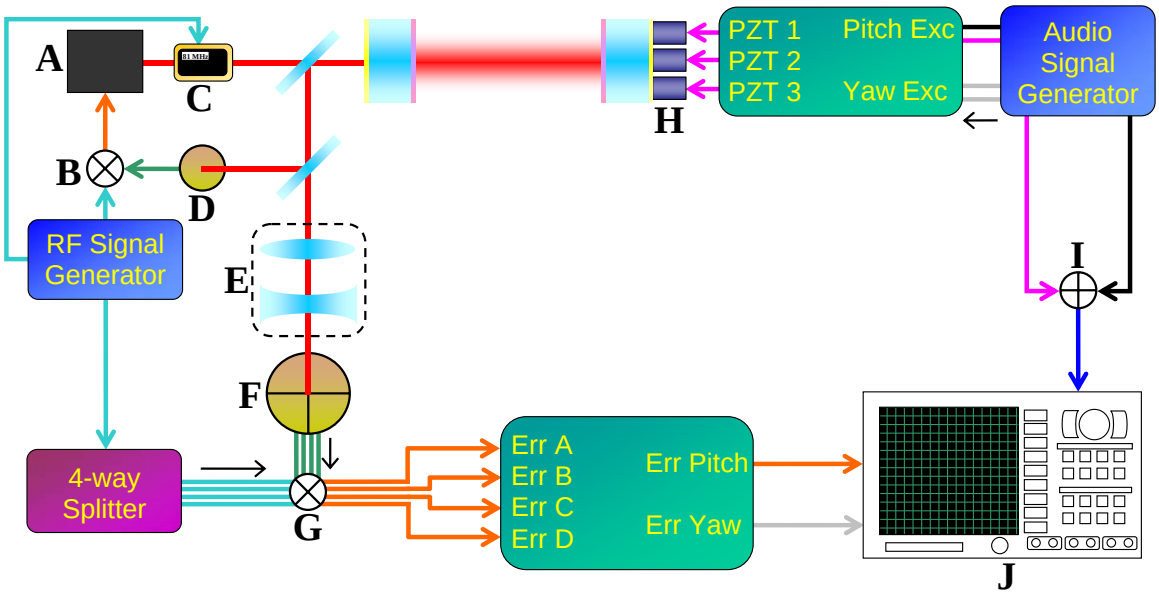

Figure 3.11: Mesa WFS experimental apparatus configured for pitch measurements. Both mirrors were excited simultaneously. Only excitations of the cavity end mirror are shown. A - Laser, B - Mixer, C - Electro-optic modulator, D - RF photodiode, E - Gouy phase telescope, F - WFS quadrant photodiode, G - Mixer, H - PZT triplet (input mirror PZTs not shown), I - Summing junction, J - Spectrum analyser.

The response of the optical detection chain was studied using a diode laser operating at 1064 nm. By inserting a bias tee between the diode and its current source, radio frequency amplitude modulation could be impressed upon the laser's output. The resulting modulation index around our experiment's sideband frequency was calculated using a fast commercial photodiode with known responsivity and gain [138].

In this way a laser beam with well characterised RF amplitude modulation could be applied to each quadrant of our split photodiode. Subsequently recording the output of each mixer allowed us to fully calibrate the WFS head and associated demodulation electronics.

The PZT tilt actuators (see §2.2.3.3) were calibrated using a long arm optical lever. A He-Ne laser positioned on the input bench was oriented such that its beam was incident on the rear surface of the input or MH mirror. The reflected beam was then relayed to the beam capture table at the opposite end of the cavity and back toward the laser, giving a total arm length >14 m. Measurements taken as a function of frequency and amplitude were found to give consistent results.

3.4.3 Results and discussion

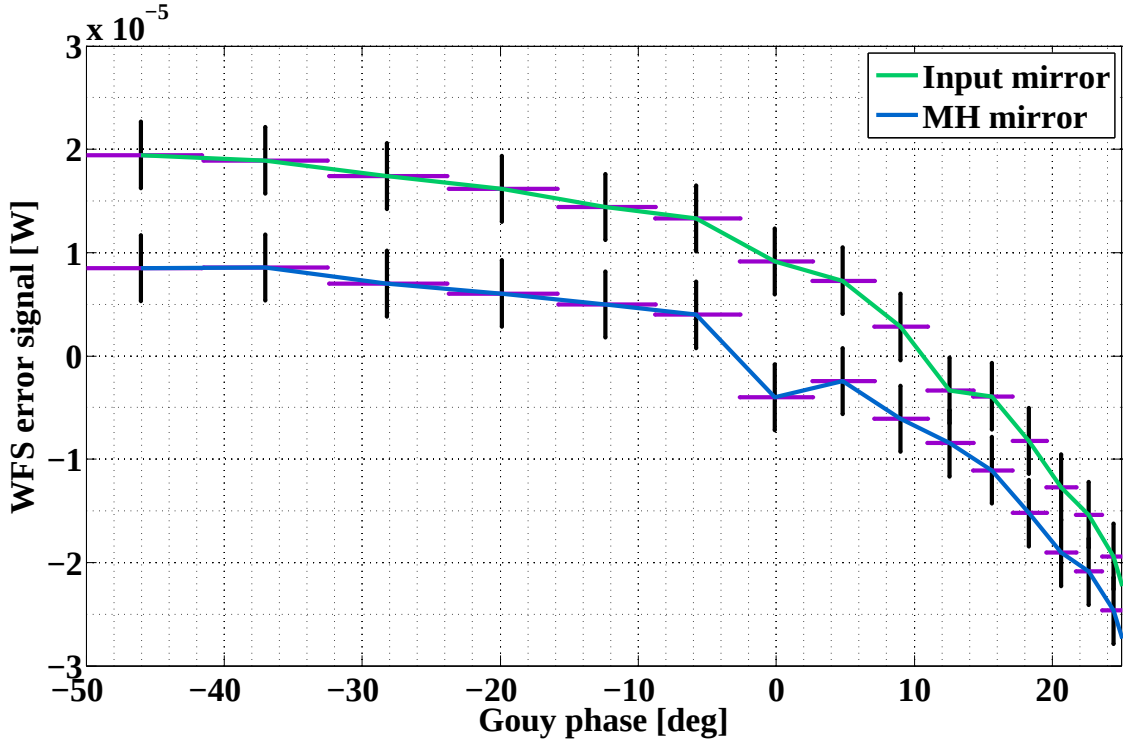

Figure 3.12: Experimental WFS signals as a function of Gouy phase. These results should be compared to those of fig. 3.8. Errors are dominated by uncertainties in the layout of the Gouy phase telescope and in the calibration of the tilt induced by our excitations.

Fig. 3.12 shows differential wavefront sensing signals measured using our prototype mesa beam cavity. These signals are linear for small excursions from the optimal alignment and bi-polar about it, indicating that closed loop control is feasible. To our knowledge these results are the first experimental demonstration of the WFS technique in a non-Gaussian interferometer.

Comparing our measurements to model prediction (see fig. 3.8) we see that the overall form, trends and relative magnitudes are well respected. The absolute size of the experimental signals falls short of expectation, suggesting a neglected systematic effect. Despite ardent investigation the source of this discrepancy remains unknown.[24]

[24]The beam parameters and focal lengths used in the design of our Gouy phase telescopes were experimentally measured on a number of occasions. Exhaustive calibration of mirror actuators, photodiodes and demodulation circuits produced consistent results. Varying laser power, phase modulation index and angular excitation levels across numerous data taking runs showed that signals scaled as expected. All electronics were found to perform as designed with no hidden saturations or oscillations.

The recorded data shows that signals from the input and MH mirrors become null at 10.62° and 0.80° respectively compared to the predicted values of 15.8° and 13.5°. Subsequent study revealed that including the measured imperfections of the MH mirror modifies the predicted WFS signals, shifting the optimal detector positions (see fig. 3.13).

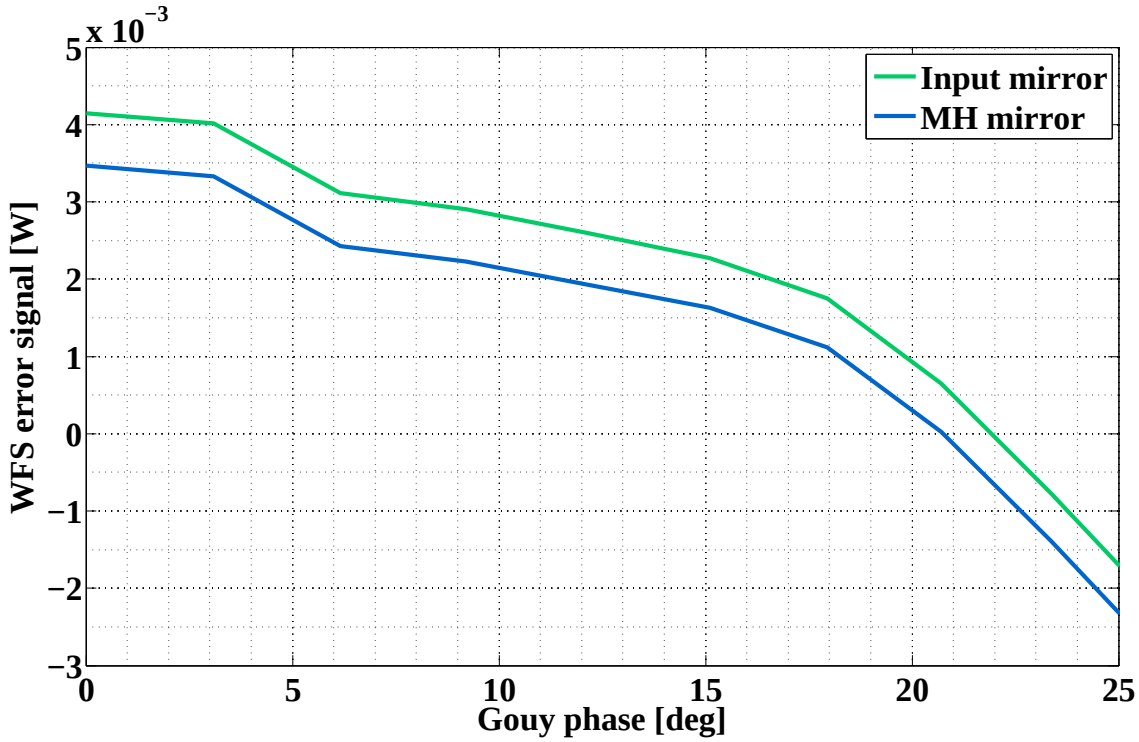

Figure 3.13: Predicted mesa WFS signals including measured mirror imperfections. Signals were found to vary greatly as a function of rotation axis and corrective tilt.

The orientation of the experimental MH mirror with respect to its measured phase map is unknown. It is also uncertain whether the corrective tilt applied in simulation accurately matches that used in the real interferometer. Utilising this freedom it is possible to shift the null positions over a wide range which includes the experimentally measured values. However there is no evidence to suggest that such configurations should be preferred over any other. Experimental measurements tilting about an orthogonal axis found both null positions close to 19°.

Future continuation of this work should endeavour to explore these issues with a view to defining manufacturing tolerances for the construction of MH mirrors. However,

as stated previously, large optics suitable for gravitational wave detectors should be significantly easier to produce, meaning that the interesting features of the reported results are peculiar to our apparatus.

In extending our work to create a full auto-alignment system a number of differences between Gaussian and mesa beams may prove significant. Even in the presence of optimal input mode coupling and perfect alignment, excited transverse modes are present in the mesa cavity. With our imperfect MH mirror it was observed that even the lowest order transverse mode,[25] whose presence we relate to angular misalignments, was excited. This effect is shown in fig. 3.14 where we also see that mirror imperfections shift the locations of HOM resonances. The mesa modes are shifted in a complex, non-uniform way; polishing errors of a spherical mirror would simply modify the HOM spacing.

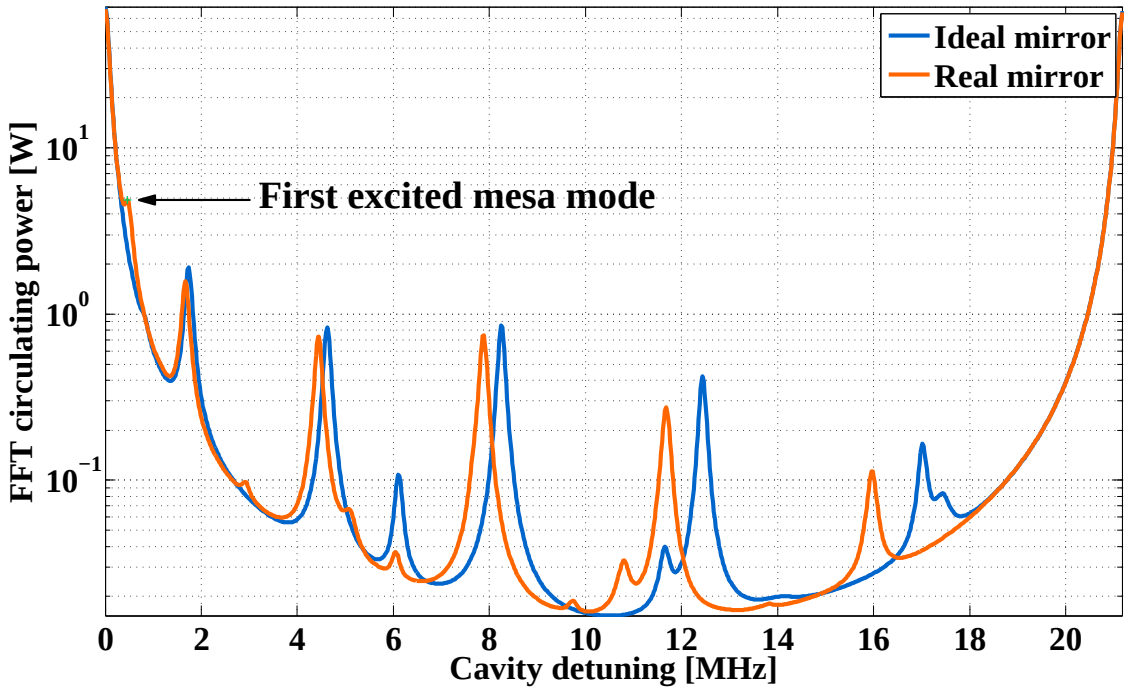

Figure 3.14: Simulated transverse mode spectra of our prototype resonator using ideal and measured MH mirror phase maps.

A second issue of interest is the shift in the resonant frequency of mesa HOMs as a function of tilt (see fig. 3.15). Such effects are not witnessed in spherical mirror

[25] Excluding the fundamental mesa beam itself.

resonators and may make the construction of independent sensing signals difficult in near degenerate cavities. The frequency shift is non-linear going approximately as θ^3.

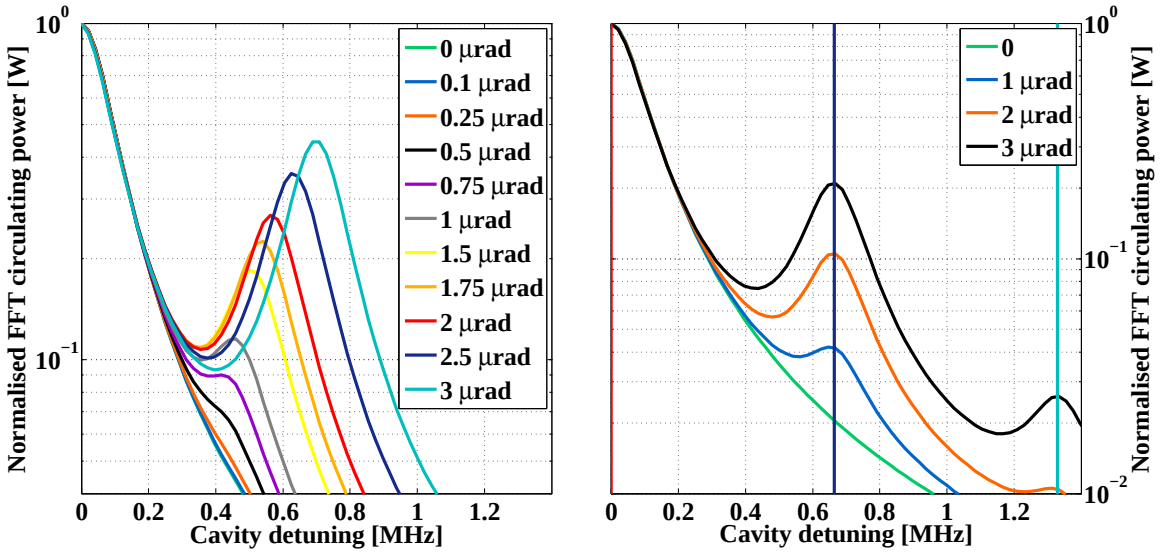

Figure 3.15: Position of the first excited transverse mode as a function of end mirror tilt in Gaussian (right) and mesa beam (left) resonators. The shift in resonant frequency with tilt observed for mesa beams may be significant for future auto alignment schemes in non-Gaussian interferometers. Mesa beam results use the ideal mirror profile. Vertical lines in the Gaussian plot indicate theoretical resonance frequencies.

3.5 Summary

During the initial work which led to mesa beams being proposed as an alternative to Gaussian modes for AdvLIGO it was discovered that mesa beam interferometers were moderately more sensitive to angular misalignments of their optics. This realisation prompted the experimental study of angular misalignments in our prototype cavity.

Our first investigation focused on the changes in the mesa beam intensity profile as the Mexican hat end mirror was misaligned. The results of this work confirmed that mesa beams were slightly more sensitive to mirror tilts than the equivalent Gaussian and showed that our FFT based simulation methods were able to accurately reproduce the eigenmodes of a misaligned resonator.

Extending these simulation tools we began to investigate whether differential wavefront sensing, the standard technique employed to control interferometer alignment with Gaussian beams, could be usefully applied to mesa beam instruments. We first presented the theory behind WFS before testing our model using well understood and theoretically manageable spherical mirror resonators. Encouraged by the similarity between numerical output and theory, we designed an experiment based around the predictions of our simulations with mesa beams.

Agreement between the resulting data and our expectations was excellent, with the trends, relative magnitudes and overall behaviour of input and end mirror signals well anticipated. All signals were found to be linear with tilt and zero at optimal alignment. Furthermore, the possibility of differentiating between misalignments of longitudinally separated optical components was demonstrated. These results represent an important step toward closed loop alignment control of non-spherical mirrors for future gravitational wave detectors.

Chapter 4

Thermal effects

Thermal effects are already important in currently operating interferometric gravitational wave detectors.[1] Planned upgrades of these interferometers involve increasing optical power to combat quantum shot noise, leading to commensurately increased thermal perturbations. Absorbed heat will distort the mirror surfaces, changing the structure of the resonant electromagnetic field. In turn this will change the measured thermal noise and potentially reduce the stored power due to scattering of light out of the fundamental arm cavity mode or by degrading the coupling to the injected beam. In this chapter we consider the ramifications of such thermal effects for the mesa beams described in §2.1.

In sections 4.1 and 4.2 we outline the theory underpinning our investigation prior to introducing the simulation methods used in section 4.3. We subsequently study thermally induced perturbations of a single Fabry-Perot cavity in the presence of high circulating power, considering how a thermoelastically distorted test mass affects the intensity profile of the resonant optical mode (§4.4.1). We then evaluate the thermal noise performance of the new eigenmode in section 4.4.3 before discussing possible methods of compensating for the deformed test masses in section 4.5. At each stage we contrast our results with those of a comparable Gaussian cavity.

[1] The LIGO and VIRGO detectors already employ thermal compensation systems to correct some mirrors' radial profiles against thermal effects arising from absorption of stored optical power [153, 154].

4.1 Thermoelastic deformation

We begin our investigation by considering the thermal deformation of the test masses' highly reflective surfaces due to absorption in their dielectric coatings. This calculation may be divided neatly into two parts, the evaluation of the temperature field throughout the test mass arising from absorbed optical power and the determination of the resulting surface displacement. In both cases we follow a well-known approach [100, 155].

Absorption in the input mirror substrates is also generally present and also contributes to the thermoelastic deformation, however this effect is negligible due to the high arm cavity finesse and weak coupling between substrate and coating deformations [156].

4.1.1 Temperature field

In this section we consider the heating of a cylindrical test mass by absorption of laser radiation in its reflective coating. Taking advantage of the problem's axial symmetry we are able to construct an analytical expression for the temperature field $\mathcal{T}$ in the test mass bulk.

Fourier's equation for heat transfer is written in cylindrical coordinates (r, ϕ, z) as

$$\rho C \frac{\partial \mathcal{T}(t, r, \phi, z)}{\partial t} - K_{\mathrm{th}} \nabla^2 \mathcal{T}(t, r, \phi, z) = \varsigma(r), \tag{4.1}$$

where ρ is the mass density, C is the specific heat capacity, K_{th} is the thermal conductivity and $\varsigma(r)$ is the density of power deposited in the material. We seek equilibrium solutions ($\partial \mathcal{T}/\partial t = 0$) for a system with no internal heat sources ($\varsigma = 0$). For an axially symmetric beam (4.1) becomes

$$\nabla^2 \mathcal{T}(r, z) = 0, \tag{4.2}$$

a Laplace equation.

For our purposes the important mechanism of heat transfer is radiation. Conduction through the thin suspension fibres is limited and there is no appreciable convection in vacuum. Thus our boundary conditions are defined by balance of heat fluxes on the test mass surfaces i.e.

$$\vec{n} \cdot [\vec{F} + K_{\rm th} \nabla \mathcal{T}] = 0, \tag{4.3}$$

where $\vec{F}$ is the outward flux, $-K_{\rm th}\nabla\mathcal{T}$ is the inward flux and $\vec{n}$ is the outward pointing surface normal. For thermal radiation alone we have

$$\vec{F} = \sigma'[\mathcal{T}^4 - T_0^4], \tag{4.4}$$

where σ' is the Stefan-Boltzmann constant corrected for emissivity[2] and T_0 is the ambient temperature. In practice the deposited power is small compared to the radiative heat exchange with the thermal bath and the temperature of the test mass does not rise significantly above T_0 ($\Delta T \sim 10$ K). We may thus linearise (4.4) via series expansion about T_0. In this way we obtain

$$\vec{F} \simeq \sigma'[4T_0^3(\mathcal{T} - T_0)] = 4\sigma' T_0^3 T, \tag{4.5}$$

where we have defined $T = (\mathcal{T} - T_0)$. We proceed to solve for T, the temperature rise caused by the beam, knowing that $\mathcal{T}$ may be easily recovered.

For easy comparison with the literature we allow our test mass to occupy the region $r \in [0, a]$, $z \in [-h/2, h/2]$, with the coated surface at $z = -h/2$. With this notation our boundary conditions must be

$$z = h/2 : \qquad -K_{\rm th}\frac{\partial T}{\partial z}(r, h/2) = 4\sigma' T_0^3 T(r, h/2), \tag{4.6}$$

$$z = -h/2 : \qquad -K_{\rm th}\frac{\partial T}{\partial z}(r, -h/2) = \epsilon|\Psi(r)|^2 - 4\sigma' T_0^3 T(r, -h/2), \tag{4.7}$$

$$r = a : \qquad -K_{\rm th}\frac{\partial T}{\partial r}(a, z) = 4\sigma' T_0^3 T(a, z), \tag{4.8}$$

where ϵ is the absorption rate of the coating and $|\Psi(r)|^2$ is the intensity profile of the

[2]Our chosen correction factor is 0.9.

incident optical beam.

We now assume an harmonic *ansatz* of form

$$T(r,z) = J_0(kr)[C_1 e^{kz} + C_2 e^{-kz}], \tag{4.9}$$

where k and the C_i are arbitrary constants and J_i is a Bessel function of the first kind of order i. In attempting to satisfy our final boundary condition (4.8) we find that we must have[3]

$$kaJ_1(ka) - \chi J_0(ka) = 0, \tag{4.10}$$

where χ is the reduced radiation constant $\chi = 4\sigma' T_0^3 a/K_{\text{th}}$. Equations of this form have an infinite number of distinct solutions. Let us define the values of k which yield solutions as members of the set $\{k_m : m \in \mathbb{N}^+\}$. Knowing that k takes discrete values we modify our proposed solution to become the series expansion.

$$T(r,z) = \sum_m [C_{1,m} e^{k_m z} + C_{2,m} e^{-k_m z}] J_0(k_m r). \tag{4.11}$$

It may be shown that the $J_0(k_m r)$ form a complete set. Exploiting this property we can also express our incident beam as a series expansion. Denoting the integrated power in our incident beam by P_0 we may write

$$|\Psi|^2 = P_0 \sum_m p_m J_0(k_m r), \tag{4.12}$$

$$\text{where} \quad p_m = \frac{1}{P_0} \frac{2k_m^2}{(\chi^2 + k_m^2 a^2) J_0^2(k_m a)} \int_0^a |\Psi(r)|^2 J_0(k_m r) r \, \mathrm{d}r. \tag{4.13}$$

Considering the incident beam in this way allows our remaining boundary conditions (4.6) and (4.7) to be set down as purely algebraic expressions for each m

$$(k_m a + \chi) C_{1,m} - (k_m a - \chi) e^{-k_m h} C_{2,m} = 0, \tag{4.14}$$

$$(k_m a - \chi) e^{-k_m h} C_{1,m} - (k_m a + \chi) C_{2,m} = -\epsilon p_m P_0 a e^{-k_m h/2} / K_{\text{th}}, \tag{4.15}$$

[3]It may be useful to recall $\partial J_0(x)/\partial x = -J_1(x)$ and $\partial J_1(x)/\partial x + J_1(x)/x = J_0(x)$.

which are simply solved for $C_{1,m}$ and $C_{1,m}$. Our final solution is given by

$$T(r,z) = \sum_m \theta_m(z) J_0(k_m r), \tag{4.16}$$

$$\text{where} \quad \theta_m(z) = \frac{\epsilon P_0 a}{K_{\text{th}}} p_m \exp(-k_m h/2) \times \frac{(k_m a - \chi)\exp(k_m(z-h)) - (k_m a + \chi)\exp(-k_m z)}{(k_m a + \chi)^2 - (k_m a - \chi)^2 \exp(-2k_m h)}. \tag{4.17}$$

The total power absorbed in the coating is ϵP_0, expected to be of order 1 W for second generation interferometers.

4.1.2 Dini series

This solution in terms of Dini series is particularly well suited to numerical implementation. Our (4.10) may be rapidly solved to find the k_m using Newton's method, as there exists a recurrence relation for finding good initial guesses. Once the first few solutions $x_1, x_2, x_3, \ldots$ have been found, an increasingly accurate initial guess for subsequent solutions x_i is $x_{i-1} + \pi$.

The Dini expansion is also incredibly efficient in reconstructing our incident beam, figures 4.1 and 4.2 demonstrate that excellent fidelity is achieved with few terms. This reconstruction can provide useful guidance in determining how many terms must be considered for the series in (4.16) to converge. In our analysis we took a different approach, unconditionally implementing the first ten terms and adding subsequent terms only if their expansion coefficient was within a factor of 10^{-6} of p_1, the coefficient of the principal term. For unperturbed beams this corresponds to over 80 terms (see fig. 4.3).

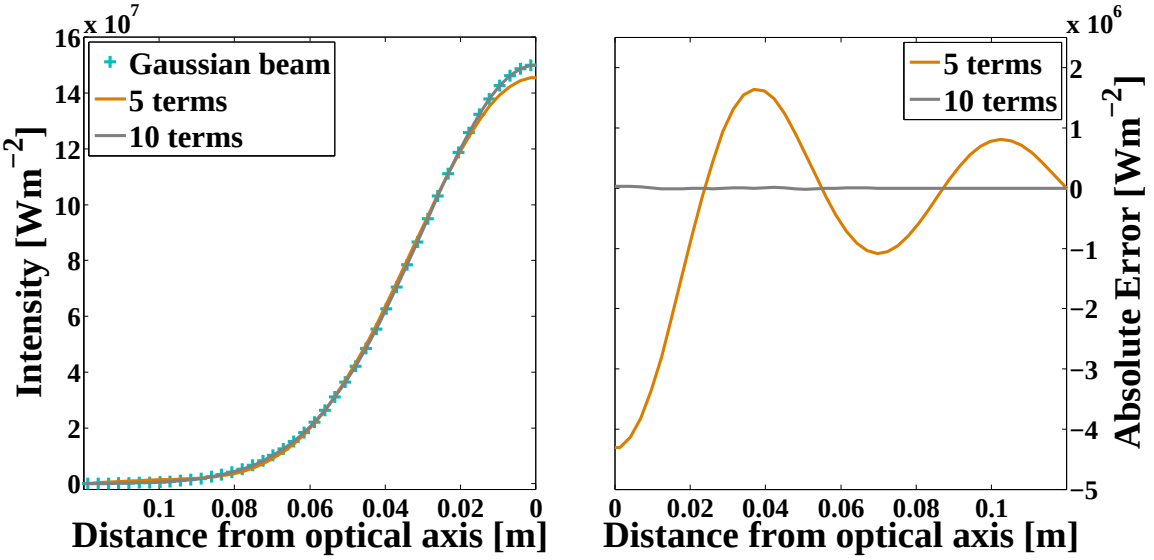

Figure 4.1: Much of the work described herein relies on Dini expansions. Here we show how efficiently the Dini expansion is able to approximate a Gaussian beam. Left: A series representation of the true intensity profile (crosses) using 5 and 10 terms. Right: Absolute error on the reconstruction.

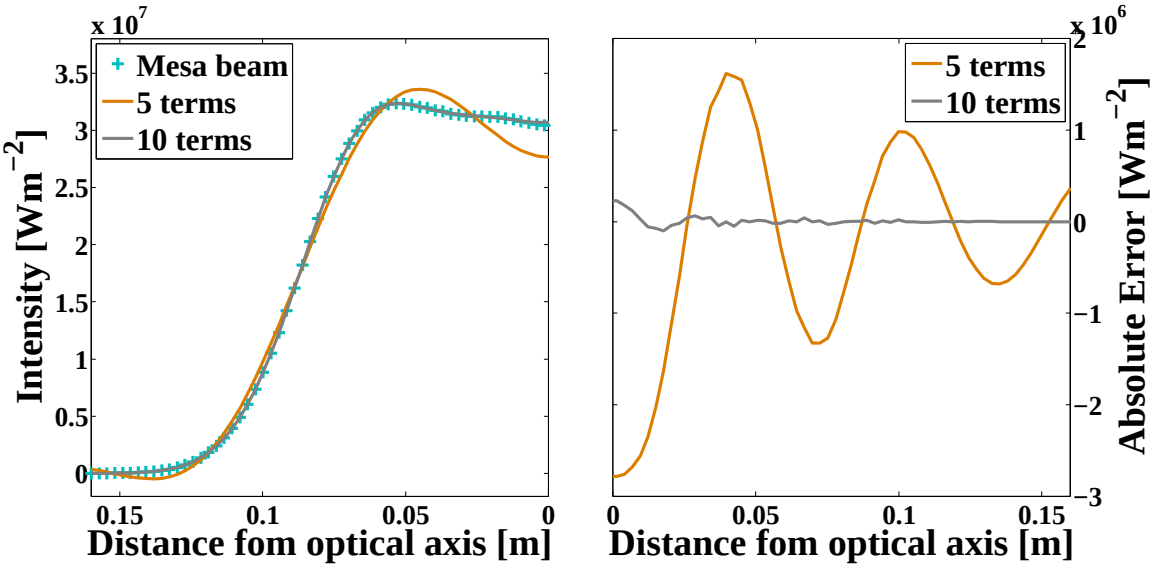

Figure 4.2: The Dini expansion is also able to accurately approximate a mesa beam. Left: A series representation of the true intensity profile (crosses) using 5 and 10 terms. Right: Absolute error on the reconstruction.

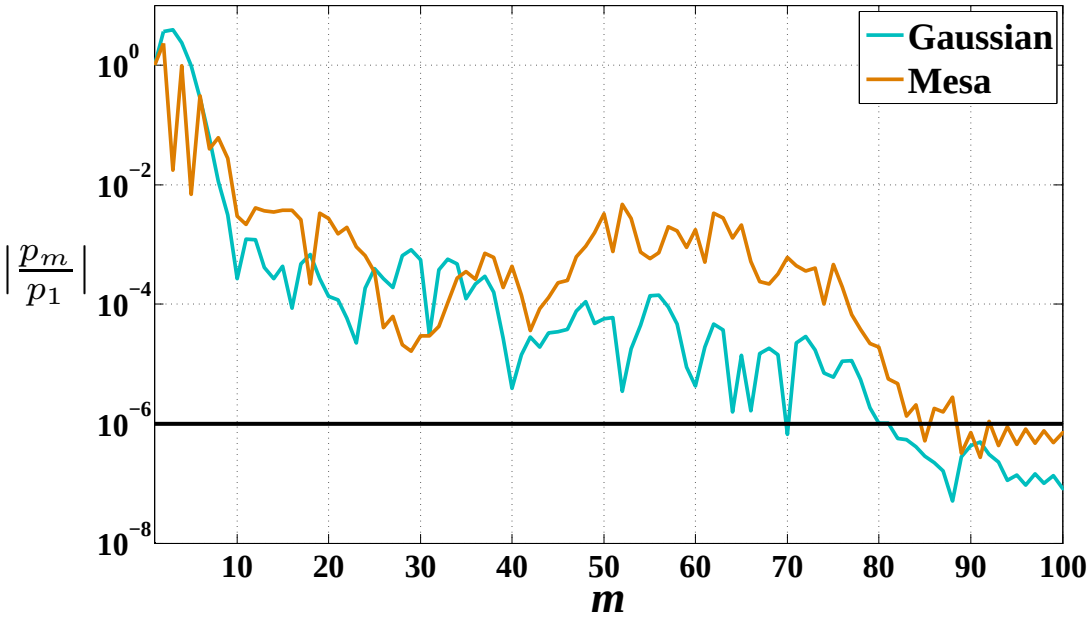

Figure 4.3: Dini expansions are able to reconstruct the incident optical intensity profile with a minimum of terms. In our analysis we incorporate all terms with expansion coefficients greater than 10^{-6} times the first term p_1. For nominal mode shapes this corresponds to more than 80 terms.

4.1.3 Surface displacement

Above we calculated the temperature field throughout the test mass caused by heat absorbed in the mirror's high reflectivity coating. Under the influence of this temperature field the test mass will expand thermoelastically, altering its surface figure. It is important to understand such effects as even small changes to the mirror's shape can have significant consequences for interferometer operations.

The form of Hooke's law applicable in an isotropic solid, such as fused silica, experiencing an additional temperature based stress is [157]

$$\Theta_{ij} = \delta_{ij}(\lambda E - \nu T) + 2\mu E_{ij}, \tag{4.18}$$

where λ and μ are the Lamé coefficients, Θ_{ij} is the stress tensor, E_{ij} is the strain tensor with trace E and ν is the stress temperature modulus.[4] The Lamé coefficients

[4]The stress temperature modulus is related to the linear thermal expansion coefficient α_{th} by

are given by

$$\lambda = \frac{Y\sigma}{(1+\sigma)(1-2\sigma)}, \tag{4.19}$$

$$\mu = \frac{Y}{2(1+\sigma)}, \tag{4.20}$$

where Y is Young's modulus and σ is Poisson's ratio.

In the absence of any external applied forces we must solve the equilibrium equation

$$\partial_j \Theta_{ij} = 0 \tag{4.21}$$

in cylindrical polar coordinates subject to boundary conditions

$$\Theta_{rr}(a,z) = 0, \qquad \Theta_{rz}(a,z) = 0,$$

$$\Theta_{rz}(r,\pm h/2) = 0, \qquad \Theta_{zz}(r,\pm h/2) = 0,$$

representing the absence of net forces or torques on the test mass surface. Gravity and forces from the suspension are neglected.

We begin by assuming a solution for the displacement vector $\vec{u}$ of form

$$u_r(r,z) = \frac{\nu}{2(\lambda+\mu)}\frac{1}{r}\int_0^r T(r',z)r'\,\mathrm{d}r', \tag{4.22}$$

$$u_z(r,z) = \frac{\nu}{2(\lambda+\mu)}\left[\int_{-h/2}^{z} T(r,z')\,\mathrm{d}z' + \Phi(r)\right], \tag{4.23}$$

where $\Phi(r)$ is some unknown function.[5] From this proposed solution we may readily

$\nu = \alpha_{\mathrm{th}}(3\lambda + 2\mu)$.

[5] On inspection one sees that $\Phi(r)$ is indeed our goal, the displacement of the mirror's surface at $z = -h/2$.

calculate the stresses and strains,

$$\begin{aligned}
E_{rr}(r,z) &= \frac{\partial}{\partial r}\, u_r(r,z),\\
E_{\phi\phi}(r,z) &= \frac{u_r(r,z)}{r},\\
E_{zz}(r,z) &= \frac{\partial}{\partial z}\, u_z(r,z),\\
E_{rz}(r,z) &= \frac{1}{2}\left(\frac{\partial}{\partial z}\, u_r(r,z) + \frac{\partial}{\partial r}\, u_z(r,z)\right),\\
\Theta_{rr}(r,z) &= \lambda E(r,z) + 2\mu E_{rr}(r,z) - \nu T(r,z),\\
\Theta_{\phi\phi}(r,z) &= \lambda E(r,z) + 2\mu E_{\phi\phi}(r,z) - \nu T(r,z),\\
\Theta_{zz}(r,z) &= \lambda E(r,z) + 2\mu E_{zz}(r,z) - \nu T(r,z),\\
\Theta_{rz}(r,z) &= 2\mu E_{rz}(r,z),
\end{aligned} \tag{4.24}$$

each of which has only 4 components due to our cylindrical symmetry, and substitute them into (4.21) to find Φ. The harmonic nature of T (see (4.2)) is beneficial throughout this process, allowing great simplifications to be made.

Subsequently applying our boundary conditions, we find that all but $\Theta_{rr}(a,z) = 0$ are immediately satisfied. Closer scrutiny reveals that, for our putative solution, the dependence of $\Theta_{rr}(a,z)$ with z is *almost* linear. Hence the addition of a supplementary stress of form $\Theta_{rr} = C_3 + C_4 z$ will allow almost perfect cancellation.

The corrective displacement

$$\delta u_r(r,z) = \frac{\lambda + 2\mu}{2\mu(3\lambda + 2\mu)}(C_3 r + C_4 r z), \tag{4.25}$$

$$\delta u_z(r,z) = -\frac{\lambda}{\mu(3\lambda + 2\mu)}(C_3 z + C_4 z^2/2) - \frac{\lambda + 2\mu}{4\mu(3\lambda + 2\mu)}(C_4 r^2), \tag{4.26}$$

where C_3 and C_4 are arbitrary constants, satisfies the equilibrium equation and gives $\Theta_{rr} = C_3 + C_4 z$ as desired. It may also be shown that $\Theta_{rz} = \Theta_{zz} = 0$. So by appropriately choosing the constants C_3 and C_4 and adding the correction $\delta\vec{u}$ to $\vec{u}$ we can construct a displacement which satisfies our governing equation and boundary

conditions. By Saint-Venant's principle[6] we can conclude that this displacement well approximates the exact solution everywhere except close to the boundary $r = a$ where we introduced our fictitious additional strain. Since the optical field near this boundary is negligible by design, a solution formed in this way is valid for our purposes.

Our total displacement $\vec{U} = \vec{u} + \delta\vec{u}$ is now completely defined up to a constant vector, historically chosen such that $\vec{U}(0, -h/2) = 0$. Switching from the Lamé coefficients λ and μ to the more intuitive Young's modulus Y and Poisson's ratio σ the final result for the displacement of the mirror's highly reflective surface is

$$U_z(r, -h/2) = \sum_m \Big[u_m(1 - J_0(k_m r))\Big] - \frac{1-\sigma}{2Y} C_4 r^2, \tag{4.27}$$

where the second term is the Saint-Venant correction[7] and the coefficients u_m are given by

$$u_m = \frac{\alpha_{\text{th}}(1+\sigma)\epsilon P_0 a}{K_{\text{th}}} \frac{p_m}{k_m} \frac{k_m a + \chi - (k_m a - \chi)\exp(-2k_m h)}{(k_m a + \chi)^2 - (k_m a - \chi)^2 \exp(-2k_m h)} \tag{4.28}$$

Our constant C_4 is found by minimising $\int_{-h/2}^{h/2} (\Theta_{rr}(a, z) + C_3 + C_4 z)^2 \, \mathrm{d}z$. Whence

$$C_3 = -\frac{1}{h} \int_{-h/2}^{h/2} \Theta_{rr}(a, z) \, \mathrm{d}z, \tag{4.29}$$

$$\begin{aligned} C_4 &= -\frac{12}{h^3} \int_{-h/2}^{h/2} \Theta_{rr}(a, z) z \, \mathrm{d}z, \\ &= -\frac{12\alpha_{\text{th}} Y \chi}{h^3} \frac{\epsilon P_0}{K_{\text{th}} a} \sum_m \frac{p_m J_0(k_m a)}{k_m^4} \frac{1 - k_m h/2 - (1 + k_m h/2)\exp(-k_m h)}{k_m a - \chi + (k_m a + \chi)\exp(-k_m h)}. \end{aligned} \tag{4.30}$$

This series expansion solution provides an economical way of including thermoelastic deformations in our later simulation work (see §4.3). These deformations will alter the intensity profile of the cavity eigenmode, leading to changes in the observed thermal

[6] Quoting [157], "... if the forces acting on a small portion of the surface of an elastic body are replaced by another statically equivalent system of forces acting on the same portion of the surface, this redistribution of loading produces substantial changes in the stresses locally but has a negligible effect on the stresses at distances which are large in comparison with the linear dimensions of the surface on which the forces are changed."

[7] The Saint-Venant correction term was applied with incorrect sign in Vinet's original publication [100].

noise. In the following section we describe how the thermal noise from various sources may be calculated.

4.2 Thermal noise

As discussed previously, test mass thermal noise is expected to limit terrestrial gravitational wave detectors in the frequency band where they are most sensitive. This noise arises through a number of mechanisms and is evident in both the test mass substrates and their highly reflective coatings. In this section we outline how thermal noise in its various forms may be calculated. The approach used is applicable to any azimuthally symmetric beam allowing us to consider both nominal beam shapes and those which have been thermally perturbed.

In the following subsection we show how thermal noise calculations can be distilled into evaluation of the power dissipated in response to an applied oscillatory pressure. This pressure is distinguished by having the same form as the incident beam under study. We subsequently solve the elastic problem to find the test mass's response to this applied pressure, the first step toward quantifying the dissipated power.

The remaining subsections build on these preliminary results, considering the thermal noise resulting from four principal mechanisms. For each mechanism we endeavour to give a readable account of the calculation, presenting governing equations, overall strategies, boundary conditions and complete solutions without labouring the details of each step.

4.2.1 Fluctuation-Dissipation theorem

The Fluctuation Dissipation Theorem (FDT) is a fundamental law of great utility and generality in statistical mechanics which relates the spectra of dissipation and thermal noise in linear systems at equilibrium. By the principle of microscopic reversibility, any

pathway permitting energy to escape from a system must equally provide a route for energy to enter the system. The FDT describes the equilibrium level of this exchange process and thus the average energy in the thermalised system. A form of the theorem was first published by Nyquist in 1928 [158] during his work on electrical systems but it was not until 1951 that Callen and Welton [159] presented the first general proof. Subsequent extensions by Callen himself [160, 161] and Kubo [162] form what we know as the theory today.

For our purposes, the most useful formulation of the theorem is [163]

$$S_q(f) = \frac{k_B T_0}{\pi^2 f^2} \Re[Y(f)], \tag{4.31}$$

where $S_q(f)$ is the spectral density of thermal fluctuations in the variable q, k_B is Boltzmann's constant, T_0 is the ambient temperature and $Y(f) = 1/Z(f)$ is the complex admittance associated with q.

In [65] Levin developed a new formalism for calculating test mass thermal noise by applying the FDT directly to the quantity sensed by the interferometer

$$x(t) = \int f(r,\phi) U_z(r,\phi,t)\, \mathrm{d}r\mathrm{d}\phi. \tag{4.32}$$

Here $f(r,\phi) = |\Psi(r,\phi)|^2/P_0$ is the normalised intensity profile of the incident optical mode in m^{-2} and $U_z(r,\phi,t)$ is the displacement of the mirror's reflective surface. In order to determine the spectrum of thermal fluctuations in x we evaluate $\Re[Y(f)]$ as follows.

Consider applying a generalised force $F(t)$ to the test mass which drives the momentum conjugate to x but no other generalised momenta. The corresponding Hamiltonian is

$$H_{\mathrm{int}} = -F(t)x. \tag{4.33}$$

The physical distribution of this force may be deduced by substituting (4.32) into (4.33)

to find

$$H_{\text{int}} = -\int F(t) f(r,\phi) U_z(r,\phi,t)\, \mathrm{d}r\mathrm{d}\phi, \tag{4.34}$$

clearly the Hamiltonian of a force $F(t)$, with pressure profile $f(r,\phi)$, acting on a mirror with surface displacement $U_z(r,\phi,t)$.

In order to evaluate the coupling between test mass dissipation and our observable x, we apply the generalised force $F(t) = F_0 \cos(2\pi f t)$. This corresponds to applying the physical oscillatory pressure

$$P(r,\phi,t) = F_0 \cos(2\pi f t) f(r,\phi) \tag{4.35}$$

to the reflective surface of the test mass. Our original Hamiltonian (4.33) still holds, hence the average power W_{diss} dissipated in the test mass by our force can be calculated in the usual way

$$W_{\text{diss}} = \langle \Re[F]\Re[\dot{x}] \rangle = \langle \Re[F]\Re[F/Z] \rangle = \langle F_0^2 \cos^2(2\pi f t)\Re[1/Z] \rangle = \frac{1}{2} F_0^2 \Re[Y], \tag{4.36}$$

where $\langle \cdot \rangle$ denotes a time average. Substituting this expression into (4.31) to eliminate $\Re[Y]$, we obtain the following result for the spectral density of thermal displacement noise associated with a single test mass

$$S_x(f) = \frac{2k_B T_0}{\pi^2 f^2} \frac{W_{\text{diss}}}{F_0^2}. \tag{4.37}$$

Levin's direct approach represents a huge advance over previous techniques based on expansions in the space of test mass eigenmodes (e.g. [164, 165]). Foremost it is able to accommodate *inhomogeneous* loss due to coatings, magnets, suspension wire stand-offs, acoustic mode dampers etc. The addition of such items to the test mass can have a large impact on modal Qs but their effect on test mass thermal noise is strongly location dependent, with the noise generally increasing as one moves closer to the incident beam. Estimates based on modal expansion will overestimate dissipation far from the beam spot e.g. magnets glued to the rear surface of the test mass and underestimate loss

close to the beam spot e.g. dielectric coatings.

Modal expansion methods are also computationally taxing. In order to achieve good precision one must determine the Q, frequency and effective mass of $\sim$100 test mass eigenmodes. As we shall endeavour to show in the following section, direct approaches are generally more efficient.

4.2.2 Stresses and strains

Levin [65] informs us that to quantify the spectral density of thermal displacement noise we must simply calculate the average[8] power dissipated $W_{\rm diss}$ in response to an applied oscillatory pressure $P(r,\phi,t)$ with the same spatial distribution $f(r,\phi)$ as the beam under study

$$P(r,\phi,t) = F_0 \cos(2\pi f t) f(r,\phi). \tag{4.38}$$

Thus our task is to quantify $W_{\rm diss}$ for each of the dissipative mechanisms in which we are interested.

In this section, before examining dissipation, we first investigate the stresses and strains in the test mass substrate induced by our applied force. Here we adopt the techniques of Bondu, Hello and Vinet (BHV) [166] subsequently corrected by Liu and Thorne [68]. To facilitate comparison with these publications, our test mass now occupies the region $r \in [0,a]$, $z \in [0,h]$, with the coated surface at $z = 0$. Note that this construction differs from that used previously in §4.1.

In our work we make two approximations:

Quasi-static We immediately ignore the temporal dependence of the oscillatory applied force as the oscillation period of the gravitational wave signals in which we are interested ($\gtrsim$ 1 ms) is far greater than the time taken for a pressure wave to propagate across the test mass ($\sim h/c_{\rm sound} \approx 30\mu$s).

Adiabatic Since the characteristic time scale of diffusive heat flow is several orders of

[8] Over the period $1/f$.

magnitude longer than the pressure-oscillation period, we approximate the oscillations of stress, strain and temperature as adiabatic. N.B. This approximation does not hold for coating thermoelastic noise – there can be substantial heat flow through the thin coating over time scales comparable to the oscillation period.

Under these assumptions we must again solve the equilibrium equation

$$\partial_j \Theta_{ij} = 0, \tag{4.39}$$

subject to the following boundary conditions, representing balance of internal stresses and external pressures at the test mass boundaries,

$$\begin{aligned} \Theta_{rr}(a,z) &= 0 & \Theta_{rz}(a,z) &= 0, \\ \Theta_{zz}(r,h) &= 0 & \Theta_{rz}(r,h) &= 0, \\ \Theta_{rz}(r,0) &= 0 & \Theta_{zz}(r,0) &= -f(r), \end{aligned} \tag{4.40}$$

where $f(r)$ is the form factor of our incident light beam. In what follows we sketch the solution procedure and present important results without dwelling on the minutiae of the calculation.

Excepting two changes, namely the modified boundary condition introduced by our applied pressure and the use of a more familiar form of Hooke's law

$$\Theta_{ij} = \delta_{ij} \lambda E + 2\mu E_{ij}, \tag{4.41}$$

this problem parallels the calculation of thermoelastic deformations in §4.1. This similarity encourages us to adopt a similar solution strategy.

Again we seek a solution in terms of Dini expansions. i.e. we propose solutions of form

$$u_r(r,z) = \sum_m A_m(z) J_1(\eta_m r), \tag{4.42}$$

$$u_\phi(r,z) = 0, \tag{4.43}$$

$$u_z(r,z) = \sum_m B_m(z) J_0(\eta_m r), \tag{4.44}$$

where A_m and B_m are arbitrary functions of z and the η_m are arbitrary constants.

From our supposed solution the stresses and strains may be found using the standard relations in cylindrical coordinates

$$\begin{aligned}
E_{rr}(r,z) &= \frac{\partial}{\partial r} u_r(r,z), \\
E_{\phi\phi}(r,z) &= \frac{u_r(r,z)}{r}, \\
E_{zz}(r,z) &= \frac{\partial}{\partial z} u_z(r,z), \\
E_{rz}(r,z) &= \frac{1}{2}\left(\frac{\partial}{\partial z} u_r(r,z) + \frac{\partial}{\partial r} u_z(r,z) \right), \\
\Theta_{rr}(r,z) &= \lambda E(r,z) + 2\mu E_{rr}(r,z), \\
\Theta_{\phi\phi}(r,z) &= \lambda E(r,z) + 2\mu E_{\phi\phi}(r,z), \\
\Theta_{zz}(r,z) &= \lambda E(r,z) + 2\mu E_{zz}(r,z), \\
\Theta_{rz}(r,z) &= 2\mu E_{rz}(r,z).
\end{aligned} \tag{4.45}$$

Substituting the appropriate quantities into (4.39), the equilibrium equation collapses into a pair of coupled ODEs in A_m and B_m. With the introduction of four new series of arbitrary constants $\alpha_m, \beta_m, \gamma_m, \delta_m$ this system is easily solved, giving expressions for

A_m and B_m

$$\begin{aligned} A_m(z) &= \gamma_m \exp(-\eta_m z) + \delta_m \exp(\eta_m z) \\ &\quad + \frac{\lambda+\mu}{2(\lambda+2\mu)}\eta_m z(\alpha_m \exp(-\eta_m z) + \beta_m \exp(\eta_m z)), \end{aligned} \tag{4.46}$$

$$\begin{aligned} B_m(z) &= \left(\frac{\lambda+3\mu}{2(\lambda+2\mu)}\alpha_m + \gamma_m\right)\exp(-\eta_m z) + \left(\frac{\lambda+3\mu}{2(\lambda+2\mu)}\beta_m - \delta_m\right)\exp(\eta_m z) \\ &\quad + \frac{\lambda+\mu}{2(\lambda+2\mu)}\eta_m z(\alpha_m \exp(-\eta_m z) - \beta_m \exp(\eta_m z)), \end{aligned} \tag{4.47}$$

We now apply the boundary conditions (4.40), expanding our pressure/intensity distribution function $f(r)$ in a Dini series as before

$$f(r) = \sum_m \varrho_m J_0(\eta_m r) \tag{4.48}$$

$$\text{where} \quad \varrho_m = \frac{2}{a^2 J_0^2(\eta_m a)} \int_0^a f(r) J_0(\eta_m r) r \mathrm{d}r. \tag{4.49}$$

The absence of shear on the test mass barrel $\Theta_{rz}(a, z) = 0$ implies that $J_1(\eta_m a) = 0$, defining our η_m. The remaining five boundary conditions combine to provide four additional equations, allowing our four new constants $\alpha_m, \beta_m, \gamma_m, \delta_m$ to be found. Writing $x_m = \eta_m h$ and $q_m = \exp(-2x_m)$, we have

$$\alpha_m = \frac{\varrho_m(\lambda+2\mu)}{\eta_m \mu(\lambda+\mu)} \frac{1 - q_m + 2q_m x_m}{(1-q_m)^2 - 4q_m x_m^2}, \qquad \beta_m = \frac{\varrho_m(\lambda+2\mu)}{\eta_m \mu(\lambda+\mu)} \frac{q_m(1 - q_m + 2x_m)}{(1-q_m)^2 - 4q_m x_m^2},$$

$$\gamma_m = -\frac{\varrho_m}{2\eta_m \mu} \frac{2q_m x_m^2 + \frac{\mu}{\lambda+\mu}(1 - q_m + 2x_m)}{(1-q_m)^2 - 4q_m x_m^2}, \quad \delta_m = -\frac{\varrho_m q_m}{2\eta_m \mu} \frac{2x_m^2 - \frac{\mu}{\lambda+\mu}(1 - q_m + 2x_m)}{(1-q_m)^2 - 4q_m x_m^2}.$$

If not for a necessary but insignificant correction our solution would now be completely constrained; as it stands our work is incomplete.

The BHV paper had been used to guide the design of advanced gravitational wave detectors for more than two years before Liu and Thorne discovered a subtle error (see section A of [68]). To facilitate a solution BHV expanded the applied pressure as a Dini series. In doing so they neglected to include a uniform pressure term in the sum.[9]

[9]The sum is from $m = 1$ to ∞.

Consequently the applied pressure has zero average over the surface of the test mass. To remedy this situation we must add an additional displacement to our proposed solution – that caused by the uniform pressure $F_0/\pi a^2$.

This pressure integrates over the test mass surface to give a force F_0 in the $\hat{z}$ direction. Liu and Thorne noted that such an additional force creates an acceleration $\vec{a} = (F_0/M)\hat{z}$. In the frame of the accelerating test mass all parts of the test mass feel an acceleration equal and opposite to $\vec{a}$, $\vec{g}$ say. Hence the resulting displacement is equivalent to that experienced by a test mass residing in the field $g\hat{z}$ with a uniform pressure on its face to counteract the force due to $\vec{g}$. Solutions to such problems were found [167] and adapted to this situation. Here and henceforth we assume an integrated force of $F_0 = 1$ N, in this case the appropriate corrective displacements are given by

$$\Delta u_r = \frac{\lambda \varrho_0 r}{2\mu(3\lambda + 2\mu)}\left(1 - \frac{z}{h}\right) \tag{4.50}$$

$$\Delta u_\phi = 0 \tag{4.51}$$

$$\Delta u_z = \frac{\lambda \varrho_0 r^2}{4\mu h(3\lambda + 2\mu)} - \frac{(\lambda + \mu)\varrho_0}{\mu(3\lambda + 2\mu)}\left(z - \frac{z^2}{2h}\right) \tag{4.52}$$

where $\varrho_0 = 1/\pi a^2$.

With the addition of this displacement our solution satisfies the equilibrium equation and all of our boundary conditions except that of vanishing radial stress on the barrel $\Theta_{rr}(a, z) = 0$. Inspection reveals that the radial stress is pseudo-linear with zero average. Thus, in the same manner as above (see §4.1.3), it can be almost totally cancelled by the addition of a second displacement $\delta\vec{u}$

$$\delta u_r = \frac{\lambda + 2\mu}{2\mu(3\lambda + 2\mu)}(C_5 r + C_6 r z), \tag{4.53}$$

$$\delta u_\phi = 0, \tag{4.54}$$

$$\delta u_z = -\frac{\lambda}{\mu(3\lambda + 2\mu)}(C_5 z + C_6 z^2/2) - \frac{(\lambda + 2\mu)}{4\mu(3\lambda + 2\mu)} C_6 r^2, \tag{4.55}$$

whose only effect is to produce an extra radial stress $\delta\Theta_{rr}(z) = C_5 + C_6 z$. By minimising

the integral

$$\int_0^h [\Theta_{rr}(a,z) + \delta\Theta_{rr}(z)]^2 \, \mathrm{d}z, \tag{4.56}$$

appropriate values for C_5 and C_6 may be found

$$C_5 = 6\frac{a^2}{h^2}\sum_m \frac{\varrho_m J_0(\eta_m a)}{\eta_m^2 a^2}, \tag{4.57}$$

$$C_6 = \frac{-2C_5}{h}. \tag{4.58}$$

In this way our final boundary condition is satisfied and by Saint-Venant's principle our displacement approximates the exact solution in all areas of interest.

Having highlighted the key features in our approach above, we present the final solution for the displacement in its entirety

$$\begin{aligned} U_r(r,z) &= u_r + \Delta u_r + \delta u_r \\ &= \sum_m A_m(z) J_1(\eta_m r) + \frac{\lambda\varrho_0 r}{2\mu(3\lambda+2\mu)}\left(1-\frac{z}{h}\right) + \frac{\lambda+2\mu}{2\mu(3\lambda+2\mu)}(C_5 r + C_6 r z), \end{aligned} \tag{4.59}$$

$$U_\phi(r,z) = 0, \tag{4.60}$$

$$\begin{aligned} U_z(r,z) &= u_z + \Delta u_z + \delta u_z \\ &= \sum_m B_m(z) J_0(\eta_m r) + \frac{\lambda\varrho_0 r^2}{4\mu h(3\lambda+2\mu)} - \frac{(\lambda+\mu)\varrho_0}{\mu(3\lambda+2\mu)}\left(z - \frac{z^2}{2h}\right) \\ &\quad - \frac{\lambda}{\mu(3\lambda+2\mu)}\left(C_5 z + \frac{C_6 z^2}{2}\right) - \frac{\lambda+2\mu}{4\mu(3\lambda+2\mu)} C_6 r^2. \end{aligned} \tag{4.61}$$

Substituting this solution into (4.45), the stresses and strains throughout the test mass may be found. With this information we can begin to investigate the dissipation associated with various forms of thermal noise.

4.2.3 Substrate Brownian noise

Noise from internal friction, often called Brownian noise, in solids is the thermally excited motion associated with intrinsic internal damping. It manifests itself as a phase shift between applied stress and resultant strain. This effect is quantised by the introduction of a complex elastic modulus $Y = Y_0[1 + j\Phi(f)]$. The key to reducing this internal damping is to choose a substrate material having a small loss angle $\Phi(f)$ or equivalently a high mechanical quality factor.

The time averaged[10] dissipation associated with the imaginary part of the Young's modulus is [68]

$$W_{\text{diss}} = 4\pi f \Phi(f) \langle U \rangle = 2\pi f \Phi(f) U. \tag{4.62}$$

We utilise the usual expression for the energy density per unit volume [167], $\rho_{\text{E}} = \frac{1}{2} E_{ij} \Theta_{ij}$, so that the total elastic strain energy U is

$$U = 2\pi \int_0^h \int_0^a \rho_{\text{E}}(r,z) r \, \mathrm{d}r \, \mathrm{d}z \tag{4.63}$$

$$\text{where} \quad \rho_{\text{E}}(r,z) = \frac{1}{2} \Big(E_{rr}(r,z)\Theta_{rr}(r,z) + E_{\phi\phi}(r,z)\Theta_{\phi\phi}(r,z) + E_{zz}(r,z)\Theta_{zz}(r,z) + 2E_{rz}(r,z)E_{rz}(r,z) \Big).$$

This integral is easily evaluated using the stresses and strains found above. Ignoring any frequency dependence of Φ,[11] (4.37) gives that the spectral density of substrate Brownian noise is:

$$S_x^{SB}(f) = \sqrt{\frac{4k_B T_0}{\pi f} \Phi U} \quad \left[\frac{\text{m}}{\sqrt{\text{Hz}}} \right] \tag{4.64}$$

[10] $\langle X \rangle$ is always equal to $\frac{1}{2}X$ for our sinusoidal forces.

[11] In any case changes will likely be small across the terrestrial gravitational wave detection band.

4.2.4 Substrate thermoelastic noise

Although the test mass is in thermal equilibrium, energy is continually exchanged between it and its surroundings. It is convenient to interpret this fluctuation in energy as a fluctuation in temperature. Since test mass materials exhibit non-vanishing coefficients of thermal expansion, these energy fluctuations give rise to displacements which can dominate the thermal noise for certain substrate materials (e.g. sapphire) [168].

To calculate the impact of this thermoelastic noise we again employ Levin's direct method. The period of the fictitious pressure applied to the test mass is significantly shorter than the characteristic timescale for heat flow in the substrate, so we may assume a quasistatic system in which the temperature evolves adiabatically. Under this condition the standard expression [167] for the rate of thermoelastic dissipation is

$$W_{\rm diss} = \left\langle \int\limits_{\rm test\,mass} \frac{K_{\rm th}}{T_0} (\nabla T)^2 {\rm d}\mathcal{V} \right\rangle, \tag{4.65}$$

where $K_{\rm th}$ is the thermal conductivity, T_0 is the ambient temperature and T is the deviation of the test mass temperature from T_0.

In calculating $T(r,z)$ we exploit the adiabatic and quasistatic approximations outlined above, allowing us to write [167]

$$T = -\frac{\alpha_{\rm th} Y T_0}{C_{\rm v}(1-2\sigma)}\Omega, \tag{4.66}$$

where $\Omega = \nabla \cdot \vec{u} = E_{rr}(r,z) + E_{\phi\phi}(r,z) + E_{zz}(r,z)$. Upon substitution (4.65) becomes

$$W_{\rm diss} = 2\pi K_{\rm th} T_0 \left(\frac{Y \alpha_{\rm th}}{(1-2\sigma) C_{\rm v}} \right)^2 \frac{1}{2} \int\limits_0^h \int\limits_0^a (\nabla\Omega)^2 r {\rm d}r{\rm d}z \tag{4.67}$$

$$\text{and} \quad \therefore S_x^{ST}(f) = \sqrt{\frac{2 k_B T_0 W_{\rm diss}}{\pi^2 f^2}} \quad \left[\frac{\rm m}{\sqrt{\rm Hz}} \right] \tag{4.68}$$

4.2.5 Stresses in the coating

We began our consideration of thermal noise by examining the test mass substrate, however, as we shall soon see, the most significant contribution to displacement noise arises in the test masses' reflective coatings. In order to treat these sources we must understand the stresses and strains in the coating. Fortunately these quantities are simply related to those calculated above [169].

The mirror coatings are comprised of alternating layers of high and low refractive index materials, forming a Bragg reflector. To account for this structure we use compound values for material properties, found using the volumetric averaging operator of Fejer et al. [170]. The average value of the quantity X is given by

$$[X]_{\mathrm{avg}} = \left(\frac{d_{\mathrm{high}\,n}}{d_{\mathrm{high}\,n} + d_{\mathrm{low}\,n}}\right) X_{\mathrm{high}\,n} + \left(\frac{d_{\mathrm{low}\,n}}{d_{\mathrm{high}\,n} + d_{\mathrm{low}\,n}}\right) X_{\mathrm{low}\,n}, \tag{4.69}$$

where $d_{\mathrm{low}\,n}$ and $d_{\mathrm{high}\,n}$ are the thicknesses of the high and low index materials respectively. The Lamé parameters in the coating, λ_{c} and μ_{c} are calculated in this way from (4.19) and (4.20) using compound values for Y and σ.

With the additional subscript c denoting a quantity evaluated in the coating we have

$$\begin{aligned}
E_{rrc}(r,z) &= E_{rr}(r,z),\\
E_{\phi\phi c}(r,z) &= E_{\phi\phi}(r,z),\\
E_{zzc}(r,z) &= \frac{\lambda-\lambda_{\mathrm{c}}}{\lambda_{\mathrm{c}}+2\mu_{\mathrm{c}}}(E_{rr}(r,z)+E_{\phi\phi}) + \frac{\lambda+2\mu}{\lambda_{\mathrm{c}}+2\mu_{\mathrm{c}}}E_{zz}(r,z),\\
E_{rzc}(r,z) &= E_{rz}(r,z),\\
\Theta_{rrc}(r,z) &= (\lambda_{\mathrm{c}}+2\mu_{\mathrm{c}})E_{rr}(r,z) + \lambda_{\mathrm{c}}E_{\phi\phi}(r,z) + \lambda_{\mathrm{c}}E_{zzc}(r,z),\\
\Theta_{\phi\phi c}(r,z) &= \lambda_{\mathrm{c}}E_{rr}(r,z) + (\lambda_{\mathrm{c}}+2\mu_{\mathrm{c}})E_{\phi\phi}(r,z) + \lambda_{\mathrm{c}}E_{zzc}(r,z),\\
\Theta_{zzc}(r,z) &= \Theta_{zz}(r,z),\\
\Theta_{rzc}(r,z) &= E_{rz}(r,z).
\end{aligned} \tag{4.70}$$

4.2.6 Coating Brownian noise

We evaluate the Brownian noise contribution in the coating using a model developed by Harry et al. [169]. This approach assumes that losses occur inside the coating materials themselves, neglecting any contribution from friction between the dielectric layers. As stated for Brownian noise in the substrate, the loss angle is of critical importance. This model allows for the anisotropic layered structure of the coating by defining an equivalent loss angle Φ_{readout} which treats strains parallel and perpendicular to the coating separately.[12] Assuming that the total energy stored in the test mass under the influence of Levin's applied pressure is approximately equal to that stored in the substrate U (see (4.63)), Φ_{readout} is given by

$$\Phi_{\text{readout}} = \Phi_{\text{substrate}} + \frac{\delta U_{||} d}{U}\Phi_{||} + \frac{\delta U_{\perp} d}{U}\Phi_{\perp}, \tag{4.71}$$

where only the second and third terms pertain to the coating noise. Here d is the total coating thickness and $\Phi_{||}$ & $\Phi_{\perp}$ are the loss angles associated with strains parallel and perpendicular to the test mass surface. $\delta U_{||}$ & $\delta U_{\perp}$ are the linear energy densities in the coating at its interface with the substrate and are given by

$$\delta U_{||} = 2\pi \int_0^a r\rho_{\text{E},||}(r)\mathrm{d}r, \tag{4.72}$$

$$\delta U_{\perp} = 2\pi \int_0^a r\rho_{\text{E},\perp}(r)\mathrm{d}r, \tag{4.73}$$

$$\text{where} \quad \rho_{\text{E},||}(r) = \frac{1}{2}\Big(E_{rrc}(r,0)\Theta_{rrc}(r,0) + E_{\phi\phi c}(r,0)\Theta_{\phi\phi c}(r,0)\Big),$$

$$\rho_{\text{E},\perp}(r) = \frac{1}{2}E_{zzc}(r,0)\Theta_{zzc}(r,0).$$

Recalling that d is the total coating thickness, one sees that we assume constant linear energy density throughout the coating and evaluate the total energy stored via expressions of form $U_{\text{coating}} = \delta U_{\text{coating}} d$.

[12] Recent work by Ting Hong at Caltech suggests that alternative representations may be preferable.

As before, $W_{\rm diss} = 2\pi f \Phi_{\rm readout} U$, so that substitution into (4.37) gives the Brownian dissipation in the entire test mass – coating and substrate. The noise due to internal friction in the coating alone is

$$S_x^{CB}(f) = \sqrt{\frac{4k_B T_0}{\pi f} d(\delta U_{||}\Phi_{||} + \delta U_{\perp}\Phi_{\perp})} \quad \left[\frac{\rm m}{\sqrt{\rm Hz}}\right]. \tag{4.74}$$

In the following calculations we take $\Phi_{||} = \Phi_{\perp}$, giving the general formula for completeness only.

4.2.7 Coating thermoelastic noise

As with Brownian noise, thermoelastic noise is present in both the substrate and the coating. If we write the characteristic thermal diffusion length as $L_{\rm diffusion} = \sqrt{K_{\rm th}/2\pi f \rho C}$ we have

$$d \lesssim L_{\rm diffusion} \ll a, w, \tag{4.75}$$

where d is the coating thickness, a is the test mass radius and w is the spot size of the incident beam. These relationships allow one to make two useful simplifications.

The first inequality tells us that inter-layer diffusion effects are only important at frequencies outside the detection band of ground-based interferometers, so that the coating may be well-approximated by a uniform layer having appropriately averaged properties (see (4.69)); the second implies that we only need consider heat flow normal to the coated surface i.e. heat flow is adiabatic in the transverse dimension. In this situation a perturbative approach is useful, we follow the methods of Fejer et al. [170].

We embark on our analysis from a one dimensional (that dimension normal to the coated surface) thermal conductivity equation [171], our goal is to find the thermal field $\mathcal{T}(z,t)$ satisfying

$$\frac{\partial \mathcal{T}_l}{\partial t} - \kappa_l \frac{\partial^2 \mathcal{T}_l}{\partial z^2} = -\frac{Y_l \alpha_{\mathrm{th,l}} T_0}{(1-2\sigma_l) C_{\mathrm{v},l}} \frac{\partial}{\partial t} \sum_{i=1}^{3} E_{0,ii,l}, \tag{4.76}$$

where $\kappa_l = K_{\mathrm{th},l}/C_{\mathrm{v},l}$ is the thermal diffusivity and $E_{0,ii,l}$ is the zeroth order, i-polarised compressional strain.[13] The subscript l denotes either s or c, meaning substrate or coating – we must solve this equation in both regions. Assuming sinusoidal time dependence we may more elegantly write

$$\begin{aligned} j\omega \mathcal{T}_l(z) - \kappa_l \frac{\partial^2 \mathcal{T}_l}{\partial z^2} &= -j\omega \Gamma_l, \\ \text{where} \quad \Gamma_l &= \frac{Y_l \alpha_{\mathrm{th,l}} T_0}{C_{\mathrm{v},l}} \frac{E_l}{1-2\sigma_l}, \\ \text{and} \quad E_l &= \sum_{i=1}^{3} E_{0,ii,l}. \end{aligned} \tag{4.77}$$

As we are averaging the layered structure of the coating we must also devise an average heat equation for the propagation of $\mathcal{T}_c(z)$. Multiplying through (4.77) by $C_{\mathrm{v},l}$ we obtain

$$j\omega C_{\mathrm{v},q} \mathcal{T}_q(z) - \frac{\partial}{\partial z}\left(K_{\mathrm{th},q} \frac{\partial \mathcal{T}_q}{\partial z} \right) = -j\omega C_{\mathrm{v},q} \Gamma_q. \tag{4.78}$$

In this instance the subscript $q = \mathrm{high}, \mathrm{low}$ denotes a quantity evaluated in a high or low index layer. Averaging the first term is trivial; the second and final terms demand deeper thought.

To ensure continuity of heat flux we must have $K_{\mathrm{th,low}} \partial \mathcal{T}_{\mathrm{low}}/\partial z = K_{\mathrm{th,high}} \partial \mathcal{T}_{\mathrm{high}}/\partial z = [K_{\mathrm{th}} \partial \mathcal{T}/\partial z]_{\mathrm{avg}}$. Defining the average thermal conductivity $K_{\mathrm{th,c}}$ by writing the average heat flux as

$$K_{\mathrm{th,c}} \left[\frac{\partial \mathcal{T}_c}{\partial z} \right]_{\mathrm{avg}} = \left[K_{\mathrm{th}} \frac{\partial \mathcal{T}}{\partial z} \right]_{\mathrm{avg}} \tag{4.79}$$

and solving for $K_{\mathrm{th,c}}$, we discover

$$K_{\mathrm{th,c}}^{-1} = [K_{\mathrm{th}}^{-1}]_{\mathrm{avg}}. \tag{4.80}$$

[13] i.e. that strain due to the applied Levin force.

We are now in a position to write the averaged form of (4.77) as

$$j\omega\mathcal{T}_{\mathrm{c}}(z) - \kappa_{\mathrm{c}}\frac{\partial^2\mathcal{T}_{\mathrm{c}}}{\partial z^2} = -j\omega\Gamma_{\mathrm{c}}, \tag{4.81}$$

where the averaged coating properties are given by

$$C_{\mathrm{v,c}} = [C_{\mathrm{v}}]_{\mathrm{avg}}, \quad \kappa_{\mathrm{c}} = \frac{K_{\mathrm{th,c}}}{C_{\mathrm{v,c}}} \tag{4.82}$$

$$\text{and} \quad \Gamma_{\mathrm{c}} = \frac{[C_{\mathrm{v}}\Gamma]_{\mathrm{avg}}}{C_{\mathrm{v,c}}} = \frac{1}{C_{\mathrm{v,c}}}\left[\frac{Y\alpha_{\mathrm{th}}T_0E}{1-2\sigma}\right]_{\mathrm{avg}}. \tag{4.83}$$

In order to average the final term of (4.81) we must evaluate E_{avg}. We may write E_l as linear combination of two solutions, one having $\Theta_0(r) = \Theta_{zz}(r,0) = 0$ and a specified in-plane strain $E_0(r) = 1/2[E_{rr}(r,0) + E_{\phi\phi}(r,0)]$ and a second with vanishing in-plane strain ($E_0 = 0$) and specified normal stress $\Theta_0(r)$ [170] i.e.

$$E_l = \frac{2(1-2\sigma_l)}{1-\sigma_l}E_0(r) + \frac{(1-2\sigma_l)(1+\sigma_l)}{1-\sigma_l}\frac{1}{Y_l}\Theta_0(r). \tag{4.84}$$

Expressing the elastic fields in this way we see that

$$\Gamma_{\mathrm{s}}(r) = \frac{T_0}{C_{\mathrm{v,s}}}\left(\frac{2Y_{\mathrm{s}}\alpha_{\mathrm{th,s}}}{1-\sigma_{\mathrm{s}}}\right)E_0(r) + \left(\frac{(1+\sigma_{\mathrm{s}})\alpha_{\mathrm{th,s}}}{1-\sigma_{\mathrm{s}}}\right)\Theta_0(r). \tag{4.85}$$

We may now easily apply our averaging operator to obtain the average fields in the coating and thus Γ_{c}

$$\Gamma_{\mathrm{c}}(r) = \frac{T_0}{[C_{\mathrm{v}}]_{\mathrm{avg}}}\left[\frac{2Y\alpha_{\mathrm{th}}}{1-\sigma}\right]_{\mathrm{avg}}E_0(r) + \left[\frac{(1+\sigma)\alpha_{\mathrm{th}}}{1-\sigma}\right]_{\mathrm{avg}}\Theta_0(r). \tag{4.86}$$

All that remains is to solve (4.77) and (4.81) in the apposite regions subject to appropriate boundary conditions. We enforce the following

$$\mathcal{T}_{\mathrm{c}}|_{z=d} = \mathcal{T}_{\mathrm{s}}|_{z=d}, \qquad K_{\mathrm{th,c}}\left.\frac{\partial\mathcal{T}_{\mathrm{c}}}{\partial z}\right|_{z=d} = K_{\mathrm{th,s}}\left.\frac{\partial\mathcal{T}_{\mathrm{s}}}{\partial z}\right|_{z=d},$$

$$\left.\frac{\partial\mathcal{T}_{\mathrm{c}}}{\partial z}\right|_{z=0} = 0, \qquad \left.\frac{\partial\mathcal{T}_{\mathrm{s}}}{\partial z}\right|_{z=h} = 0,$$

i.e. continuity of temperature and flux across the coating-substrate boundary and van-

ishing heat flux at the surfaces of the test mass.[14]

Equations (4.77) and (4.81) are simply solved with general solutions given by

$$\mathcal{T}_l = -\Gamma_l + C_{1,l}e^{\gamma_l z} + C_{2,l}e^{-\gamma_l z}, \tag{4.87}$$

where again the subscript l denotes substrate or coating and $\gamma_l = (1+j)\sqrt{\pi f/\kappa_l}$ is the complex propagation constant of the damped thermal waves. Application of our boundary conditions defines the constants $C_{1,\mathrm{s}}, C_{2,\mathrm{s}}, C_{1,\mathrm{c}}, C_{2,\mathrm{c}}$ to be

$$C_{1,\mathrm{s}} = \frac{K_{\mathrm{th,c}}\gamma_{\mathrm{c}}e^{\gamma_{\mathrm{s}}d}(e^{2\gamma_{\mathrm{c}}d}-1)(\Gamma_{\mathrm{c}}-\Gamma_{\mathrm{s}})}{D}, \tag{4.88}$$

$$C_{2,\mathrm{s}} = C_{1,\mathrm{s}}e^{2\gamma_{\mathrm{s}}h}, \tag{4.89}$$

$$C_{1,\mathrm{c}} = \frac{K_{\mathrm{th}}\gamma_{\mathrm{s}}e^{\gamma_{\mathrm{c}}d}(e^{2\gamma_{\mathrm{s}}d}-e^{2\gamma_{\mathrm{s}}h})(\Gamma_{\mathrm{c}}-\Gamma_{\mathrm{s}})}{D}, \tag{4.90}$$

$$C_{2,\mathrm{c}} = C_{1,\mathrm{c}} \tag{4.91}$$

$$\begin{aligned}\text{where}\quad D = {} & e^{2\gamma_{\mathrm{s}}h}(K_{\mathrm{th,c}}\gamma_{\mathrm{c}} - K_{\mathrm{th}}\gamma_{\mathrm{s}}) - e^{2(\gamma_{\mathrm{c}}+\gamma_{\mathrm{s}})d}(K_{\mathrm{th,c}}\gamma_{\mathrm{c}} - K_{\mathrm{th}}\gamma_{\mathrm{s}}) + \\ & e^{2\gamma_{\mathrm{s}}d}(K_{\mathrm{th,c}}\gamma_{\mathrm{c}} + K_{\mathrm{th}}\gamma_{\mathrm{s}}) - e^{2\gamma_{\mathrm{c}}d+2\gamma_{\mathrm{s}}h}(K_{\mathrm{th,c}}\gamma_{\mathrm{c}} + K_{\mathrm{th}}\gamma_{\mathrm{s}}),\end{aligned} \tag{4.92}$$

completely defining $\mathcal{T}_s$ and $\mathcal{T}_{\mathrm{c}}$.

Using the standard expression of (4.65) with $T = \mathcal{T}$ we can compute W_{diss} as follows[15]

$$W_{\mathrm{diss}} = \frac{1}{2}\left(\frac{K_{\mathrm{th,c}}}{T_0}2\pi\int_0^d\int_0^a |\nabla\mathcal{T}_c|^2 r\mathrm{d}r\mathrm{d}z + \frac{K_{\mathrm{th}}}{T_0}2\pi\int_d^h\int_0^a |\nabla\mathcal{T}_s|^2 r\mathrm{d}r\mathrm{d}z\right) \tag{4.93}$$

Although we integrate over the entire test mass we are calculating coating thermoelastic noise only – we use the zeroth order fields at the surface as the source term in both regions. For the final time we note that

$$S_x^{CTE}(f) = \sqrt{\frac{2k_BT_0}{\pi^2 f^2}W_{\mathrm{diss}}} \quad \left[\frac{\mathrm{m}}{\sqrt{\mathrm{Hz}}}\right]. \tag{4.94}$$

[14]We assume a mirror of finite thickness, rather than the infinite half-plane Fejer studies. The substrate is so much thicker than the coating that this leads to no quantitative difference in the result.

[15]This step represents a departure from the methods of [170].

4.3 Simulation

In order to gauge the impact of thermal effects in future interferometers having mesa beams a series of simulations were undertaken. The goal of this work was to find the intensity distribution of the thermally perturbed cavity eigenmodes as a function of coating absorption and to estimate the resulting thermal noise measured by a kilometre scale gravitational wave detector.

Here we give details of the systems investigated and the techniques employed in obtaining the thermally distorted modes. For more details on the simulation tools themselves and the FFT method in general please see §1.6.

Two cavities supporting non-Gaussian mesa beams were considered; one nearly flat, the other nearly concentric (see sections 1.5.2.3 and 2.1). As a foil to these cases we also examined a nearly concentric spherical cavity supporting well-known Gaussian modes. Each mirror of this cavity had a 2076 m radius of curvature. All three cavities had a length of 4 km. These parameters are representative of an arm cavity in a second generation gravitational wave detector.

The choice of where to convert from Gaussian to mesa beams is not obvious. In this investigation we assumed that the interferometer arm cavity will be driven by a Gaussian field. We assigned to this input beam an integrated power of 1070 W, a value considered for AdvLIGO.

For each cavity the input beam parameters were chosen to yield optimal coupling to the unperturbed or 'cold' cavity. Hence, the spot size of the incident Gaussian differed among the three cavity configurations: For the spherical mirror cavity it was 6 cm to match the mode resonating in the unperturbed cavity. For the mesa beam cavities the input spot size was 8.4 cm in the flat case and 8.2 cm for the concentric system, to optimise the coupling to the unperturbed cavity's mesa beam mode. This optimised coupling was 95% in both cases. Thus the circulating power in the unperturbed mesa cavities was only 808 kW in contrast to 850 kW achievable in the perfectly matched

Gaussian case.[16] The chosen injection beam remained fixed for all calculations in each case.

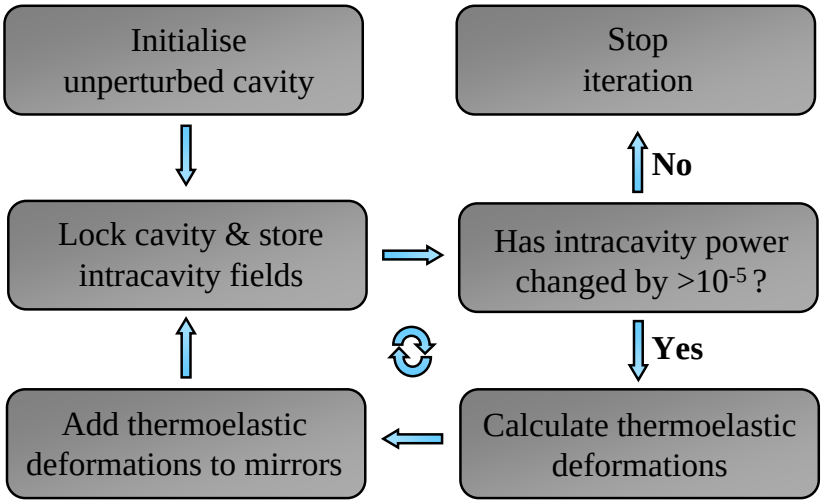

Figure 4.4: Flowchart detailing the iteration procedure used to find static self-consistent intracavity fields and the thermoelastic deformations they produce.

In this study we sought static, self-consistent solutions of the optical fields and thermal deformations using the following procedure: Starting with an unperturbed cavity and no stored optical power, a field is injected through the input mirror and the fields throughout the cavity propagated and updated. These fields are re-propagated and updated iteratively until the stored intracavity power is stable to one part in 10^5 between successive iterations.[17] We then calculate the thermoelastic distortion of the mirror surfaces for the intracavity mode shape and power obtained and some assumed mirror coating absorption (see §4.1). This distortion is then added to the mirror phase profile and the optical simulation restarted with no stored intracavity power. Again we seek a stable optical solution, but generally with a different mode shape and stored power due to the added thermal perturbation. The thermoelastic effect of this new intracavity optical field is applied to the mirrors and the procedure of finding new optical fields and deformations repeated until the stored intracavity power is stable

[16]Thermorefractive aberrations will also be present in the input mirror substrate (see §4.6), but these have been ignored in this study so as to better understand the cavity effects.

[17]The cavity is also simultaneously 'locked' by altering the longitudinal position of the ETM to maintain resonance.

between these larger distortion iterations to within one part in 10^5. This process is summarised in figure 4.4.

We found that for low coating absorption rates convergence was achieved within 10 iterations; with greater absorbed power convergence was slower. In some high absorption cases numerical oscillations between distinct optical modes and thermal distortions were observed. These problems were easily overcome by implementing a simple bisection procedure, averaging the perturbation of successive iterations (see figure 4.5).

These convergence issues are numerical rather than physical. They arise from our instantaneous approach to a system that exhibits thermal lag. Our model treats the thermal response of the mirror as being comparably rapid to the optical buildup within the cavity. In reality the cavity response is many orders of magnitude faster and the optical field adapts nearly instantaneously to the thermal deformation of the mirror, but not vice-versa.

Nevertheless we believe that our result represents the true physical solution. If we reduce our 'step size' adding only a small portion of the mirror perturbation (reality being the limit of infinitesimal step size) we arrive at the same equilibrium but with much slower convergence.

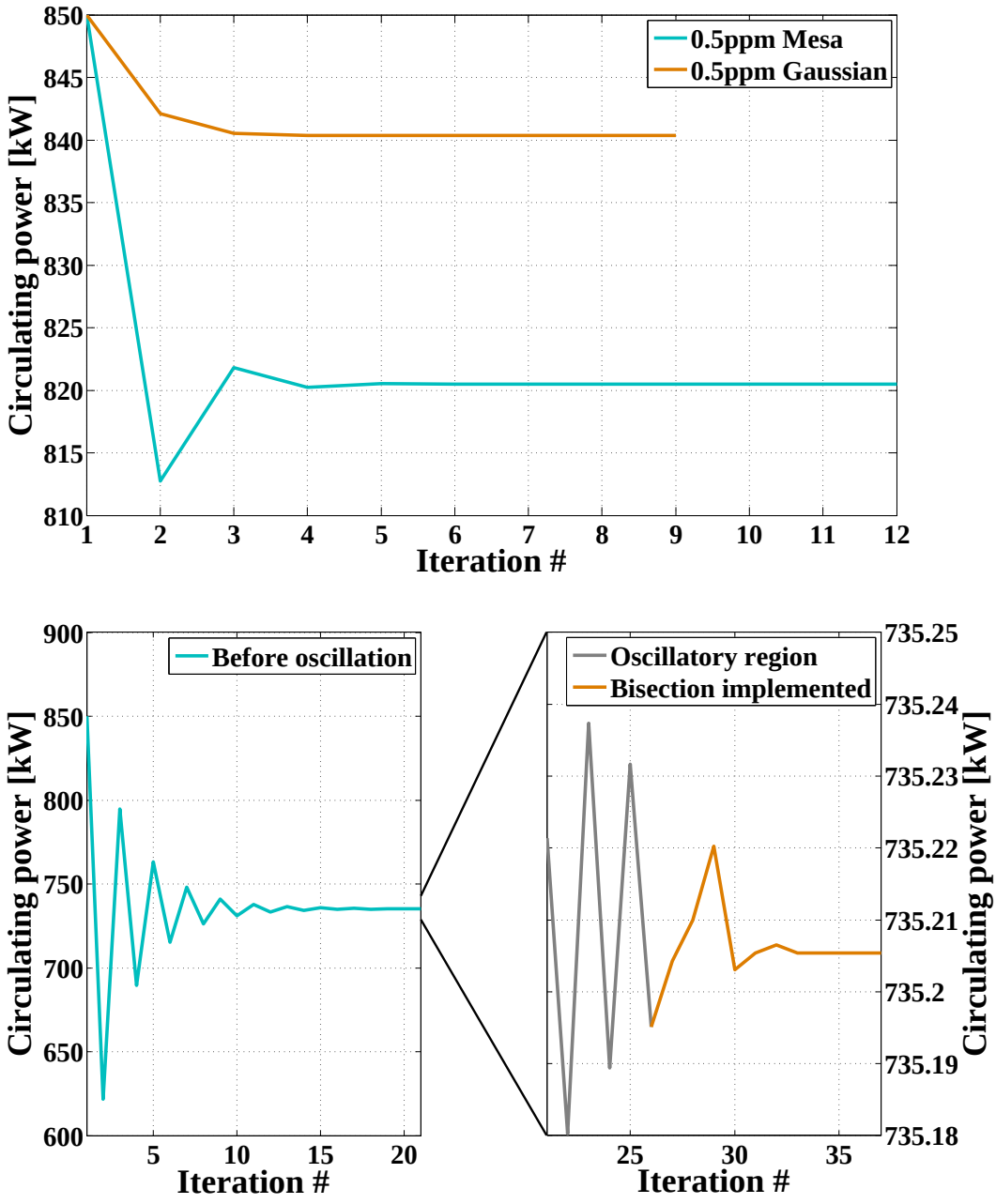

Figure 4.5: Top: Intracavity power as a function of iteration number for 0.5 ppm absorption. Convergence is achieved within 10 iterations in the Gaussian case; the mesa system requires 15 refinements. At higher absorption rates low level numerical oscillations were found. A simple bisection algorithm was implemented and rapid convergence achieved. The bottom panes demonstrate this in the flat mesa beam case for 2.5 ppm absorption. Bottom left: Gross convergence is achieved within 20 iterations. Bottom right: On closer inspection a low level numerical oscillation is present. Convergence is expedited by our bisection algorithm. To allow for easy comparison of different systems, the mesa intracavity powers have been normalised such that unperturbed mesa and Gaussian cavities store the same power. In reality the power stored in the mesa cavity is somewhat lower.

4.4 Results

4.4.1 Thermoelastic deformation and resultant mode shape

The left hand column of figure 4.6 shows the steady state thermoelastic perturbations of both mesa and Gaussian cavity mirrors. The shapes of the deformations are strongly dependent on the thermal gradients imposed by the beam. At low power levels flat and concentric mesa beams induce similar thermoelastic deformations; as greater power is absorbed the concentric beam tends toward a more Gaussian intensity profile and hence gives rise to the larger deformations typical of Gaussian beams. Flat mesa beams retain their greater width under thermal loading and produce deformations around 50% smaller than equivalent Gaussian modes. This is consistent with the general results of Vinet [100] and is due to the more even deposition of heat into the mirror. The thermal deformation due to the mesa beams also more closely resembles a pure radius of curvature change, which may be easier to correct.[18]

Although the shapes of the thermal distortions are of interest, the change in the structure of the resonant light field has greater impact on the performance of the interferometer. The right-hand column of figure 4.6 shows the effects of the thermal deformations on the cavity eigenmode. The Gaussian beam is fairly robust in its functional form as the absorbed power increases. For small amounts of heating the spot size on the mirrors decreases as the thermoelastic bump effectively increases the mirrors' radii of curvature, making the cavity more stable. The stored power, as we show in the next section (table 4.1), does not substantially decrease until the absorbed power becomes relatively large.

The mesa beam cavities, on the other hand, undergo striking changes. The flat mesa beam deforms into a more annular shape, even under modest heat loads, whilst the overall width of its intensity profile changes little. This is likely due to confinement of the optical field by the mirror's steep rim, which is relatively immune to thermal dis-

[18] For example, by heating the rear faces of the test masses, an approach clearly better suited to the end test masses of gravitational wave detectors.

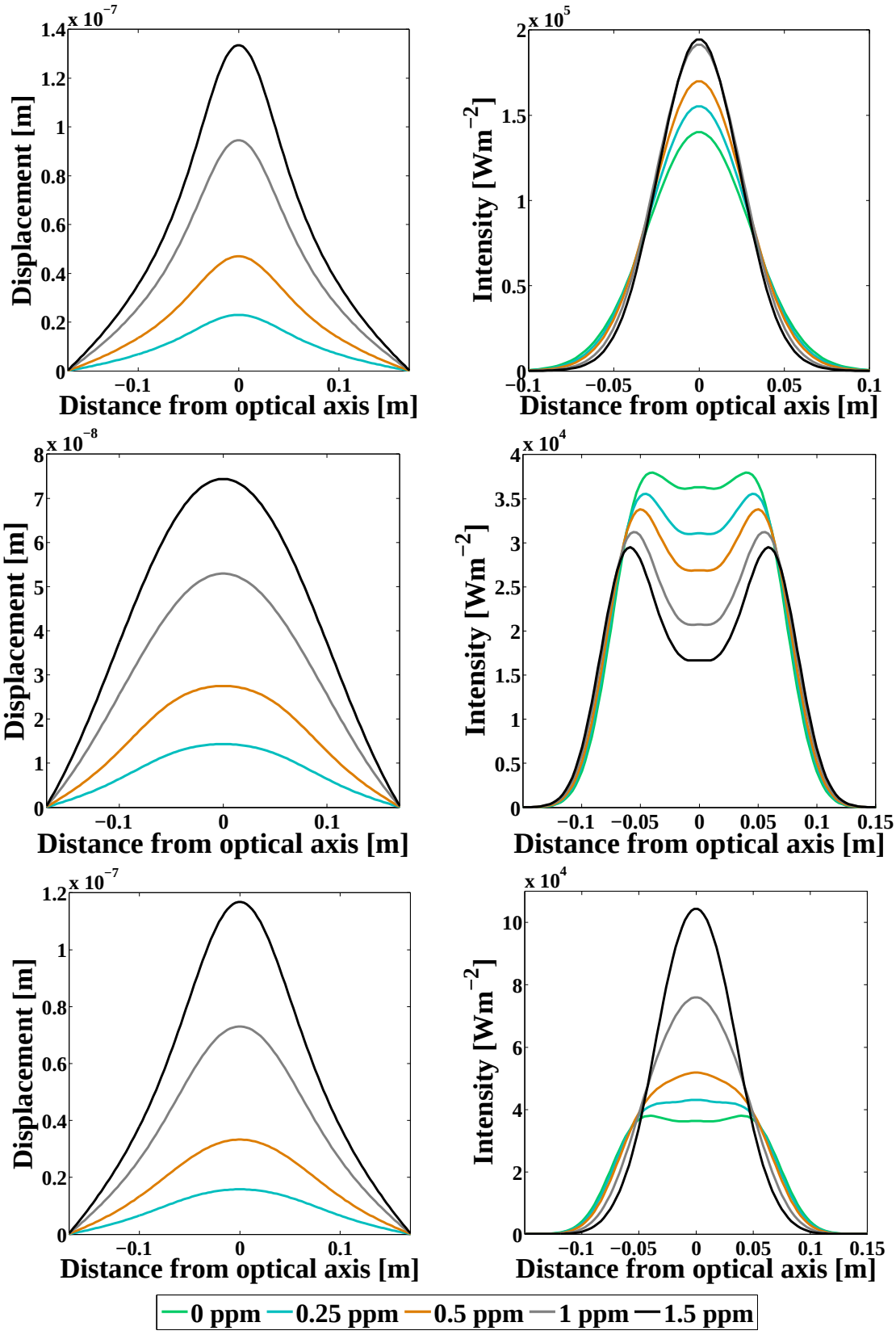

Figure 4.6: Thermoelastic deformation (left) and resonant mode shape (right) as a function of coating absorption. Top row: spherical cavity; middle row: flat mesa cavity; bottom row: concentric mesa cavity.

tortions. The concentric mesa beams are also grossly deformed but instead of retaining their width these beams become strongly peaked.

This differing behaviour may be understood by considering the profiles of the two mesa mirrors (see fig. 2.4). Both mirrors are only a small deviation away from optics which support Gaussian modes. The flat mesa mirror is realised by *adding* a small deviation to a flat surface; the concentric mirror is constructed by *subtracting* the same small deviation from a spherical surface. Thermal effects *add* a small perturbation to the existing mirror profile making the flat mirror less flat and the concentric mirror more spherical. Hence these effects will tend to push the concentric mesa mirror toward supporting narrower beams whilst the flat mesa mirror should be more resilient.

It is known that unstable cavities can show similar changes in their optical fields when the microscopic length of the cavity is changed [172]. In our case this effect was ruled out. Sweeping the cavity length by many linewidths around the lock point, no change in mode shape was observed. We also found that peak power build up was achieved at the lock point found by SIS (see §1.6.2).

4.4.2 Losses

Given the need for very high circulating light power, losses are significant even at the part per million level. In a power recycled interferometer (see §1.2.3) recycling gain is inversely proportional to the losses in the FPM.[19] Arm cavity losses of a few parts per million can, depending on finesse, translate into losses of a few percent in the FPM, reducing recycling gain and circulating power considerably.

Further, depending on the optical design margin, unforeseen losses can alter the coupling of the recycling mirror-FPM cavity, a serious issue for any interferometer control scheme.

In table 4.1 we present a summary of diffraction and mode matching losses as a function

[19] Assuming negligible loss in the power recycling mirror itself.

of coating absorption.

Table 4.1: Cavity gain and diffraction losses as a function of coating absorption.

Cavity	Coating Absorption ppm	Cavity Gain	Diffraction Loss ppm	Mode Matching Loss %
Gaussian	0	795	0.43	0
	0.25	792	0.19	< 1
	0.5	786	1.16	1
	1	755	32.42	4
	1.5	689	189.32	7
Flat Mesa	0	755	0.48	5
	0.25	747	0.80	6
	0.5	737	1.37	7
	1	717	3.20	10
	1.5	697	6.63	12
Concentric Mesa	0	756	0.49	5
	0.25	763	0.33	4
	0.5	768	0.29	3
	1	764	0.76	4
	1.5	733	6.12	8

We derive the dominant mode coupling loss from a comparison between the theoretical intracavity power and that which is recorded in simulation. Once diffraction effects are accounted for, we assign the residual loss to mode coupling error, in doing so we ignore other loss mechanisms such as scatter and absorption. The values obtained using this method are in excellent agreement with those calculated directly from the inner product of the intracavity and injected fields. One could envisage mitigating these losses via thermal compensation in the recycling cavity. Such ideas are not discussed in this work.

Cavity round trip power loss which cannot be attributed to the finite mirror reflectivities alone is ascribed to diffraction loss. The quoted numbers represent a complete round trip; losses per bounce are half as large. Our values for the unperturbed cavities are in accord with the literature [105, 173]. To our knowledge the results for perturbed cavities are the first to be published.

4.4.3 Thermal noise

Non-Gaussian beams, including mesa beams, are being studied theoretically and experimentally as they are expected to reduce test mass thermal noise in interferometric gravitational wave detectors [107, 109, 117, 174]. Thermoelastic distortion of the cavity mirrors changes the intensity profile of the cavity mode and thus alters the expected thermal noise.[20]

It has been shown that a thermally perturbed spherical cavity continues to support a nearly Gaussian beam [175], the main consequence of moderate heating is that the beam waist shrinks, increasing total thermal noise by around 10%. Thermal effects in non-Gaussian cavities are less well understood. Using the techniques outlined in §4.2, the thermal noise expected from our thermally perturbed eigenmodes (see fig. 4.6) was determined. Our findings are presented below.

Fig. 4.7 shows the thermal displacement noise arising from four different sources as a function of coating absorption. All values were evaluated at 100 Hz for a cylindrical fused silica substrate (34 cm $\varnothing \times 20$ cm tk.) and silica-tantala quarter wave coating.

Fig. 4.8 shows how these noise effects sum in an interferometric detector with Fabry-Perot arms. The total equivalent strain noise is evaluated as $\sqrt{4\sum_i N_i^2}/L$, where L is the length of the arm cavity and each N_i represents the displacement noise arising from a single mechanism. Our calculation assumes that all four cavity mirrors have the same coating and hence overestimates the total thermal noise.[21]

As expected the thermal noise associated with the Gaussian and concentric mesa beams increases with absorbed power as the beam waist shrinks; the effects of beam size on thermal noise are well documented [166, 73, 113, 168, 170]. Conversely, the noise of the thermally perturbed flat mesa beam decreases under the same conditions.[22] This effect is less intuitive and is likely due to the small increase in beam width under heating. The

[20] Strictly speaking, thermoelastic distortion is also associated with increased thermal noise by virtue of the extra heat in the mirror. We ignore this effect here.

[21] The ITMs have lower reflectivity, thinner coatings contributing less dissipation.

[22] An effect verified by finite element methods.

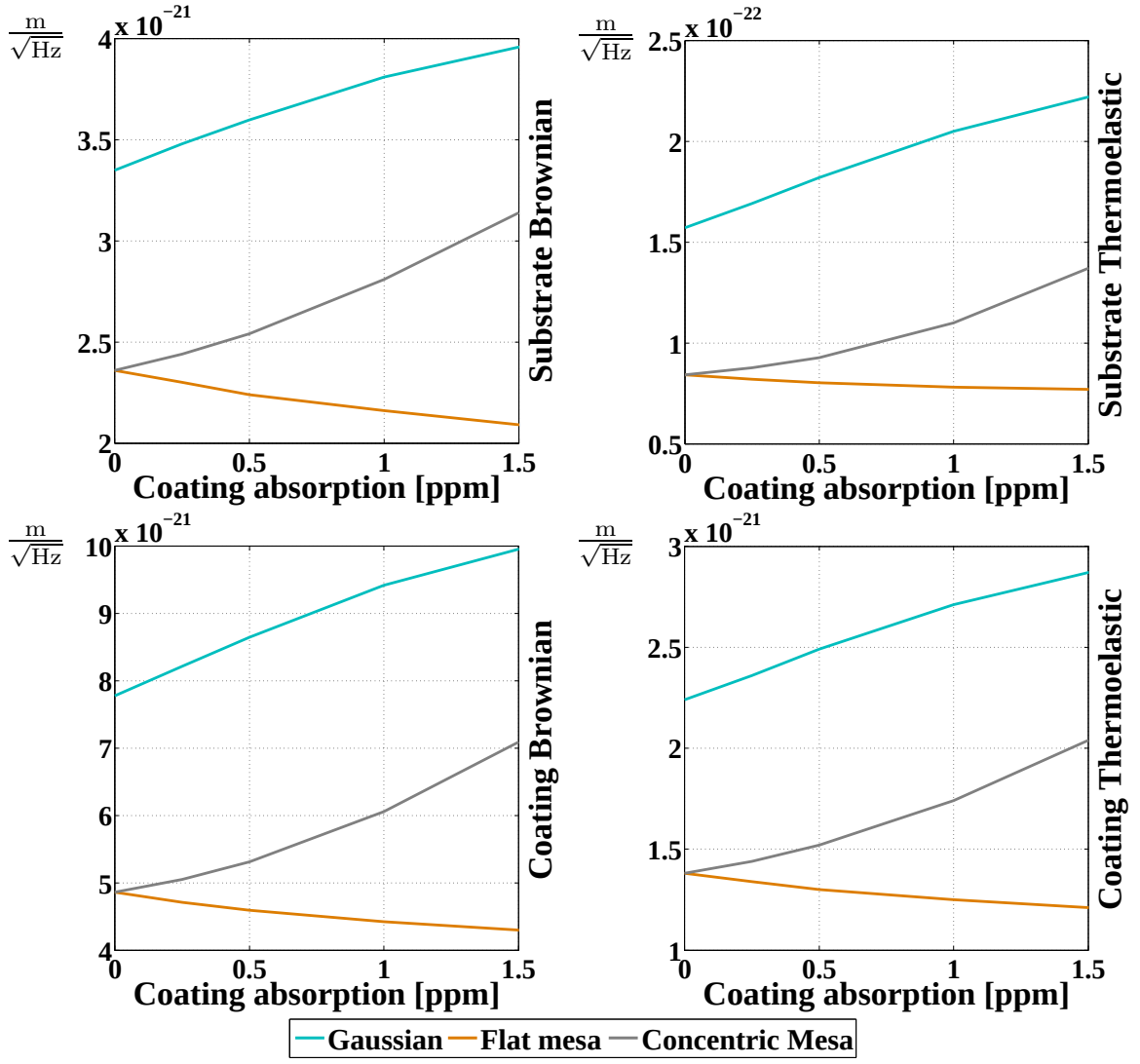

Figure 4.7: Thermal displacement noise as a function of coating absorption for a single test mass.

width of flat mesa beams is modified only very slowly with heating, a fact reflected in the shallower gradients seen in figures 4.7 and 4.8. Note that these results are a strong function of the material parameters used in their evaluation, for a complete listing of the values used see Appendix A.

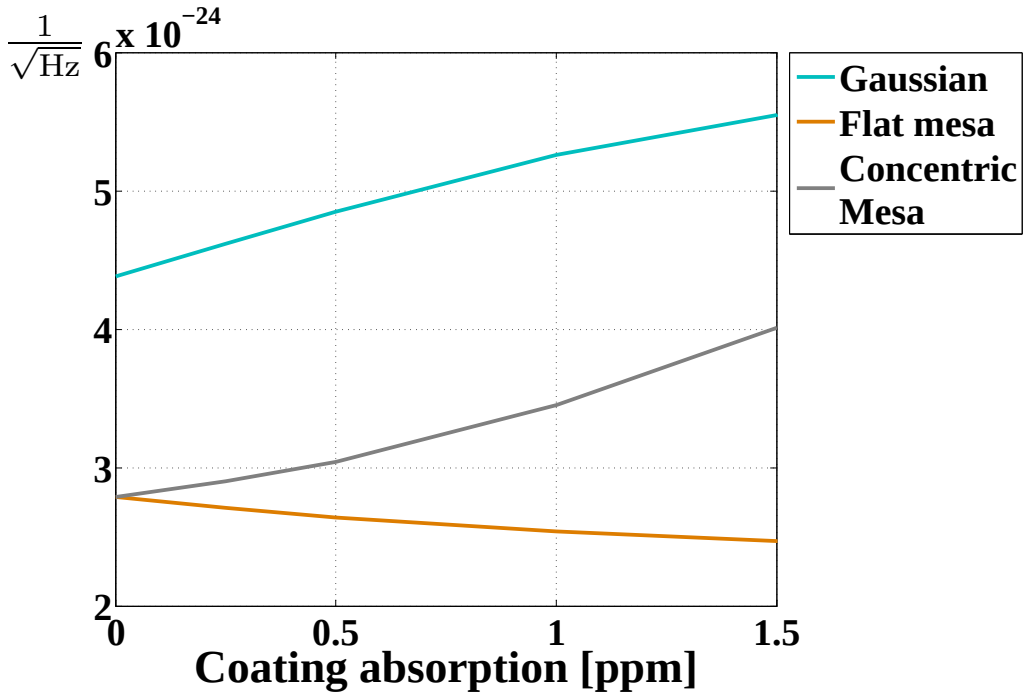

Figure 4.8: Total equivalent strain noise as a function of coating absorption.

4.5 Passive thermal compensation system

Although thermoelastic effects may reduce the thermal noise associated with flat mesa beams, the modes which produce these reductions would simultaneously impair the sensitivity of any detector, as they have a poor coupling to the Gaussian modes outside the interferometer's arms. We must maintain the standard mesa mode even if the thermal noise will be greater.[23]

The Mexican hat mirrors which support mesa beams are constructed using a multi-step silica deposition process over a micro-polished flat substrate (see §2.2.1.1 and [176]). Currently this technique can achieve up to 2 nm precision and is able to create almost any mirror profile desirable in a full scale interferometric detector at no additional cost.

Exploiting this technology, we resolved to design a mirror which only achieves the correct figure after thermoelastic deformation caused by the impinging optical power. This approach would reduce the compensation required from (and hence noise introduced

[23]It is of course possible to devise a scheme whereby gravitational wave readout is effected by injecting a suitable mode at the output port of the interferometer.

by) external sources such as a carbon dioxide laser or ring heater.[24]

4.5.1 Method

Using the methods described in §4.1 we are able to find the thermoelastic deformation caused by an almost arbitrary intensity profile. Such perturbations are easily incorporated into our optical simulations to find the eigenmode of the thermally perturbed cavity. The self-correcting mirror profile, supporting the nominal cavity eigenmode only when thermally deformed, may then be found iteratively.

Beginning from an unperturbed cavity, the system is allowed to evolve to its steady state as described by fig. 4.4. We then subtract the resulting thermoelastic deformation from the ideal mirror profiles and allow the system to reach a new equilibrium. Iteratively repeating this process one eventually arrives at the mirror figure which deforms under thermal loading to support the desired mode.

4.5.2 Results and discussion

In figures 4.9, 4.10 and 4.11 below we show how such a system might operate for Gaussian and mesa modes. We chose to study the case of 0.5 ppm coating absorption, which at the time of writing is a reasonable value for future gravitational wave detectors.

4.5.2.1 Gaussian

The upper plot of fig. 4.9 shows the uncorrected thermoelastic deformation arising from 0.5 ppm coating absorption (blue) and the profile which must be subtracted from the ideal cavity mirrors so that they support the nominal mode after heating (orange). As one would expect, these profiles are not equal.

[24] A more recent proposal by Kamp et al. may also be useful for thermal compensation in non-Gaussian interferometers [177].

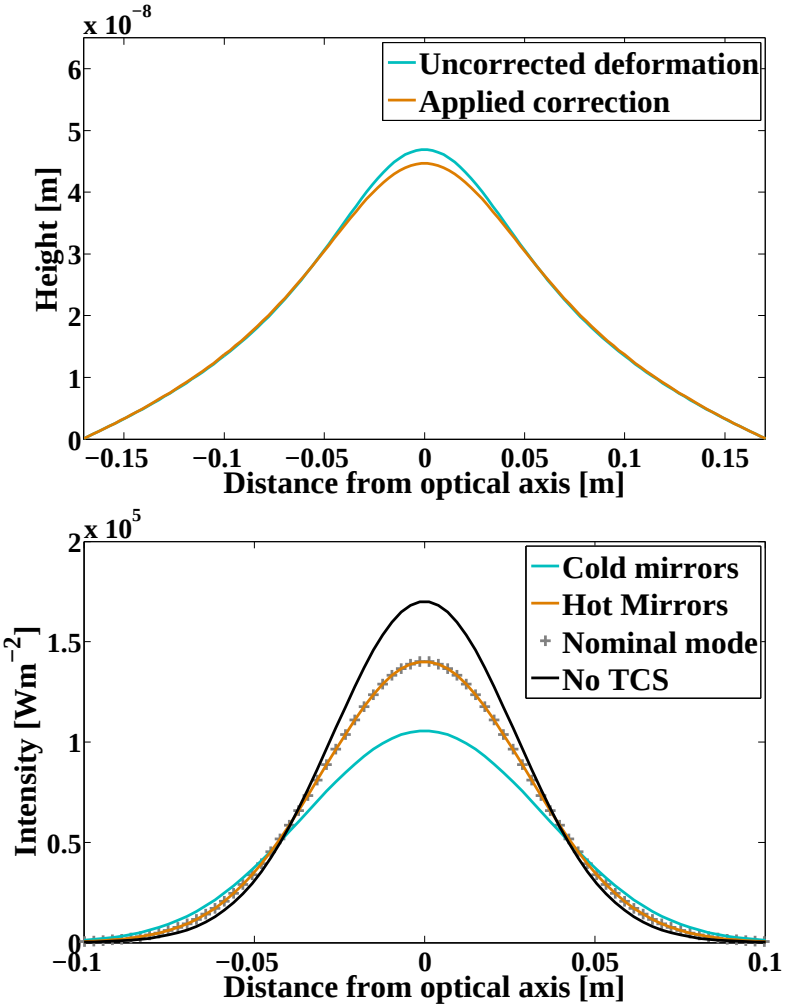

Figure 4.9: Using self-correcting mirrors for thermal compensation - Gaussian beams. Top: Thermoelastic deformation with no correction and the correction which must be subtracted from the ideal mirror profile to restore the nominal mode. Bottom: Cavity eigenmodes with no TCS (black), with our doctored TCS mirrors 'cold' (blue) and at equilibrium (orange). Notice that the recovered mode overlaps exactly with the ideal cavity mode (grey crosses).

The cavity formed by self-correcting mirrors always supports a mode having power less than or equal to that of the fiducial Gaussian.[25] These lower power modes yield weaker thermal deformation of the cavity mirrors than does the standard Gaussian. We desire that these small deformations restore the ideal mirror shape, thus the profile subtracted from the nominal figure to create our self-correcting mirrors must be smaller than the deformation caused by the fiducial Gaussian mode. An identical argument holds for the concentric mesa beam case whilst an analogous approach is suitable for flat mesa

[25] With equality only realised at equilibrium.

beams where the cavity with self-correcting mirrors always stores power greater than or equal to that of the fiducial mode.

The lower plot of fig. 4.9 presents theoretical results showing how the cavity eigenmode is affected by our compensation scheme. The theoretical intensity profile ignoring thermal effects is marked by grey crosses; the black curve represents the mode to be expected if no correction is implemented. Using a blue line we show the mode which is resonant when our compensating mirrors are cold whilst the orange curve shows the profile recovered once these mirrors are at operating temperature. As expected this profile agrees excellently with the ideal cavity mode.

4.5.2.2 Mesa

Figures 4.10 and 4.11 convey analogous results for flat mesa and concentric mesa cavities respectively. For both configurations the mode recovered after heating again shows superb agreement with the nominal mode.

In order for the corrective mirror profiles calculated above to be practicable in a real interferometer we may require some auxiliary source to heat the test mass before resonance is attained (such as a carbon dioxide laser or ring heater). Once stably locked this compensating source may have its heating significantly reduced so that noise is injected at a level which is acceptable for recording astrophysical data.

We acknowledge that the results of this section present a single point solution and neglect multiple real-world effects. For example fabrication errors and vague knowledge of or inconsistency in the coating absorption. Effects such as these were responsible for the variable success of a similar scheme used in the polishing of the initial LIGO power recycling mirrors. Nonetheless we believe that passive approaches such as this one may find applications in the future as researchers strive to increase the circulating power in interferometers' arms.

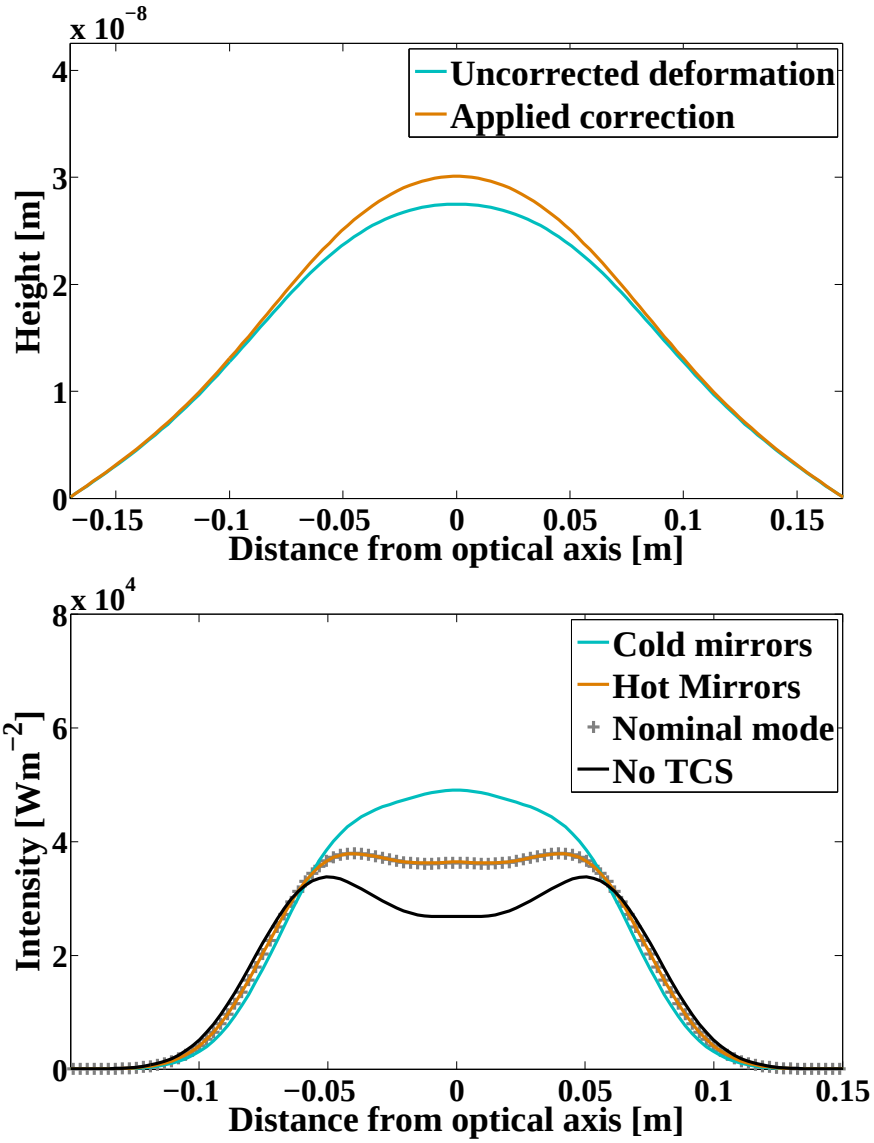

Figure 4.10: Using self-correcting mirrors for thermal compensation - Flat mesa beams. Top: Thermoelastic deformation with no correction and the correction which must be subtracted from the ideal mirror profile to recover the nominal mode. Bottom: Cavity eigenmodes with no TCS (black), with our doctored TCS mirrors 'cold' (blue) and at equilibrium (orange). Notice that the recovered mode overlaps exactly with the ideal cavity mode (grey crosses).

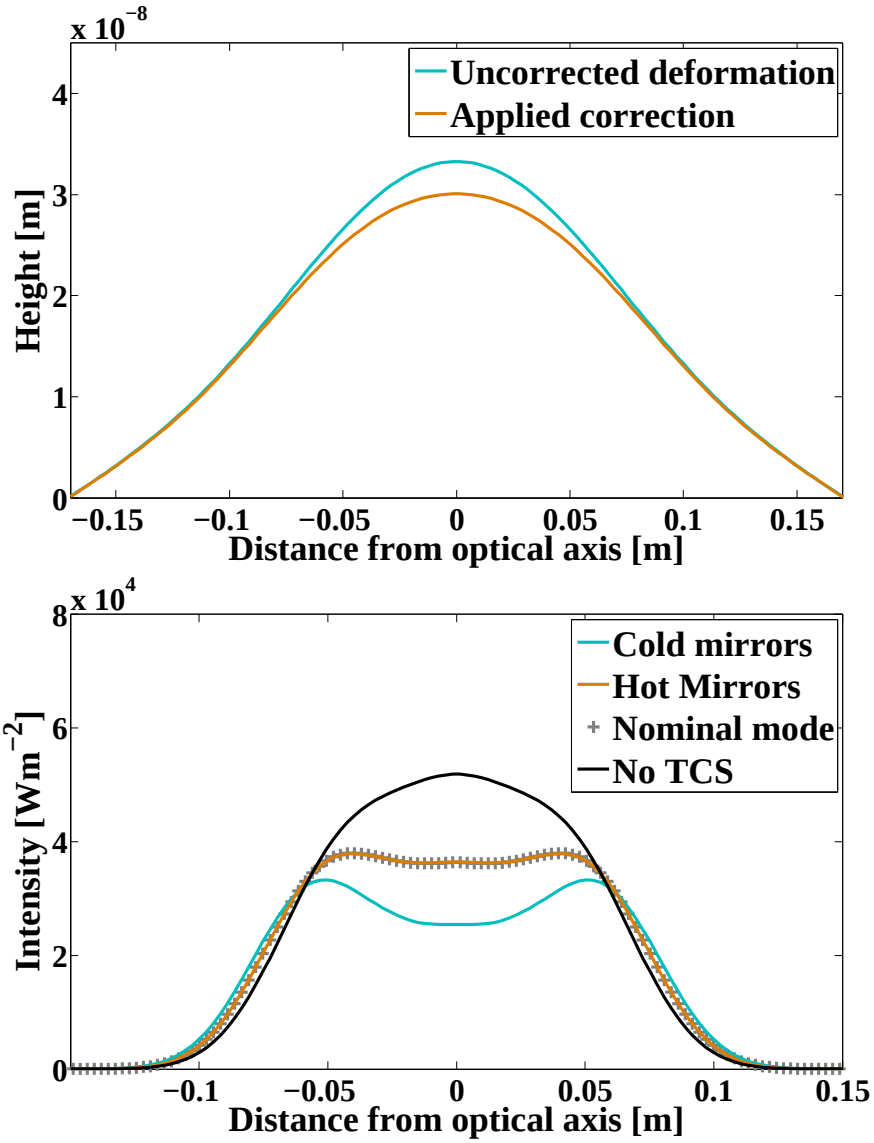

Figure 4.11: Using self-correcting mirrors for thermal compensation - Concentric mesa beams. Top: Thermoelastic deformation with no correction and the correction which must be subtracted from the ideal mirror profile to recover the nominal mode. Bottom: Cavity eigenmodes with no TCS (black), with our doctored TCS mirrors 'cold' (blue) and at equilibrium (orange). Notice that the recovered mode overlaps exactly with the ideal cavity mode (grey crosses).

4.6 Thermal lensing

In addition to thermoelastic distortion of the mirror coatings, thermorefractive aberrations will also be present in the input mirror substrates. This complication was neglected in the above sections so as to better understand cavity effects.[26] Here we discuss the consequences of such aberrations and briefly examine how Gaussian and mesa beams differ in their susceptibility to them.

The maximum permissible level of circulating power in an interferometer is usually set by the finite absorption of the transmissive optics.[27] This absorbed laser power gives rise to optical path length distortion in the mirror substrates through the thermo-optic coefficient $\mathrm{d}n/\mathrm{d}T$. We call such distortion *thermal lensing*.

Thermal lensing can limit the sensitivity of interferometric detectors in numerous ways [156]. It reduces carrier gain in the arm and power recycling cavities, decreasing the power stored in the arms; it affects sideband gain in the recycling cavity, which can noticeably reduce the efficiency of any RF readout scheme and finally this effect also enhances the contrast defect, contributing to increased shot noise.

The form taken by these thermorefractive distortions is clearly dependent on the spatial distribution of the incident optical power. As an indication of the relative magnitude of lensing effects with Gaussian and mesa beams, the additional optical path lengths experienced traversing the test masses of Gaussian and mesa cavities[28] were determined.

The additional optical path length or thermal lens in the test mass substrate is calculated from the integral

$$Z(r) = \beta \int_{-h/2}^{h/2} T(r,z)\,\mathrm{d}z, \tag{4.95}$$

where $\beta = \mathrm{d}n/\mathrm{d}T$ is the thermo-optic coefficient. Using the notation and techniques

[26] This is equivalent to assuming that the purely thermorefractive aberrations have been compensated on the input field prior to injection into the cavity. It should be noted that such compensation is far from trivial.

[27] Radiation pressure induced instabilities aside.

[28] The mesa beam intensity profile is equal for flat and concentric cavities.

of §4.1 (specifically (4.16)) this expression can be written

$$Z(r) = \sum_m z_m J_0(k_m r) \tag{4.96}$$

$$\text{where} \quad z_m = \beta \frac{\epsilon P_0 a}{K_{\text{th}}} \frac{p_m}{k_m} \frac{1 - \exp(-k_m h)}{k_m a + \chi - (k_m a - \chi)\exp(-k_m h)}. \tag{4.97}$$

Evaluating this formula using the parameters of Appendix A, fig. 4.12 clearly shows that the mesa beam gives rise to a much weaker thermal lens. Fits to these profiles,

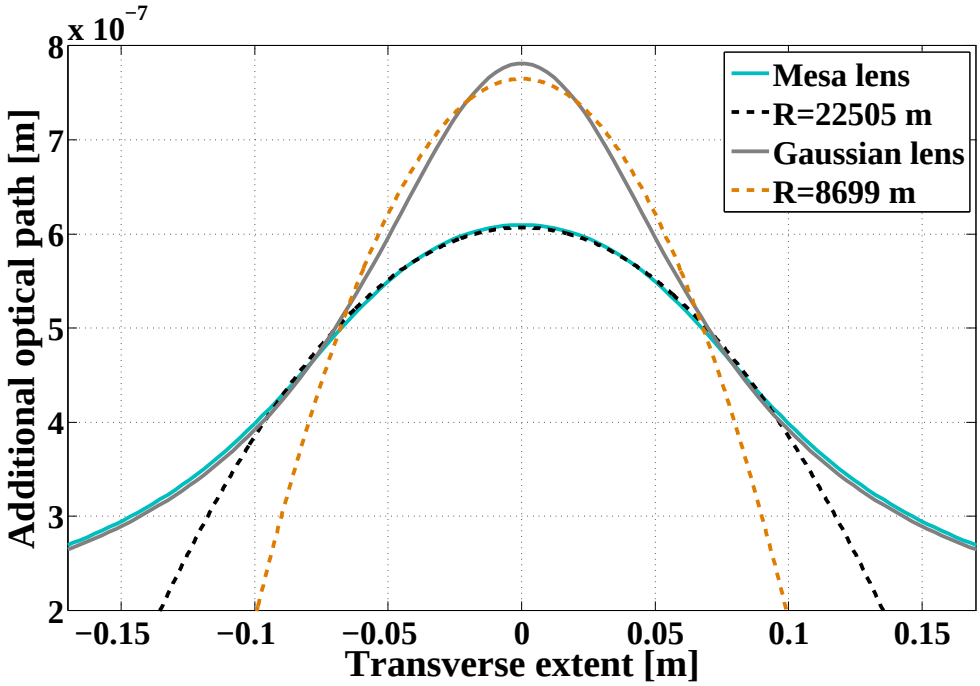

Figure 4.12: Thermal lenses induced by Gaussian and mesa beams. Fits giving the effective radius of curvature are weighted by the intensity profile of the appropriate arm cavity eigenmode.

weighted by the intensity of the appropriate arm cavity eigenmode, reveal that the effective focal length of the mesa thermal lens is approximately three times longer than that seen in the Gaussian case. The mesa lens also has a more spherical profile and may therefore be easier to correct via ring heaters or by suitably modifying the input beam.[29]

[29] Although in this case differences between the arms will be a limiting factor.

4.7 Summary and discussion

We have illustrated how the resonant modes of mesa and Gaussian beam cavities are modified by thermoelastic effects as a function of coating absorption. In doing so we have demonstrated that the losses of mesa cavities are *relatively* unaffected by optical power absorbed in their coatings.

Along with other candidates, mesa beams are being considered for use in future detectors as they ameliorate the effects of test mass thermal noise. We find for flat mesa beams, in contrast to Gaussian and concentric mesa modes, that thermal noise decreases with absorbed power.

Although this thermal noise reduction is welcomed, overall interferometer operation will be more stable if the nominal mesa mode is preserved. To this end we have outlined a possible method of thermal compensation for non-Gaussian beams. Such passive techniques may also be a useful complement to standard Gaussian beam TCS systems as interferometers' circulating power enters the MW range.

The above results neglected thermorefractive effects in the test mass substrates so as to better understand the cavity behaviour. A preliminary investigation revealed that mesa beams are far less susceptible to thermal lensing than their Gaussian counterparts.

Collectively, our findings indicate that non-Gaussian beams are potentially more robust with respect to thermal aberrations than equivalent Gaussian modes. However, before one can draw any strong conclusions it is essential that thermoelastic, thermo-optic[30] and subtle differential arm effects be considered simultaneously. Such work requires complex full-interferometer simulations but would ultimately place limits on acceptable material properties and define manufacturing tolerances.

[30] And perhaps even elasto-optic, depending on the test mass material.

Chapter 5

Parametric instabilities

In this chapter we move away from the problem of thermal noise and the proposed solution of mesa beams to study another issue which may inhibit future interferometers – parametric instabilities.

Parametric instabilities (PIs) result from the non-linear coupling of optical energy stored in the interferometer's arm cavities into mechanical energy stored in internal mechanical modes of the test masses. This coupling is driven by radiation pressure and is strongly dependent on the mechanical quality factor of the test masses. As such it is of concern for advanced detectors which hope to employ high power lasers and optics with extremely low mechanical loss. If the coupling is sufficiently strong, exponentially growing mechanical motion of the test mass will compromise detector noise performance and control. In some cases the interferometer will lose lock. Given the consequences of uncontrolled PIs, work is ongoing to investigate means by which they may be mitigated. We investigate one such scheme.

The majority of currently operating gravitational wave detectors utilise coil-magnet actuators to control the positions and alignment of their suspended optics. Problems associated with this system (see §5.1.5) led to the development of electrostatic actuators. In this chapter we evaluate the possibility of using these electrostatic actuators to damp mechanical modes of the test masses and thus ameliorate PIs.

We begin in section 5.2.1 by theoretically determining the force required to damp a PI to an arbitrary safe level. Then, by numerical methods, we obtain the force available from a prototype Electrostatic Drive (ESD) (sections 5.2.5 and 5.2.6). Comparing these two quantities in section 5.2.9, our model predicts that an ESD can successfully damp any potential PI. We conclude our investigation in section 5.3 with an experimental study of the same prototype ESD, validating our model and predictions.

5.1 Background

We commence by introducing the physical mechanisms which drive PIs, describing why they have not been seen in first generation interferometers but are expected to prove troublesome for future detectors. We present a new, intuitive approach to the calculation of parametric gain which allows easy generalisation to complex interferometer topologies. Continuing, we review previously proposed methods of controlling PIs before outlining our plans for an improved scheme.

5.1.1 Parametric instabilities

Spontaneously excited parametric instabilities are not a issue of concern for currently operating gravitational wave detectors and to date have only been observed in a small number of specially designed experiments (e.g. [178, 179, 180]). However, in efforts to reduce test mass thermal noise (see §4.2) and photon shot noise (see §1.4), second generation interferometers will employ extremely low-loss test masses and strive to maximise the power circulating in their arms. These changes have inadvertently brought PIs into prominence.

Parametric instabilities (PIs) arise when radiation pressure forces result in a nonlinear coupling between optical energy stored in the interferometer's arm cavities and mechanical energy stored in the acoustical mode of a test mass. This process may be easily understood as a classical feedback effect.

Excitation, thermal or otherwise, of a test mass eigenmode initiates the process, scattering light from the fundamental cavity mode into a pair[1] of sideband fields with frequency spacing equal to the mechanical mode frequency. The spatial profile of the test mass mode is also imprinted onto these fields. The sidebands then experience the, generally different, optical response of the system before arriving back to the excited optic together with the main cavity field. Radiation pressure then couples the scattered light into mechanical motion, thus closing the feedback loop. Based on the overall loop phase the mechanical mode may be suppressed or further excited, leading to an instability.

The entire parametric instability process may be quantified by a single dimensionless quantity, the parametric gain R_m. In the following section we discuss the evaluation of this key parameter.

5.1.2 Calculation of the parametric gain

The possible problem of PIs was highlighted by Braginsky and colleagues in 2001 when they published an analytic expression for the parametric gain in a single Fabry-Perot cavity [181]. This work was subsequently generalised to increasingly complex interferometer topologies [182, 183, 184, 185, 186]. Unfortunately the formalism and vernacular adopted were somewhat esoteric. Recently Evans et al. showed that equivalent results could more easily be obtained [187]. Applying techniques well-known in the field, he developed an approach which may easily be generalised to arbitrary optical systems. This approach was adopted in the following sections and is recounted here.

The calculation of parametric gain may be treated as a classical feedback problem whereby test mass mechanical modes influence the optical modes in the system through scattering and the optical modes in turn influence the mechanical modes via radiation pressure. In this section we evaluate the parametric gain associated with a single mechanical mode with resonant frequency ω_m. This shall be the frequency of interest

[1] In this work we consider terms only up to linear order, a reasonable approximation for the small oscillation amplitudes under study.

for our feedback calculation. We begin by examining the scattering process.

First consider the simple case of plane wave of wavelength λ_0, frequency ω_0, reflecting from a mirror oscillating with small amplitude ϕ at frequency ω_m.

$$\begin{aligned} \text{If} \quad & \Psi_{\text{inc}} = E_{\text{inc}} \exp[j(w_0 t)] && (5.1) \\ \text{then} \quad & \Psi_{\text{refl}} = E_{\text{refl}} \exp[j(w_0 t + 2\frac{2\pi}{\lambda_0}\phi\cos(\omega_m t))] \\ & \simeq E_{\text{refl}}(1 + j(2\frac{2\pi}{\lambda_0}\phi\cos(\omega_m t))) \exp[j(w_0 t)] && (5.2) \\ & = (E_{\text{refl}} + j\frac{2\pi}{\lambda_0}\phi E_{\text{refl}}(e^{j\omega_m t} + e^{-j\omega_m t})) \exp[j(w_0 t)]. \end{aligned}$$

Notice how audio sidebands with amplitude $j2\pi\phi E_{\text{refl}}/\lambda_0$ and frequency ω_m are created symmetrically about the fundamental frequency. For parametric gain calculations this simple example must be extended to include spatial information. Consider an optical mode of form

$$\Psi_{\text{circ}} = E_{\text{circ}} f_0 e^{j\omega_0 t}, \tag{5.3}$$

with amplitude E_{circ}, frequency ω_0 and spatial distribution f_0, having just left a surface with time varying spatial profile

$$\phi = A_m(\vec{u}_m \cdot \hat{z})e^{j\omega_m t}, \tag{5.4}$$

where $\hat{z}$ is the unit vector along the cavity direction, A_m is the modal amplitude of test mass mechanical mode m, $\vec{u}_m = (u, v, w)$ is its displacement field and ω_m its eigenfrequency. With this notation $A_m(\vec{u}_m \cdot \hat{z})$ is the displacement along the cavity axis.

The resultant scattered field will consist of upper and lower audio sidebands at frequency ω_m with spatial profiles dependent on ϕ. We describe these fields in the space of Higher Order Modes (HOMs) with basis functions f_n

$$\Psi_{\text{scat}} = \sum_{n=0}^{\infty} E_{\text{scat},n} f_n e^{j\omega_0 t}(e^{j\omega_m t} + e^{-j\omega_m t}). \tag{5.5}$$

Similarly to (5.2) the sideband pairs have amplitudes given by

$$E_{\mathrm{scat},n} = j\frac{2\pi}{\lambda_0} A_m E_{\mathrm{circ}} B_{m,n}, \tag{5.6}$$

where λ_0 and E_{circ} are the wavelength and amplitude of the fundamental optical mode driving the scattering process and $B_{m,n}$ is the geometric overlap of mechanical mode m with the n^{th} HOM defined via

$$B_{m,n} = \iint\limits_{\mathcal{S}} f_0 f_n (\vec{u}_m \cdot \hat{z})\, \mathrm{d}\mathcal{S}, \tag{5.7}$$

where $\mathcal{S}$ is the test mass surface normal to the direction of beam propagation. The modal displacement and basis functions have normalisations

$$\iint\limits_{\infty} |f_n|^2\, \mathrm{d}\mathcal{S} = 1 \quad \text{and} \quad \iiint\limits_{\mathcal{V}} \rho |\vec{u}_m|^2\, \mathrm{d}\mathcal{V} = 1, \tag{5.8}$$

where ρ is the mass density of the test mass and $\mathcal{V}$ is its volume.

We must now consider how each of the scattered sideband fields interacts with the optical system. In general the upper and lower sidebands will experience different gain. Denoting the closed loop transfer function of the n^{th} HOM as $G_n^{\pm}$, the modal amplitudes of the field reflected from the excited optic's surface after a round trip through the system may be written in the HOM basis as

$$\Psi_{\mathrm{rt}} = \sum_{n=0}^{\infty} E_{\mathrm{scat},n} f_n e^{j\omega_0 t} (G_n^{+} e^{j\omega_m t} + G_n^{-} e^{-j\omega_m t}) = \Psi_{\mathrm{rt}}^{+} + \Psi_{\mathrm{rt}}^{-}. \tag{5.9}$$

(For full details regarding the calculation of $G_n^{\pm}$ please see §5.1.3.)

This scattered field couples the optical system to mechanical oscillations of the test mass via radiation pressure

$$P_{\mathrm{rad}} = \frac{2}{c} |\Psi_{\mathrm{refl}}|^2 \quad \text{where} \quad \Psi_{\mathrm{refl}} = \Psi_{\mathrm{circ}} + \Psi_{\mathrm{rt}}^{+} + \Psi_{\mathrm{rt}}^{-}. \tag{5.10}$$

The component of the radiation pressure at the mechanical mode frequency is given

by

$$P_{\mathrm{rad},m} = \frac{2}{c}\left(E^*_{\mathrm{circ}} f_0 \sum_{n=0}^{\infty} E^-_{\mathrm{rt},n} f_n + E_{\mathrm{circ}} f_0 \sum_{n=0}^{\infty} E^{+*}_{\mathrm{rt},n} f_n\right)$$
$$= \frac{2}{c}\left(E^*_{\mathrm{circ}} f_0 \sum_{n=0}^{\infty} (G^-_n E_{\mathrm{scat},n}) f_n + E_{\mathrm{circ}} f_0 \sum_{n=0}^{\infty} (G^+_n E_{\mathrm{scat},n})^* f_n\right). \tag{5.11}$$

Integrating this pressure over the surface of the optic to obtain the force coupled into the mechanical mode of interest, i.e. performing integrals of the form given in (5.7), we arrive at

$$F_{\mathrm{rad},m} = \frac{2}{c}\left(E^*_{\mathrm{circ}} \sum_{n=0}^{\infty} (G^-_n E_{\mathrm{scat},n}) B_{m,n} + E_{\mathrm{circ}} \sum_{n=0}^{\infty} (G^+_n E_{\mathrm{scat},n})^* B_{m,n}\right)$$
$$= j\frac{2\pi}{\lambda_0}\frac{2P_{\mathrm{circ}}}{c} A_m \sum_{n=0}^{\infty} (G^-_n - G^{+*}_n) B^2_{m,n} \tag{5.12}$$
$$= j\frac{2\pi}{\lambda_0}\frac{2P_{\mathrm{circ}}}{c} A_m \sum_{n=0}^{\infty} (G_n) B^2_{m,n},$$

where we have introduced $G_n = G^-_n - G^{+*}_n$.

The change in modal amplitude ΔA_m brought about by this radiation pressure force is given by the transfer function of a mechanical oscillator at its resonant frequency ω_m

$$\Delta A_m = \frac{-jQ_m}{\mu_m \omega_m^2} F_{\mathrm{rad},m}$$
$$= \frac{Q_m}{\mu_m \omega_m^2}\frac{4\pi P_{circ}}{c\lambda_0} A_m \sum_{n=0}^{\infty} G_n B^2_{m,n}, \tag{5.13}$$

where μ_m is the modal mass of the oscillating eigenmode.[2] Thus the open loop gain of the PI considered as a classical feedback loop is

$$\frac{\Delta A_m}{A_m} = \frac{4\pi Q_m P_{circ}}{\mu_m \omega_m^2 c\lambda_0} \sum_{n=0}^{\infty} (G_n) B^2_{m,n}. \tag{5.14}$$

[2]With Evans' normalisation ((3) of [187]) $\mu_m = M$, the total mass of the test mass, for all modes. For consistency with later work we adopt a slightly different normalisation which leads to $\mu_m = 1$ for all modes.

The parametric gain $\mathcal{R}$ is the real part of this open loop gain

$$\begin{aligned}\mathcal{R}_m &= \Re\left[\frac{\Delta A_m}{A_m}\right] \\ &= \frac{4\pi Q_m P_{\rm circ}}{\mu_m \omega_m^2 c \lambda_0} \sum_{n=0}^{\infty} \Re[G_n] B_{m,n}^2. \end{aligned} \tag{5.15}$$

Since $\mathcal{R}_m$ is the open loop gain of a feedback loop we have instability for $\mathcal{R}_m > 1$ and optical damping for $\mathcal{R}_m < 0$. In arriving at this expression we have tacitly assumed that only a single mechanical mode of a single test mass is involved in any PI [3] and that the power stored in the fundamental cavity mode $P_{\rm circ}$ is unaltered by any scattering processes.

Quantifying the entire parametric instability process with a single quantity is indeed elegant but it is not until one considers the calculation of G_n that the true power of this formulation is revealed.

5.1.3 Transfer functions of the optical plant

Using the audio sideband formalism [188, 189] the closed loop gain of each HOM scattering sideband may be calculated as it traverses the optical system. This quantity is complex and will generally be different for upper and lower sidebands.

We begin by constructing a matrix $\mathbf{S}$ whose $ij^{\rm th}$-entry is the transfer coefficient from the field evaluated at node j to the field evaluated at node i, $E_j \rightsquigarrow E_i$ i.e.

$$\mathbf{S} = \begin{pmatrix} E_1 \rightsquigarrow E_1 & E_2 \rightsquigarrow E_1 & \dots & E_n \rightsquigarrow E_1 \\ E_1 \rightsquigarrow E_2 & E_2 \rightsquigarrow E_2 & \dots & E_n \rightsquigarrow E_2 \\ \vdots & \vdots & \ddots & \vdots \\ E_1 \rightsquigarrow E_n & E_2 \rightsquigarrow E_n & \dots & E_n \rightsquigarrow E_n \end{pmatrix}, \tag{5.16}$$

a zero is entered for unconnected nodes.We demonstrate this idea with two basic ex-

[3] Given the high Q of the mechanical modes it is unlikely that more than one mode will play a significant role at a single frequency.

amples. For the case of a simple mirror (fig. 5.1), showing only non-zero entries

$$\mathbf{S}_{\text{mirr}} = \begin{array}{c} \\ E_1 \\ E_2 \\ E_3 \\ E_4 \end{array} \begin{array}{c} \begin{array}{cccc} E_1 & E_2 & E_3 & E_4 \end{array} \\ \begin{pmatrix} \cdot & \cdot & \cdot & \cdot \\ jt & \cdot & r & \cdot \\ \cdot & \cdot & \cdot & \cdot \\ r & \cdot & jt & \cdot \end{pmatrix} \end{array}, \tag{5.17}$$

where r and t are the amplitude reflectivity and transmissivity of the mirror. Similarly

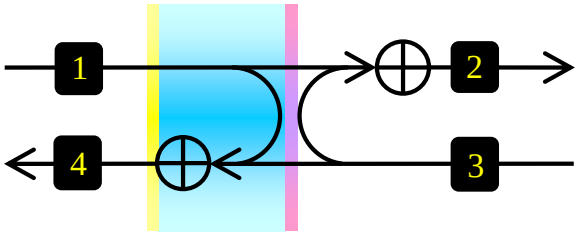

Figure 5.1: Node diagram of a single mirror used to construct matrix of transfer coefficients.

for a Fabry-Perot cavity (fig. 5.2)

$$\mathbf{S}^{\pm}_{n,\text{FP}} = \begin{array}{c} \\ E_1 \\ E_2 \\ E_3 \\ E_4 \\ E_5 \\ E_6 \\ E_7 \\ E_8 \end{array} \begin{array}{c} \begin{array}{cccccccc} E_1 & E_2 & E_3 & E_4 & E_5 & E_6 & E_7 & E_8 \end{array} \\ \begin{pmatrix} \cdot & \cdot & \cdot & \cdot & \cdot & \cdot & \cdot & \cdot \\ jt_A & \cdot & \cdot & \cdot & \cdot & \cdot & r_A & \cdot \\ \cdot & P^{\pm}_{L;n} & \cdot & \cdot & \cdot & \cdot & \cdot & \cdot \\ \cdot & \cdot & jt_B & \cdot & r_B & \cdot & \cdot & \cdot \\ \cdot & \cdot & \cdot & \cdot & \cdot & \cdot & \cdot & \cdot \\ \cdot & \cdot & r_B & \cdot & jt_B & \cdot & \cdot & \cdot \\ \cdot & \cdot & \cdot & \cdot & \cdot & P^{\pm}_{L;n} & \cdot & \cdot \\ r_A & \cdot & \cdot & \cdot & \cdot & \cdot & jt_A & \cdot \end{pmatrix} \end{array}, \tag{5.18}$$

where $P^{\pm}_{L;n}$ is the propagation operator

$$P^{\pm}_{L;n} = e^{j(\Phi_n \pm \omega_m L/c)}. \tag{5.19}$$

We take the plus sign for upper scattering sidebands and the minus for lower. The

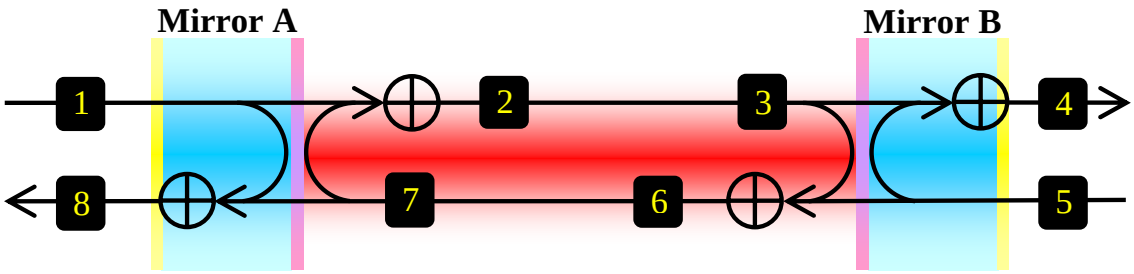

Figure 5.2: Node diagram of a Fabry-Perot cavity used to construct matrix of transfer coefficients.

propagation phase Φ_n depends on the propagation phase of the fundamental mode Φ_0 and the additional Gouy phase Φ_G accumulated by the HOM

$$\Phi_n = \Phi_0 - \mathcal{O}_n \Phi_G, \tag{5.20}$$

where $\mathcal{O}_n$ is the order of the n^{th} HOM. The simplicity with which the **S** matrices are constructed makes this technique easily extensible to complex interferometer topologies and to other systems where optomechanical interactions are of interest – a decisive advantage over previous methods.

The algorithm can be further generalised to include mode dependent losses. This can be achieved by modifying $\mathbf{S}_n^{\pm}$ for each higher order mode or by splitting it into diagonal propagation matrix $\mathbf{P}_n^{\pm}$ and a constant 'mirror' matrix **M**. A distinct loss matrix $\mathbf{C}_n$ may then be constructed for each HOM with the new total matrix formed as $\mathbf{S}_n^{\pm} = \mathbf{M}\mathbf{C}_n^{\pm}\mathbf{P}_n^{\pm}$ [187].

In our analyses diffraction losses are included via the clipping approximation. These losses are insignificant for low order optical modes but strongly limit the optical gain of modes of order $\gtrsim 9$. For all mirrors we set the radius of the clipping aperture equal to the radius of a test mass, 0.17 m. For the beamsplitter we take 0.133 m, the innermost radius of the ITM ESD pattern. This choice accounts for loss suffered passing through the reaction masses inside the recycling cavity.

With the scattering matrix of the optical system fully defined we may calculate the

closed loop gain of each scattering sideband HOM as

$$G_n^{\pm} = \vec{e}_i^{\,T}(\mathbf{I} - \mathbf{S}_n^{\pm})^{-1}\vec{e}_i, \tag{5.21}$$

where $\vec{e}_i$ is the i^{th} column of the identity matrix $\mathbf{I}$ with transpose $\vec{e}_i^{\,T}$. The index i corresponds to the node at which we wish to evaluate the PI. For example if we wished to consider PIs excited by oscillations of mirror B in fig. 5.2 we would use $\vec{e}_6$.

Recall that $G_n^{\pm}$ represents the closed loop of each HOM sideband. Still examining fig. 5.2, notice how the G_n take the form $1/(1 - \text{round trip gain})$, in exact analogy to a classical feedback loop

$$G_{n;2,3,6,7}^{\pm} = \frac{1}{1 - r_A r_B (P_{L;n}^{\pm})^2}. \tag{5.22}$$

To reinforce the parallel between our system and a classical feedback loop we sketch a derivation of G_n. Omitting $\pm$ for clarity and considering a single HOM we may write

$$\begin{pmatrix} E_1^{t_1} \\ E_2^{t_1} \\ \vdots \\ E_N^{t_1} \end{pmatrix} = \mathbf{S} \begin{pmatrix} E_1^{t_0} \\ E_2^{t_0} \\ \vdots \\ E_N^{t_0} \end{pmatrix} + \begin{pmatrix} E_1^{SB} \\ E_2^{SB} \\ \vdots \\ E_N^{SB} \end{pmatrix}, \tag{5.23}$$

where N is the number of nodes in our system, the $E_i^{t_0}$ and $E_i^{t_1}$ are the field amplitudes at node i separated by some small increment of time and the E_i^{SB} are the scattering sidebands injected at node i. If we impose a steady state condition $E_i^{t_0} = E_i^{t_1} = E_i$ we may write

$$\begin{pmatrix} E_1 \\ E_2 \\ \vdots \\ E_N \end{pmatrix} = [\mathbf{I} - \mathbf{S}]^{-1} \begin{pmatrix} E_1^{SB} \\ E_2^{SB} \\ \vdots \\ E_N^{SB} \end{pmatrix}. \tag{5.24}$$

We seek the closed loop transfer function of the scattering sidebands i.e. E_i/E_i^{SB}. Post multiplying both sides of the equation by

$$\begin{pmatrix} 1/E_1^{SB} & 1/E_2^{SB} & \cdots & 1/E_N^{SB} \end{pmatrix} \tag{5.25}$$

and suppressing irrelevant matrix entries we obtain

$$\begin{pmatrix} E_1/E_1^{SB} & & & \\ & E_2/E_2^{SB} & & \\ & & \ddots & \\ & & & E_N/E_N^{SB} \end{pmatrix} = [\mathbf{I}-\mathbf{S}]^{-1} \begin{pmatrix} 1 & & & \\ & 1 & & \\ & & \ddots & \\ & & & 1 \end{pmatrix}. \quad (5.26)$$

Selecting the node of interest

$$\vec{e}_i^{\,T} \begin{pmatrix} E_1/E_1^{SB} & & & \\ & E_2/E_2^{SB} & & \\ & & \ddots & \\ & & & E_N/E_N^{SB} \end{pmatrix} \vec{e}_i = \vec{e}_i^{\,T}[\mathbf{I}-\mathbf{S}]^{-1} \begin{pmatrix} 1 & & & \\ & 1 & & \\ & & \ddots & \\ & & & 1 \end{pmatrix} \vec{e}_i$$

i.e. $$E_i/E_i^{SB} = \vec{e}_i^{\,T}[\mathbf{I}-\mathbf{S}]^{-1}\vec{e}_i$$

or $$G = \vec{e}_i^{\,T}[\mathbf{I}-\mathbf{S}]^{-1}\vec{e}_i. \quad (5.27)$$

Reintroducing modal dependence and our $\pm$ we recover (5.21).

5.1.4 Proposed methods of damping

Several analyses suggest parametric instabilities may prove troublesome in second generation interferometers, hence efforts are underway to evaluate methods of mitigating them. Schemes currently under study fall into two broad categories: those which modify G_n [190, 191] and those which modify Q_m [192, 193]. We discuss a selection of these schemes below in advance of introducing the method we considered in the following section.

5.1.4.1 Thermal ROC tuning

To realise a high parametric gain we require that a scattering sideband experiences considerable optical gain upon making a round trip through our optical system. This

is achievable when a mechanical mode has a strong spatial overlap with a particular HOM and the frequency of the mechanical mode closely matches the spacing of the HOM from the carrier field. If the HOM spacing may be appropriately controlled then optical and consequently parametric gain may be reduced.

The frequency spacing in Hz of the N^{th} order HOM from the fundamental is given by

$$\Delta f_N = \frac{N f_{\text{FSR}} \cos^{-1}(\pm\sqrt{g})}{\pi}, \tag{5.28}$$

where $f_{\text{FSR}} = c/(2L_{\text{cavity}})$ is the cavity free spectral range and $g = g_1 g_2 = (1 - L_{\text{cavity}}/R_1)(1 - L_{\text{cavity}}/R_2)$ is the cavity g factor. We take the plus sign for a cavity in the upper right quadrant of the cavity stability diagram ($g_1, g_2 > 0$) and the negative sign for cavities in the lower left quadrant ($g_1, g_2 > 0$). The cavity length is fixed, leaving the mirror radii of curvature as the only free parameters.

Thermal radius of curvature tuning is a well studied technique [156]. It has been successfully used in GEO600 to correct for manufacturing errors, matching the radii of curvature of the far folding mirrors [194]. Incandescent ring heaters will also be used

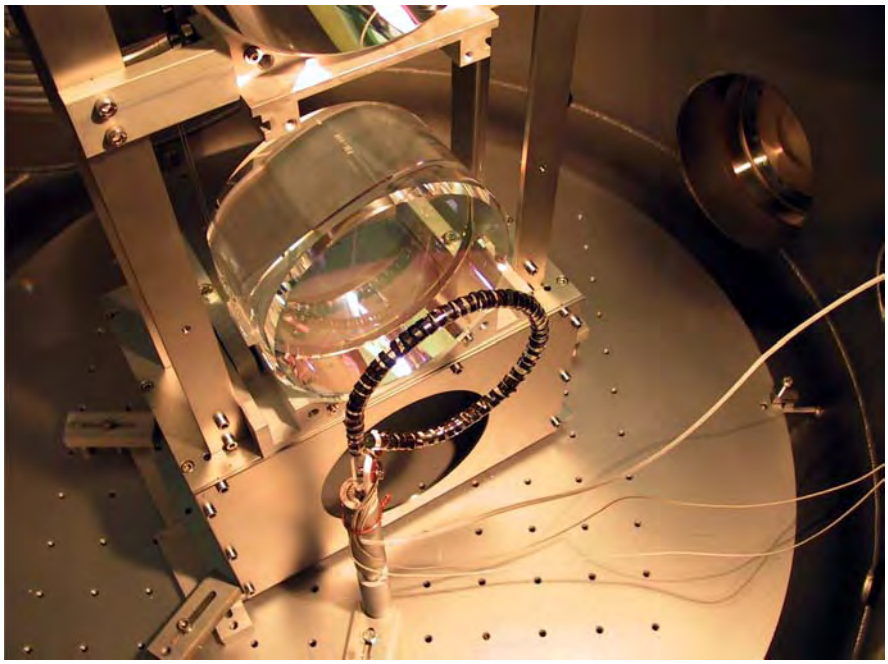

Figure 5.3: The ring heater behind GEO600's East folding mirror used to match the radius of curvature of this optic to that of North folding mirror.

in AdvLIGO to control the arm cavity mode [195].

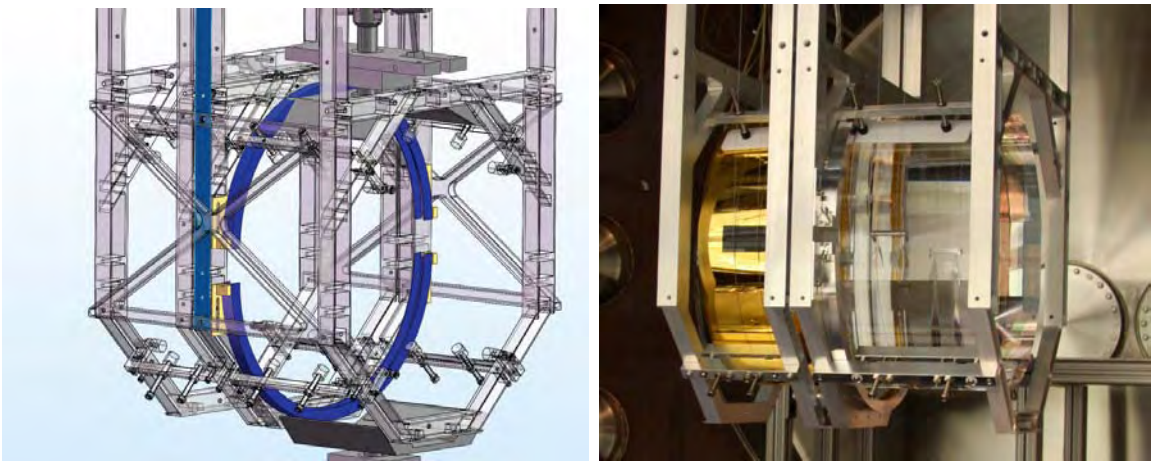

Figure 5.4: Rendering and image showing Advanced LIGO ring heater positioned 40 mm from the AR face of the test mass.

In 2005 Zhao et al. proposed to use similar techniques to alleviate parametric instabilities by thermally tuning the HOM spacing [196, 190]. Unfortunately, what initially appears to be an imaginative solution to the problem of PIs suffers from a number of practical problems.

At frequencies above ∼20 kHz the mechanical mode spacing is around 50 Hz compared to the cavity line width of order 100 Hz. Hence tuning the radius of curvature to suppress one mode may lead to unintentional excitation of an adjacent mode. Further, altering the radius of curvature of a test mass not only degrades single cavity mode matching it also increases the contrast defect as the arm cavities will no longer be matched.

The thermal effects themselves are also a source of concern. Heating must be limited to the ETMs as any thermal distortion of the ITM substrates will affect the recycling cavity mode and impact matching into the arms. Additionally, it is likely that heating the front surface of the test mass will introduce prohibitive levels of noise so that heating must be limited to the rear surface. This configuration only allows radii of curvature to be reduced meaning that the parametric gain may not always be reduced monotonically. Also, PIs are a dynamic process with perhaps several being encountered

as the interferometer is brought to full power. A mitigation scheme based around a thermal actuator will always be limited by the thermal time constant of the test mass (∼10 min) limiting its effectiveness. Finally we mention that this scheme may not be the ideal choice for cryogenic detectors. Introducing additional heat sources is contrary to the design principles of such an instrument and the reduction in coefficients of thermal expansion at low temperature compounds this issue.[4]

Although this scheme benefits from using existing hardware and is likely to introduce little noise[5] it is not the optimal choice for fused-silica masses. It may however be worth exploring for use with other test mass materials exhibiting greater thermal conductivity and more sparsely distributed eigenmodes such as sapphire.

5.1.4.2 Optical interference

A second mitigation scheme tasked with reducing optical gain is the subject of current experimental work. In this design no cavity parameters are doctored, gain is instead modified via optical mode interference [191].

If the scattering sidebands are particularly well coupled to a single HOM, injecting this same mode into the system with opposite phase drastically attenuates the scattered field with a commensurate reduction in parametric gain. Recent studies using a tunable cavity and externally driven mechanical oscillations have demonstrated the principle of this technique [197].

It may however be a formidable task to extend this work to spontaneously excited instabilities in a full size detector. One must detect which HOM is resonant, subsequently create an accompanying mode with appropriate spatial profile, orientation, amplitude, frequency and phase before injecting it back into the interferometer without introducing excess noise. The complexity and technical challenges presented are non-negligible. For example, to mitigate noise due to backscattering of light into the

[4]Relative to room temperature more heat is required to effect the same change in radius of curvature.

[5]If ring heaters are used they will thermally average any noise from their power supplies.

arm cavities it is desirable that this system be seismically isolated and under vacuum. Such difficulties will be compounded if multiple modes operate above threshold at a single time, each requiring its own companion mode to interfere with. This said, optical mode interference is a compelling idea in its own right which certainly merits a thorough exploration.

5.1.4.3 Lossy rings/coatings

Equation (5.15) illustrates the proportional dependence of the parametric gain R_m on the mechanical mode quality factor Q_m. This leads one to imagine reducing parametric gains by increasing the effective loss of the test mass. However in doing so one must also be mindful of the competing demands of mirror thermal noise (see §4.2). Fortunately this noise depends strongly on the distribution of loss throughout the test mass [65, 66, 198].

DeSalvo and colleagues were the first to investigate regions where lossy material could be added with relative impunity, locating a ring around the circumference of the test mass [199]. This discovery motivated proposals to place a ring of damping material material around this circumference. Gras et al. performed a comprehensive analysis of this idea concluding that the all the test mass modes could be effectively damped if one is willing to accept a 20% penalty in thermal noise [193, 200].

Enthusiasm for this idea also stimulated experimental work at Caltech's TNI. Fig. 5.5 shows two of three types of ring damper tested there – Buna O-rings, Kapton tape and a copper ring (not shown).

The Buna O-rings were 1/8 inch thick and held in place by their own tension. These dampers were found to reduce modal Qs to a level where they could no longer be measured. However, this promising result was accompanied by an increase in broadband noise. This excess noise was later attributed to internal mechanical modes of the O-ring.

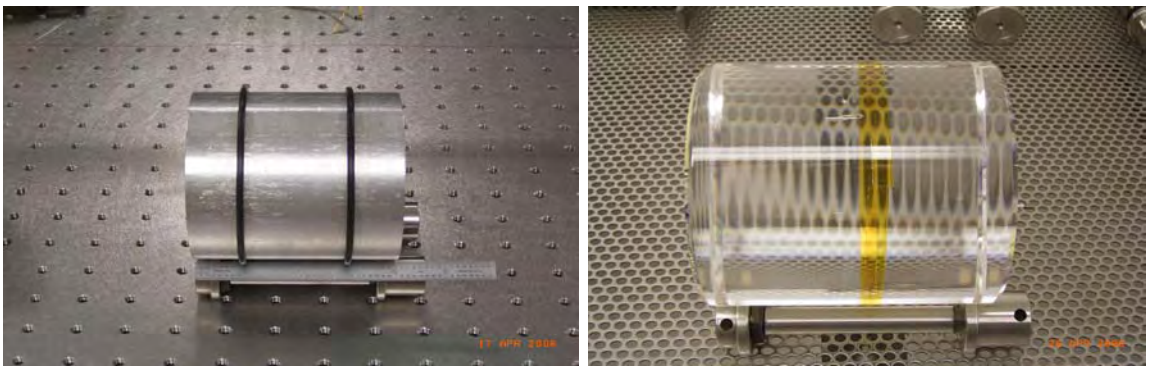

Figure 5.5: Prototype ring dampers tested at Caltech's Thermal Noise Interferometer. Left: Buna O-rings. Right: Kapton tape.

Work continued with Kapton tape – a good approximation to the types of damper studied by Gras. With shallower profile and reduced mass the Kapton was thought less susceptible to internal oscillations. Results showed no excess of noise but also limited damping capability. The maximum Q reduction was just a factor of two.

Concluding that the ideal damper must have appreciable mass like the O-ring, but no internal resonances like the Kapton, copper rings were investigated. A ring of 4 mm thickness with its first resonances above 100 kHz was selected. This ring successfully suppressed Qs so that they could not be measured but again introduced noise. In addition to the broadband noise seen previously, sharp resonances were also observed. It is believed that the screw fastening used to tighten the ring around the test mass was liable for this behaviour.

Experiments were planned to test a second copper ring. This ring was to be inductively heated and positioned over the test mass before being allowed to cool in position. This monolithic design promised to damp test mass eigenmodes without becoming itself excited. At the time of writing this idea has not yet been implemented.

Simple, yet effective, ring dampers remain an area of interest for passively damping parametric instabilities.

5.1.4.4 Resonant dampers

In addition to ring dampers there exists another promising passive damping scheme – resistively-shunted piezoelectric Acoustic Mode Dampers (AMDs) [201]. As well as simple mechanical damping these devices also dissipate energy into piezoelectric material shunted with passive electrical circuits.[6] By altering the properties of the external circuit the overall performance of the damper may be tuned.

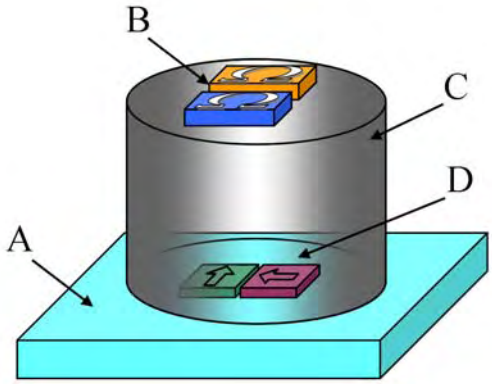

Figure 5.6: A cylinder of tungsten (C) is mounted atop two orthogonally poled PZTs (D). A resistor (B) is connected across each PZT to provide electrical damping (connections omitted for clarity). The entire assembly is attached to a rigid base plate (A). The PZT electrical connections are made on their top and bottom surfaces. This suggests the use of an entirely solder based construction with components coated as necessary. The overall dimension of the damper is around 20 mm.

For our application these devices will be constructed as illustrated in fig. 5.6. A small cylinder of tungsten is mounted atop two orthogonally poled PZTs. Each PZT has an associated resistor connected across it. These resistors shall be fixed to the tungsten mass as shown. By careful mechanical and electrical design the principal resonances of the damper can be made to coincide with the two main series of potentially dangerous acoustic modes at 15 and 50 kHz (see fig. 5.19). The tails of these and other resonances are able to damp the remaining modes. The asymmetric mounting of the cylinder[7] ensures modal degeneracy is broken extending the useful damping range.

[6] In our configuration the addition of a shunt resistor lowers the Q by a factor of ∼10.

[7] The base formed by the two PZTs is rectangular rather than square presenting different spring constants along orthogonal axes.

Unlike ring dampers these devices are expected to have a negligible noise contribution due to the properties of the PZT, their resonant design and location on the test mass. Any excess noise will likely be introduced in fixing the device to the test mass (e.g. glue). To ensure that even this component is inconsequential we limit ourselves to 1 cm^2 of contact area per damper [202].

Owing to their tuning flexibility AMDs can be accurately targeted on the most dangerous acoustic modes. In this way it is likely that excellent results can be achieved with a small number of AMDs. Although AdvLIGO is currently providing for 8 damper locations around the barrel of each test mass it is unlikely that all will be filled. Fig. 5.7 shows how the AMDs might be positioned in AdvLIGO. First experimental tests of

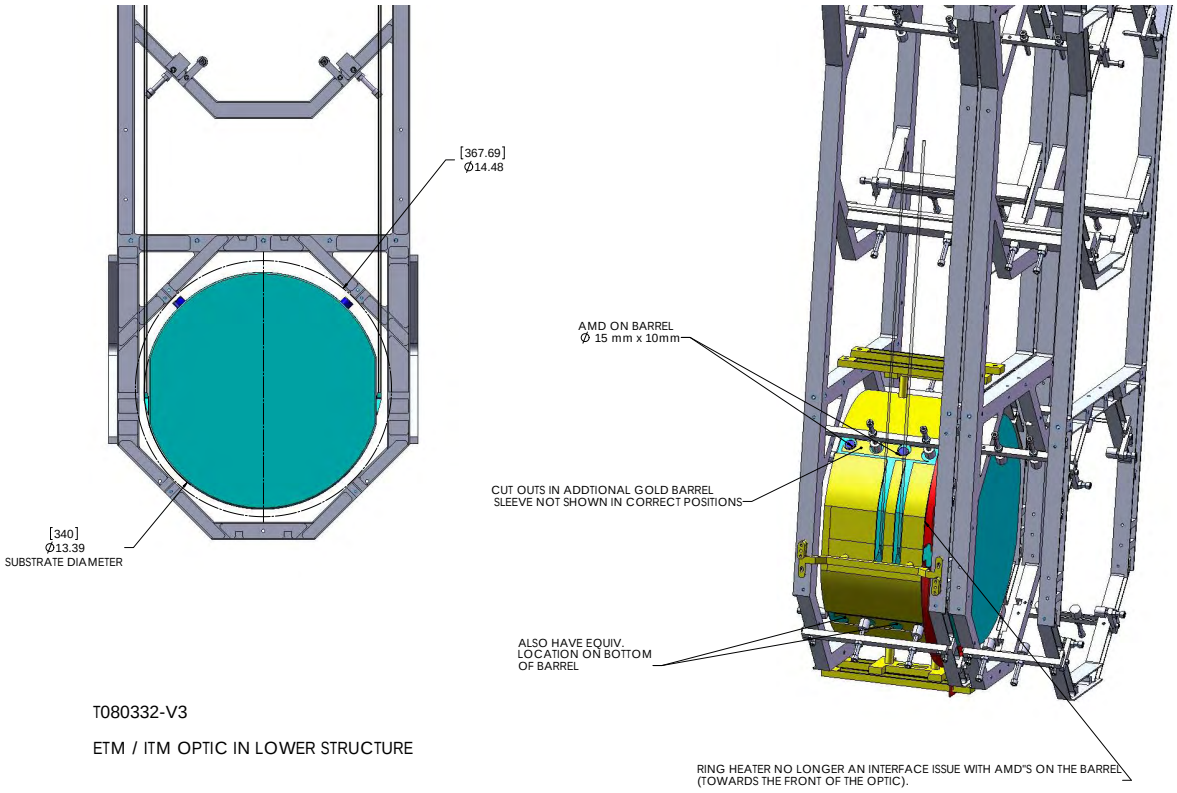

Figure 5.7: Possible locations of acoustic mode dampers (blue) in AdvLIGO. Image and annotation courtesy of C. Torrie.

this idea have been undertaken at Massachusetts Institute of Technology (MIT) using a simple PZT accelerometer in place of a bespoke damper [192]. This work confirmed the ability of such instruments to effectively reduce modal Qs and corroborated the TNI result (see §5.1.4.3) that it is essential to account for internal modes of one's damper

in order to accurately model damping performance. AMDs are a leading candidate for PI mitigation and future results are eagerly anticipated.

Having reviewed the leading schemes currently considered for ameliorating PIs the next section begins to introduce the idea investigated in this work by examining an electrostatic actuator.

5.1.5 ESD

The majority of currently operating gravitational wave detectors employ coil-magnet actuators [203] to control the position and angular orientation of their suspended optics.[8] The permanent magnets attached to the interferometer test masses are known to introduce noise through a number of mechanisms [204, 66, 205]. We give a brief account of these noise couplings and subsequently describe a new type of electrostatic actuator which will eliminate the need for magnets in future detectors.

5.1.5.1 Thermal noise due to magnets

There exists a large body of evidence highlighting the detrimental effect magnets have on test mass modal Qs, in some cases increasing loss by more than an order of magnitude (see e.g. [206]). Previously these Q modifications were translated directly into increased noise [164]; current understanding of thermal noise from inhomogeneous sources indicates that loss localised far from the beam spot is less significant [66]. Measured losses may also overestimate the effect magnets have in the GW detection band.[9] It is nevertheless prudent to take all reasonable precautions for AdvLIGO where noise

[8] GEO600 being the notable exception – it currently uses ESDs.

[9] In Initial LIGO actuator magnets are attached to metal standoffs (see fig. 5.9), raising them from the surface of the optic [207]. Internal mechanical resonances of the magnet-standoff assembly are predicted to give the loss associated with this structure an f^4 frequency dependence below resonance. This attenuation at lower frequencies suggests that values inferred from measurements at test mass eigenmode frequencies represent an upper limit on the loss which will be observed in the gravitational wave detection band. Initial measurements confirmed the f^4 dependence [208] while later studies proved inconclusive [209].

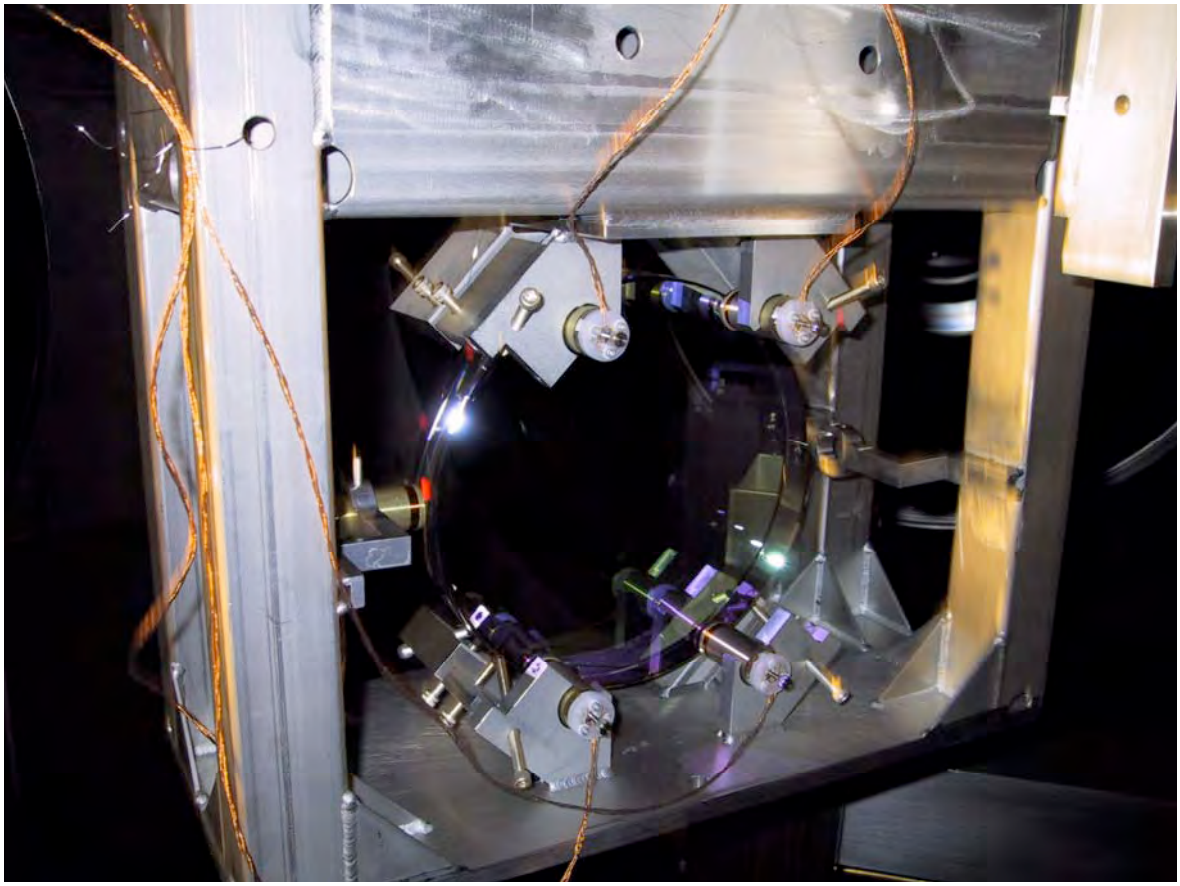

Figure 5.8: Initial LIGO test mass showing five coil-magnet actuators (OSEMs). Due to known magnetic noise couplings these actuators will be replaced with ESDs in AdvLIGO.

requirements will be around ten times more stringent. The switch to ESDs will remove the need for any actuator components on the test mass.

5.1.5.2 Barkhausen noise

During its fifth science run LIGO exhibited exquisite noise performance reaching its design sensitivity across all but a small portion of its frequency band [210]. However in the region between 50-100 Hz known sources were unable to fully explain the observed noise [211]. A series of experiments showed that non-linear upconversion of actuator coil currents to broadband noise via the Barkhausen effect was a likely candidate [212].

Barkhausen noise arises in unsaturated ferromagnetic material, such as the NdFeB

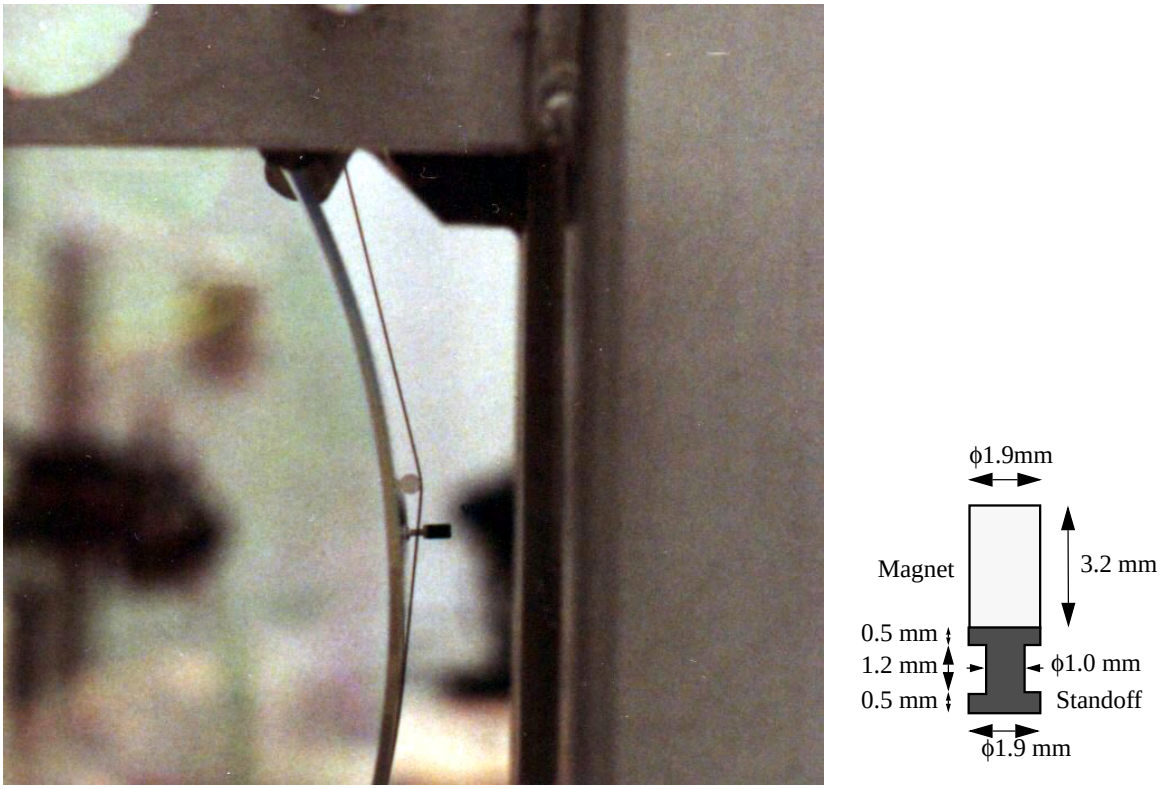

Figure 5.9: Left: Suspension wire stand off and side magnet on Initial LIGO test mass. Right: Magnet/standoff dimensions.

magnets used in Initial LIGO, due to the discrete nature of magnetic domains [205, 213]. These domains are smaller than ∼10 µm in size and contain polarised electrons with aligned magnetic moments. Each domain is effectively a quantum for the magnetisation process. When domains re-orient themselves in response to an external magnetic field (e.g. from the actuator coils) there is friction at the boundaries between domains. This friction gives rise to magnetic dissipation when the material is driven by time varying fields. In addition the domains do not respond smoothly to the external field creating stochastic fluctuations in magnetisation.

Guided by experiment the decision was made to swap the ETM magnets from Nd-FeB to saturated SmCo. The SmCo magnets were expected to be less susceptible to Barkhausen noise by a factor of more than 100. Although a conclusive study remains to be made preliminary measurements suggest that upconversion is no longer present [214]. Despite this positive result the elevated noise at low frequency remains. Current suspicion is focused on auxiliary control noise and poorly designed wire stand offs (see

fig. 5.9) which provide an ill-defined boundary condition for the suspension wires [215]. Although it appears that this magnetic problem has been efficiently diagnosed and solved it is included to illustrate the types of issues which may have been uncovered if magnets were retained for AdvLIGO.

5.1.5.3 Coupling to ambient magnetic fields

It is clearly advantageous to install strong magnets providing large control forces on the test masses of a gravitational wave interferometer. However one must ensure that such measures do not adversely affect instrument performance through coupling to ambient magnetic fields. In this section we make an estimate of the maximum permissible magnet strength which still allows AdvLIGO's technical displacement noise limit of $x_0 = 10^{-20}$ m/$\sqrt{\text{Hz}}$ at 10 Hz to be met. These arguments are based on the work of Fritschel and Schofield [216].

Despite being arranged with alternating polarity a measurable interaction exists between test mass magnets and external magnetic fields. This coupling has been characterised for Initial LIGO test masses by production of a magnetic field frequency comb near each test mass chamber [217]. Accounting for shielding by the Beam Splitter Chambers (BSCs) chambers the average coupling factor is $k = 10$ NT^{-1}(Am^2)$^{-1}$.

Ambient magnetic fields at LIGO's sites have also been investigated using both commercial and purpose built magnetometers. This work guided us in setting a conservative upper limit of $B = 10^{-11}$ T/$\sqrt{\text{Hz}}$ for the prevailing field in our calculations.[10]

A comprehensive model of the AdvLIGO quadruple suspension system has been developed over recent years by Barton [218]. Using this model the transfer function from applied actuation force to test mass displacement is easily obtained [219]. Combining the given value of $H = 6.45\times10^{-6}$ m/N with the above measurements allows us to

[10]There is some suspicion that this number is inflated by a factor of 2-3 due to magnetometer motion. This remains to be investigated.

compute a maximum allowable single magnet strength of

$$\begin{aligned} \mu_{\max} &= \frac{x_0}{BkH} \\ &= 15.5 \text{ µAm}^2, \end{aligned} \tag{5.29}$$

450 times smaller than the magnets used in initial LIGO.

Although this number represents a conservative upper limit it nevertheless illustrates the severity of the problem. Consider that, for typical actuation coefficients seen in Initial LIGO (2.2 $\text{NA}^{-1}(\text{Am}^2)^{-1}$) and a reasonable maximum rms coil current of 0.1 A this magnet strength allows a force of just 14 µN. Compare this with 200 µN expected from the ESD. Put another way, magnets able to produce a force equal to that of the ESD could inject noise up to the 1.5×10^{-19} $\text{m}\sqrt{\text{Hz}}$ level at 10 Hz.

Magnets will continue to be used to control the higher pendulum stages in AdvLIGO where residual motion requirements are more relaxed but this work clearly shows that environmental couplings prohibit their use to control the test masses. One might worry that an ESD is equally susceptible to variations in external electric fields. This is not foreseen as a problem due to the excellent shielding provided by the highly conductive vacuum chamber.

Having highlighted a selection of problems associated with coil-magnet actuators the following section introduces the electrostatic drive developed as its replacement.

5.1.5.4 The electrostatic actuator

Before describing the specifics of the ESD used in this work we introduce the working principle of the device with a simple example. With reference to fig. 5.10, consider a dielectric mass with two electrodes fixed to its surface. This construction is held at some small distance from a second dielectric mass which we wish to control. Imagine two molecules in the target dielectric placed symmetrically about the mid plane of the diagram. Creating a potential difference across the electrodes gives rise to a fringing

field which polarises these molecules. Since the electric field is non-uniform the forces acting on the the positive and negative charges are not quite collinear leading to a resultant force on each molecule F_1, F_2. By symmetry the total force on the pair of molecules $F_1 + F_2$ is downward (negative z direction). The total force on the target dielectric is obtained by summing over all such molecule pairs.

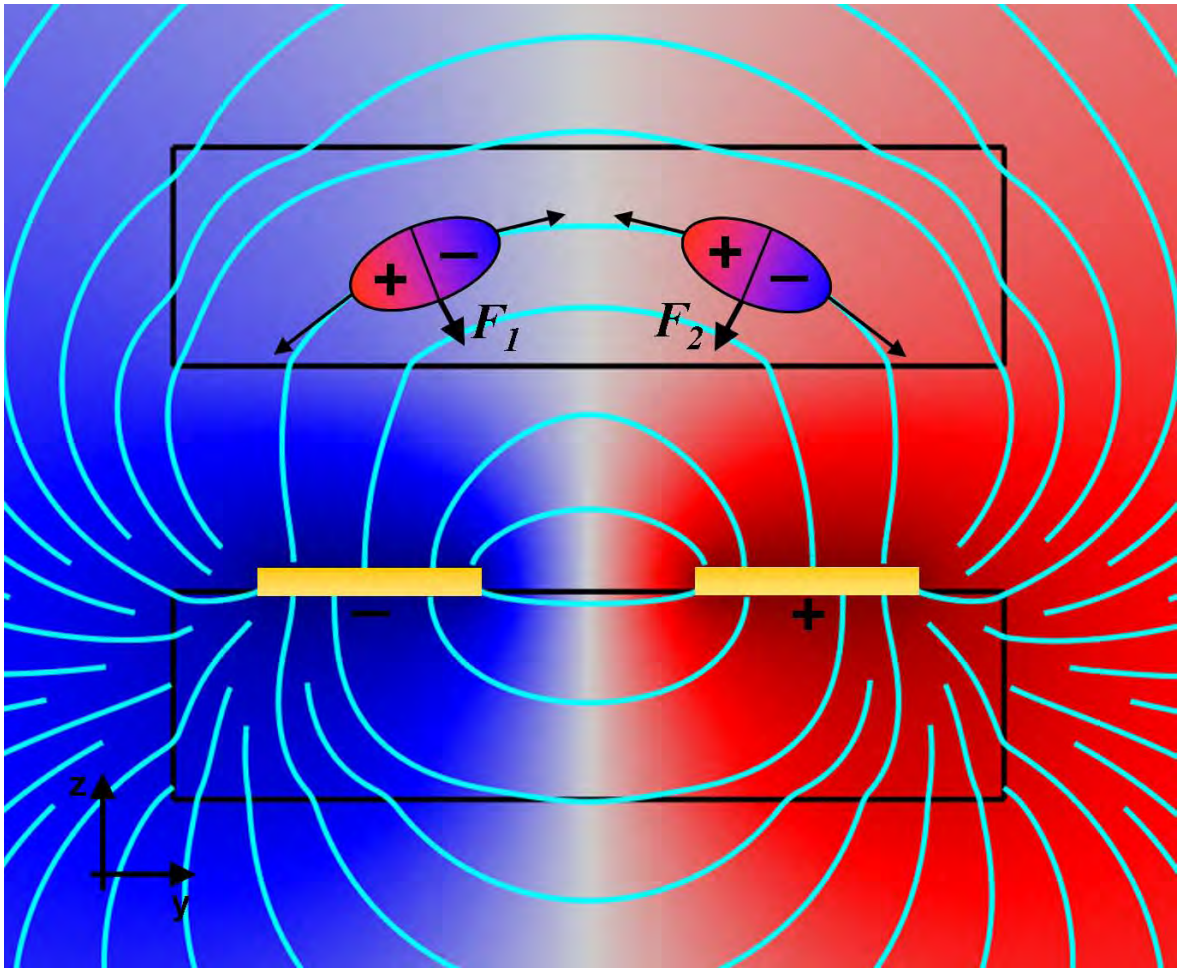

Figure 5.10: Cartoon diagram illustrating the working principle of the ESD. The upper rectangle represents the test mass containing two polarised molecules; the lower rectangle represents the reaction mass bearing two electrodes. Surface plot shows electrical potential with electric field lines shown in cyan.

Although crude, this example serves to reveal several key properties of the ESD.

- The force experienced by the test mass is entirely due to fringing electric fields. Deriving analytical descriptions of the ESD actuator is thus extremely challenging, leading us to adopt a numerical approach (see §5.2.2).

- The ESD is a non-linear device. The actuation forces are due to the interaction of polarised material with an external field. Thus we should expect the total force to be proportional to the electric field (and therefore potential difference between the electrodes) squared – one factor to induce the polarisation and a second to describe the force on the dipoles.

- This description also highlights that the force from the ESD is uniformly attractive.[11]

An ESD, as applied to gravitational wave interferometers, consists of a comb-like pattern of four interleaving electrode pairs deposited in gold onto the surface of a cylinder of high quality fused silica. This cylinder is known as a *reaction mass*. In operation four electrodes, one from each pair or quadrant, are connected to a common bias potential. Control signals are applied to the remaining electrodes providing four distinct actuators. In this way both angular and longitudinal position may be controlled.

The force produced by an ESD may be characterised as

$$F_{\mathrm{ESD}} = \alpha(\Delta V)^2, \tag{5.30}$$

where ΔV is the potential difference between the electrode pairs and α is our constant of proportionality. This constant is dependent on the separation between the test mass and the reaction mass; the material properties of the two optics and the specific geometry of the ESD pattern. In the following sections α is both numerically modelled and experimentally measured.

ESDs have been used successfully in the GEO600 interferometer for some time [220]. Drawing on this experience ESDs have been chosen as the baseline test mass actuator for AdvLIGO. In fig. 5.11 we show a prototype reaction mass bearing a pattern design considered for AdvLIGO's input test masses. All numerical and experimental work was carried out using this article. Technical drawings of the mask used in the construction of this pattern may be found in figs. B.1 and B.2 of Appendix B.

[11] This and the previous point are dealt with in §5.3.1.3.

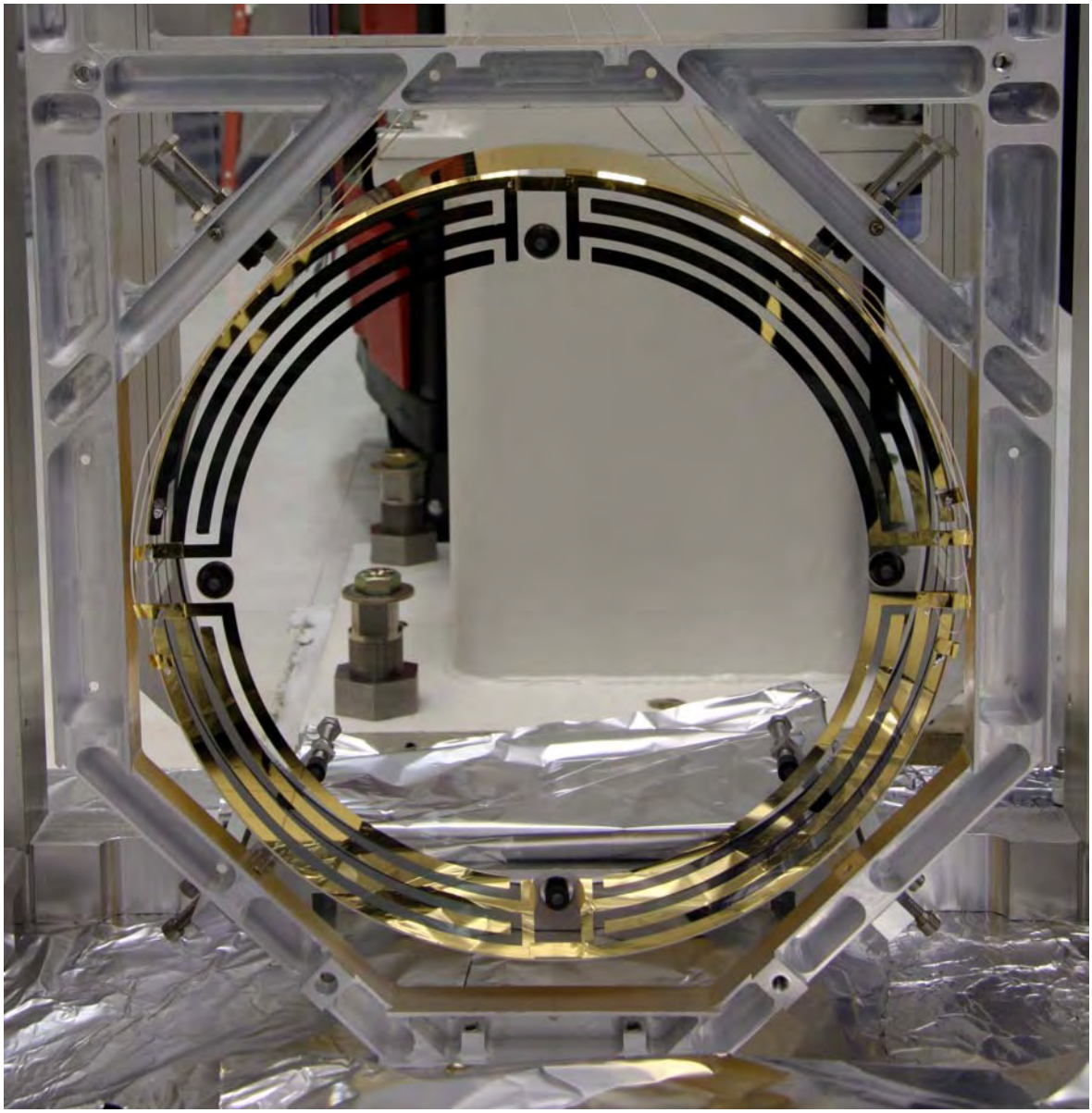

Figure 5.11: Advanced LIGO noise prototype reaction mass and ESD. This is the pattern being considered for the reaction masses for the input test masses. This design is used for all numerical and experimental work discussed herein.

In order for the fringing fields to effectively penetrate the test mass, the electrode spacing should be approximately equal to the gap between the test mass and reaction mass. For AdvLIGO this number is expected to be 5 mm. Fig. 5.12 shows the relationship of the reaction mass to the test mass pictorially.

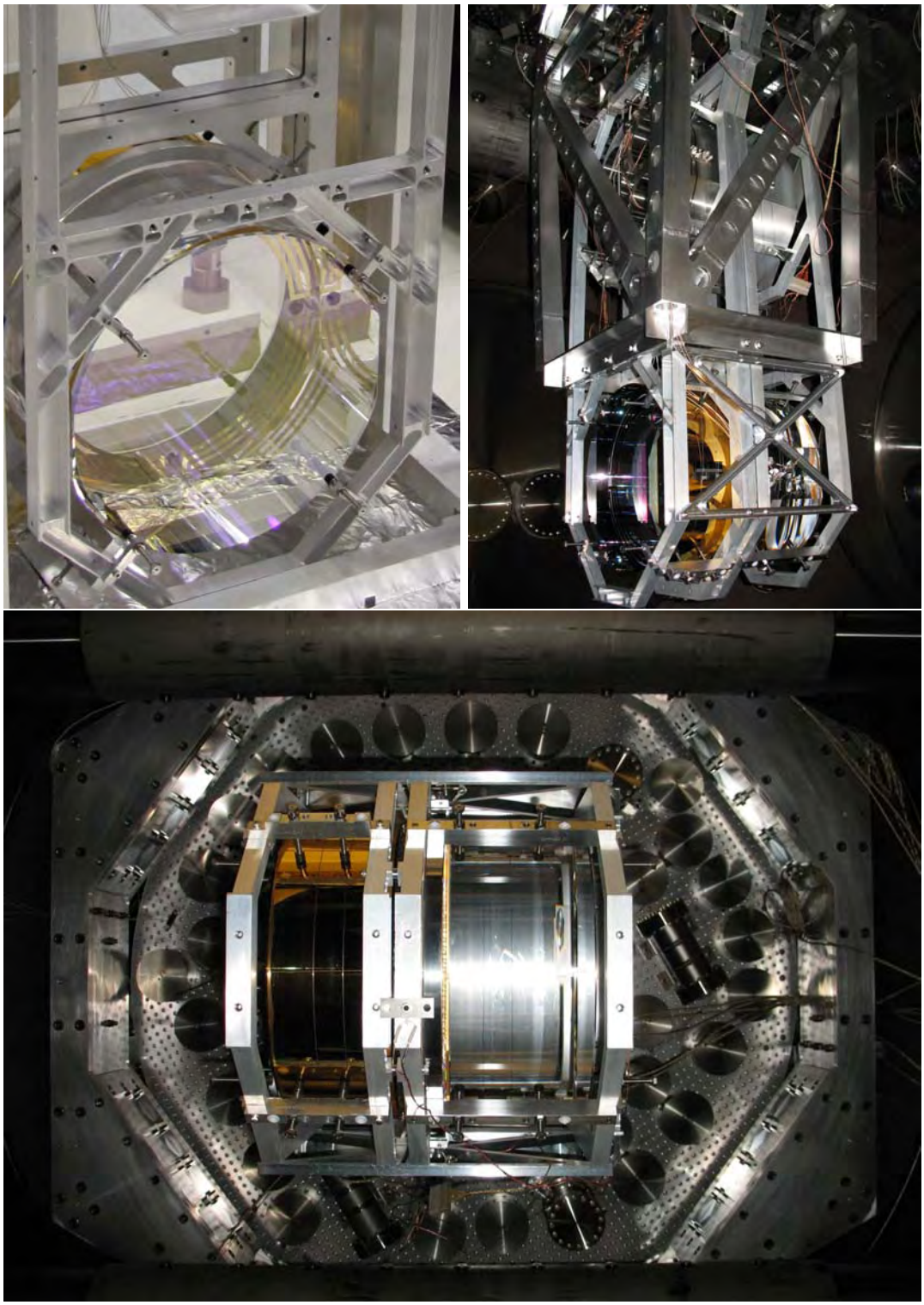

Figure 5.12: Photographs showing the relationship of the reaction mass to the test mass. Upper left: View of ESD through test mass before installation. Upper right: Complete noise prototype quadruple pendulum installation. Observe the ESD (with gold coating) immediately behind test mass. Lower: View of reaction mass (left) and test mass (right) from below.

5.1.5.5 Drawbacks

Having outlined the problems associated with magnet based actuators above, this section presents a similar discussion of the ESD.

There is risk associated with placing high voltage electrodes in such close proximity to the test masses. In 2006, after electrical problems at the GEO600 site left the optics undamped, the functionality of the ESDs was found to be seriously compromised. It is believed that, whilst the optics were freely swinging, contact was made between the test masses and live ESD electrical connections, allowing the test masses to become charged. Although the following work by Hewitson et al. [221] led to the development of techniques for gauging and removing test mass charge this incident would have been happily avoided.

Measurements carried out at Moscow State University have revealed a frequency dependent damping mechanism associated with electrostatic drives [222, 223]. It was shown that this mechanism depends greatly on the preparation of, what in our case would be, the rear surface of the test mass. The effects of this damping fall off as $1/f$ with bias voltage, recommending the use of an AC bias. It is probable that only implementation in AdvLIGO will determine whether an AC bias is truly necessary but all ESD electronics are designed to preserve this option.[12]

Accounting for the non-linearity of the ESD one normally operates with a bias large compared to the typical control forces. This large bias may couple strongly to stray charges on the dielectric test masses and also present a wider pathway for actuation noise.

A further source of damping associated with the ESD is Joule loss in the electrodes, wiring and drive amplifier. Motion of the test mass about its nominal position changes the capacitance of the drive and allows a current to flow. Any resistance in the drive

[12]The use of an AC bias has the potential to dissipate several watts of power. The current driver design uses water cooling to cope with this as cooling by convection could introduce excess noise through fans etc. It may be that commercial voltage drivers will eventually be used.

electronics leads to damping of the test mass and can thus introduce thermal noise. Fortunately the magnitude of this effect is easily reduced by minimising the real impedance presented by the electronics. Experience has shown that the electrodes can be deposited with a resistance of $\sim 5\ \Omega$ so that this effect is essentially controlled by the output impedance of the drive amplifier where there is ample design freedom.

Despite these minor issues it is our proposal that the ESD described here be used to actively suppress PIs. In the following section we begin to investigate this possibility.

5.2 Modelling

Below we describe how a theoretical estimate of the force required to damp PIs using the ESD was obtained. We begin in §5.2.1 by constructing a simple model of the system. This allows us to extract an analytical expression for the required damping force. In the following sections we populate the unknown parameters in this expression, namely the test mass mode shapes and frequencies (§5.2.3), the force distribution of the ESD (§5.2.5), the undamped parametric gains (§5.2.7) and the force coupling between the ESD and each mechanical mode (§5.2.8). We conclude in §5.2.9 by evaluating the force required to damp each mode of the test mass and comparing it to that which is available.

5.2.1 Damping forces

In this section we derive a closed form expression for the force demanded of the ESD to effectively damp a PI. Considering each acoustical mode of the test mass as a damped oscillator with resonant frequency $\omega_{0,m}$ rads^{-1} and modal mass μ_m we have

$$\mu_m \ddot{x}_m + \frac{\omega_{0,m}\mu_m}{Q_m}\dot{x}_m + k_m x_m - F_{\mathrm{app},m} = 0, \tag{5.31}$$

where $F_{\text{app},m}$ is that portion of the total ESD force which is effectively coupled into mode m. Assuming viscous damping,

$$F_{\text{app},m} = -K_m \dot{x}_m, \tag{5.32}$$

we write

$$\mu_m \ddot{x}_m + \left[\frac{\omega_{0,m}\mu_m}{Q_{\text{eff},m}}\right]\dot{x}_m + k_m x_m = 0. \tag{5.33}$$

In doing so we have defined an effective Q,

$$Q_{\text{eff},m} = \left(\frac{1}{Q_m} + \frac{K_m}{\mu_m \omega_{0,m}}\right)^{-1}, \tag{5.34}$$

whence

$$K_m = \mu_m \omega_{0,m}\left(\frac{1}{Q_{\text{eff},m}} - \frac{1}{Q_m}\right). \tag{5.35}$$

Assuming sinusoidal time variation, so that we may write $\dot{x}_m = j\omega_{0,m}x_m$,

$$\begin{aligned} F_{\text{app},m} &= -K_m \dot{x}_m \\ &= -\mu_m \omega_{0,m}\left(\frac{1}{Q_{\text{eff},m}} - \frac{1}{Q_m}\right) j\omega_{0,m} x_m. \end{aligned} \tag{5.36}$$

For thermal excitations we have

$$x_m \;=\; \sqrt{k_B T_0/\mu_m \omega_{0,m}^2}, \tag{5.37}$$

where k_B is Boltzmann's constant and T_0 is the ambient temperature. Thus

$$F_{\text{app},m} = -j\omega_{0,m}\sqrt{\mu_m k_B T_0}\left(\frac{1}{Q_{\text{eff},m}} - \frac{1}{Q_m}\right). \tag{5.38}$$

To account for the coupling between the ESD actuation force and the mechanical mode in question we introduce an additional parameter b_m defined through $F_{\text{app},m} = b_m F_{\text{ESD},m}$. This coupling may be calculated as follows

$$b_m = \iint_{\mathcal{S}} f_{\text{ESD}}(\vec{u}_m \cdot \hat{z})\,\mathrm{d}\mathcal{S}, \tag{5.39}$$

where f_{ESD} is the force density of the ESD and $\vec{u}_m \cdot \hat{z}$ is the displacement of the mirror's surface along the cavity axis. These quantities have normalisations

$$\iint_{\mathcal{S}} f_{\mathrm{ESD}}\,\mathrm{d}\mathcal{S} = 1 \quad \text{and} \quad \iiint_{\mathcal{V}} \rho|\vec{u}_m|^2\,\mathrm{d}\mathcal{V} = 1, \tag{5.40}$$

ρ being the uniform mass density of the test mass, $\mathcal{S}$ the rear surface of the optic normal to the cavity axis and $\mathcal{V}$ the test mass volume. With this normalisation $\mu_m = 1$ for all modes.

Including the overlap parameter b_m and making use of the proportionality of Q and R, i.e.

$$Q_{\mathrm{eff},m} = Q_m \frac{R_{\mathrm{eff},m}}{R_m}, \tag{5.41}$$

we find the magnitude of force demanded from the ESD to reduce the parametric gain from R_m to $R_{\mathrm{eff},m}$ for a thermally excited mode is

$$F_{\mathrm{ESD},m} = \sqrt{\mu_m k_B T_0}\frac{\omega_{0,m}}{b_m}\left(\frac{R_m - R_{\mathrm{eff},m}}{Q_m R_{\mathrm{eff},m}}\right). \tag{5.42}$$

As (5.42) shows, $F_{\mathrm{ESD},m}$ is a strong function of b_m and R_m. In order to accurately calculate required damping forces we must have a solid estimate of both factors. To achieve this we require the ESD force density f_{ESD}, the mechanical mode shapes $\vec{u}_m$ and their frequencies $\omega_{0,m}$. Given the complexities involved, a numerical approach was adopted.

5.2.2 Finite element model

The Finite Element Method (FEM) is a well-known technique for numerically solving differential equations. Unlike some other numerical methods, like the finite difference method [224] for example, it is particularly well suited to problems involving the strange geometries often found in engineering and the physical sciences. The FEM converts a problem with an infinite number of unknowns (e.g. values of scalar field) into a soluble

problem with a finite, albeit sometimes large, number of unknowns. This is achieved via a number of steps.

The region of the problem is first divided into a number of smaller domains, the *finite elements*. An example of this division process, called *meshing*, may be seen in fig. 5.14. The locations where element boundaries intersect are known as *nodes*.

An interpolation function is then assumed for each element. The value of the unknown at any point within an element is uniquely determined by the values at the nodes and the interpolation function. These functions are often chosen to be polynomials since they may easily be integrated and differentiated. The order of the polynomial typically depends on the number of nodes the element possesses.

The appropriate matrix equation is then formed on each element from the global governing equation. There exist a number of standard methods for completing this task (e.g. Galerkin's method [225]) which shall not be discussed here.

Using the fact that the unknown must be equal for all elements sharing a node, the element equations are assembled into a global system of equations. At this point boundary conditions are applied.

In static situations this system may be solved algebraically. In cases with temporal variation the global PDE is transformed into a system of ODEs which may be solved via standard methods (e.g. Runge-Kutta [226]). This solution provides the nodal values, using the interpolation functions we extend the solution to the whole domain. Further post-processing allows one to compute gradients, fluxes and the like.

This piecewise approximation provides good accuracy even for simple interpolation functions. However we must remember that solutions are always approximate. By increasing the number of elements, arbitrary precision may be achieved at the expense of computation time. In reality the mesh resolution is often tailored to better capture behaviour in regions of interest.

Modern FEM packages (e.g. [227, 228]) are extremely powerful tools which often hide the above method from the casual user. Great care must be taken to ensure that the correct questions are well posed and that the solutions provided are both valid and accurate.

Finite element models are ideally suited to problems where the global governing equation is well-known but complex geometry or boundary conditions make finding closed form solutions difficult. Below we describe two such problems which were encountered in our study of parametric instabilities, one in continuum mechanics and one in electromagnetism. We begin by outlining the derivation of the governing equations before describing the models themselves and presenting typical results.

5.2.3 Eigenfrequency analysis

The fundamental equation for linear elasticity is the equilibrium equation. In engineering notation

$$\vec{F} - \nabla \cdot \Theta = 0, \tag{5.43}$$

where Θ is the stress tensor and $\vec{F}$ denotes the body/volume forces.

In eigenfrequency analysis the solution we seek is a frequency-displacement pair, hence it is beneficial to formulate the equilibrium equation in terms of displacements. To do so we must define two relationships; that between strain and displacement and that between stress and strain.

For our three dimensional problem we write the deformation as $\vec{u} = (u, v, w)$. The six independent components of the strain tensor are then given by

$$\begin{aligned} E_x &= \frac{\partial u}{\partial x} & E_{xy} &= \frac{1}{2}\left(\frac{\partial u}{\partial y} + \frac{\partial v}{\partial x}\right), \\ E_y &= \frac{\partial v}{\partial y} & E_{yz} &= \frac{1}{2}\left(\frac{\partial v}{\partial z} + \frac{\partial w}{\partial y}\right), \\ E_z &= \frac{\partial w}{\partial z} & E_{xy} &= \frac{1}{2}\left(\frac{\partial w}{\partial x} + \frac{\partial u}{\partial z}\right). \end{aligned} \tag{5.44}$$

Treating the components of stress and strain as entries in column vectors, the standard stress strain relationship $\Theta = C_{\text{elast}}E$ may be written as

$$\begin{pmatrix} \Theta_x \\ \Theta_y \\ \Theta_z \\ \Theta_{xy} \\ \Theta_{yz} \\ \Theta_{xz} \end{pmatrix} = \frac{Y}{(1+\sigma)(1-2\sigma)} \begin{pmatrix} 1-\sigma & \sigma & \sigma & 0 & 0 & 0 \\ \sigma & 1-\sigma & \sigma & 0 & 0 & 0 \\ \sigma & \sigma & 1-\sigma & 0 & 0 & 0 \\ 0 & 0 & 0 & \frac{1-2\sigma}{2} & 0 & 0 \\ 0 & 0 & 0 & 0 & \frac{1-2\sigma}{2} & 0 \\ 0 & 0 & 0 & 0 & 0 & \frac{1-2\sigma}{2} \end{pmatrix} \begin{pmatrix} E_x \\ E_y \\ E_z \\ 2E_{xy} \\ 2E_{yz} \\ 2E_{xz} \end{pmatrix}, \tag{5.45}$$

where Y is Young's modulus, σ is Poisson's ratio and C_{elast} is the elasticity matrix. Isotropic behaviour is assumed.

Through substitution of our newly defined relationships (5.44) and (5.45) we obtain the equilibrium equation (5.43) in displacement form

$$\vec{F} - \nabla \cdot (c_0 \nabla \vec{u}) = 0, \tag{5.46}$$

where c_0 is a constant dependent on material properties. This equation governs static motion. In order to perform a modal analysis we must include the mass. Assuming sinusoidal solutions we write

$$-\chi c_1 \vec{u} - \nabla \cdot c_0 \nabla \vec{u} = 0, \tag{5.47}$$

where the c_1 coefficient includes the density of our object and χ is our eigenvalue.

(5.47) is solved to find the eigenvectors/mode shapes $\vec{u}$ and eigenvalues χ. The modal frequency is obtained from the eigenvalue as

$$f = \frac{\sqrt{\chi}}{2\pi}. \tag{5.48}$$

Accurately modelling a complex system in contemporary FEM software involves many choices. For example, which type of elements, pre-conditioning, solvers and smoothing

to use. For readability we omit a comprehensive discussion of all options, instead highlighting those choices critical to our arguments. The main properties of the FEM models are described in tables 5.1 and 5.2.

Table 5.1: Parameters used in eigenmode analysis of Advanced LIGO test mass.

	Quantity	Value
Fused silica	Young's Modulus	72 GPa
	Poisson's ratio	0.17
	Density	2202 kg m^{-3}
Test mass	Radius	0.17 m
	Thickness	0.2 m
	Flats on side of mass	0.095 m
	Wedge angle	0.167°
Eigenfrequency simulation	# elements	100,000
	# nodes	160,000

Mode shapes and frequencies of an AdvLIGO test mass were found using ANSYS [228]. The elements used each had 10 nodes with three degrees of freedom per node (u, v, w). Plasticity, hyperelasticity, creep, stress stiffening, large deflection, and large strain capabilities were all incorporated into the model.

This analysis produced several thousand mode shapes with frequencies in the 10-90 kHz band. We limit ourselves to this region as higher frequency modes typically couple to high order optical modes which suffer from significant clipping losses and thus yield low parametric gain. Figure 5.13 shows typical output from our model – the total test mass displacement and the displacement along the beam direction. These data was subsequently used in the calculation of theoretical parametric gains and damping forces.

5.2.4 Electrostatic model

As a consequence of the complex electrode geometry and non-uniform electric fields involved, the calculation of the force produced by the ESD is a demanding problem also well suited to finite element analysis. We begin by deriving the appropriate governing

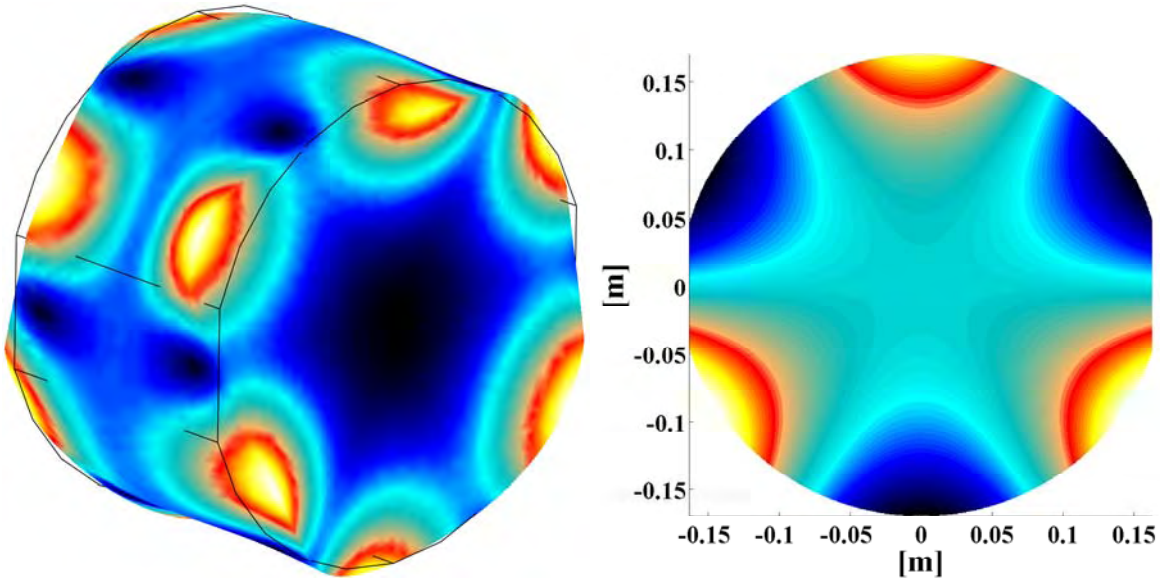

Figure 5.13: Output of eigenmode analysis. Test mass acoustical mode at 14275 Hz. Left: Total displacement $\sqrt{\Re[u]^2 + \Re[v]^2 + \Re[w]^2}$ where $\vec{u}_m = (u, v, w)$. Right: Surface displacement along beam axis $\vec{u}_m \cdot \hat{z}$.

equation. Gauss' law gives

$$\nabla \cdot D = \rho_{\text{free}}. \tag{5.49}$$

Applying our chosen constitutive relation

$$D = \varepsilon_0 \varepsilon_r E = \varepsilon E, \tag{5.50}$$

we find

$$\nabla \cdot E = \frac{\rho_{\text{free}}}{\varepsilon}. \tag{5.51}$$

Now, the electrostatic potential may be defined as

$$E = -\nabla V, \tag{5.52}$$

so that combining (5.51) and (5.52) we may eliminate E and arrive at

$$\nabla^2 V = -\frac{\rho_{\text{free}}}{\varepsilon}, \tag{5.53}$$

a form of Poisson's equation. A second model solving this equation was constructed using COMSOL Multiphysics [227]. The field variable solved for in this electrostatic

simulation is the electric potential V, all fields and quantities of interest are easily derived from this.

For concreteness and in order to facilitate verification by experiment the following sections limit their discussions to the particular ESD shown in figure 5.11. This pattern is a design considered for AdvLIGO's input test mass reaction chains. The electrode dimensions entered into our model were taken from the mask used in their manufacture. Technical drawings of this mask may be found in figs. B.1 and B.2 of Appendix B. Other model parameters are given in table 5.2.

Table 5.2: Parameters used in finite element model of electrostatic drive.

	Quantity	Value
Fused silica	Young's Modulus	72 GPa
	Poisson's ratio	0.17
	Density	2202 kg m^{-3}
	Relative permittivity	3.75
Test mass	Radius	0.17 m
	Thickness	0.2 m
	Flats	0.095 m
	Wedge angle	0.167°
Reaction mass	Radius	0.17 m
	Thickness	0.13 m
Max. element sizes	Volume of test mass	1 cm
	Rear surface of test mass	1.5 mm
	Front surface of reaction mass	1 cm
	Electrodes	5 mm
Mesh	# elements	445,060†
	# nodes	601,272†

† For 5mm separation.

The electrostatic simulation incorporated several sub domains – the test mass, the reaction mass, the electrodes and the *outside world* – making it decidedly more complicated than the eigenfrequency analysis. This added complexity necessitated a number of measures.

Finite element methods often encounter difficulties when the ratio of scales in the problem is large. In our model we were bound to accurately describe both a test

mass of thickness 0.2 m and the gold electrodes of thickness ∼500 nm. Pre-scaling the model geometry can often allay this problem but in this instance a different strategy was preferred. We chose to implement the electrodes as a 2D object within the greater 3D model. As such the electrodes had vanishing extent along the cavity direction. The negligible change in electric field at the test mass is more than offset by the number of elements which are liberated for use in other areas.

The electrical characteristics of the electrodes were also simplified. To each piece of the gold pattern a uniform potential was ascribed, effectively assuming perfect conductivity. In doing so practicalities associated with connectors and their positioning were avoided allowing one to focus on more pertinent aspects of the problem.

Even with these approximations it was found that describing the entire domain with good fidelity was outside the capabilities of the computing resources available. Model output was found to vary as a function of model parameters at an unacceptable level. In order to reduce computational cost, symmetry was employed.

Exploiting the natural four-fold symmetry of the ESD pattern (see figs. B.1 and B.2) the application of appropriate boundary conditions enables one to accurately simulate the behaviour of the entire ESD through study of a single quadrant (see fig. 5.14). This reduction in scope permitted the use of a finer mesh in key areas allowing convergence to be achieved. Fig. 5.14 shows the final meshing of the model.

Recall that the field variable solved for in this electrostatic simulation is the potential V. Fig. 5.15 shows a representative model solution plotting V across the rear surface of the test mass.

To evaluate the force coupling between the ESD and the various mechanical modes we must however convert this potential into a force distribution.

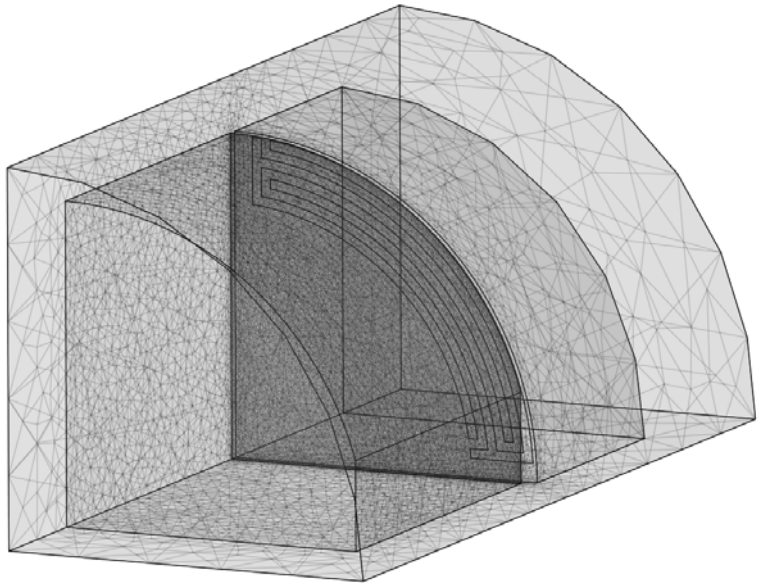

Figure 5.14: Finite element model of a prototype AdvLIGO ESD showing test mass (front) and reaction mass with ESD (rear). We exploit the four-fold symmetry of the problem to reduce computational cost. Note the concentration of elements on the rear surface of the test mass.

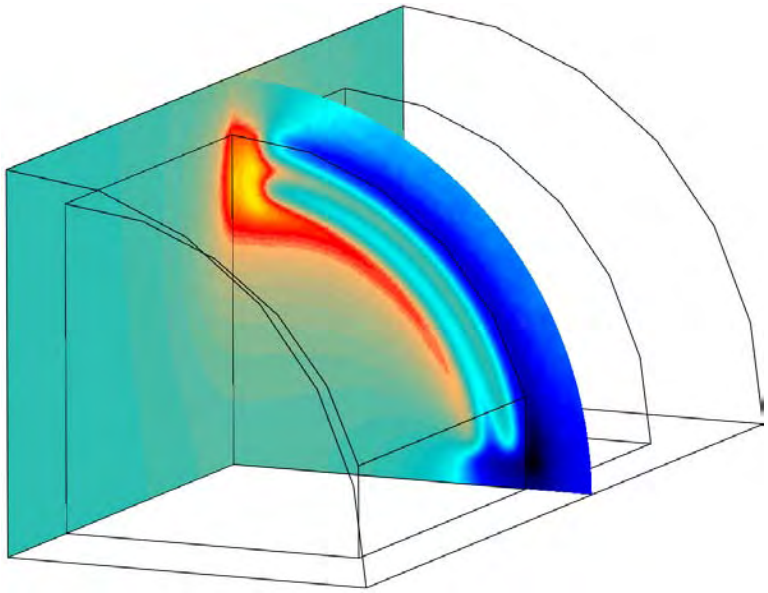

Figure 5.15: Finite element model of a prototype AdvLIGO ESD showing test mass (front) and reaction mass with ESD (rear). This slice plot displays the electrical potential across the rear surface of the test mass. Yellow is positive; blue negative. With ±100 V on the electrode pairs one finds approximately ±50 V on the test mass.

5.2.5 Force distribution

COMSOL possesses a wide array of advanced post-processing capabilities allowing one to extract fields and quantities of interest from the solution variable. With a view to finding the force density $f_{\mathrm{ESD}}(x, y)$ across the transverse dimensions of the test mass the Maxwell stress tensor (MST) was constructed from the electrical potential. For our electrostatic simulation

$$\Upsilon_{ij} = E_i D_j - \frac{1}{2}\delta_{ij} \sum_{k=1}^{3} E_k D_k, \tag{5.54}$$

where E_i and D_i are the i^{th} Cartesian components of electric and displacement fields and δ_{ij} is the Kronecker delta.

The analysis then proceeded in the following way

Export interior data Both $\Upsilon_{zx}, \Upsilon_{zy}$ are evaluated over a uniform 3 dimensional grid encompassing the test mass (total number of points $\sim 5 \times 10^6$) and exported.

Export boundary data Variously $\Upsilon_{zx}, \Upsilon_{zy}, \Upsilon_{zz}$ as appropriate are evaluated at nodes residing on the test mass boundary and exported. These components are then interpolated onto the uniform grid of the interior data.

Integrate MST The test mass was subsequently divided, in the abstract sense, into an array of right rectangular prisms whose long axes were oriented along the beam direction. The edges of these prisms ran along the vertices of our grid. The MST was then numerically integrated over the exterior of specific combinations of prisms to determine the force experienced by the volumes of test mass enclosed.[13]

Convert force data into a force density The selection of prism combinations was carefully orchestrated so that, by later subtraction, the force on every prism could be obtained. Dividing each force by the area of the prism base we obtain the

[13]N.B. Although the MST integrates over a closed volume to give a force it is not itself a force density. See for example [229].

force density evaluated on a fine 2D grid across the transverse dimension of the test mass.

The force density obtained for our selected ESD pattern (fig. 5.11) is shown in figure 5.16.

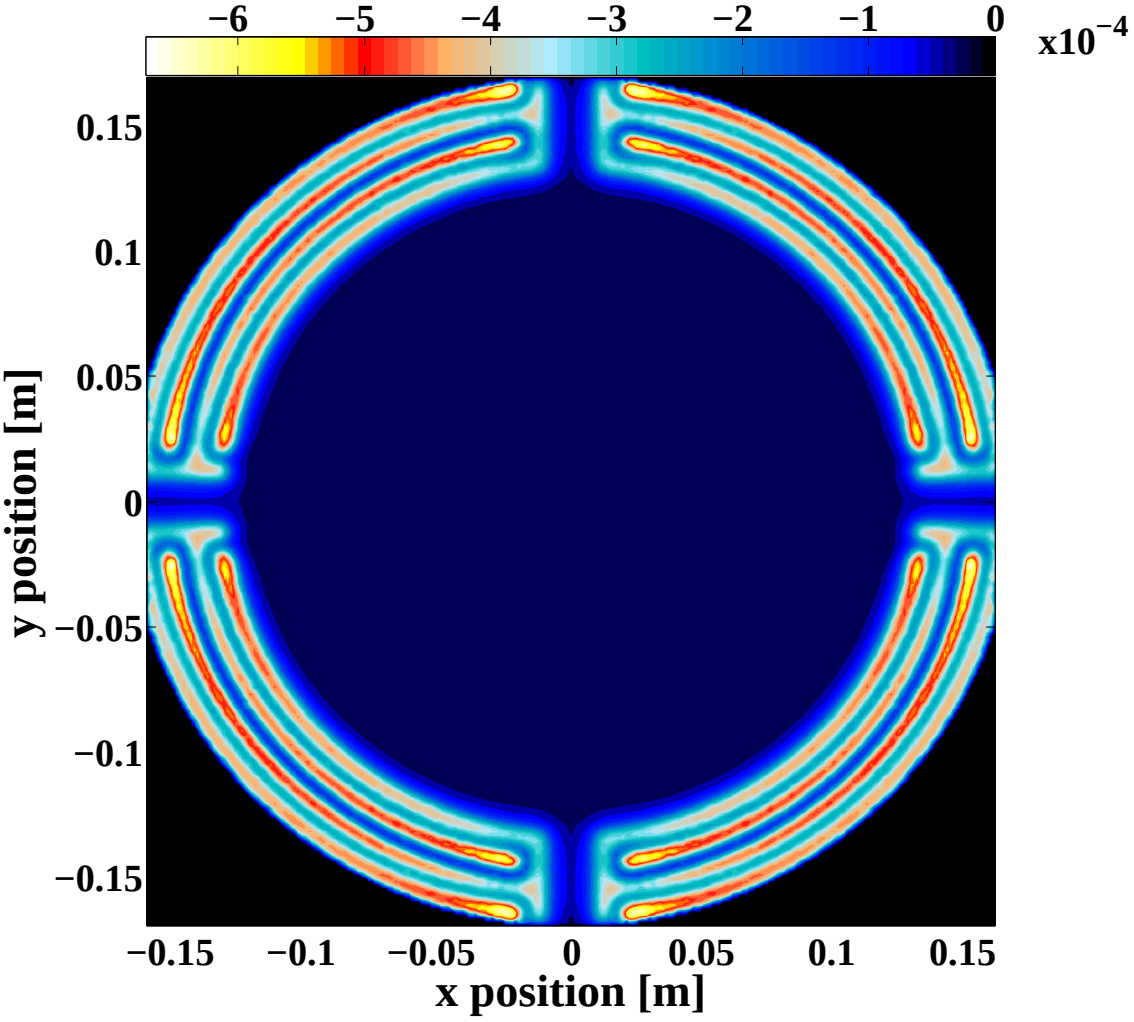

Figure 5.16: Force density as a function of transverse position across the test mass in Nm^{-2}. Forces are uniformly attractive and most significant directly in front of the electrode pattern. Values shown for $\Delta V = 200$ V.

5.2.6 Absolute force

A critical parameter for lock acquisition and interferometer control is the peak force available from the ESD. Integrating our force density over the test mass (or equivalently integrating the MST over the test mass boundary) we find that $\alpha = 2.9 \times 10^{-10}$ N/V^2.[14] For $\Delta V = 800$ V, a reasonable value for a wide bandwidth, low noise voltage amplifier and one considered for AdvLIGO, this corresponds to a nominal maximum force of $\sim$190 µN. The effects of small variations in model parameters on this prediction shall be investigated in this section.

The nominal separation between the test mass and reaction mass is 5 mm. However given the elaborate nature of the quadruple suspension (see §5.3.1.1) it is not unreasonable to expect that this value may have a static offset of as much as ± 0.5 mm [230]. There is also potential for this gap to vary as a function of time, driven by thermal gradients for example.[15] Considering the implications this might have for interferometer control and calibration it is important to quantify this effect.

To this end the existing FEM model was invoked in a loop, varying the intermass separation in a stepwise manner. Upon each iteration the model was remeshed according to the rules set forth in table 5.2 and the usual limits on mesh growth rate and curvature. From the resulting model solutions one is able to determine the coupling coefficient α as a function of separation. This dependence is illustrated in fig. 5.17.

A standard least square fit reveals that $\alpha \propto d^{-2.4}$. Over our estimated range of static deviations this would allow α to vary by as much as $\pm 30\%$. Static offsets are not the only cause for concern. Although not achieved in Initial LIGO [231] one would hope to achieve a calibration accuracy of around 1%. In order for stochastic changes in the separation of the masses not to compromise this effort the separation must be controlled to within $\pm 2 \times 10^{-5}$ m. Recent modelling work suggests that this is easily achievable.

[14] Recall that $F = \alpha \Delta V^2$

[15] Seismic effects are likely negligible as the test mass and reaction mass will move together at low frequencies and are well isolated at high frequencies.

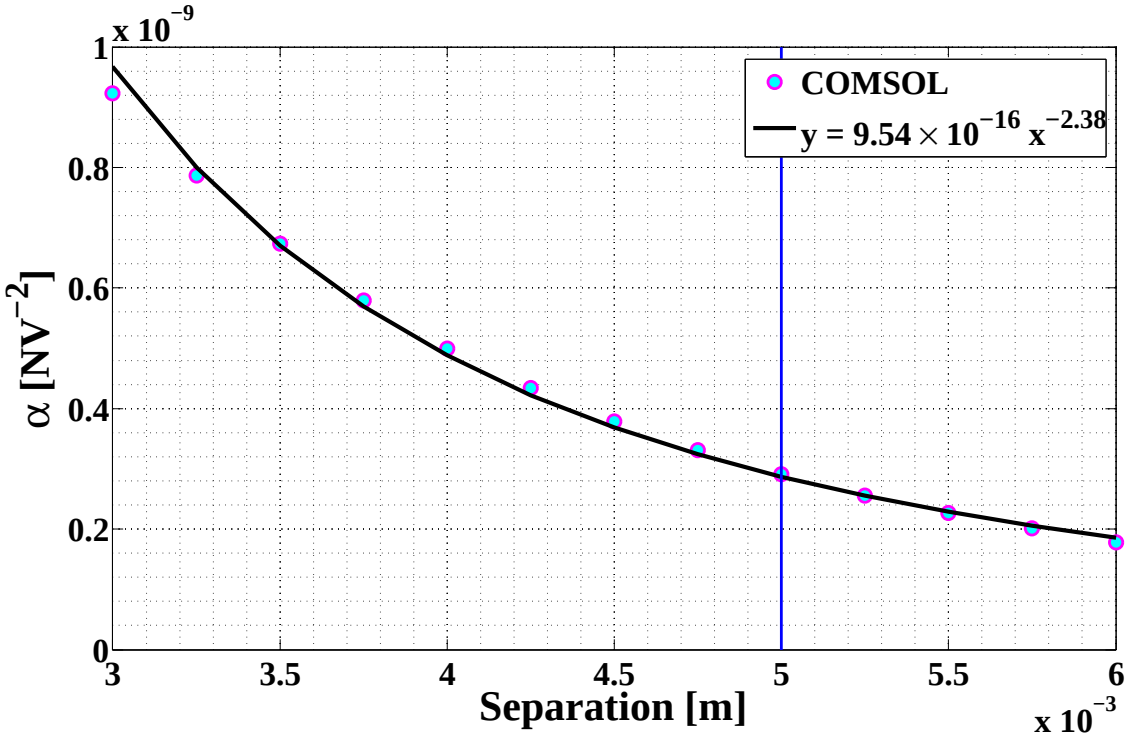

Figure 5.17: The ESD coupling coefficient α as a function of separation between the reaction mass and the test mass. Vertical line shows nominal separation corresponding to 2.9×10^{-10} NV^{-2}. Least squares fitting reveals that dependence is stronger than quadratic.

Another area in which there is often great uncertainty is in the selection of material properties. For our fused silica masses we chose to use $\varepsilon_r = 3.75$. So that we might study the implications of this decision a second series of simulations were run.

Fixing the separation to 5 mm the relative permittivity of both masses was varied simultaneously. Again a new mesh was constructed and a value for α extracted upon each iteration. The resulting data is shown in fig. 5.18. The dependence is purely quadratic with coefficients (-7.932e-012,1.167e-010,-3.566e-011) in order of descending power – a dramatically weaker effect than variation in separation. The potential for changes in α is of the order ± 5 % for a reasonable range of ε_r.

Both results suggest that all parameters should be verified before model output is used with confidence. With this caveat in mind we begin to evaluate the parametric gain R_m and the ESD mechanical mode coupling b_m in the next section.

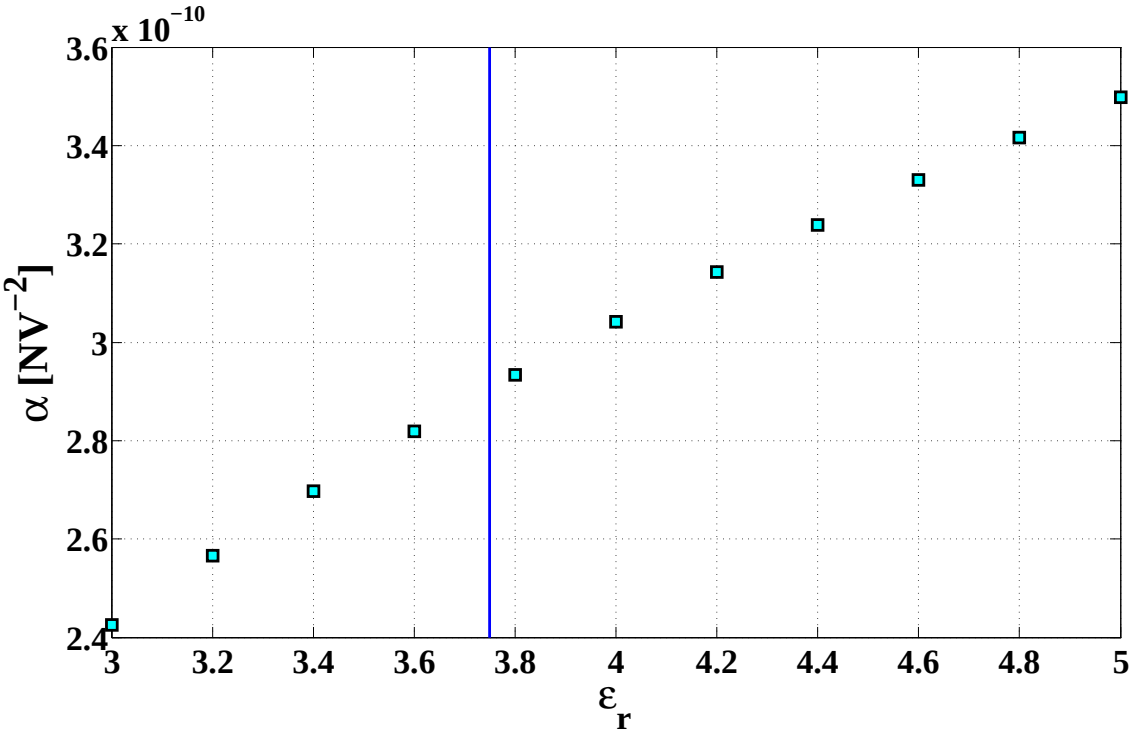

Figure 5.18: α as a function of relative permittivity ε_r of both masses. Assumed value of 3.75 is indicated by vertical line.

5.2.7 Parametric gain

Section 5.1.2 exposed the relationship between parametric gain and $B_{m,n}$, the geometric overlap of the scattered HOM fields with the test mass eigenmode. Having calculated the mechanical mode shapes in §5.2.3 the numerical value of $B_{m,n}$ may be determined. Using this information, the methodology developed in §5.1.2 may be applied to investigate whether PIs are of concern in future dual recycled Fabry-Perot interferometers.

Our model parameters are listed in table 5.3. These values are broadly representative of AdvLIGO but by no means definitive.

At the time of writing there exists some ambiguity regarding a selection of these values. In these cases we make educated order of magnitude estimates. For example, in AdvLIGO circulating arm power is expected to be ∼850 kW whereas we assume 1 MW and in keeping with current measurements [56] and experience of full size suspended

Table 5.3: Interferometer parameters used in the theoretical evaluation of parametric gain.

	Quantity	Value
Lengths	Arm cavity	3994.5 m
	Power recycling cavity	57.175 m
	Signal recycling cavity	55.475 m
Gouy phases♯	Arm cavity	135°
	Power recycling cavity	20°
	Signal recycling cavity	25°
Optical properties	Circulating arm power	1 MW
	Input mirror power transmittance	0.014
	End mirror power transmittance	10^{-5}
	Power recycling mirror power transmittance	0.03
	Signal recycling mirror power transmittance	0.2
	Beam splitter power transmittance	10^{-5}
	Laser wavelength	1064 nm
Mechanical properties	Mass of test mass	40 kg
	Mechanical mode Q	10^7

♯ The one way Gouy phases listed above are calculated from $\Delta\psi = \arccos(\pm\sqrt{g})$. $g = (A + D + 2)/4$ is the generalised cavity g factor, where A and D are the diagonal elements of the cavity round trip ABCD matrix.

optics within the field we assume a value of $Q_m = 10^7$ for all modes.[16]

There is potential for large discrepancies between theoretical values of parametric gain and any eventual experimental measurement. Mode frequencies obtained from finite element models may not accurately match those witnessed experimentally due to small differences in material properties or prevailing temperature.[17] Control issues may prevent the circulating power from reaching its design value. Optical gain may be different due to deviations of mirror radii of curvature from their nominal values, causing small but consequential changes in Gouy phase.

To allow for realistic variations in model parameters 'worst case' R_m values were calculated. The parametric gain is predominantly sensitive to the overlaps in frequency space between the mechanical modes and higher order cavity modes. By randomly

[16]Estimated Q values will only become more accurate once a prototype of AdvLIGO's quasi monolithic suspension design is available.

[17]Due to thermal compensation systems for example.

varying the Gouy phases of the cavities about their fiducial values an upper limit – the smallest value greater than 99% of the results – was found for each mode. 120,000 trials were conducted varying the phase in the arms over 5×10^{-3} degrees and the phases of the recycling cavities over a few degrees.

Results are shown in fig. 5.19. We find 212 modes with $R > 0.1$ and 32 modes with $R > 1$. The maximum gain is less than 30. Comparable with other investigations, such results suggest that parametric instabilities are an issue of concern for second generation interferometers.

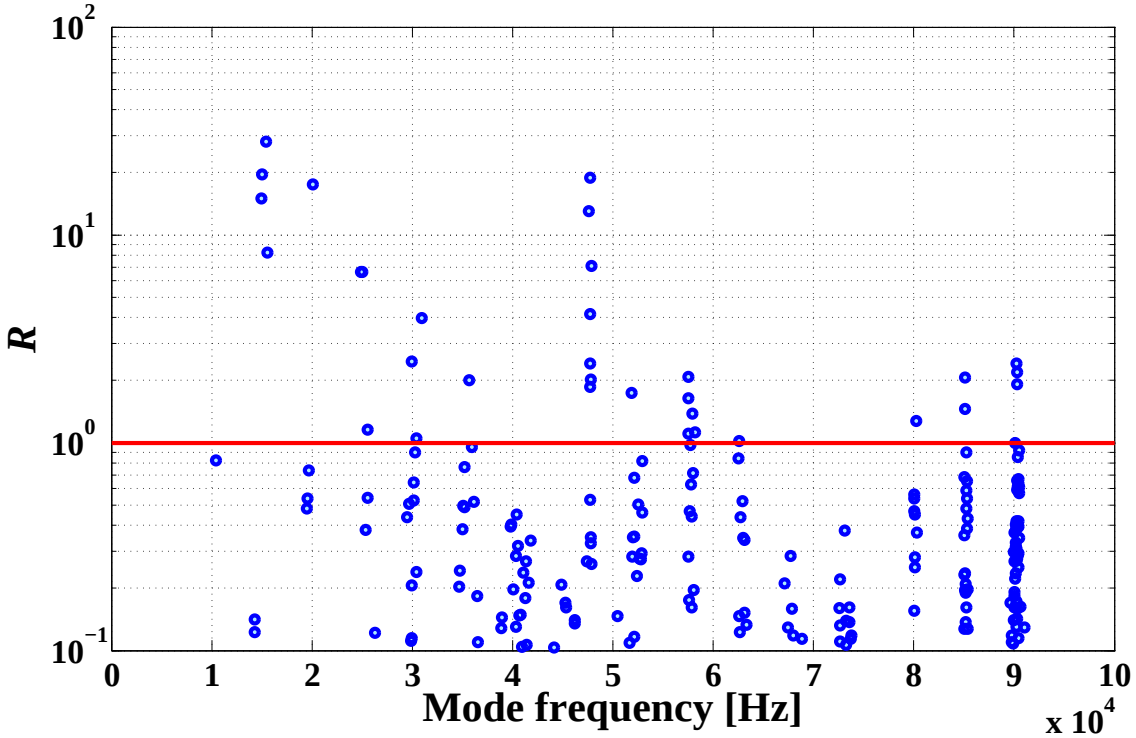

Figure 5.19: "Worst case" R_m values for an interferometer configuration representative of AdvLIGO. In our evaluation we randomly sweep over realistic model parameters, setting an upper limit on R for each mode as the lowest value greater than 99% of the results. Diffraction losses are included via the clipping approximation. We find 212 modes with $R > 0.1$ and 32 modes with $R > 1$.

Observing these numbers we return to our proposed mitigation scheme with renewed fervour to quantify the force coupling between the ESD and each mechanical mode.

5.2.8 Overlaps

Having completed a modal analysis of the test mass and determined the distribution of ESD forces, we are equipped to evaluate b_m,[18] the penultimate step in estimating the force required to damp PIs.

Due to diffraction loss, optical gain is highest for low order transverse modes. This leads one to surmise that these modes are most likely to give rise to PIs. In addition, low order modes exhibit low order symmetries implying that their coupling to the four-fold symmetric ESD pattern will be poor and that they will thus require large damping forces. Indeed, if not for symmetry breaking wedges some modes, such as that in figure 5.20, would have vanishing overlap with the ESD and could therefore never be damped via the methods we propose.

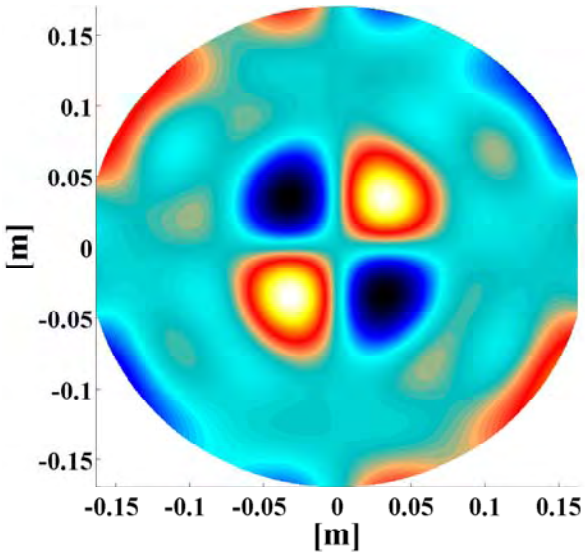

Figure 5.20: Some mechanical modes possess symmetries which make them difficult to damp using the four fold symmetric ESD pattern. By operating with a single ESD quadrant vast gains are available. For this 40.3 kHz mode b increases from 4.3×10^{-5} to 0.05.

To address this issue we sought to introduce small asymmetries into the ESD design before realising that a more elegant solution was already at hand. Simply by operating with a single ESD quadrant the ESD-mechanical mode coupling may be enhanced

[18] This simply amounts to evaluating (5.68) numerically.

markedly. For the mode of fig. 5.20 b is increased from 4.3×10^{-5} to 0.05. Larger overlaps allow effective damping to be realised with smaller applied forces and consequently less noise.[19]

In fig. 5.21 we compare the theoretical overlaps obtained using a lone quadrant to those obtained from the entire ESD pattern. Valuable improvements are available for most modes with the median value of b growing from 0.003 to 0.013.

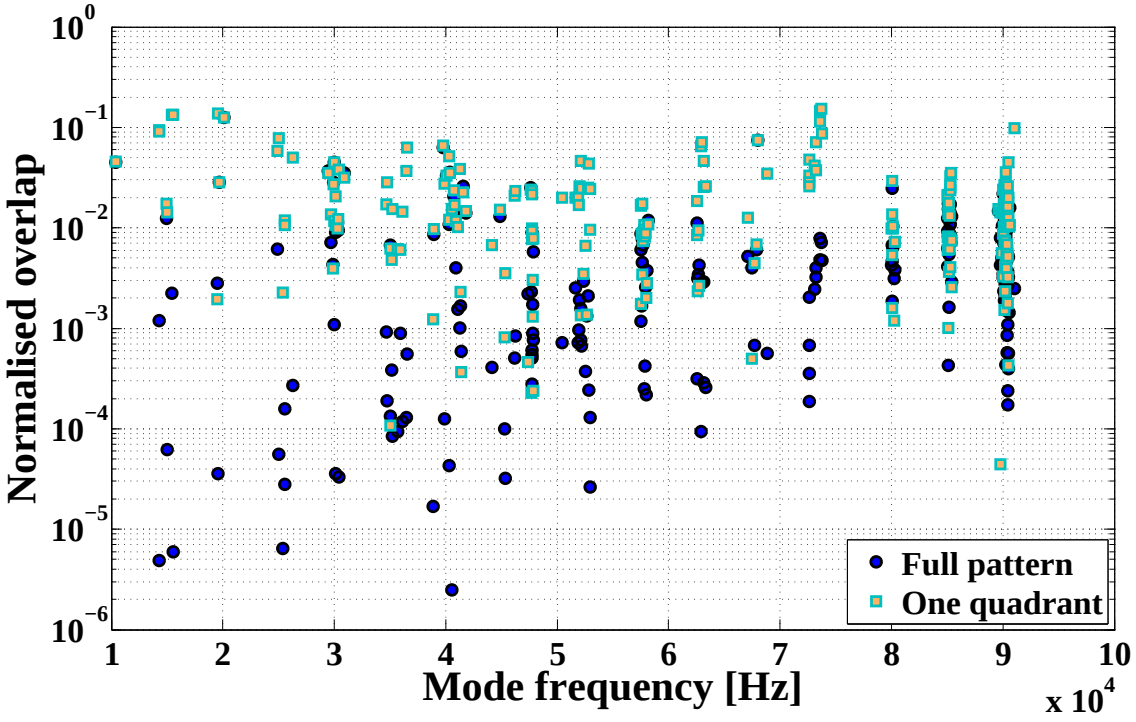

Figure 5.21: Normalised force coupling b_m between the ESD and test mass eigenmodes considering both the full ESD pattern (circles) and a single quadrant (squares). Larger overlaps and thus smaller damping forces are observed when considering a single quadrant.

With the coupling between the ESD and each mechanical mode well defined, we compute the force required to successfully mitigate any PI and measure this value against available capacity in the following section.

[19]It is nevertheless still desirable to include small asymmetries in the ESD pattern. Their negligible impact on the total available force is more than compensated for by the prospect of damping an otherwise evasive mode.

5.2.9 Required damping forces

In advance of calculating any force using our numerical data we must select an appropriate value for $R_{\mathrm{eff},m}$, the residual parametric gain which we deem tolerable. Recalling that the criterion for instability is $R > 1$, we select $R_{\mathrm{eff},m} = 0.1$. The consequences of this choice are revealed in fig. 5.22 where we present the fraction of the available ESD force required to damp each mode using all four quadrants. We assume $\Delta V = 800$ V.

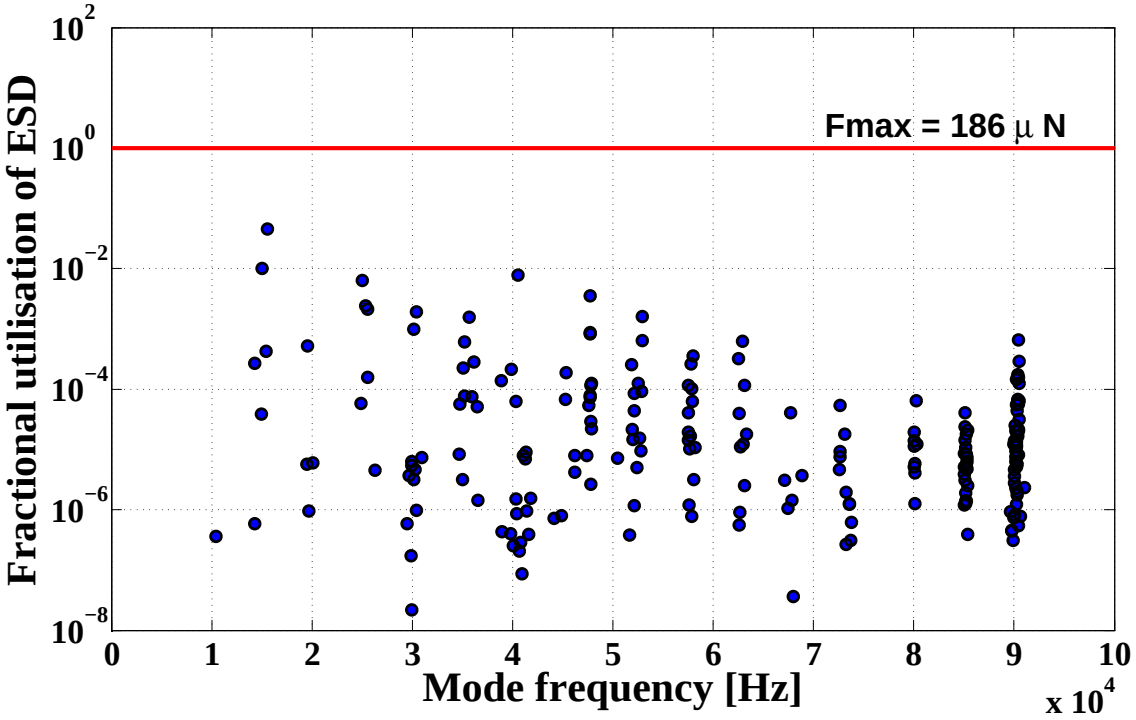

Figure 5.22: Fraction of total ESD force from all four quadrants required to reduce the parametric gain to 0.1. All modes are successfully damped with a maximum utilisation of 4.6%. The maximum force is evaluated for $\Delta V = 800$ V.

In all cases we see that successful damping is theoretically achievable using just a few percent of the available force. In fig. 5.23 we show how these results are modified when one takes advantage of the improved coupling (see fig. 5.21) available in single quadrant operation.

Whilst median values of the damping forces are comparable in both cases the maximum force required in the single quadrant case is reduced by more than an order of magnitude. This leads us to recommend single quadrant operation as the baseline mode for

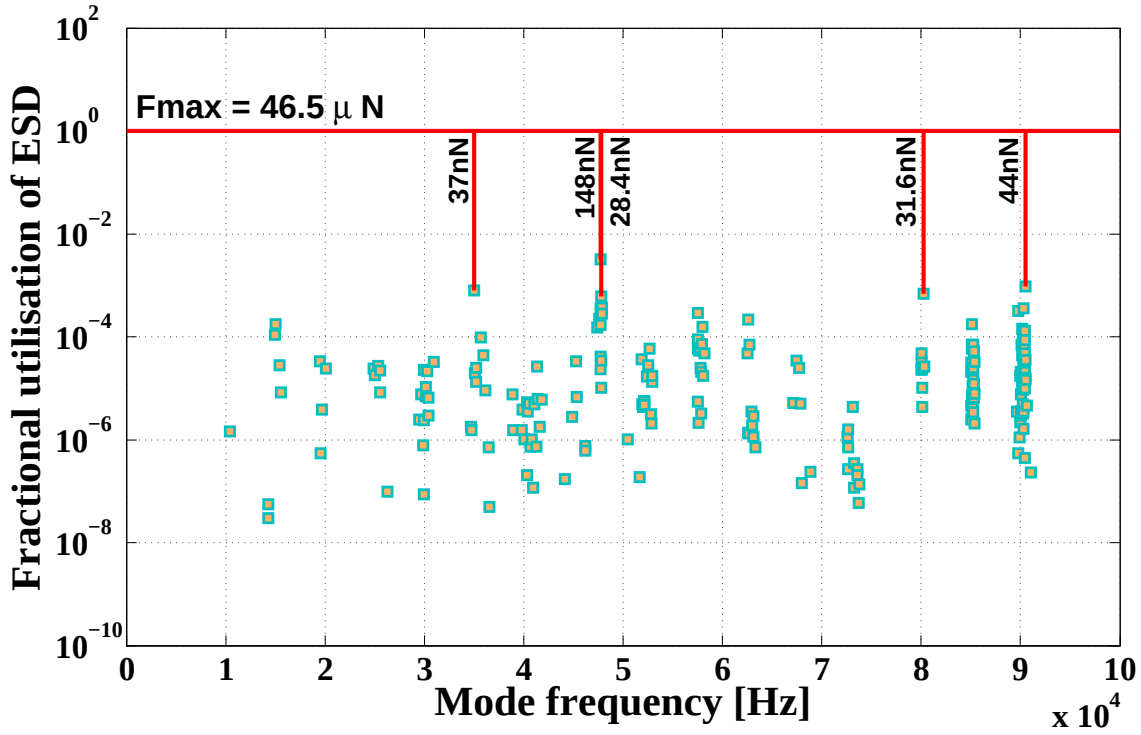

Figure 5.23: Damping forces required when using a just a single ESD quadrant. Maximum utilisation is 0.3%. The force required to damp the five most troublesome modes is indicated. Again, the maximum force is evaluated for an assumed ΔV of 800 V.

our scheme.

This investigation has shown that, theoretically, all potential parametric instabilities in a second generation dual recycled interferometer can be efficiently damped using electrostatic actuators intended for test mass alignment and control. In order to strengthen this argument and validate our modelling effort experimental confirmation is necessary. Such confirmation is presented below in §5.3.

5.2.10 Future work

With well-developed tools available there exist a number of investigations which, although beyond the remit of this thesis, are worthy of attention.

It has been shown that all potentially unstable modes may be damped using just a single quadrant of the ESD. We expect that further gains could be realised by recruiting

several quadrants simultaneously with mode dependent phasing. For example, the mode depicted in figure 5.20 would benefit from the use of all four quadrants with adjacent quadrants driven out of phase. Such operation promises to reduce the required damping force by as much as a factor of four.

Experience with GEO's photon calibrator has shown that we can no longer consider the test masses as rigid bodies [232, 233]. It may therefore be important to consider the implications of test mass deformation caused by the ESD forces for both PI damping and detector calibration.

Not all high power interferometers possess electrostatic drives, similar modelling techniques could be applied to determine whether coil-magnet actuators are able to usefully damp test mass eigenmodes. This idea could be tested in Enhanced LIGO using thermally excited test mass modes near the first free spectral range.

5.3 Experiment

In order to verify the predictions of our numerical model an experimental investigation was carried out, we describe this work below. Beginning in §5.3.1 we introduce the experimental setup before moving on to discuss the measurements of α (§5.3.2) and b_m (§5.3.3). At each stage we compare our results with model output.

5.3.1 Apparatus

All measurements were conducted at LIGO's Advanced Systems Test Facility (LASTI) at MIT. This laboratory is a testbed for hardware destined for use at the LIGO sites. Hence much of this work was carried out using prototype AdvLIGO equipment. In the following sections we describe the experimental setup including optical system and digital controls. In §5.3.1.3 we describe how the ESD drive is linearised before presenting the overall displacement sensitivity.

5.3.1.1 Seismic isolation

In Enhanced LIGO the dominant noise source below ∼40 Hz is residual seismic motion. AdvLIGO hopes to have a detection band extending down to ∼10 Hz. In order to achieve this the current single pendulum suspensions [203] and four layer passive isolation stacks [234] shall be replaced with three new systems operating in series, with each system providing isolation for the following stage (see fig. 5.24) [235]. Below we describe each system in sufficient detail for our purposes, providing appropriate references for the curious reader.

The first stage of attenuation is a Hydraulic External Pre-Isolator (HEPI) system which resides outside the vacuum envelope [236]. HEPI uses a combination of position sensors, geophones and hydraulic actuators to provide low frequency ($\lesssim$ 5 Hz) alignment and isolation in six degrees of freedom. HEPI has a large actuation range of ±1 mm and is used to correct for tides, seasonal temperature variations and to relieve other actuators.

Mounted atop HEPI inside the vacuum chamber is the Internal Seismic Isolation (ISI) system [237, 238]. The ISI is an active isolation platform suspended using stiff cantilever springs and short pendulum links. The ISI is also appropriately instrumented (low frequency seismometers, high frequency geophones, capacitive position sensors and electromagnetic actuators) to provide sensing and control in all six degrees of freedom. Isolation ranges from a factor of ∼100 at 1 Hz to ∼1000 at 10 Hz. Fig. 5.25 shows a computer rendering of the two stage BSC ISI.

LIGO employs two different sizes of vacuum tank. Horizontal Access Modules (HAMs) are used for the input mode cleaner optics, recycling cavity mirrors and OMC whereas larger Beam Splitter Chambers (BSCs) are needed for the test masses and beam splitter. Variations of the HEPI and ISI systems have been developed for each type of chamber.

The interferometer optics are suspended from the ISI tables using coupled pendulum systems derived from those developed by the GEO collaboration [239]. The test masses

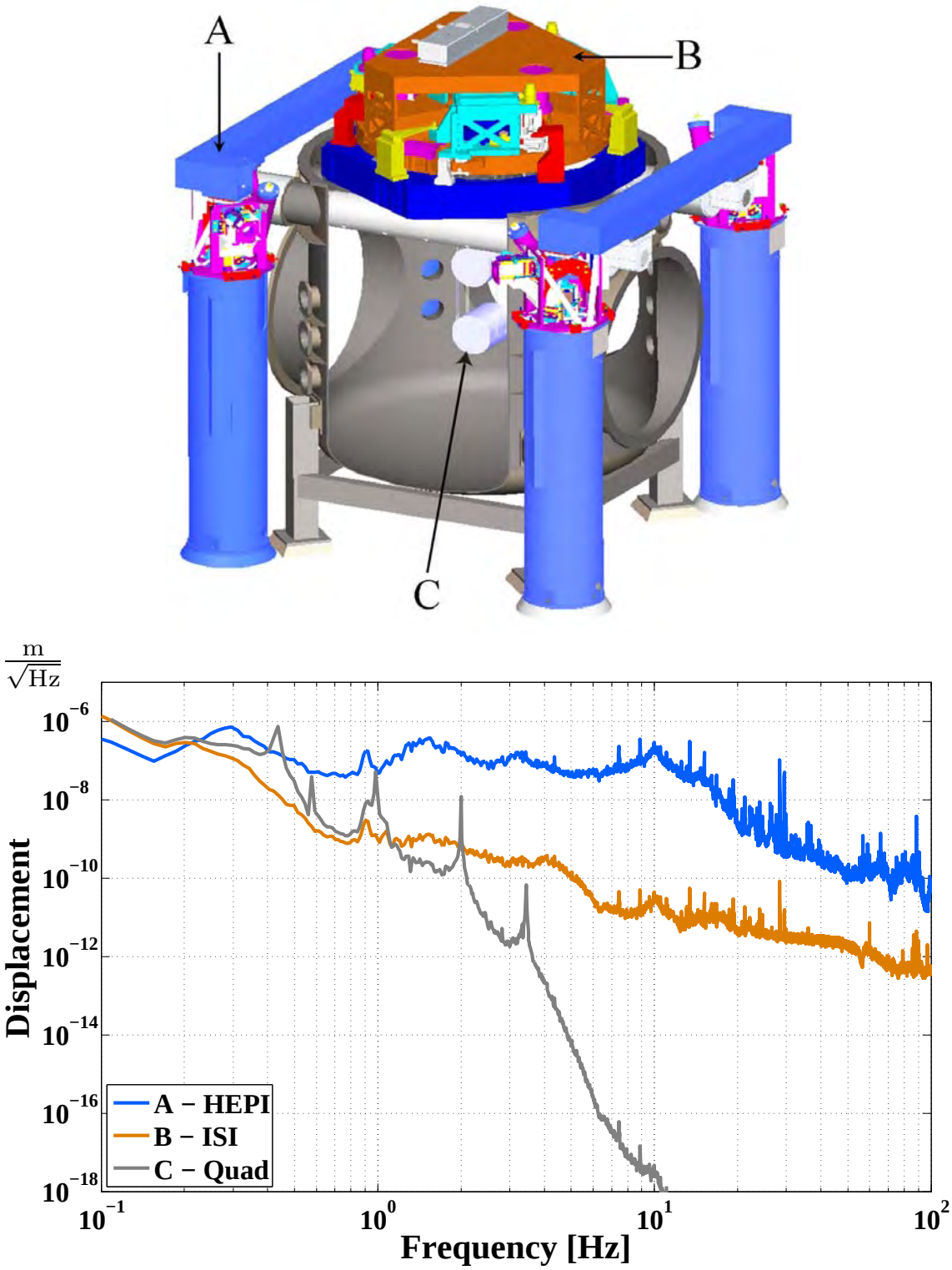

Figure 5.24: Top: Illustration showing the three layers of seismic isolation present in an AdvLIGO BSC chamber. A - The HEPI structure is shown in light blue with sensor-actuators in red/white/magenta. B - Above HEPI sits the ISI shown in dark blue (stage 0), cyan (stage 1) and orange (stage 2). C - Finally the quadruple pendulum (partially obscured) is fixed to stage 2 of the ISI. Bottom: Displacement noise after each stage of isolation at LASTI.

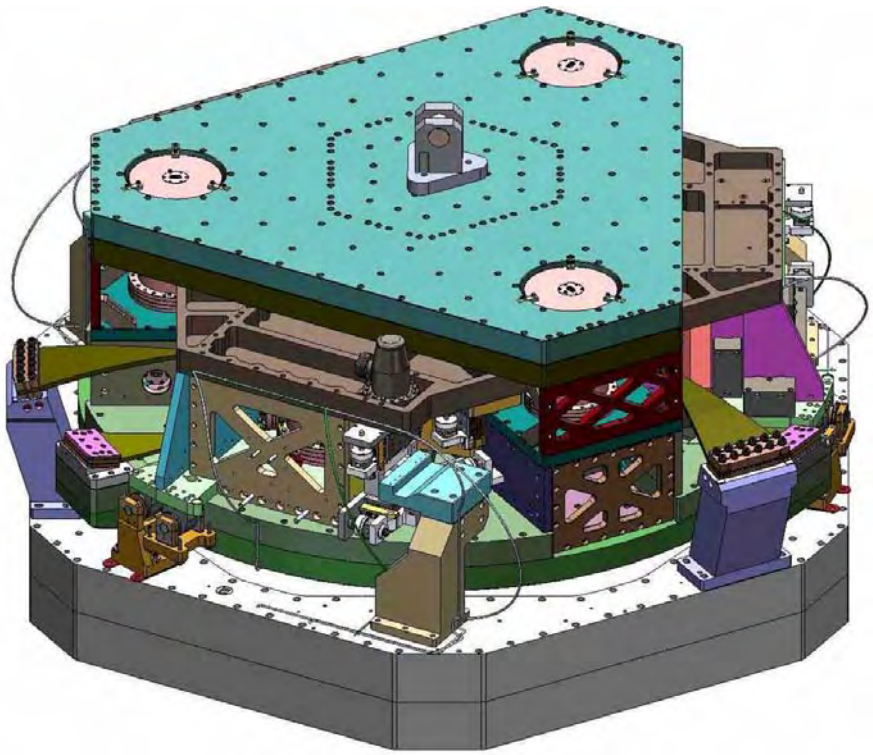

Figure 5.25: Rendering of redesigned BSC ISI. The ISI is rigidly fixed to HEPI and provides two stages of active isolation for the chamber's optical table.

require quadruple pendulums whilst all other optics employ simpler triple suspensions.

Fig. 5.26 shows an AdvLIGO quadruple pendulum [240]. The upper stages are suspended from maraging steel cantilever blade springs to provide vertical isolation. These stages use metal suspension wire whilst the final fourth stage adopts fused silica fibres in the interests of thermal noise [241, 242]. To avoid seismic shorts the actuators for each pendulum stage are suspended immediately behind the appropriate mass on a *reaction chain* at a nominal separation of 5 mm. Global control forces for the first three stages are provided by coil-magnet pairs whilst the final stage is endowed with an ESD.

Less sensitive optics are suspended from various incarnations of triple pendulum (see fig. 5.27) [243]. These suspensions adopt the same design principles as the quadruple pendulum but relaxed requirements remove the need for any reaction chain, silica fibres or electrostatic actuator. For a comprehensive discussion of the small triple pendulum and expected performance see [244].

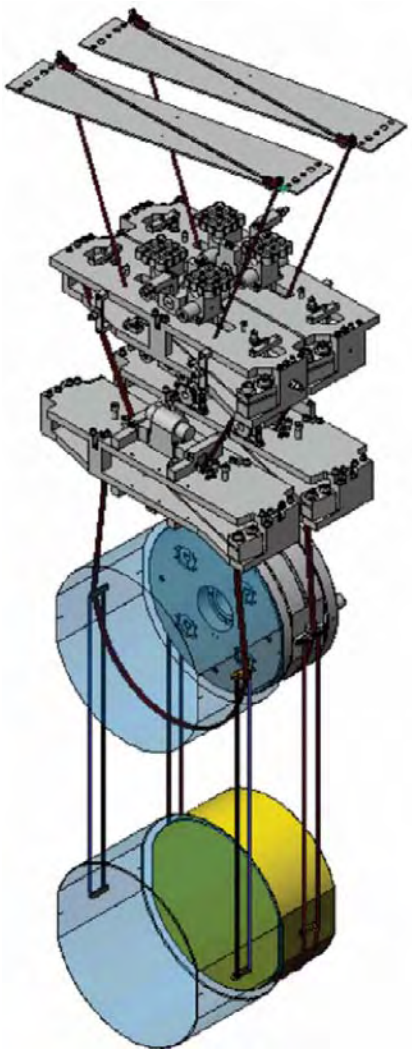

Figure 5.26: Engineering rendering of AdvLIGO quadruple suspension system. The upper pendulum stages will continue to use coil-magnet actuators with only the critical final stage meriting an ESD. The ESD pattern is deposited onto the surface of the reaction mass (highlighted in yellow). Figure 5.11 shows a prototype reaction mass in more detail.

Our experimental cavity is formed between a BSC and a HAM, with the HAM housing the input test mass. Both chambers have the appropriate HEPI installed whilst only the BSC has an active ISI. The optical table in the HAM is supported by a passive initial LIGO stack (see fig. 5.28). The HAM houses a small triple suspension with a final mass fashioned from metal. This dummy mass approximates the mechanical properties of a 150 mm diameter x 75 mm thick fused silica cylinder but allows one to mount standard 25.4 mm diameter optics. The BSC is home to the AdvLIGO noise prototype quad. The reaction mass of the quad is that shown in figure 5.11 and

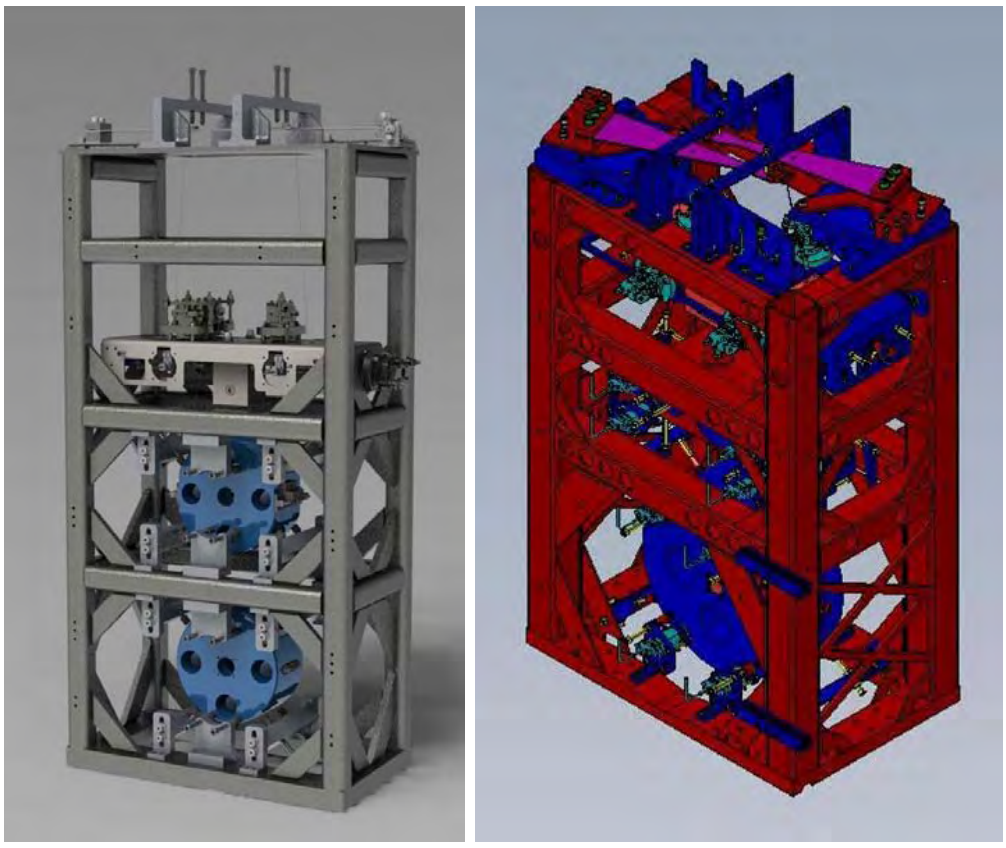

Figure 5.27: Left: HAM small triple suspension designed for 150 mm diameter optics. This design is appropriate for the input mode cleaner mirrors and the small recycling cavity optics. Right: HAM large triple suspension for 265 mm diameter optics. This design shall be used for the large recycling cavity mirrors. There exists a third triple suspension (not shown) for beam splitters and folding mirrors.

modelled in section 5.2.2.

5.3.1.2 Optics and control

Experimental measurements were conducted on the 16 m Fabry-Perot resonator formed between the triple and quadruple suspensions. Henceforth this cavity shall be referred to as the *arm* to clearly distinguish it from the reference cavity used for frequency stabilisation. The parameters of both cavities are given in table 5.4.

The cavity was driven by a sub-W Nd:YAG NPRO (Lightwave/JSDU 126 [245]). Fig. 5.29 shows the input bench where the laser light was imprinted with phase side-

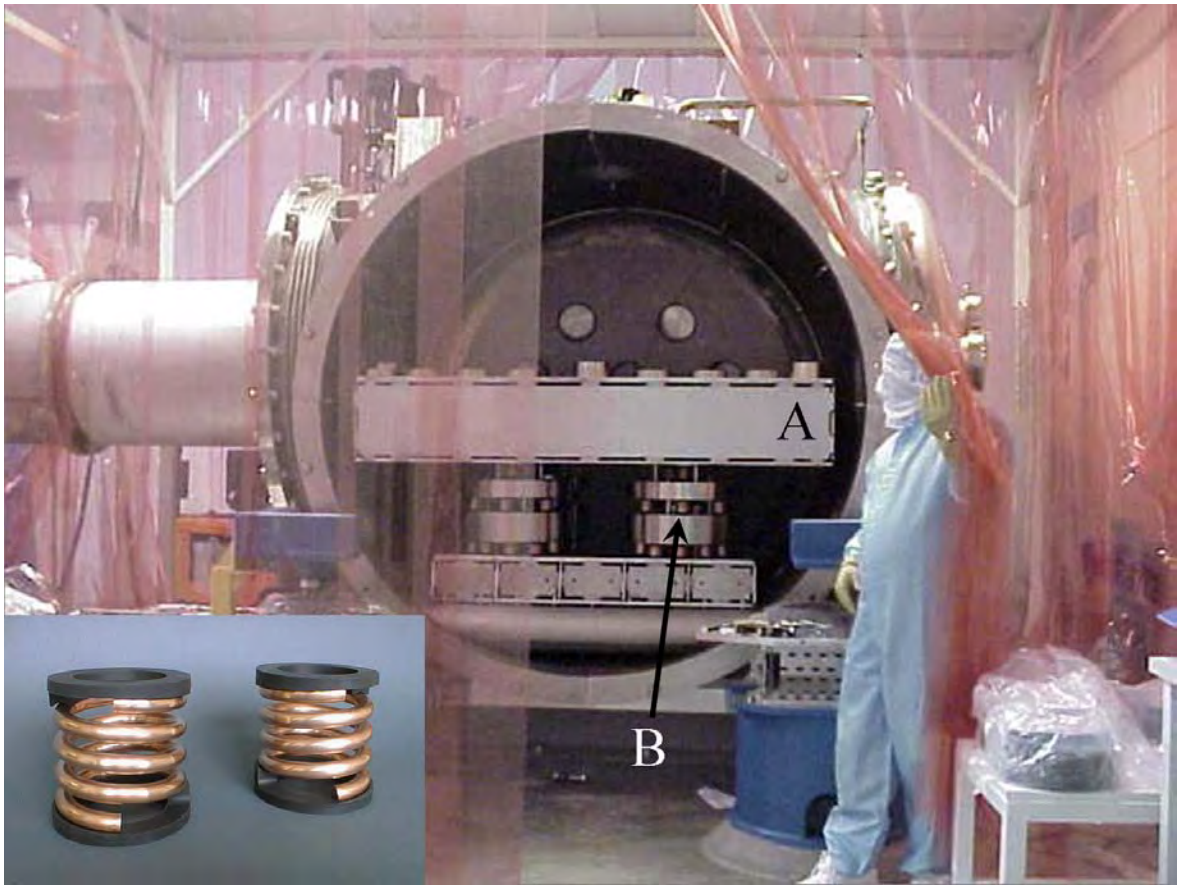

Figure 5.28: An open HAM chamber reveals the optical table (A) supported by mass spring stacks (B). Inset: Springs in more detail.

Table 5.4: Optical properties of experimental apparatus.

	Quantity	Value
Arm cavity	Length	16 m
	Input mirror power transmission	0.01
	End mirror power transmission	50 ppm
	Input mirror radius of curvature	20 m
	End mirror radius of curvature	∞
	Finesse	623
	Cavity pole	7.516 kHz
	Input power	10 mW
	Unity gain	100 Hz
Reference cavity	Length	20 cm
	Mirror radius of curvature$^\flat$	50 cm
	Finesse	5300

$^\flat$ Cavity is nominally symmetric

bands[20] before being attenuated and split into two paths. The majority of the light (90 %) was sent through a mode matching telescope to the arm cavity whilst the remainder was directed toward our reference cavity enclosure (fig. 5.30). The reference cavity is of pseudo monolithic fused silica construction and is suspended from two wire loops inside an anechoic chamber.

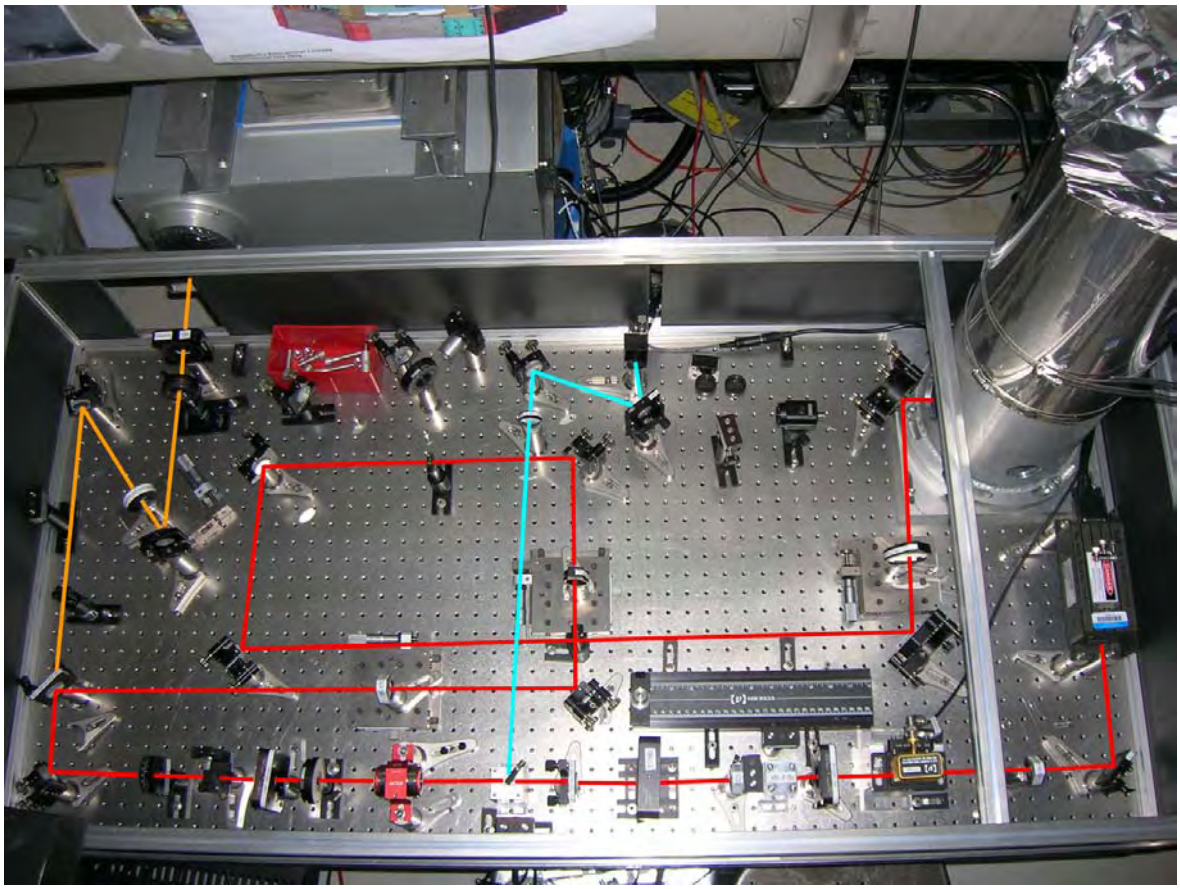

Figure 5.29: Input optics bench. Red - arm cavity injection beam; Orange - reference cavity input; Cyan - reflected beam selected by polarising beam splitter and directed toward RF photodiode.

The laser was locked to the reference cavity using standard PDH reflection locking [92] with the dc light transmitted through the cavity used to trigger control actuators. A blended feedback loop was implemented with low frequency signals being sent to the laser temperature controller whilst high frequency signals were routed to the PZT mounted atop the laser crystal. The bandwidth of this loop was ∼12 kHz with a

[20]A lithium niobate crystal doped with magnesium oxide (to prevent optical damage) was driven via a resonant tank circuit. The modulation depth was chosen to be 0.3.

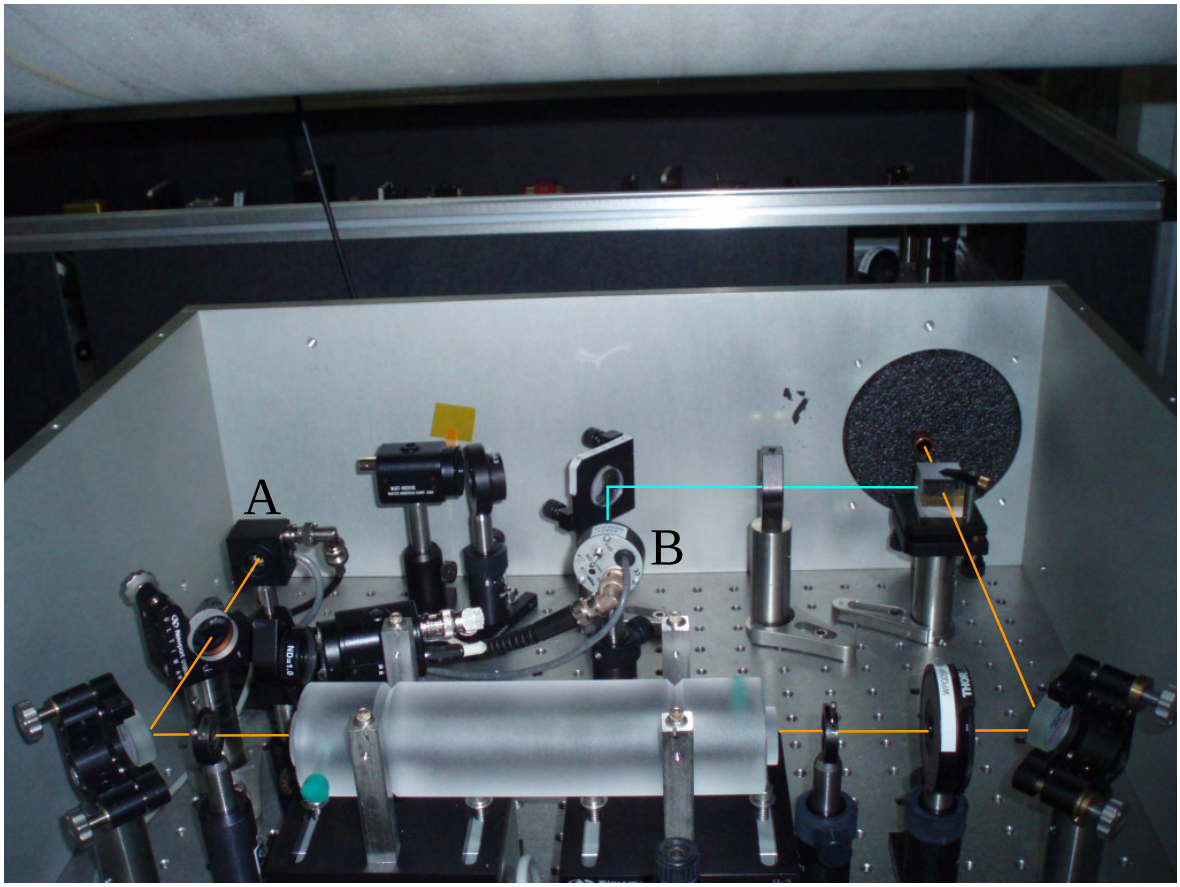

Figure 5.30: Reference cavity enclosure. Orange - Input beam; Cyan - reflected beam. Diode A is the DC transmitted diode used to trigger control signals. Diode B is the RF diode in reflection used for generation of the error signal. To allow for in-vacuo operation the reference cavity has two ports. These orifices have been filled with viscoelastic damping material to reduce acoustic couplings.

crossover frequency around 1 Hz. The reference cavity loop was entirely analogue to avoid the bandwidth restriction of a digital system.

The arm cavity length was controlled to match the frequency of the pre-stabilised laser light, again using PDH locking. Use was made of a digital control system to facilitate rapid commissioning and allow for easy extension to more complicated control architectures in the future. The digital system also allowed for more complex triggering and linearisation of the error signal by the dc transmitted light. Arm cavity control signals were applied to the coil-magnet actuators on the final stage of the triple pendulum. The unity gain frequency was set to 100 Hz. Fig. 5.31 shows a model of the open loop gain, the components of which are outlined in table 5.5

Table 5.5: Components of arm cavity locking loop.

Quantity	Frequency [Hz]	Description
Pendulum	0.65	Complex pole (Q=3)
Cavity pole	7516	Simple pole
Anti-alias	7500	3rd order Butterworth
Anti-image	7500	3rd order, 0.5 dB ripple Chebyshev
Sampling delay	—	One half sample
Processing delay	—	Two samples
Boost 1	0.1;5	Simple pole-zero pair
Boost 2	0.1;5	Simple pole-zero pair
Control filter	1,800;20	Simple zero at 1 Hz, complex zero at 800 Hz (Q=0.6); complex pole at 20 Hz (Q=0.6)

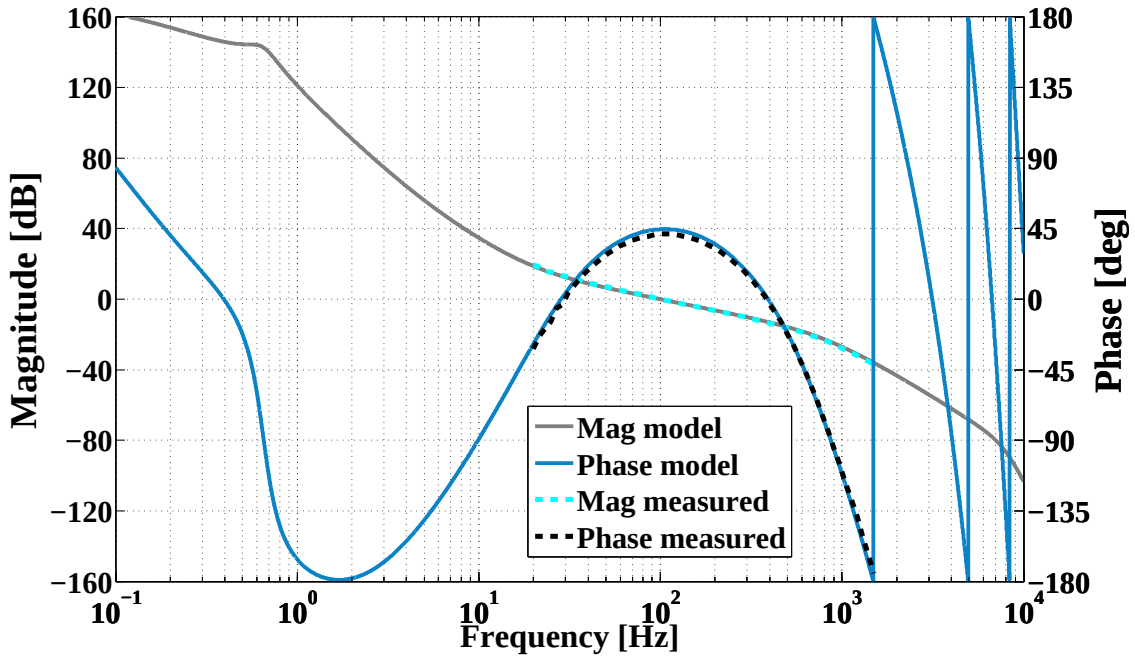

Figure 5.31: Model of arm cavity open loop gain. Measured data is also plotted near unity gain.

LASTI's digital control system is also designed to mimic that which will eventually be used in AdvLIGO. The key properties of the system are described in table 5.6. Each interferometer subsystem (e.g. HEPI, ISI or the suspensions) has a dedicated front-end computer running realtime code. Experimental Physics and Industrial Control System (EPICS) Motif Editor and Display Manager (MEDM) [246] provides a user interface allowing one to interact with the realtime system for commissioning work. Well developed tools are available allowing one to inject arbitrary waveforms, view,

acquire and process data in real time.

Table 5.6: Optical parameters of experiment.

Quantity	Description
Sampling frequency	16384 Hz
Resolution	16-bit
DAC/ADC range	± 10 V
Anti-alias	f_c=7.5 kHz 3rd order Butterworth
Anti-image	f_c=7.5 kHz 3rd order, 0.5 dB ripple, Chebyshev

5.3.1.3 How we drive the ESD

Two features of the ESD which hinder rapid commissioning are its non-linear actuation and uniformly attractive nature. We have resolved these issues by incorporating a simple linearisation algorithm into our digital control system. The derivation of this code is discussed below with digital quantities represented by sans serif fonts.

In standard operation, signals from the digital control system are passed through a Digital to Analogue Converter (DAC) to a low noise, wide bandwidth voltage amplifier known as the ESD driver. The ESD driver used in this work was an early prototype largely based on the GEO design [247]. The ESD driver provides 4 identical channels and a fifth of increased gain for the bias electrode. The channels are DC coupled but are designed with the possibility of an AC bias in mind [223]. Each channel has a differential receiver (LT 1125) to accept low voltage signals from the DAC followed by a high voltage stage (APEX PA94) with ±300 V symmetrical supplies. The gain of the four control channels was 40; the bias channel had a gain of 80. The frequency response of both stages was uniform to ∼20 kHz.

In the absence of any linearisation, input signals translate directly into voltages applied to ESD quadrants. Our code instead treats inputs as a desired force (in arbitrary units) and calculates the appropriate control signals which must be sent to achieve this force.

The standard force output is simply $\mathsf{F} = \mathsf{k}\Delta\mathsf{V}^2 = \mathsf{k}(\mathsf{V}_{\rm sig} - \mathsf{V}_{\rm bias})^2$, where k is a positive

constant. Assuming $|V_{sig}| \leq |V_{bias}|$

$$F_{min} = 0 \qquad \text{for } V_{sig} = V_{bias}, \tag{5.55}$$

$$\text{and } F_{max} = 4kV_{bias}^2 \qquad \text{for } V_{sig} = -V_{bias}. \tag{5.56}$$

In order to permit bipolar operation we desire that our eventual force have form

$$F = k(V_{sig} - V_{bias})^2 - F_{offset}. \tag{5.57}$$

Most useful operation is achieved when F_{offset} is equal to half of the maximum force

$$F_{offset} = \frac{1}{2}F_{max} = 2kV_{bias}^2. \tag{5.58}$$

With this choice solving (5.57) for V_{sig} gives

$$V_{sig} = V_{bias} \pm \sqrt{2V_{bias}^2 + \frac{F}{k}} \tag{5.59}$$

where due to our assumption that $|V_{sig}| \leq |V_{bias}|$ we must take the plus sign for $V_{bias} < 0$ and the negative for $V_{bias} > 0$.

In our code we take

$$k = -\frac{1}{2V_{bias}} \tag{5.60}$$

to ensure that both F and V_{sig} have range $\pm V_{bias}$ (i.e. within our DAC range). Thus we arrive at our final result

$$V_{sig} = V_{bias}\left(1 \pm \sqrt{2}\sqrt{1 - F/V_{bias}}\right) \text{ for } V_{bias} \lessgtr 0. \tag{5.61}$$

Figure 5.32 plots V_{sig} as a function of requested force for one particular choice of V_{bias}.

Experimental measurements have shown the linearisation method described above to

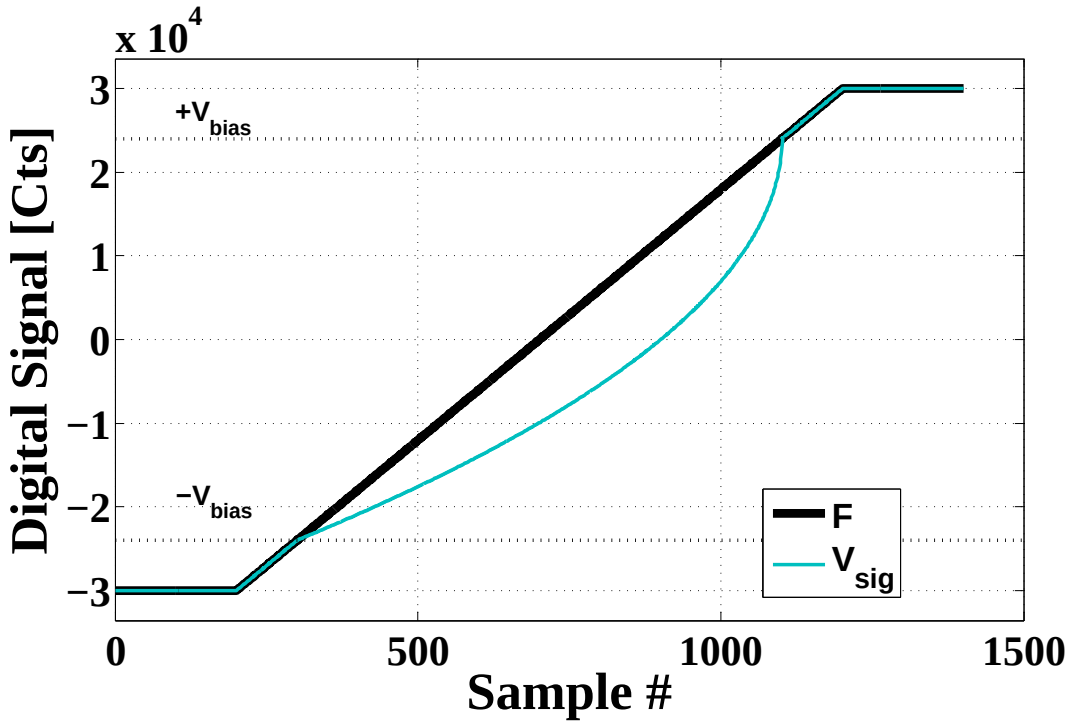

Figure 5.32: Illustration of linearisation code in action. The requested force and the signal which must be sent to the ESD to realise it are denoted by F and $\mathsf{V}_{\mathrm{sig}}$ respectively. Note that linearisation only occurs for $|\mathsf{F}| < |\mathsf{V}_{\mathrm{bias}}|$.

be effective. In Fig. 5.33 we demonstrate how the second harmonic of a sinusoidal drive is suppressed by around a factor of 5. Better suppression is desirable and it is expected that further work shall be undertaken in this area.

5.3.1.4 Sensitivity

Figure 5.34 shows typical displacement sensitivity of our apparatus. Given that we operate with a single cavity, our noise floor is dominated by laser frequency noise. In order to reduce this effect a small reference cavity was added to our system (fig. 5.30). The results of stabilising the laser in this fashion are shown in fig. 5.35. Even after additional damping efforts acoustic couplings were still strong in the 10-100 Hz decade (see figure 5.36). Preparations have been made and the reference cavity will soon be placed under vacuum to mitigate this coupling.

Achieving optimum sensitivity and the development of an exhaustive noise budget

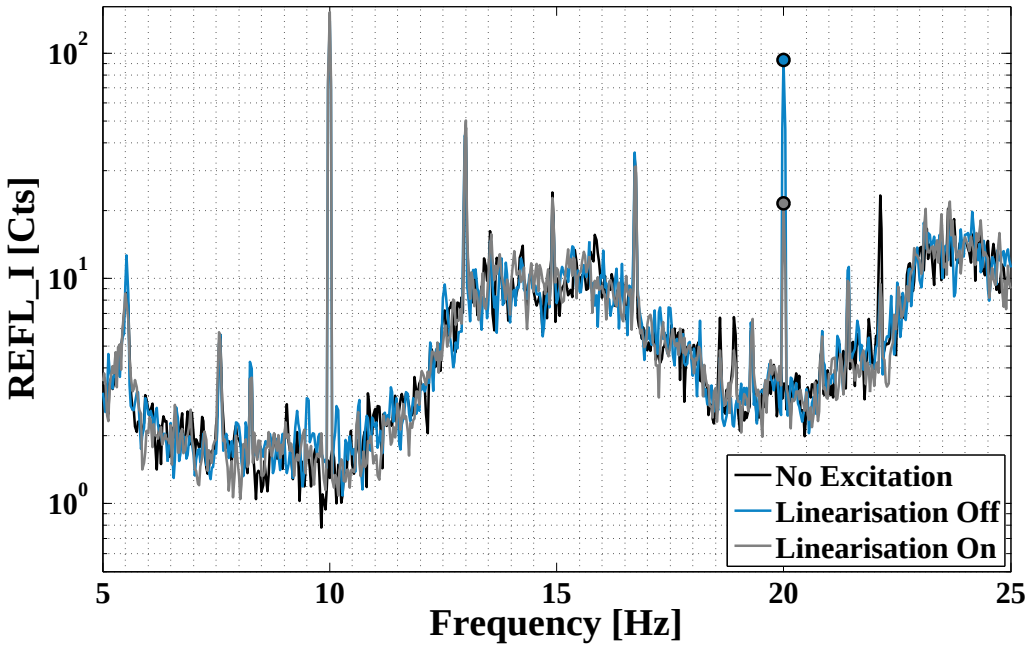

Figure 5.33: Experimental data showing the linearisation of a monochromatic ESD signal in the cavity length error signal REFL_I. Note how linearisation suppresses the second harmonic of the drive.

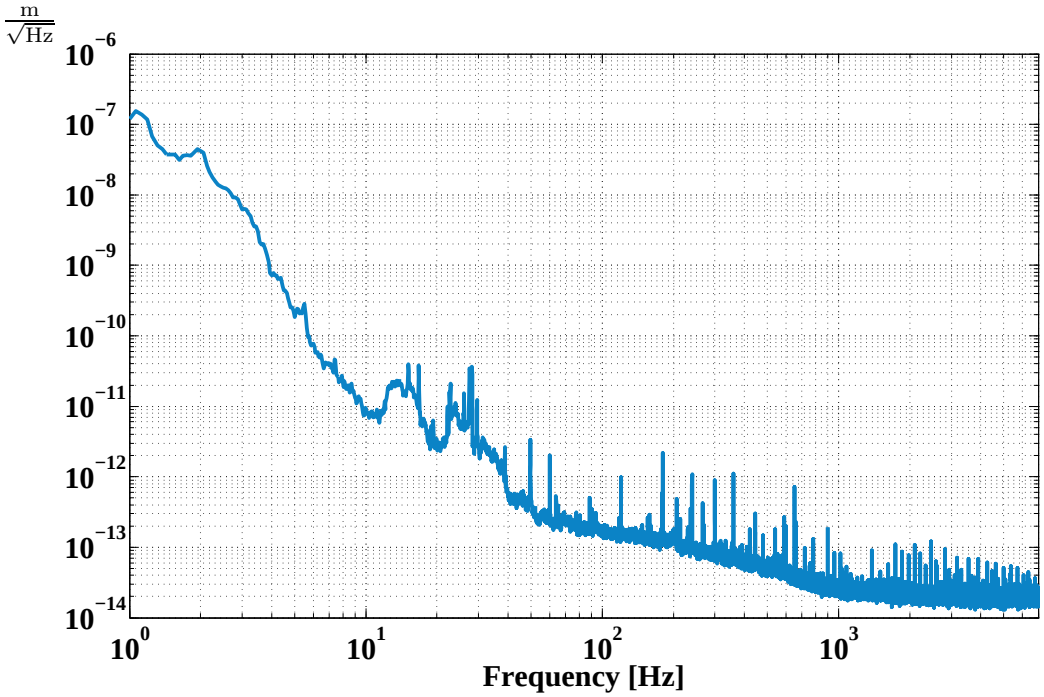

Figure 5.34: Amplitude spectral density of arm cavity displacement sensitivity.

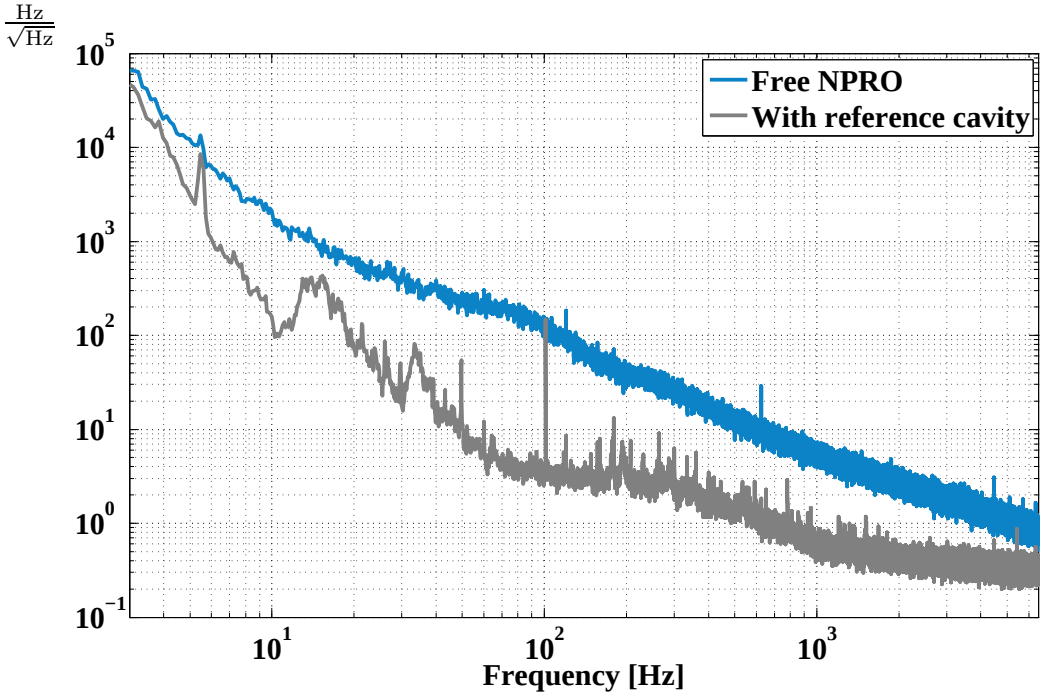

Figure 5.35: Reduction in frequency noise seen by arm cavity after stabilising laser to reference cavity. Calibration lines at 50 and 100 Hz.

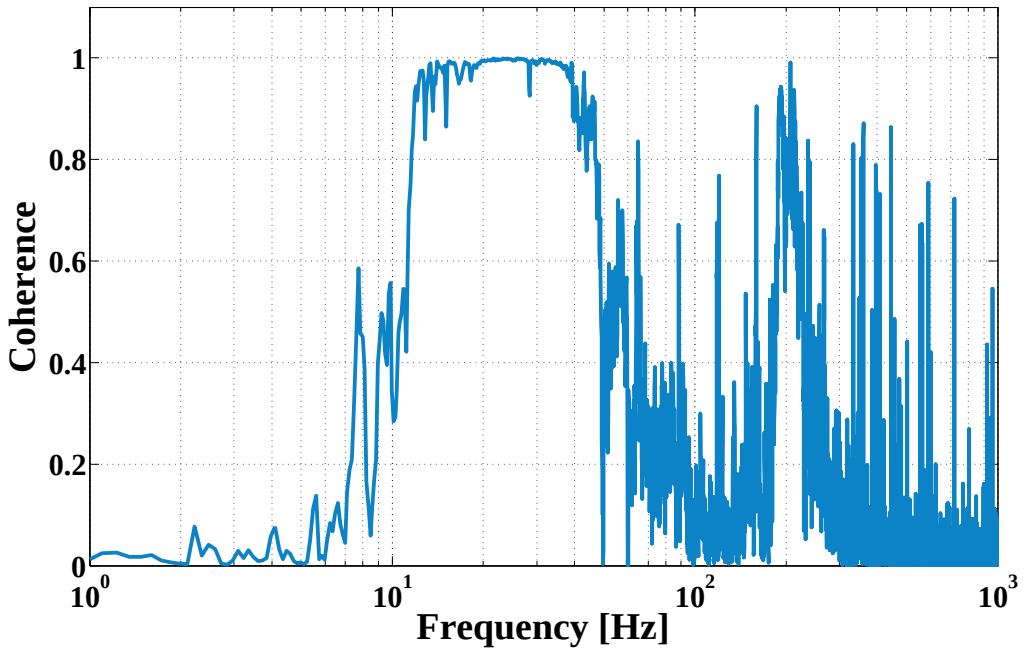

Figure 5.36: Coherence between microphone placed in reference cavity enclosure and cavity error signal.

for our apparatus was neither a goal of nor a prerequisite for our investigations into PIs. Our noise floor was only a hindrance in locating test mass mechanical modes. In the frequency range of interest our sensitivity was $1.5 - 2 \times 10^{-14}$ m/$\sqrt{\text{Hz}}$. This performance did not allow the observation of thermally excited modes. However, guided by FEM results the modes were easily found by other means (see §5.3.3.2). With ample sensitivity for our purposes we were able to accurately measure α and investigate our theoretically predicted ESD-mechanical mode couplings b_m.

5.3.2 α measurement

The construction of suitable apparatus allowed us to begin verifying the predictions of our model. The most transparent test was chosen for the first investigation – an experimental measurement of α, the ESD force coupling coefficient.

With the system globally controlled as described previously the end mirror was driven longitudinally by applying a sinusoidal excitation to all four quadrants of the ESD. The resulting mirror motion was recorded in the cavity error signal. Knowing the excitation waveform applied to the ESD driver and the mechanical response of the system, a calculation of the applied force allows α to be found.

For excitation frequencies above the highest pendulum resonance (∼3.5 Hz) and below the first internal mode of the test mass (∼6 kHz) we may write the peak-to-peak ESD force as

$$F_{\text{pp}} = m\omega_{\text{exc}}^2 x_{\text{pp}}, \tag{5.62}$$

where m is the total mass of the test mass, ω_{exc} is our excitation frequency in rads^{-1} and x_{pp} is the peak-to-peak test mass displacement. Having characterised the apposite electronics, the peak-to-peak differential voltage ΔV_{pp} applied across the ESD electrodes is easily found for known excitation waveforms. Thus from (5.30) we have

$$\alpha = \frac{F_{\text{pp}}}{\Delta V_{\text{pp}}^2}. \tag{5.63}$$

Measurements of the test mass response x_{pp} were made as a function of excitation amplitude and frequency over the 10-100 Hz band. Subsequent calculations revealed α to have a mean value of $2.95 \pm 0.08 \times 10^{-10}$ N/V^2, in excellent agreement with the predicted value of 2.91×10^{-10} N/V^2. The most significant contributions to our error budget came from uncertainties in cavity displacement measurements and PDH signal calibration. Both quantities were assigned a relative uncertainty of 5%. Fig. 5.37 shows typical data.

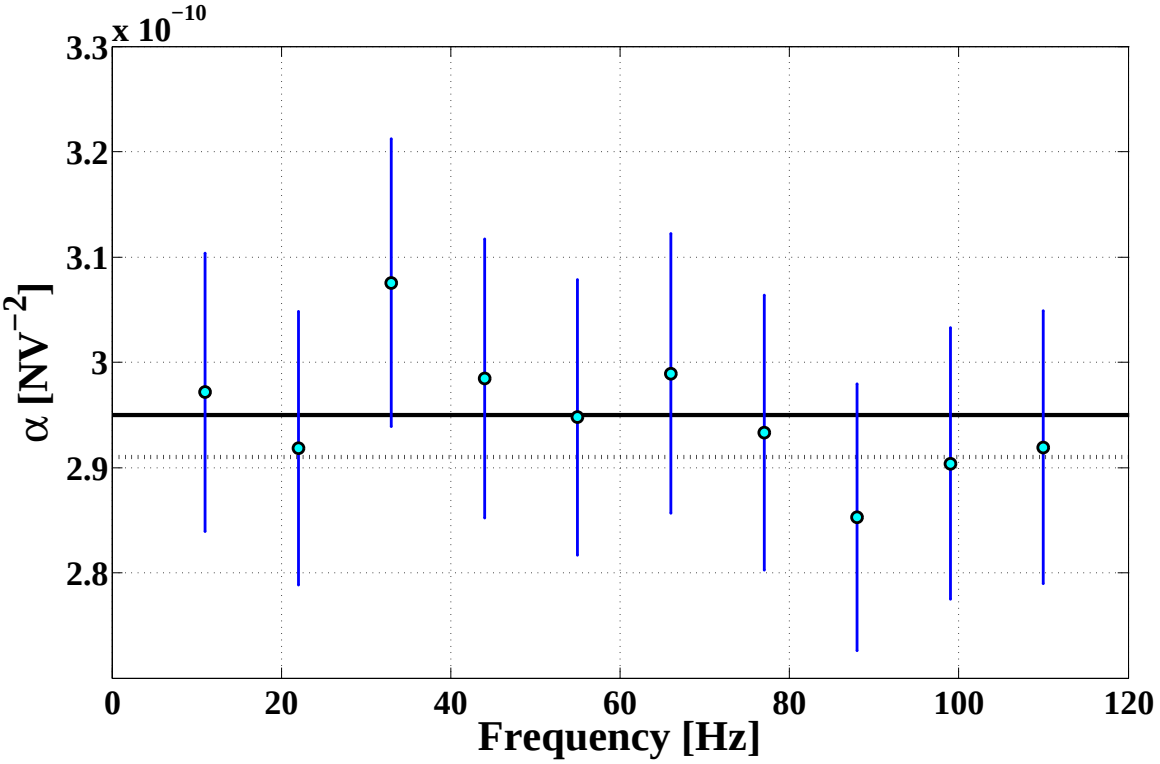

Figure 5.37: Typical ESD actuation coefficient measurement. Solid line indicates mean value of 2.95×10^{-10} N/V^2; dashed line shows theoretically predicted value of 2.91×10^{-10} N/V^2.

This experimental confirmation of our model's predictions encouraged us to proceed with more challenging work. In the next section we attend to the coupling between the ESD and the eigenmodes of the test mass.

5.3.3 Overlap measurement

Given the limitations of our setup, namely low input power and optical gain, there was little hope of observing spontaneously excited PIs. Further, the characteristics of our system did not allow thermally excited modes to penetrate the instrument noise. Hence the scope for demonstrating our ability to damp internal modes of the test mass was limited to those modes which we could ourselves excite. Given this somewhat unsatisfactory prospect we adopted a different approach. We sought to demonstrate that all modes could successfully be damped by showing that the principal unknown in our expression for the required damping force was accurately predicted by our model. We would measure b_m.

5.3.3.1 Theory

In order to experimentally measure these coupling coefficients we appealed to simple conservation of energy. When a test mass eigenmode is excited into a steady-state oscillation we know that we must have balance between energy applied to the system and energy dissipated from the system.

Modelling the system as an oscillator with angular resonant frequency ω_0

$$Q = \omega_0 \frac{E_{\text{stored}}}{P_{\text{loss}}}, \tag{5.64}$$

$$E_{\text{stored}} = \frac{1}{2} k A^2 = \frac{1}{2} \omega_0^2 \mu A^2, \tag{5.65}$$

$$\therefore \; P_{\text{loss}} = \frac{\frac{1}{2}\omega_0^3 \mu A^2}{Q}, \tag{5.66}$$

where μ is the modal mass and A is the modal amplitude.

The input power required to maintain an oscillation of amplitude A at resonance is given by [248]

$$P_{\text{input}}(\omega_0) = \frac{1}{2} \omega_0 A F_{\text{app}}, \tag{5.67}$$

where $F_{\rm app}$ is the fraction of the ESD force which is effectively coupled into the mechanical mode. We define our ESD-mechanical mode force coupling b_m through $F_{{\rm app},m} = b_m F_{{\rm ESD},m}$. Thus at equilibrium we have for each mode

$$\begin{aligned} P_{\rm loss} &= P_{\rm input}, \\ \text{i.e.} \quad \frac{\frac{1}{2}\omega_{0,m}^3 \mu_m A_m^2}{Q_m} &= \frac{1}{2}\omega_{0,m} A_m F_{{\rm ESD},m} b_m, \\ \text{whence} \quad b_m &= \frac{\omega_{0,m}^2 \mu_m A_m}{Q_m F_{{\rm ESD},m}}. \end{aligned} \tag{5.68}$$

The unknown parameters in this expression $F_{{\rm ESD},m}$, A_m and Q_m are treated in turn below.

The amplitude of $F_{{\rm ESD},m}$ is calculated as[21]

$$F_{{\rm ESD},m} = \frac{1}{2}\alpha \left[V_{{\rm exc},m} - V_{{\rm bias},m} \right]^2, \tag{5.69}$$

where $V_{\rm exc}$ is the excitation voltage applied to the control electrodes and $V_{\rm bias}$ is the constant voltage applied to the bias electrode. The modal amplitude A_m is determined from the cavity error signal via

$$A_m = \frac{x_m}{c_m}, \tag{5.70}$$

where x_m is the measured test mass displacement and c_m is a geometric overlap factor which accounts for the fraction of mechanical mode amplitude sensed by the cavity. For example, if the cavity beam is incident on the mirror near a node, c_m will be smaller than if the beam were incident near an anti-node. This overlap is calculated as

$$c_m = \left| \iint_{\mathcal{S}} I_{00}(\vec{u}_m \cdot \hat{z}) \, {\rm d}\mathcal{S} \right|. \tag{5.71}$$

$\vec{u}_m$ has the same normalisation as before (see (5.40)) and I_{00}, the intensity profile of the fundamental cavity mode, is normalised by

$$\iint_{\infty} I_{00} \, {\rm d}\mathcal{S} = 1. \tag{5.72}$$

[21] We gain a factor of 1/2 since we are no longer considering peak-to-peak values.

The theoretical expression for b_m is given by (5.39). In what follows we describe the measurements leading to an experimental estimate of b_m via (5.68) above. In §5.3.3.4 we compare the two sets of values.

5.3.3.2 Feedback loop

An experimental measurement of b_m requires that we are able to locate, excite and measure the losses of each test mass eigenmode. Unable to use our digital control system for work at mechanical mode frequencies ($f_{\text{sample}} = 16384$ Hz) simple analogue electronics were constructed.[22]

As discussed previously, thermally excited modes were not visible above instrument noise. In order to locate and study these mechanical modes they first had to be excited. Modes were initially found by applying analogue excitations to the ESD driver using a signal generator. The spectrum of the demodulated cavity error signal REFL_I was observed whilst the the frequency of the injected signal was slowly swept (0.1 Hzs^{-1}). FEM predictions provided invaluable guidance in the choice of which band to study and several modes were quickly found. Fig. 5.38 shows the modes which were selected for our final analysis. Their predicted and observed frequencies may be found in table 5.7.

To excite the observed modes into steady state oscillation and allow easy calculation of losses via ringdown measurements, a rudimentary servo loop was constructed (fig. 5.39). The demodulated arm cavity error signal REFL_I was tapped prior to the Analogue to Digital Converter (ADC) and bandpass filtered before being amplified and sent to the ESD driver. The bandpass was constructed using a programmable filter with two distinct stages – an 8-pole, 6-zero low pass elliptic filter[23] and an equivalent 8-zero, 6-pole high pass filter [249]. This bandpass served to reduce noise and limit gain to a

[22] The digital system can in fact be used to excite test mass modes beyond the Nyquist frequency by utilising the nonlinearity of the ESD. Driving the first sub harmonic of the mode with no linearisation creates sufficient signal at the internal mode frequency to ring up high Q modes. However this method was rejected in favour of an all analogue approach.

[23] 115 dB/decade roll off, 0.1 dB passband ripple and 80 dB stop band attenuation.

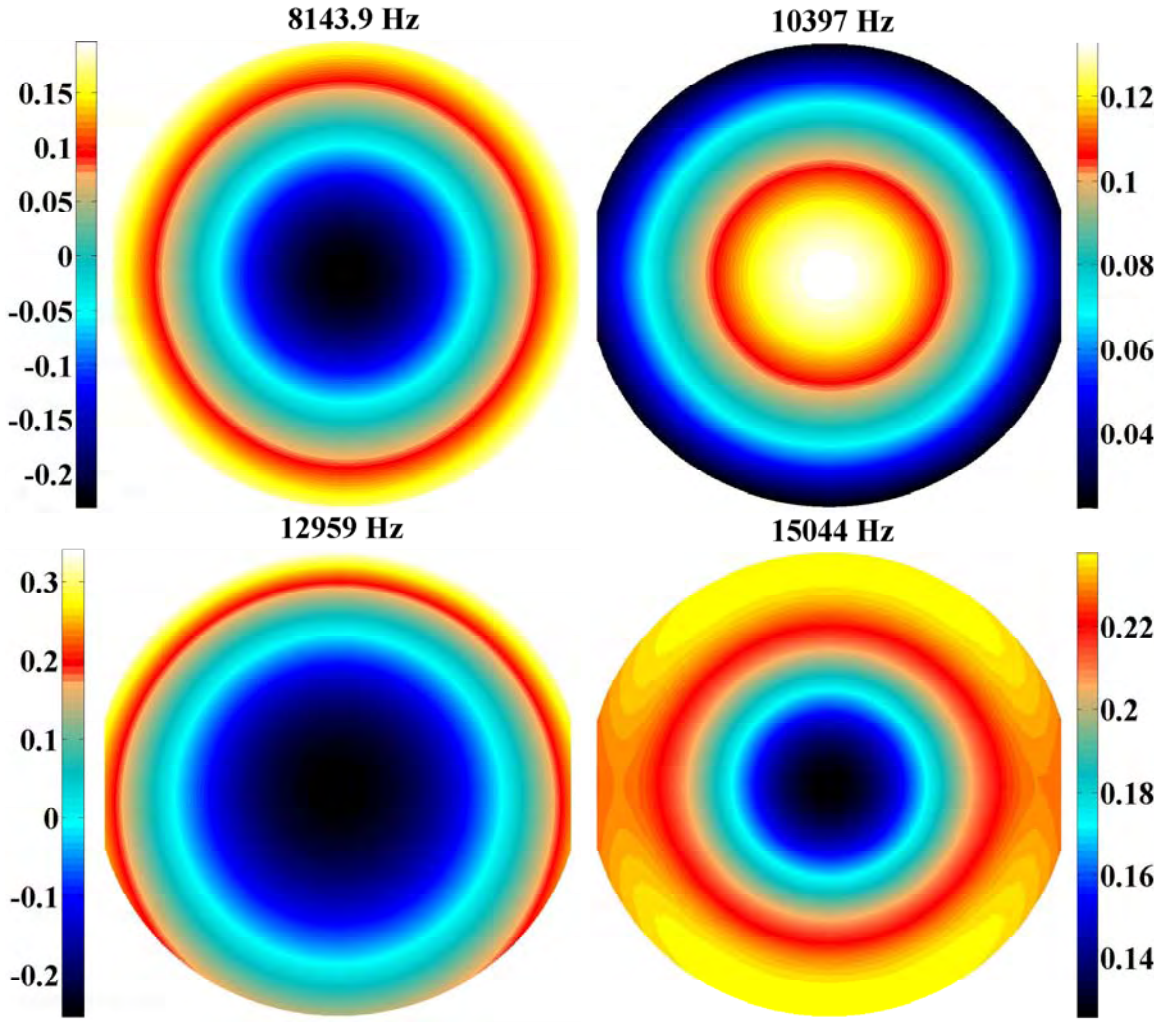

Figure 5.38: Modelled face displacements, $\vec{u}_m \cdot \hat{z}$, of the experimentally studied test mass modes. Asymmetry in the 13 kHz mode is due to the wedge of the test mass.

narrow band around our acoustic mode frequency. Moreover, by finely adjusting the corner frequencies of the filter we were able to tune the loop phase.

The loop was initiated by a small excitation applied at the (now known) modal frequencies. Once a signal to noise $\gtrsim 5$ was achieved the excitation was removed and the loop closed. Excitations were made with only a single quadrant of the ESD as our modelling predicts that all potentially unstable modes may be effectively damped in this way. The feedback loop remained closed until the system reached equilibrium, typically with S/N$\simeq$ 100. At this point the modal amplitude and ESD drive signal were recorded.

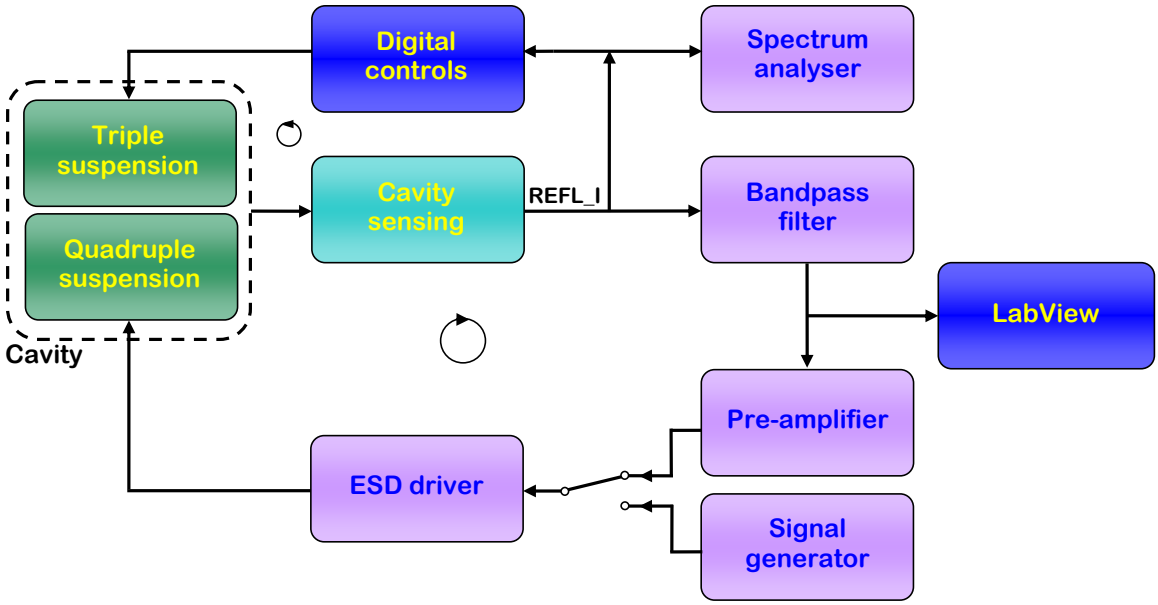

Figure 5.39: Representation of the servo loop used to excited test mass eigenmodes. Excitations were initiated using the signal generator before closing the feedback loop. The upper left loop is the standard arm cavity control scheme feeding back to coil magnet actuators on the final stage of the triple pendulum. REFL_I is the in phase demodulated cavity error signal.

5.3.3.3 Q measurements

The losses associated with each test mass eigenmode were quantified by observing the internal mode oscillations decay in the demodulated cavity error signal REFL_I. With the test mass in an excited state, data capture was initiated and the feedback loop broken, removing any excitation. Modal amplitudes subsequently underwent exponential decay. The ringdown was captured using bespoke *LabView* continuously buffered acquisition code. Sample rate was varied as a function of Q and modal frequency to produce manageable data sets whilst still capturing the character of the process.

The recorded data was post-processed in *MatLab* in order to extract the Q value. Spurious data (e.g. that data recorded whilst excitations were present) was culled before the application of a resonant filter at the internal mode frequency.[24] The envelope of the decay was then extracted by squaring and low pass filtering[25] before the absolute

[24] $Q = 100, G = 1$.
[25] $f_p = 30, 60; Q_p = 0.7, 2$ with a further notch at twice the mode frequency $f_z = 2f_0, Q_z = 100$.

value and square root were taken.[26] The rms noise level of the raw data was found and any envelope data with magnitude smaller than 1/3 of this value were removed from the final analysis.

The amplitude of the test mass oscillation decays exponentially

$$A(t) = A_0 e^{-\frac{t}{\tau}}, \tag{5.73}$$

with time constant

$$\tau = \frac{Q}{\pi f_0}. \tag{5.74}$$

A standard least squares fit of the natural logarithm of the envelope was performed. The gradient of this fit gives $-1/\tau$ and thus Q. In finding Q the measured frequency was used for f_0 since the detuning due to losses is small for large Qs viz

$$f = f_0 \left(1 - \frac{1}{2Q^2}\right)^{1/2} \simeq f_0 \left(1 - \frac{1}{4Q^2}\right) \quad \text{for } Q \gg 1. \tag{5.75}$$

A typical ringdown measurement is shown in fig. 5.40. A complete list of measured Q

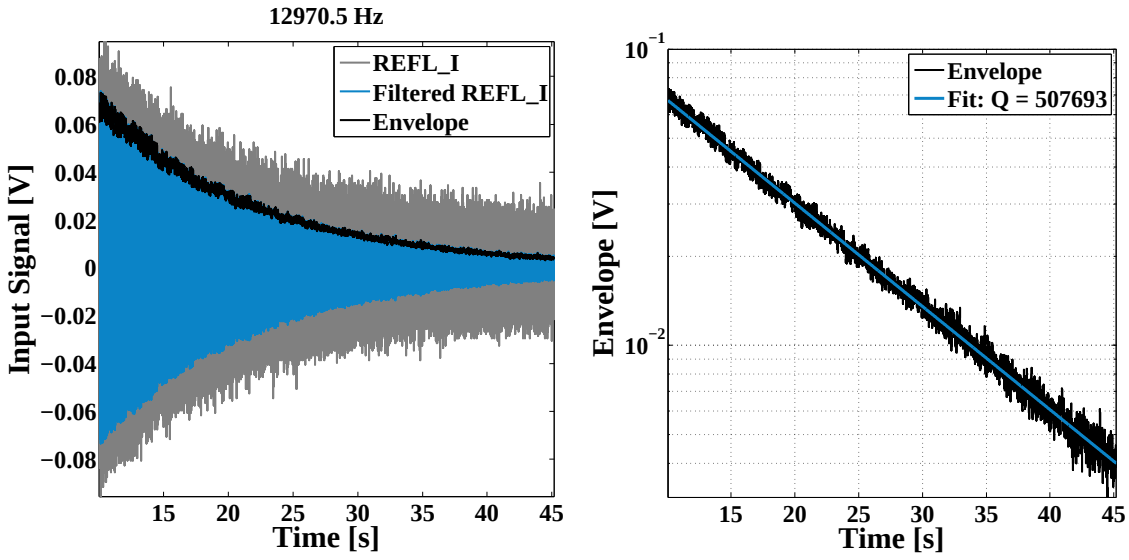

Figure 5.40: Typical ringdown measurement. Left: Raw data, filtered data and extracted envelope. REFL_I is the 0° demodulated cavity error signal.
Right: Q values are found from standard least-squares fits.

[26] Envelope extraction via Hilbert transforms was also tested and found to be equivalent.

values is given in table 5.7 along with predicted and observed mode frequencies.

Table 5.7: Comparison of mode frequencies predicted by FEM and those measured experimentally. Measured test mass Q values are also listed.

f measured kHz	f predicted kHz	Q
8.149	8.1439	412,170 ± 1003
10.4115	10.397	604,158 ± 4728
12.9705	12.959	508,666 ± 2473
15.0405	15.0439	409,504 ± 4139

Observe that measured Q values are significantly lower than the value of 10^7 we assume in our calculations. This illustrates the difficulties associated with preserving the high Qs of 10 kg scale optics and hints that we are perhaps setting an upper limit for the parametric gain. We speculate that the two main loss mechanisms at work may be dissipation due to violin modes of the four lengths of wire suspending the mass [250] and friction associated with wire stand-offs (see fig. 5.41) [215]. Note that these Qs were measured with a metal wire suspension, AdvLIGO will adopt a quasi-monolithic fused silica design [240].

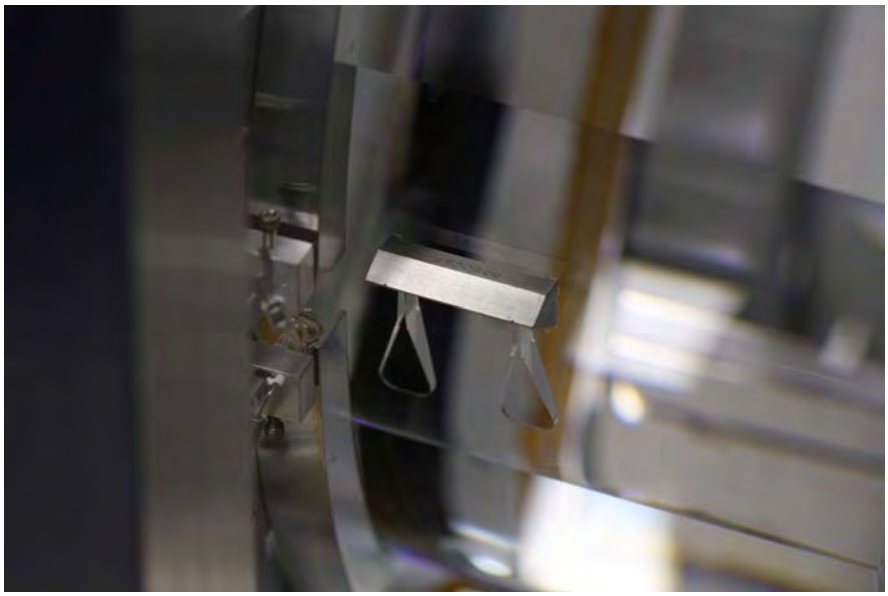

Figure 5.41: Test mass suspension wire stand off. We speculate that this item may contribute excess loss leading to low experimentally measured Qs. Below the metal standoff one can see fused silica ears to which a quasi-monolithic suspension was to be attached.

5.3.3.4 Results

Before presenting measured values and comparing them to those predicted by our numerical model we first discuss possible sources of uncertainty. In evaluating c_m (i.e. (5.71)) we make two assumptions: firstly that we know the shape of the excited mode under study and secondly that the cavity optical mode is well centred on the test mass.

The superb agreement between mode frequencies predicted by finite element modelling and those observed experimentally (see table 5.7) leads us to assert that modal displacements produced by FEM closely matched those of our experimental test mass.

The issue of beam centring on the test mass is not so easily dispatched. Comprehensive steps were taken to ensure that the cavity axis passed through the centre of the mirrors.[27] However perfect alignment can never be assumed. To further mitigate any errors introduced by deviations from perfect centring we limited our analysis to 'drumhead' type modes with smoothly varying mode shapes near their centres. The four modes remaining after this cut are shown in figure 5.38. In our final analysis we assume a centring error of 3 cm. This results in variations in c_m of up to 10%. These effects are included in the error bars of fig. 5.42.

Comparing the overlaps calculated using measured data and those found theoretically (fig. 5.42) agreement was found to be better than 20%. This is a strong endorsement of our modelling work and prior conclusions as both mode shapes and ESD force density were numerically obtained.

5.3.4 Future work

LASTI's principal goal is to prototype systems for the LIGO sites. For our apparatus this will entail the development of a hierarchical control scheme for the quadruple

[27] Alignment with visible lasers, minimising evidence of angular excitations, CCD cameras observing cavity mirrors etc.

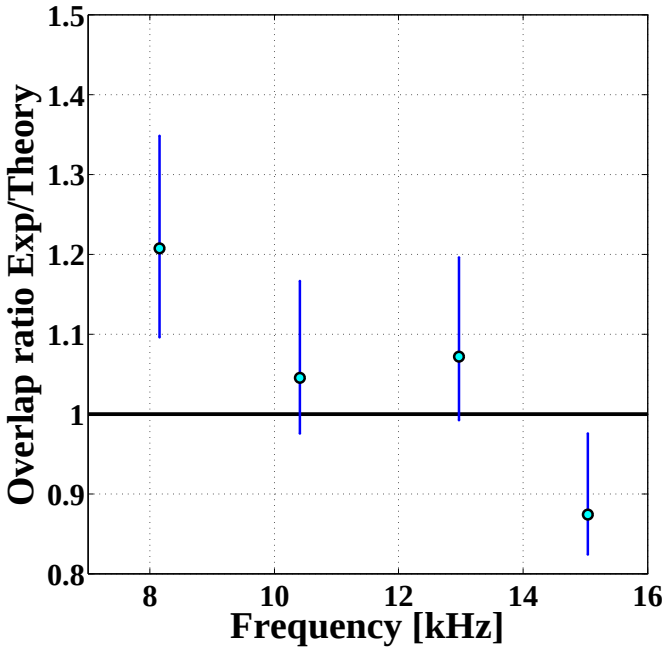

Figure 5.42: Force coupling between ESD and test mass eigenmodes. Ratio of experimental to theoretical b_m coefficients. The shallow downward trend observed in the results suggests a small systematic effect which remains to be accounted for.

pendulum. Once mature this work will be exported to LIGO's sites to expedite detector commissioning.

Since we operate with a single arm there is no common mode rejection of laser noise. Stabilising the laser to a separate reference cavity is of some benefit but more suppression is desirable. Significant correlation was observed between acoustic noise in the reference cavity enclosure and the arm cavity error signal. This leads us to propose an adaptive noise cancellation experiment [251] using a horn driver to feed back to the cavity enclosure. Such work would likely entail simple LMS adaptive filtering [252]. This investigation is more of a curiosity than a final solution as the reference cavity will soon be placed under vacuum. If this is not sufficient a 16 m reference cavity in parallel with the main arm cavity has been mooted.

The measured test mass Q values demonstrate the difficulties in suspending large optics without introducing loss. If Qs in AdvLIGO are this low[28] parametric instabilities are

[28]Remembering that our measurements were made with steel suspension wire.

unlikely to be of concern. We speculated that damping introduced by violin modes of the suspension wires was a principal loss mechanism. A thorough investigation of this issue could prove fruitful.

5.4 In a real detector

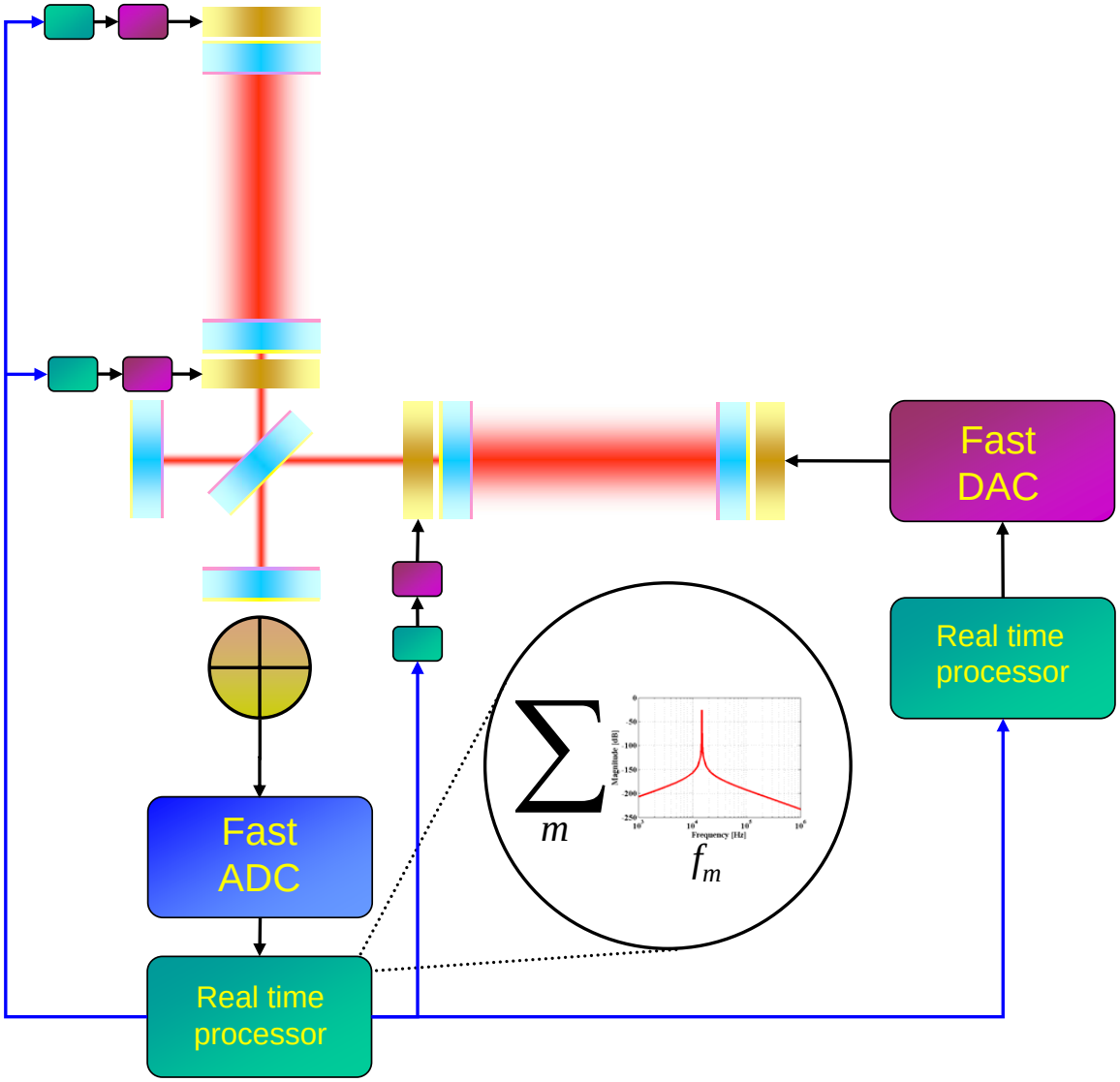

Figure 5.43: How a parametric instability mitigation scheme might work in a second generation interferometer.

5.4.1 Basic scheme

Fig. 5.43 demonstrates how one particular PI mitigation scheme based around the ESDs might operate in a second generation interferometer, in this section we provide explanatory details.

The presence of a fledgling parametric instability is detected at the anti-symmetric port through the beating of the scattered HOM mode sideband with the main carrier field on a suitably segmented detector.[29] This optical interference generates a signal at the mechanical mode frequency w_m.

The photodiode signals are acquired by a fast ADC and processed by a dedicated front end machine running in real time. This machine applies two resonant filters. The first has a Q of ∼10,000 and is centred on the mechanical mode frequency. The purpose of this stage is to limit feedback to the mode of interest and avoid introducing noise to the detection band. A second low Q filter, Q≃10 say, is used to set the phase of our loop via modest detunings from f_m.

The correction signal is then distributed to the real time suspension controllers via a reflective memory network [253]. This system has a bandwidth of approximately 30 MBs^{-1}. The suspension controller will divide the correction appropriately between the quadrants and relay them through a fast DAC to the ESD driver.

5.4.2 Operation

We envisage that this scheme might be applied as follows. With the interferometer initially locked in a stable state, attempts are made to increase the power. A growing PI is detected and the power is subsequently reduced to just below[30] the PI threshold. In this configuration the unstable mode is studied in its thermally excited state. Tuning

[29]The HOM basis functions are orthogonal over a single infinite detector (see §3.2.1.1).

[30]To, as far as possible, preserve the thermal state of the interferometer so that eigenfrequencies do not shift appreciably.

the loop phase by means of the low Q resonant filter section the mode is damped. The effective Q of the mode is now reduced so that later increases in power will not lead to instability.

Due to the frequency selective nature of our approach we expect any noise injected to be negligible. Unless the test masses have an appropriately placed resonance they will not exhibit any appreciable response to our damping forces. What little coupling there is will be evident at frequencies above $\sim$10 kHz – well beyond the gravitational wave detection band.

Sending a $\sim$100 kHz signal to the end stations does incur a delay of many cycles. However this latency does not impact the operation of our system so long as we maintain appropriate phase at the upper and lower unity gain crossings. This gain bandwidth is primarily set by the Q of the mechanical mode rather than the shape of our loop.

It is not important to determine which optic excited any instability. The correction signal can be applied equally to all test masses, the only optic to exhibit a response must have an eigenmode at the observed frequency and is thus culpable. Alternatively one can find the correct optic by applying feedback to each test mass in sequence.

If multiple distinct modes are simultaneously resonant one simply operates several damping loops in parallel. The original photodetector signal will be passed through a compound filter with one high Q resonance per mode. Each resonance will have an associated low Q section to tune the loop phase appropriately. Again, all correction signals can be applied to all optics.

5.4.3 Possible modifications

HOMs created by scattering from an excited optic are evidenced in the photodetector signal by a beat note at the test mass eigenfrequency. Thus we require an operational bandwidth $\gtrsim$100 kHz with commensurately high sampling rate. Such high rates are superfluous for other interferometer subsystems allowing us the freedom to configure a

dedicated system for our scheme.

The simplest approach, described above, would be to augment any existing scheme with fast ADCs and DACs, however a number of other options exist. For example, one could take advantage of the speed and flexibility of FPGAs or alternatively mix signals down to lower frequency before acquisition and reconstruct them at the point of use.[31]

The use of additional hardware to detect HOMs at the dark port of the interferometer may be unnecessary. Finite photodiodes and realistic alignment errors should give sufficient signal on currently available diodes, provided they are not tuned to a particular modulation frequency. Also, if the interferometer is employing homodyne detection the offset from the dark fringe may allow HOMs to be detected at dc using a CCD camera, for example. Nevertheless the benefits of sensing using a quadrant diode which has symmetry equal to that of the ESD should not be underestimated.

Finally we mention that the choice to detect HOMs at the dark port of the interferometer is by no means definitive. It is equally possible to arrange diodes in transmission from the arms or at any other of a number of ports.

5.5 Summary & Conclusion

In this chapter we have provided an introduction to the problem of PIs as applied to interferometric gravitational wave detectors. We have introduced a new way of calculating the parametric gain which is easily understandable and extensible to complex detector topologies. Several issues relating to currently used coil-magnet actuators were raised before introducing the ESD as a solution to these problems and as a possible means of mitigating PIs.

This electrostatic actuator was then modelled numerically to quantify the absolute

[31] In theory this approach should require 10-15 oscillators at both the photodetector and all four test masses to allow the entire 10-100 kHz mechanical mode frequency range to be captured by a 16 kHz ADC. In practice the number of simultaneously unstable modes is likely to be small so that the entire system might operate with 10-15 oscillators total.

force available for lock acquisition and alignment. The distribution of this force was also obtained and used to determine whether ESDs are capable of damping PIs. We contend that all potentially dangerous modes can be effectively suppressed.

A suite of experimental measurements tasked with verifying the predictions of our numerical work was then carried out. Experimental results were found to be in close agreement with our expectations.

We have shown through theoretical, numerical and experimental work that the ESD is a viable candidate for damping PIs. The close agreement between our predicted and observed values for the ESD actuation coefficient and the force coupling between the ESD and test mass eigenmodes demonstrates a sound understanding of the physical principles at work and of each component of our apparatus, including the ESD itself.

If PIs really do begin to threaten the robust operation of second generation interferometers there will likely be no panacea. It is probable that a combination of approaches will be necessary, perhaps based around passive damping with an active scheme targeted to particularly troublesome modes. The ESD entails zero (pecuniary) cost and has shown itself to be effective in suppressing test mass Qs. Therefore the ESD is capable of playing a major role in any such mitigation scheme.

Conclusions

Planned upgrades of existing interferometric gravitational wave detectors aim to increase strain sensitivity by an order of magnitude. The resulting second generation instruments will present new experimental challenges and be limited by new noise sources.

In the frequency band of peak sensitivity, the principal source of displacement noise is expected to be mirror thermal noise. Theory indicates that the impact of this noise scales in inverse proportion to the spot size of laser light incident upon the optics. However, one cannot simply increase the width of the standard Gaussian mode as diffraction losses quickly become unmanageable.

This problem led to the conception of a new non-Gaussian mode for use in long-baseline interferometers. This mode, known as the mesa beam, is wider than the equivalent Gaussian and has a predominantly flat-topped intensity profile. Theoretical analyses argue that, by switching to mesa beams, measured thermal noise can be significantly reduced without compromising interferometer control.

In order to study the properties of this mode experimentally for the first time, a prototype cavity supporting mesa beams was constructed. Unlike Gaussian fields, which are supported by standard spherical mirrors, mesa beam resonators are formed from highly specialised substrates whose intricate features give the mesa beam its unique shape. In building our prototype mirror, collaborators demonstrated that it was possible to manufacture low loss optics with non-uniform figures. Future refinements of the technique developed have proved so successful that it is now being used in the

realisation of spherical mirrors for advanced detectors.

To be useful in a real detector, it is important that the mesa beam can be created efficiently from a Gaussian input. Our work demonstrated that this is possible by coupling Gaussian input light into our mesa beam resonator with high efficiency. Depending on the eventual implementation of mesa beams, this coupling may also have important consequences for the application of recycling techniques.

In commissioning our cavity it was also confirmed that standard Pound-Drever-Hall reflection locking techniques are applicable to mesa beams. The measured discriminant closely followed theoretical prediction and was successfully used in the longitudinal control of our resonator. The widespread use of the PDH method in Gaussian beam interferometry makes this achievement all the more significant.

The fundamental mesa eigenmode supported by our resonator was found to be consistent with the best achievable, given measured mirror imperfections. These imperfections resulted from the manufacturing constraints imposed by the small size of our optic, larger optics suitable for astrophysically significant interferometers should be far easier to realise.

Mesa beam interferometers are predicted to be marginally more sensitive to angular mirror motion than their Gaussian counterparts. Using our prototype resonator this conjecture was tested. Recording the mesa beam intensity profile as a function of mirror tilts, the experimental response was shown to be in excellent agreement with prediction. Although this result confirmed that mesa beams are indeed more sensitive to mirror tilts, it also illustrated that the level of pointing accuracy achieved in currently operating detectors is sufficient for operation with mesa beams.

Following this positive result, the extension of differential wavefront sensing to mesa beams was investigated. The resulting error signals were bipolar and linear about resonance, suggesting closed loop control to be feasible. An unexplained systematic error in the magnitude of the signals remains to be explored with current suspicion falling on figure errors of the cavity mirrors.

Our study of the mesa beam continued with numerical simulations of the effects optical power absorbed in mirror coatings could have on mesa resonators. Using FFT routines the steady state eigenmodes of thermally perturbed cavities were found. These fields allowed losses and thermal noise to be calculated as a function of absorbed power.

The flat mesa beam retained its greater width under thermal loading whereas Gaussian and concentric mesa beams became sharply peaked. The thermal noise of the concentric and Gaussian modes thus increased as expected. In contrast, the measured thermal noise associated with the flat mesa beam actually decreased. The optical losses experienced by all modes grew with absorbed power. Both mesa beam configurations were slightly less susceptible to increases in diffraction loss.

We conclude our review of results regarding mesa beams by outlining possible avenues of future research for what remains an immature but greatly promising technology.

As a result of the lag between theoretical and experimental results, much of the work regarding mesa beams to date has focused on the nearly flat cavity configuration. Due to radiation pressure induced tilt instabilities it is important that concentric beams perform equally well. We therefore advise that future examinations of non-Gaussian modes concentrate on this geometry.

It has been shown that the behaviour of mesa beams meets with expectation in a single Fabry-Perot interferometer. It is our recommendation that future efforts be directed toward evaluation of this mode in dual-recycled Michelson configurations. Throughout our work the accuracy of FFT based simulations has been consistently demonstrated. Using these techniques to simulate mesa beams in a full interferometer will allow signal extraction and subtle recycling effects to be investigated with realistically imperfect optics. Results from this simulation work will likely inform the choice of subsequent experimental endeavours.

In tandem with this effort, current methods of constructing non-spherical mirrors for mesa beams should be refined and new methods sought. It is important to demonstrate that large scale optics suitable for gravitational wave detectors can indeed be

manufactured to the required specifications and the ability to realise small mirrors for table-top mesa beam experiments would dramatically accelerate development work.

Whilst this proposed research is underway, care should be taken to monitor the progress of other modes hoping to replace the fundamental Gaussian beam. Although the mesa beam was the first to be experimentally studied, it may not prove the most practical solution in a real interferometer.

Due to radiation pressure, there exists a nonlinear coupling between optical energy stored in the interferometer's arms and mechanical energy stored in the acoustic modes of its test masses. Second generation interferometers will operate with increased circulating power and lower loss test masses, increasing the strength of this coupling. Under appropriate conditions, the test masses can become so excited that interferometer operation becomes impossible. This effect is known as parametric instability and has been touted as one of the greatest experimental challenges facing advanced interferometers.

In the final part of this work we considered a proposal to mitigate parametric instabilities using the electrostatic actuators designed to control the position and orientation of the test masses. Through these actuators the test mass eigenmodes can be damped, reducing parametric gain to a safe level.

This examination began with extensive finite element modelling. A modal analysis of an Advanced LIGO style test mass was conducted to find its eigenmodes and their resonant frequencies. Simulations were also performed to determine the maximum force available from the electrostatic drive along with its spatial distribution. Using this information, a simple model was developed to predict the force required to damp each potentially dangerous acoustic mode to a safe level.

Including a reasonable margin, such force was found to be available for all modes. Thus, parametric instabilities in advanced interferometers can, theoretically at least, be eliminated without the introduction of any additional hardware.

In order to test these claims an experimental investigation was conducted using proto-

type Advanced LIGO hardware, including a full size test mass and electrostatic actuator. Since our apparatus operated at low power, it was not possible to demonstrate damping of a spontaneously excited instability. However, available measurements revealed that our model was successful in predicting the frequencies of the test mass eigenmodes, the absolute strength of the electrostatic actuator and the coupling between the electrostatic drive and all observable test mass modes. These successes bestow credibility upon our grander claims.

Future continuation of our work on parametric instabilities should seek to understand whether acoustic modes of the test masses can be effectively damped using coil-magnet actuators. Once modelled, this idea could be investigated experimentally using the thermally excited modes observed in currently operating detectors.

Although methods of implementing our approach in an operational detector have been sketched, further work is necessary to demonstrate that this scheme is truly practical. It may be that simpler passive ideas, such as resistively shunted piezoelectric dampers, are ultimately preferable.

Appendix A

Material parameters

As far as possible we use parameters which, at the time of writing, appear plausible for future second generation interferometers. We acknowledge that these values are dynamic and have thus presented sufficient detail above to allow any of our numerical values to be re-calculated.

Table A.1: The material parameters used in our calculations of thermal effects.

	Parameter	Symbol	Value
Substrate	Radius	a	0.17 m
	Thickness	h	0.2 m
	Density	ρ	2.2×10^{3} kgm^{-3}
	Poisson's ratio	σ	0.17
	Young's modulus	Y	7.2×10^{10} Nm^{-2}
	Loss angle	Φ	5×10^{-9}
	Linear thermal expansion coefficient	$\alpha_{\rm th}$	5.1×10^{-7} K^{-1}
	Thermal conductivity	$K_{\rm th}$	1.38 Wm^{-1}K^{-1}
	Specific heat at constant volume	$C_{\rm v}$	1.64×10^{6} JK^{-1}m^{-3}
Averaged parameters in SiO_2/Ta_2O_5 coating	Poisson's ratio	$\sigma_{\rm c}$	0.195
	Young's modulus	$Y_{\rm c}$	1.003×10^{11} Nm^{-2}
	Loss angle	$\Phi_{\rm c}$	2.167×10^{-4}
	Linear thermal expansion coefficient	$\alpha_{\rm c}$	1.798×10^{-6} K^{-1}
	Thermal conductivity	$K_{\rm th,c}$	2.297 Wm^{-1}K^{-1}
	Specific heat at constant volume	$C_{\rm v,c}$	1.832×10^{6} JK^{-1}m^{-3}
	Total coating thickness	d	5.975×10^{-6} m.

Appendix B

ESD mask drawings

For ease of viewing each of these drawings is granted a full page.

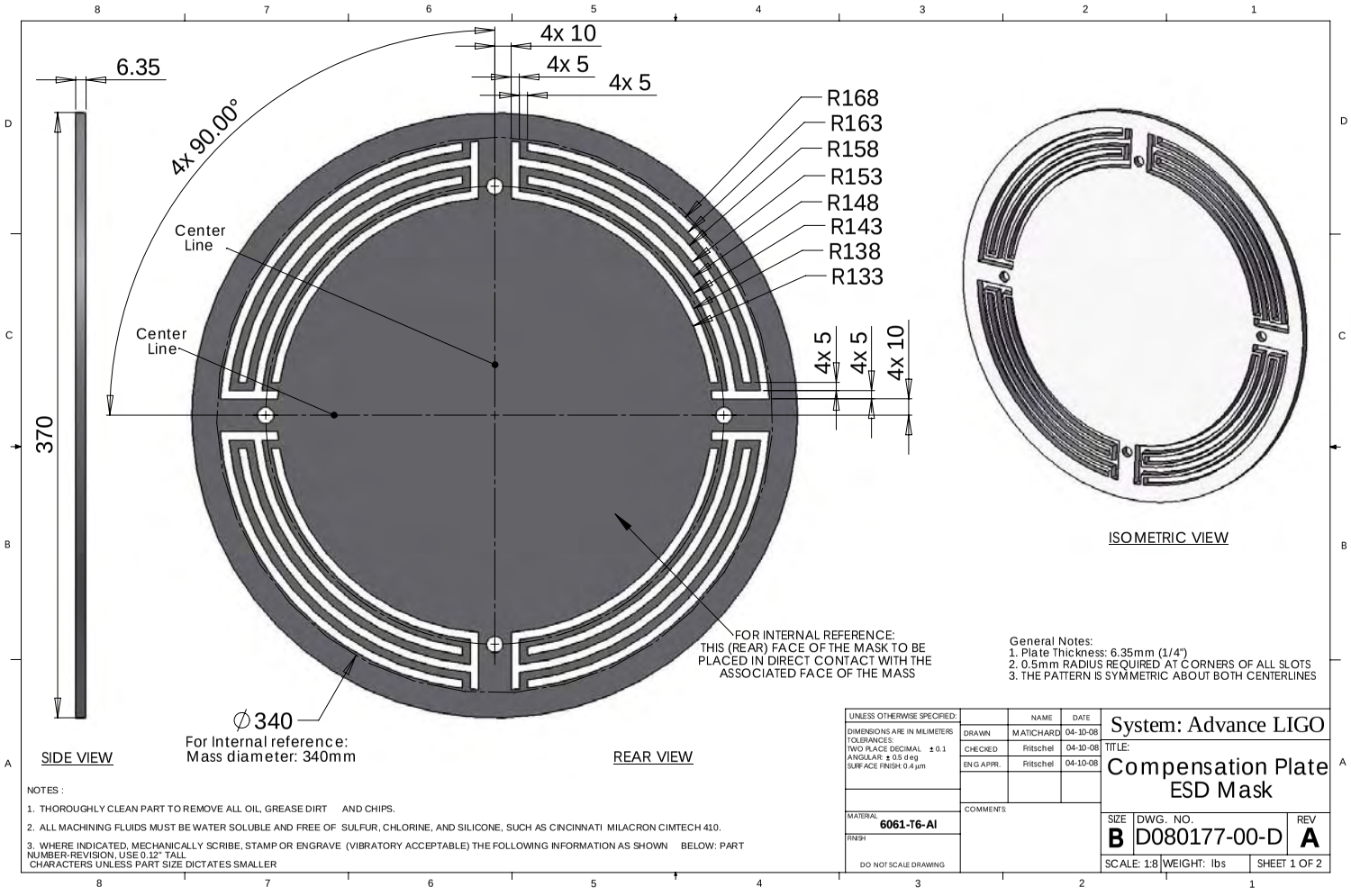

Figure B.1: Technical drawing of mask used in manufacture of LASTI prototype ESD (1 of 2). We assume perfect manufacturing and use the dimensions given in our model.

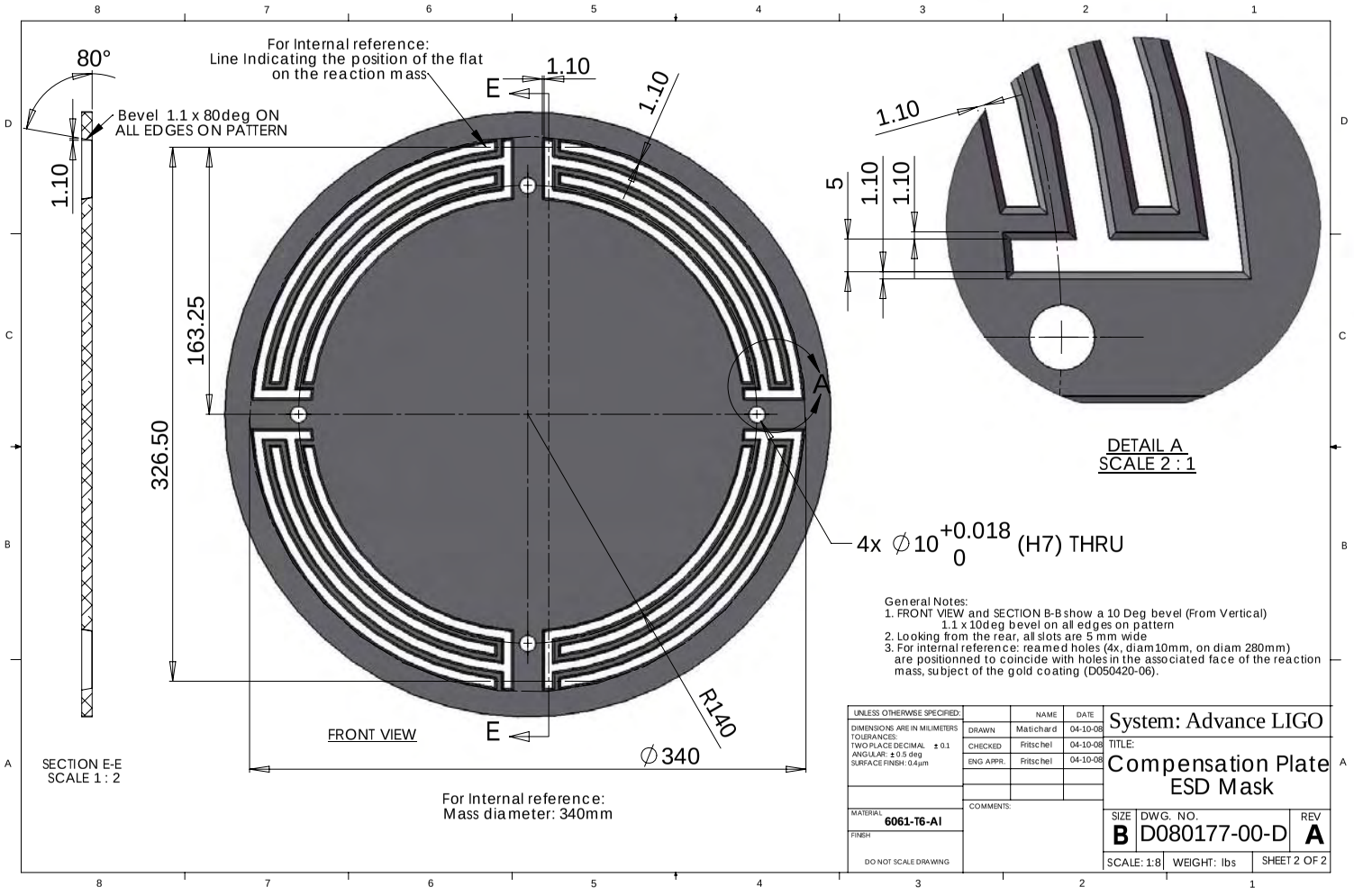

Figure B.2: Technical drawing of mask used in manufacture of LASTI prototype ESD (2 of 2). We assume perfect manufacturing and use the dimensions given in our model.

Bibliography

[1] B. Schutz. *A First Course in General Relativity.* Cambridge University Press, Cambridge, 2009.

[2] C. Misner, K. Thorne, and J. Wheeler. *Gravitation.* W. H. Freeman, San Francisco, 1973.

[3] K. G. Jansky. Radio Waves from Outside the Solar System. *Nature*, 132:66, July 1933.

[4] A. Einstein. Über Gravitationswellen. *Sitzungsberichte der Königlich Preußischen Akademie der Wissenschaften (Berlin), Seite 154-167.*, pages 154–167, 1918.

[5] A. Einstein. Die Grundlage der allgemeinen Relativitätstheorie. *Annalen der Physik*, 354:769–822, 1916.

[6] M. Ando. *Power recycling for an interferometric gravitational wave detector.* PhD thesis, University of Tokyo, 1998.

[7] P. Fritschel. *Techniques for laser interferometer gravitational waves observatories.* PhD thesis, Massachusetts Institute of Technology, 1992.

[8] E. Müller, M. Rampp, R. Buras, H.-T. Janka, and D. H. Shoemaker. Toward Gravitational Wave Signals from Realistic Core-Collapse Supernova Models. *The Astrophysical Journal*, 603:221–230, March 2004.

[9] B. P. Abbott et al. Search for gravitational waves from low mass compact binary coalescence in 186 days of LIGO's fifth science run. *Phys. Rev. D*, 80(4):047101, August 2009.

[10] B. S. Sathyaprakash and S. V. Dhurandhar. Choice of filters for the detection of gravitational waves from coalescing binaries. *Phys. Rev. D*, 44:3819–3834, December 1991.

[11] J. H. Taylor, R. N. Manchester, and A. G. Lyne. Catalog of 558 pulsars. *The Astrophysical Journal Supplement*, 88:529–568, October 1993.

[12] B. P. Abbott et al. Searches for gravitational waves from known pulsars with S5 LIGO data. *ArXiv e-prints*, September 2009.

[13] B. P. Abbott et al. An upper limit on the stochastic gravitational-wave background of cosmological origin. *Nature*, 460:990–994, August 2009.

[14] R. A. Hulse and J. H. Taylor. Discovery of a pulsar in a binary system. *The Astropysical Journal Letters*, 195:L51–L53, January 1975.

[15] J. M. Weisberg and J. H. Taylor. The Relativistic Binary Pulsar B1913+16: Thirty Years of Observations and Analysis. In F. A. Rasio & I. H. Stairs, editor, *Binary Radio Pulsars*, volume 328 of *Astronomical Society of the Pacific Conference Series*, page 25, July 2005.

[16] J. Weber. Evidence for Discovery of Gravitational Radiation. *Physical Review Letters*, 22:1320–1324, June 1969.

[17] J. Weber. Anisotropy and Polarization in the Gravitational-Radiation Experiments. *Physical Review Letters*, 25:180–184, July 1970.

[18] J. A. Tyson and R. P. Giffard. Gravitational-wave astronomy. *Annu. Rev. Astron. Astrophys.*, 16:521–554, 1978.

[19] D. H. Douglass and V. B. Braginsky. Gravitational-radiation experiments. In S. W. Hawking and W. Israel, editors, *General Relativity: An Einstein Centenary Survey*, pages 90–137. Cambridge University Press, Cambridge, U.K.; New York, U.S.A., 1979.

[20] D. G. Blair, I. S. Heng, E. N. Ivanov, and M. E. Tobar. Present Status of the Resonant Mass Gravitational Wave Antenna, NIOBE. In E. Coccia, G. Veneziano,

& G. Pizzella, editor, *Second Edoardo Amaldi Conference on Gravitational Wave Experiments*, page 127, 1998.

[21] I. S. Heng, E. Daw, J. Giaime, W. O. Hamilton, M. P. Mchugh, and W. W. Johnson. Allegro: noise performance and the ongoing search for gravitational waves. *Classical and Quantum Gravity*, 19:1889–1895, April 2002.

[22] L. Conti. The AURIGA second scientific run and the dual detector of gravitational waves. *Nuclear Instruments and Methods in Physics Research A*, 518:236–239, February 2004.

[23] P. Astone, R. Ballantini, D. Babusci, M. Bassan, P. Bonifazi, G. Cavallari, A. Chincarini, E. Coccia, S. D'Antonio, M. D. P. Emilio, V. Fafone, S. Foffa, G. Gemme, G. Giordano, M. Maggiore, A. Marini, Y. Minenkov, I. Modena, G. Modestino, A. Moleti, G. V. Pallottino, R. Parodi, G. Pizzella, L. Quintieri, A. Rocchi, F. Ronga, R. Sturani, R. Terenzi, G. Torrioli, R. Vaccarone, G. Vandoni, and M. Visco. EXPLORER and NAUTILUS gravitational wave detectors: a status report. *Classical and Quantum Gravity*, 25(11):114048, June 2008.

[24] O. D. Aguiar, L. A. Andrade, J. J. Barroso, F. Bortoli, L. A. Carneiro, P. J. Castro, C. A. Costa, K. M. F. Costa, J. C. N. de Araujo, A. U. de Lucena, W. de Paula, E. C. de Rey Neto, S. T. de Souza, A. C. Fauth, C. Frajuca, G. Frossati, S. R. Furtado, N. S. Magalhães, R. M. Marinho Jr., J. L. Melo, O. D. Miranda, N. F. Oliveira Jr., K. L. Ribeiro, C. Stellati, W. F. Velloso Jr., and J. Weber. The Brazilian gravitational wave detector Mario Schenberg: status report. *Classical and Quantum Gravity*, 23:239, April 2006.

[25] L. Gottardi, A. de Waard, O. Usenko, G. Frossati, M. Podt, J. Flokstra, M. Bassan, V. Fafone, Y. Minenkov, and A. Rocchi. Sensitivity of the spherical gravitational wave detector MiniGRAIL operating at 5K. *Phys. Rev. D*, 76(10):102005, November 2007.

[26] G. E. Moss, L. R. Miller, and R. L. Forward. Photon-noise-limited laser transducer for gravitational antenna. *Appl. Optics*, 10:2495, 1971.

[27] R. Weiss. Electromagnetically coupled broadband gravitational antenna. Technical report, Massachusetts Institute of Technology, Cambridge, U.S.A., 1972.

[28] R. W. P. Drever, J. Hough, W. A. Edelstein, J. R. Pugh, and W. Martin. On gravitational radiation detectors using optical sensing techniques. In B. Bertotti, editor, *Experimental Gravitation (Gravitazione Sperimentale)*, pages 365–369, New York, U.S.A., 1977. Accademi Nazionale Dei Lincei, Academic Press.

[29] H. Billing, K. Maischberger, A. Rüdiger, R. Schilling, L. Schnupp, and W. Winkler. An argon laser interferometer for the detection of gravitational radiation. *J. Phys. E*, 12:1043–1050, 1979.

[30] D. R. Herriott and H. J. Schulte. Folded optical delay lines. *App. Opt.*, 4:883, August 1965.

[31] S. Sato, M. Ohashi, M.-K. Fujimoto, M. Fukushima, K. Waseda, S. Miyoki, N. Mavalvala, and H. Yamamoto. High-Gain Power Recycling of a Fabry Perot Michelson Interferometer for a Gravitational-Wave Antenna. *App. Opt.*, 39:4616–4620, September 2000.

[32] B. J. Meers. Recycling in laser-interferometric gravitational-wave detectors. *Phys. Rev. D*, 38:2317–2326, October 1988.

[33] K. A. Strain and B. J. Meers. Experimental demonstration of dual recycling for interferometric gravitational-wave detectors. *Physical Review Letters*, 66:1391–1394, March 1991.

[34] S. Hild, H. Grote, M. Hewtison, H. Lück, J. R. Smith, K. A. Strain, B. Willke, and K. Danzmann. Demonstration and comparison of tuned and detuned signal recycling in a large-scale gravitational wave detector. *Classical and Quantum Gravity*, 24:1513–1523, March 2007.

[35] K. Kawabe and the LIGO Collaboration. Status of LIGO. *Journal of Physics Conference Series*, 120(3):032003, July 2008.

[36] F. Acernese et al. Virgo status. *Classical and Quantum Gravity*, 25(18):184001, September 2008.

[37] H. Grote and the LIGO Scientific Collaboration. The status of GEO 600. *Classical and Quantum Gravity*, 25(11):114043, June 2008.

[38] H. Vahlbruch. *Squeezed Light for Gravitational Wave Astronomy*. PhD thesis, Liebniz Universtät Hannover, 2008.

[39] B. Willke, P. Ajith, B. Allen, P. Aufmuth, C. Aulbert, S. Babak, R. Balasubramanian, B. W. Barr, S. Berukoff, A. Bunkowski, G. Cagnoli, C. A. Cantley, M. M. Casey, S. Chelkowski, Y. Chen, D. Churches, T. Cokelaer, C. N. Colacino, D. R. M. Crooks, C. Cutler, K. Danzmann, R. J. Dupuis, E. Elliffe, C. Fallnich, A. Franzen, A. Freise, I. Gholami, S. Goßler, A. Grant, H. Grote, S. Grunewald, J. Harms, B. Hage, G. Heinzel, I. S. Heng, A. Hepstonstall, M. Heurs, M. Hewitson, S. Hild, J. Hough, Y. Itoh, G. Jones, R. Jones, S. H. Huttner, K. Kötter, B. Krishnan, P. Kwee, H. Lück, M. Luna, B. Machenschalk, M. Malec, R. A. Mercer, T. Meier, C. Messenger, S. Mohanty, K. Mossavi, S. Mukherjee, P. Murray, G. P. Newton, M. A. Papa, M. Perreur-Lloyd, M. Pitkin, M. V. Plissi, R. Prix, V. Quetschke, V. Re, T. Regimbau, H. Rehbein, S. Reid, L. Ribichini, D. I. Robertson, N. A. Robertson, C. Robinson, J. D. Romano, S. Rowan, A. Rüdiger, B. S. Sathyaprakash, R. Schilling, R. Schnabel, B. F. Schutz, F. Seifert, A. M. Sintes, J. R. Smith, P. H. Sneddon, K. A. Strain, I. Taylor, R. Taylor, A. Thüring, C. Ungarelli, H. Vahlbruch, A. Vecchio, J. Veitch, H. Ward, U. Weiland, H. Welling, L. Wen, P. Williams, W. Winkler, G. Woan, and R. Zhu. The GEO-HF project. *Classical and Quantum Gravity*, 23:207, April 2006.

[40] S. Braccini, L. Barsotti, C. Bradaschia, G. Cella, A. di Virgilio, I. Ferrante, F. Fidecaro, I. Fiori, F. Frasconi, A. Gennai, A. Giazotto, F. Paoletti, R. Passaquieti, D. Passuello, R. Poggiani, E. Campagna, G. Guidi, G. Losurdo, F. Martelli, M. Mazzoni, B. Perniola, F. Piergiovanni, R. Stanga, F. Vetrano, A. Viceré, L. Brocco, S. Frasca, E. Majorana, A. Pai, C. Palomba, P. Puppo, P. Rapagnani, F. Ricci, G. Ballardin, R. Barillé, R. Cavalieri, E. Cuoco, V. Dattilo, D. Enard, R. Flaminio, A. Freise, S. Hebri, L. Holloway, P. L. Penna, M. Loupias, J. Marque, C. Moins, A. Pasqualetti, P. Ruggi, R. Taddei, Z. Zhang, F. Acernese, S. Avino, F. Barone, E. Calloni, R. de Rosa, L. di Fiore, A. Eleuteri,

L. Giordano, L. Milano, S. Pardi, K. Qipiani, I. Ricciardi, G. Russo, S. Solimeno, D. Babusci, G. Giordano, P. Amico, L. Bosi, L. Gammaitoni, F. Marchesoni, M. Punturo, F. Travasso, H. Vocca, C. Boccara, J. Moreau, V. Loriette, V. Reita, J. M. Mackowski, N. Morgado, L. Pinard, A. Remillieux, M. Barsuglia, M. A. Bizouard, V. Brisson, F. Cavalier, A. C. Clapson, M. Davier, P. Hello, S. Krecklbergh, F. Beauville, D. Buskulic, R. Gouaty, D. Grosjean, F. Marion, A. Masserot, B. Mours, E. Tournefier, D. Tombolato, D. Verkindt, M. Yvert, S. Aoudia, F. Bondu, A. Brillet, E. Chassande-Mottin, F. Cleva, J. P. Coulon, B. Dujardin, J. D. Fournier, H. Heitmann, C. N. Man, A. Spallicci, and J.-Y. Vinet. Measurement of the seismic attenuation performance of the VIRGO Superattenuator. *Astroparticle Physics*, 23:557–565, July 2005.

[41] M. Ando and the TAMA collaboration. Current status of TAMA. *Classical and Quantum Gravity*, 19:1409–1419, April 2002.

[42] M. Ohashi and the LCGT Collaboration. Status of LCGT and CLIO. *Journal of Physics Conference Series*, 120(3):032008, July 2008.

[43] K. Yamamoto, T. Uchiyama, S. Miyoki, M. Ohashi, K. Kuroda, H. Ishitsuka, T. Akutsu, S. Telada, T. Tomaru, T. Suzuki, N. Sato, Y. Saito, Y. Higashi, T. Haruyama, A. Yamamoto, T. Shintomi, D. Tatsumi, M. Ando, H. Tagoshi, N. Kanda, N. Awaya, S. Yamagishi, H. Takahashi, A. Araya, A. Takamori, S. Takemoto, T. Higashi, H. Hayakawa, W. Morii, and J. Akamatsu. Current status of the CLIO project. *Journal of Physics Conference Series*, 122(1):012002, July 2008.

[44] R. L. Ward, R. Adhikari, B. Abbott, R. Abbott, D. Barron, R. Bork, T. Fricke, V. Frolov, J. Heefner, A. Ivanov, O. Miyakawa, K. McKenzie, B. Slagmolen, M. Smith, R. Taylor, S. Vass, S. Waldman, and A. Weinstein. dc readout experiment at the Caltech 40m prototype interferometer. *Classical and Quantum Gravity*, 25(11):114030, June 2008.

[45] S. Hild, H. Grote, J. Degallaix, S. Chelkowski, K. Danzmann, A. Freise, M. Hewitson, J. Hough, H. Lück, M. Prijatelj, K. A. Strain, J. R. Smith, and B. Willke.

DC-readout of a signal-recycled gravitational wave detector. *Classical and Quantum Gravity*, 26(5):055012, March 2009.

[46] R. Adhikari. Enhanced LIGO. In *AAS/High Energy Astrophysics Division*, volume 9 of *AAS/High Energy Astrophysics Division*, page 21.03, September 2006.

[47] Einstein Telescope website. `http://www.et-gw.eu/`.

[48] O. Jennrich. TOPICAL REVIEW: LISA technology and instrumentation. *Classical and Quantum Gravity*, 26(15):153001, August 2009.

[49] G. B. Hobbs, M. Bailes, N. D. R. Bhat, S. Burke-Spolaor, D. J. Champion, W. Coles, A. Hotan, F. Jenet, L. Kedziora-Chudczer, J. Khoo, K. J. Lee, A. Lommen, R. N. Manchester, J. Reynolds, J. Sarkissian, W. van Straten, S. To, J. P. W. Verbiest, D. Yardley, and X. P. You. Gravitational-Wave Detection Using Pulsars: Status of the Parkes Pulsar Timing Array Project. *Publications of the Astronomical Society of Australia*, 26:103–109, June 2009.

[50] J. W. Armstrong. Low-Frequency Gravitational Wave Searches Using Spacecraft Doppler Tracking. *Living Reviews in Relativity*, 9:1, January 2006.

[51] S. Dimopoulos, P. W. Graham, J. M. Hogan, M. A. Kasevich, and S. Rajendran. Gravitational wave detection with atom interferometry. *Physics Letters B*, 678:37–40, July 2009.

[52] S. Reid, G. Cagnoli, D. R. M. Crooks, J. Hough, P. Murray, S. Rowan, M. M. Fejer, R. Route, and S. Zappe. Mechanical dissipation in silicon flexures. *Physics Letters A*, 351:205–211, March 2006.

[53] E. J. Elliffe, J. Bogenstahl, A. Deshpande, J. Hough, C. Killow, S. Reid, D. Robertson, S. Rowan, H. Ward, and G. Cagnoli. Hydroxide-catalysis bonding for stable optical systems for space. *Classical and Quantum Gravity*, 22:257, May 2005.

[54] M. van Veggel et al. Final design document ETM/ITM ears. Technical Report LIGO-T0900447-v3, Institute for Gravitational Research, 2009.

[55] G. Fowles. *Introduction to Modern Optics*. Dover Publications, New York, 1989.

[56] G. M. Harry et al. Titania-doped tantala/silica coatings for gravitational-wave detection. *Classical and Quantum Gravity*, 24:405–415, January 2007.

[57] J. Agresti, G. Castaldi, R. DeSalvo, V. Galdi, V. Pierro, and I. M. Pinto. Optimized multilayer dielectric mirror coatings for gravitational wave interferometers. In *Society of Photo-Optical Instrumentation Engineers (SPIE) Conference Series*, volume 6286 of *Society of Photo-Optical Instrumentation Engineers (SPIE) Conference Series*, September 2006.

[58] P. Fritschel et al. Adv. LIGO Arm Length Stabilisation Design. Technical Report LIGO-T0900144-v2, LIGO Laboratory, 2009.

[59] P. R. Saulson. Terrestrial gravitational noise on a gravitational wave antenna. *Phys. Rev. D*, 30:732–736, August 1984.

[60] S. A. Hughes and K. S. Thorne. Seismic gravity-gradient noise in interferometric gravitational-wave detectors. *Phys. Rev. D*, 58(12):122002, December 1998.

[61] K. S. Thorne and C. J. Winstein. Human gravity-gradient noise in interferometric gravitational-wave detectors. *Phys. Rev. D*, 60(8):082001, October 1999.

[62] J. Harms, R. Desalvo, S. Dorsher, and V. Mandic. Simulation of underground gravity gradients from stochastic seismic fields. *Phys. Rev. D*, 80(12):122001, December 2009.

[63] C. M. Caves. Quantum-Mechanical Radiation-Pressure Fluctuations in an Interferometer. *Physical Review Letters*, 45:75–79, July 1980.

[64] W. A. Edelstein, J. Hough, J. R. Pugh, and W. Martin. Limits to the measurement of displacement in an interferometric gravitational radiation detector. *J. Phys. E*, 11(7):710–711, 1978.

[65] Y. Levin. Internal thermal noise in the LIGO test masses: A direct approach. *Phys. Rev. D*, 57:659–663, January 1998.

[66] K. Yamamoto, S. Otsuka, M. Ando, K. Kawabe, and K. Tsubono. Study of the thermal noise caused by inhomogeneously distributed loss. *Classical and Quantum Gravity*, 19:1689–1696, April 2002.

[67] A. L. Kimball and D. E. Lovell. Internal Friction in Solids. *Physical Review*, 30:948–959, December 1927.

[68] Y. T. Liu and K. S. Thorne. Thermoelastic noise and homogeneous thermal noise in finite sized gravitational-wave test masses. *Phys. Rev. D*, 62(12):122002, December 2000.

[69] S. D. Penn, P. H. Sneddon, H. Armandula, J. C. Betzwieser, G. Cagnoli, J. Camp, D. R. M. Crooks, M. M. Fejer, A. M. Gretarsson, G. M. Harry, J. Hough, S. E. Kittelberger, M. J. Mortonson, R. Route, S. Rowan, and C. C. Vassiliou. Mechanical loss in tantala/silica dielectric mirror coatings. *Classical and Quantum Gravity*, 20:2917–2928, July 2003.

[70] D. R. M. Crooks, G. Cagnoli, M. M. Fejer, A. Gretarsson, G. Harry, J. Hough, N. Nakagawa, S. Penn, R. Route, S. Rowan, and P. H. Sneddon. Experimental measurements of coating mechanical loss factors. *Classical and Quantum Gravity*, 21:1059, March 2004.

[71] S. D. Penn, A. Ageev, D. Busby, G. M. Harry, A. M. Gretarsson, K. Numata, and P. Willems. Frequency and surface dependence of the mechanical loss in fused silica. *Physics Letters A*, 352:3–6, March 2006.

[72] M. R. Abernathy, G. M. Harry, F. Travasso, I. Martin, S. Reid, S. Rowan, J. Hough, M. M. Fejer, R. Route, S. Penn, H. Armandula, and A. Gretarsson. The effects of heating on mechanical loss in tantala/silica optical coatings. *Physics Letters A*, 372:87–90, January 2008.

[73] V. B. Braginsky, M. L. Gorodetsky, and S. P. Vyatchanin. Thermodynamical fluctuations and photo-thermal shot noise in gravitational wave antennae. *Phys. Lett. A.*, 264:1, 1999.

[74] B. Benthem and Y. Levin. Thermorefractive and thermochemical noise in the beamsplitter of the GEO600 gravitational-wave interferometer. *Phys. Rev. D*, 80(6):062004, Sep 2009.

[75] M. N. Inci and T. Yoshino. A Fiber Optic Wavelength Modulation Sensor Based on Tantalum Pentoxide Coatings for Absolute Temperature Measurements. *Optical Review*, 7:205–208, May 2000.

[76] M. N. Inci. Simultaneous measurements of thermal optical and linear thermal expansion coefficients of Ta_2O_5 films. In G. C. Righini & A. Consortini, editor, *Society of Photo-Optical Instrumentation Engineers (SPIE) Conference Series*, volume 4829 of *Society of Photo-Optical Instrumentation Engineers (SPIE) Conference Series*, pages 777–778, November 2003.

[77] M. Evans, S. Ballmer, M. Fejer, P. Fritschel, G. Harry, and G. Ogin. Thermo-optic noise in coated mirrors for high-precision optical measurements. *Phys. Rev. D*, 78(10):102003, November 2008.

[78] S. Rao. *Mirror Thermal Noise in Interferometric Gravitational Wave Detectors*. PhD thesis, California Institute of Technology, 2003.

[79] E. D. Black, A. Villar, K. Barbary, A. Bushmaker, J. Heefner, S. Kawamura, F. Kawazoe, L. Matone, S. Meidt, S. R. Rao, K. Schulz, M. Zhang, and K. G. Libbrecht. Direct observation of broadband coating thermal noise in a suspended interferometer. *Physics Letters A*, 328:1–5, July 2004.

[80] E. D. Black, A. Villar, and K. G. Libbrecht. Thermoelastic-Damping Noise from Sapphire Mirrors in a Fundamental-Noise-Limited Interferometer. *Physical Review Letters*, 93(24):241101, December 2004.

[81] M. E. Zucker and S. E. Whitcomb. Measurement of Optical Path Fluctuations due to Residual Gas in the LIGO 40 Meter Interferometer. In R. T. Jantzen, G. Mac Keiser, & R. Ruffini, editor, *Proceedings of the Seventh Marcel Grossman Meeting on recent developments in theoretical and experimental general relativity, gravitation, and relativistic field theories*, page 1434, 1996.

[82] A. Cavalleri, G. Ciani, R. Dolesi, A. Heptonstall, M. Hueller, D. Nicolodi, S. Rowan, D. Tombolato, S. Vitale, P. J. Wass, and W. J. Weber. Increased Brownian Force Noise from Molecular Impacts in a Constrained Volume. *Physical Review Letters*, 103(14):140601, October 2009.

[83] N. Robertson and J. Hough. Gas Damping in Advanced LIGO Suspensions. Technical Report LIGO-T0900416-v2, LIGO Laboratory, 2009.

[84] R. Weiss. Gas Damping of the Final Stage in the Advanced LIGO Suspensions. Technical Report LIGO-T0900509-v1, LIGO Laboratory, 2009.

[85] M. Evans, P. Fritschel, and R. Weiss. Gas Damping Monte Carlo. Technical Report LIGO-T0900582-v3, LIGO Laboratory, 2009.

[86] A. Yariv. *Quantum Electronics*. Wiley, New York, 1989.

[87] R. Adhikari. *Sensitivity and Noise Analysis of 4 km Laser Interferometer Gravitational Wave Antennae*. PhD thesis, Massachusetts Institute of Technology, 2004.

[88] R. W. Boyd. Intuitive explanation of the phase anomaly of focused light beams. *Journal of the Optical Society of America (1917-1983)*, 70:877, 1980.

[89] A. Perot and C. Fabry. On the Application of Interference Phenomena to the Solution of Various Problems of Spectroscopy and Metrology. *Astrophysics Journal*, 9:87, February 1899.

[90] J. F. Mulligan. Who were Fabry and Perot? *American Journal of Physics*, 66:797–802, September 1998.

[91] M. A. Arain and G. Mueller. Design of the Advanced LIGO recycling cavities. *Opt. Express*, 16(14):10018–10032, 2008.

[92] R. W. P. Drever, J. L. Hall, F. V. Kowalski, J. Hough, G. M. Ford, A. J. Munley, and H. Ward. Laser phase and frequency stabilization using an optical resonator. *Applied Physics B: Lasers and Optics*, 31:97–105, June 1983.

[93] B. J. Cusack, B. S. Sheard, D. A. Shaddock, M. B. Gray, P. K. Lam, and S. E. Whitcomb. Electro-Optic Modulator Capable of Generating Simultaneous Amplitude and Phase Modulations. *App. Opt.*, 43:5079–5091, September 2004.

[94] J. Mason. *Signal Extraction and Optical Design for an Advanced Gravitational Wave Interferometer*. PhD thesis, California Institute of Technology, 2001.

[95] A. Freise, G. Heinzel, H. Lück, R. Schilling, B. Willke, and K. Danzmann. Frequency-domain interferometer simulation with higher-order spatial modes. *Classical and Quantum Gravity*, 21:1067, March 2004.

[96] F. Bayer-Helms. Coupling coefficients of an incident wave and the modes of spherical optical resonator in the case of mismatching and misalignment. *App. Opt.*, 23:1369–1380, May 1984.

[97] B. Bochner. *Modelling the Performance of Interferometric Gravitational-Wave Detectors with Realistically Imperfect Optics*. PhD thesis, Massachusetts Institute of Technology, 1998.

[98] J.-Y. Vinet, P. Hello, C. N. Man, and A. Brillet. A high accuracy method for the simulation of non-ideal optical cavities. *Journal de Physique I*, 2:1287–1303, July 1992.

[99] H. Yamamoto. SIS (Stationary Interferometer Simulation) Manual. Technical Report LIGO-T070039-00-E, LIGO Laboratory, California Institute of Technology, 2007.

[100] P. Hello and J.-Y. Vinet. Analytical models of transient thermoelastic deformations of mirrors heated by high power cw laser beams. *J. Phys. France*, 51:2243, 1990.

[101] R. O'Shaughnessy. *Topics in Gravitational Wave Astronomy*. PhD thesis, California Institute of Technology, 2003.

[102] J. Agresti. *Researches on Non-standard Optics for Advanced Gravitational Waves Interferometers*. PhD thesis, Università di Pisa, 2007.

[103] J.-Y. Vinet. *The VIRGO Physics Book, Vol. II.* The VIRGO Collaboration, 2005.

[104] E. D'Ambrosio. Nonspherical mirrors to reduce thermoelastic noise in advanced gravitational wave interferometers. *Phys. Rev. D*, 67:10, 2003.

[105] R. O'Shaughnessy, S. Strigin, and S. Vyatchanin. The implications of mexican-hat mirrors: calculations of thermoelastic noise and interferometer sensitivity to perturbation for the mexican-hat-mirror proposal for advanced LIGO. *ArXiv General Relativity and Quantum Cosmology e-prints*, page 0409050, September 2004.

[106] E. D'Ambrosio, R. O'Shaughnessy, S. Strigin, K. S. Thorne, and S. Vyatchanin. Reducing thermoelastic noise in gravitational-wave interferometers by flattening the light beams. *ArXiv General Relativity and Quantum Cosmology e-prints*, page 0409075, September 2004.

[107] M. G. Tarallo and J. Miller et al. Generation of a flat-top laser beam for gravitational wave detectors by means of a nonspherical Fabry-Pérot resonator interferometers. *App. Opt.*, 46:6648–6654, 2007.

[108] J. A. Sidles and D. Sigg. Optical torques in suspended Fabry Perot interferometers. *Physics Letters A*, 354:167–172, May 2006.

[109] M. Bondarescu and K. S. Thorne. New family of light beams and mirror shapes for future LIGO interferometers. *Phys. Rev. D*, 74(8):082003, October 2006.

[110] J. Agresti, Y. Chen, E. D'Ambrosio, and P. Savov. A duality relation between non-spherical optical cavities and its application to gravitational-wave detectors. *ArXiv General Relativity and Quantum Cosmology e-prints*, page 0511062, November 2005.

[111] P. Savov and S. Vyatchanin. Estimate of tilt instability of mesa-beam and Gaussian-beam modes for advanced LIGO. *Phys. Rev. D*, 74(8):082002, October 2006.

[112] G. Billingsley ed. Test Mass Material Down-select Plan. Technical Report LIGO-T020103-08-D, LIGO Laboratory, California Institute of Technology, 2004.

[113] G. M. Harry, A. M. Gretarsson, P. R. Saulson, S. E. Kittelberger, S. D. Penn, W. J. Startin, S. Rowan, M. M. Fejer, D. R. M. Crooks, G. Cagnoli, J. Hough, and N. Nakagawa. Thermal noise in interferometric gravitational wave detectors due to dielectric optical coatings. *Class. Quant. Grav.*, 19:897–917, March 2002.

[114] LIGO Scientific Collaboration. Gravitational Wave Interferometer Noise Calculator. `http://ilog.ligo-wa.caltech.edu:7285/advligo/GWINC`.

[115] L. S. Finn. Binary inspiral, gravitational radiation, and cosmology. *Phys. Rev. D*, 53:2878–2894, March 1996.

[116] A. P. Lundgren, R. Bondarescu, D. Tsang, and M. Bondarescu. Finite mirror effects in advanced interferometric gravitational wave detectors. *Phys. Rev. D*, 77(4):042003, February 2008.

[117] B. Mours, E. Tournefier, and J.-Y. Vinet. Thermal noise reduction in interferometric gravitational wave antennas: using high order TEM modes. *Class. Quant. Grav.*, 23:5777–5784, October 2006.

[118] S. Chelkowski, S. Hild, and A. Freise. Prospects of higher-order Laguerre-Gauss modes in future gravitational wave detectors. *Phys. Rev. D*, 79(12):122002, June 2009.

[119] G. Lovelace. The dependence of test-mass thermal noises on beam shape in gravitational-wave interferometers. *Classical and Quantum Gravity*, 24(17):4491–4512, 2007.

[120] V. Galdi, G. Castaldi, V. Pierro, I. M. Pinto, J. Agresti, E. D'Ambrosio, and R. Desalvo. Analytic structure of a family of hyperboloidal beams of potential interest for advanced LIGO. *Phys. Rev. D*, 73(12):127101, June 2006.

[121] V. Pierro, V. Galdi, G. Castaldi, I. M. Pinto, J. Agresti, and R. Desalvo. Perspectives on beam-shaping optimization for thermal-noise reduction in advanced

gravitational-wave interferometric detectors: Bounds, profiles, and critical parameters. *Phys. Rev. D*, 76(12):122003, December 2007.

[122] M. Bondarescu, O. Kogan, and Y. Chen. Optimal light beams and mirror shapes for future LIGO interferometers. *Phys. Rev. D*, 78(8):082002, October 2008.

[123] LMA (english) website. `http://lma.in2p3.fr/Lmagb.htm`.

[124] QED website. `http://qedmrf.com`.

[125] R. DeSalvo. Passive, nonlinear, mechanical structures for seismic attenuation. *Journal of Computational and Nonlinear Dynamics*, 2:TBC, 2007.

[126] A. Stochino. The HAM-SAS Seismic Isolation System for the Advanced LIGO Gravitational Wave Interferometers. Master's thesis, Università di Pisa, 2007.

[127] A. Bertolini, G. Cella, R. DeSalvo, and V. Sannibale. Seismic noise filters, vertical resonance frequency reduction with geometric anti-springs: a feasibility study. *Nuclear Instruments and Methods in Physics Research A*, 435:475–483, October 1999.

[128] Analog Devices. OP27: Low Noise, Precision Operational Amplifier. `http://www.analog.com/en/other-products/militaryaerospace/op27/products/product.html`.

[129] Apex Precision Power. PA81J/82J Low Bias Current Power Amplifiers. `http://apex.cirrus.com/en/products/pro/detail/P1165.html`.

[130] Physik Instrumente. P-810 Piezo Actuators For Light and Medium Loads. `http://www.physikinstrumente.com/en/products/prspecs.php?sortnr=100400`.

[131] Newport. AJS Series High-Precision Adjustment Screws. `http://www.newport.com/AJS-Series-High-Precision-Adjustment-Screws/140172/1033/catalog.aspx`.

[132] Innolight. Mephisto Product Line. `http://www.innolight.de/docs/mephisto.html`.

[133] D. Z. Anderson. Alignment of resonant optical cavities. *App. Opt.*, 23:2944–2949, September 1984.

[134] H. Kogelnik. Imaging of optical mode resonators with internal lenses. *Bell Sys. Tech. J.*, 44:455–494, March 1965.

[135] Coherent Inc. website. `http://www.coherent.com/`.

[136] New Focus. Resonant Modulator to 250 MHz Model 4003. `http://www.newfocus.com/products/?navid=3&theView=modelDetail&productLineId=2&productGroupId=154&modelGroupId=1126&modelRangeId=5057&modelId=1461`.

[137] J. E. Mason and P. A. Willems. Signal Extraction and Optical Design for an Advanced Gravitational-Wave Interferometer. *App. Opt.*, 42:1269–1282, March 2003.

[138] New Focus. InGaAs 125-MHz Photoreceiver Model 1811. `http://www.newfocus.com/products/?navid=3&theView=modelDetail&productLineId=3&productGroupId=137&modelGroupId=1054&modelRangeId=1054&modelId=1377`.

[139] D. Shoemaker, A. Brillet, C. N. Man, O. Crégut, and G. Kerr. Frequency-stabilized laser-diode-pumped Nd:YAG laser. *Optics Letters*, 14:609–611, June 1989.

[140] B. Willke, O. S. Brozek, K. Danzmann, C. Fallnich, S. Goßler, H. Lück, K. Mossavi, V. Quetschke, H. Welling, and I. Zawischa. The GEO 600 stabilized laser system and the current-lock technique. In S. Meshkov, editor, *American Institute of Physics Conference Series*, volume 523 of *American Institute of Physics Conference Series*, pages 215–221, June 2000.

[141] M. Heurs, V. M. Quetschke, B. Willke, K. Danzmann, and I. Freitag. Simultaneously suppressing frequency and intensity noise in a Nd:YAG nonplanar ring oscillator by means of the current-lock technique. *Optics Letters*, 29:2148–2150, September 2004.

[142] P. Fritschel, N. Mavalvala, D. Shoemaker, D. Sigg, M. Zucker, and G. González. Alignment of an Interferometric Gravitational Wave Detector. *App. Opt.*, 37:6734–6747, October 1998.

[143] N. Mavalvala. *Alignment Issues in Laser Interferometric Gravitational-Wave Detectors*. PhD thesis, Massachusetts Institute of Technology, 1997.

[144] E. Morrison, D. I. Robertson, H. Ward, and B. J. Meers. Automatic alignment of optical interferometers. *App. Opt.*, 33:5041–5049, August 1994.

[145] E. Morrison, D. I. Robertson, H. Ward, and B. J. Meers. Experimental demonstration of an automatic alignment system for optical interferometers. *App. Opt.*, 33:5037–5040, August 1994.

[146] H. Kogelnik and T. Li. Laser beams and resonators. *App. Opt.*, 5:1550, October 1966.

[147] G. Mueller, Q.-Z. Shu, R. Adhikari, D. B. Tanner, D. Reitze, D. Sigg, N. Mavalvala, and J. Camp. Determination and optimization of mode matching into optical cavities by heterodyne detection. *Optics Letters*, 25:266–268, February 2000.

[148] Y. Hefetz, N. Mavalvala, and D. Sigg. Principles of calculating alignment signals in complex resonant optical interferometers. *Journal of the Optical Society of America B Optical Physics*, 14:1597–1605, July 1997.

[149] G. Heinzel. *Advanced optical techniques for laser-interferometric gravitational-wave detectors*. PhD thesis, University of Hanover, 1999.

[150] L. Matone. *Étude du Contrôle Global de l'Interféromètre Central de VIRGO*. PhD thesis, Université de Paris-Sud, 1999.

[151] J. Degallaix. OSCAR. `http://www.mathworks.com/matlabcentral/fileexchange/20607-oscar`.

[152] K. Kawabe. Orientation of quadrant diode for wave front sensing. Technical Report LIGO-T060035-00-D, LIGO Hanford Observatory, 2006. `http://www.ligo.caltech.edu/docs/T/T060035-00.pdf`.

[153] P. Willems. Thermal compensation status in Enhanced LIGO. Technical Report LIGO-G0900182-v1, LIGO Laboratory, 2009.

[154] A. Rocchi. TCS - Effect on data, behaviour and noise. Technical Report VIR-0512B-09, VIRGO Collaboration, 2009.

[155] J.-Y. Vinet. Reducing thermal effects in mirrors of advanced gravitational wave interferometric detectors. *Class. Quant. Grav.*, 24:3897–3910, July 2007.

[156] R. Lawrence. *Active Wavefront Correction in Laser Interferometric Gravitational Wave Detectors*. PhD thesis, Massachusetts Institute of Technology, 2003.

[157] S. Timoshenko. *Theory of Elasticity*. McGraw-Hill, New York, 1970.

[158] H. Nyquist. Thermal agitation of electric charge in conductors. *Phys. Rev.*, 32(1):110–113, Jul 1928.

[159] H. B. Callen and T. A. Welton. Irreversibility and Generalized Noise. *Physical Review*, 83:34–40, July 1951.

[160] H. B. Callen and R. F. Greene. On a Theorem of Irreversible Thermodynamics. *Physical Review*, 86:702–710, June 1952.

[161] R. F. Greene and H. B. Callen. On a Theorem of Irreversible Thermodynamics. II. *Physical Review*, 88:1387–1391, December 1952.

[162] R. Kubo. The fluctuation-dissipation theorem. *Reports on Progress in Physics*, 29:255–284, January 1966.

[163] P. R. Saulson. Thermal noise in mechanical experiments. *Phys. Rev. D*, 42:2437–2445, October 1990.

[164] A. Gillespie and F. Raab. Thermally excited vibrations of the mirrors of laser interferometer gravitational-wave detectors. *Phys. Rev. D*, 52:577–585, July 1995.

[165] F. Bondu and J.-Y. Vinet. Mirror thermal noise in interferometric gravitational-wave detectors. *Physics Letters A*, 198:74–78, February 1995.

[166] F. Bondu, P. Hello, and J.-Y. Vinet. Thermal noise in mirrors of interferometric gravitational wave antennas. *Physics Letters A*, 246:227–236, September 1998.

[167] L. D. Landau and E. M. Lifshitz. *Theory of Elasticity.* Pergamon, Oxford, third edition, 1986.

[168] V. B. Braginsky and S. P. Vyatchanin. Thermodynamical fluctuations in optical mirror coatings. *Physics Letters A*, 312:244–255, June 2003.

[169] G. M. Harry, H. Armandula, E. Black, D. R. M. Crooks, G. Cagnoli, J. Hough, P. Murray, S. Reid, S. Rowan, P. Sneddon, M. M. Fejer, R. Route, and S. D. Penn. Thermal noise from optical coatings in gravitational wave detectors. *App. Opt.*, 45:1569–1574, March 2006.

[170] M. M. Fejer, S. Rowan, G. Cagnoli, D. R. Crooks, A. Gretarsson, G. M. Harry, J. Hough, S. D. Penn, P. H. Sneddon, and S. P. Vyatchanin. Thermoelastic dissipation in inhomogeneous media: loss measurements and displacement noise in coated test masses for interferometric gravitational wave detectors. *Phys. Rev. D*, 70(8):082003, October 2004.

[171] R. Lifshitz and M. L. Roukes. Thermoelastic damping in micro- and nanomechanical systems. *Phys. Rev. B*, 61:5600–5609, February 2000.

[172] A. M. Gretarsson, E. D'Ambrosio, V. Frolov, B. O'Reilly, and P. K. Fritschel. Effects of mode degeneracy in the LIGO Livingston Observatory recycling cavity. *Journal of the Optical Society of America B Optical Physics*, 24:2821, 2007.

[173] B. Bhawal. Diffraction losses of various modes in advanced LIGO arm cavity. Technical Report LIGO-T050234-00-E, LIGO Laboratory, California Institute of Technology, 2005.

[174] M. Bondarescu. *Topics in general relativity.* PhD thesis, California Institute of Technology, 2007.

[175] M. Smith and P. Willems. Auxiliary Optics Support System Conceptual Design Document, Vol. 1 Thermal Compensation System. Technical Report LIGO-T060083-01-D, LIGO Laboratory, California Institute of Technology, 2007.

[176] B. Simoni. Design and Construction of a Suspended Fabry-Perot Cavity for Gaussian and Non-Gaussian Beam Testing. Preliminary Test with Gaussian Beam. Master's thesis, Università di Pisa, 2004.

[177] C. J. Kamp, H. Kawamura, R. Passaquieti, and R. Desalvo. Directional radiative cooling thermal compensation for gravitational wave interferometer mirrors. *Nuclear Instruments and Methods in Physics Research A*, 607:530–537, August 2009.

[178] T. Corbitt, D. Ottaway, E. Innerhofer, J. Pelc, and N. Mavalvala. Measurement of radiation-pressure-induced optomechanical dynamics in a suspended Fabry-Perot cavity. *Physical Review A (Atomic, Molecular, and Optical Physics)*, 74(2):021802, 2006.

[179] B. S. Sheard, M. B. Gray, C. M. Mow-Lowry, D. E. McClelland, and S. E. Whitcomb. Observation and characterization of an optical spring. *Phys. Rev. A*, 69(5):051801, May 2004.

[180] T. J. Kippenberg, H. Rokhsari, T. Carmon, A. Scherer, and K. J. Vahala. Analysis of radiation-pressure induced mechanical oscillation of an optical microcavity. *Phys. Rev. Lett.*, 95(3):033901, Jul 2005.

[181] V. B. Braginsky, S. E. Strigin, and S. P. Vyatchanin. Parametric oscillatory instability in Fabry-Perot interferometer. *Physics Letters A*, 287:331–338, September 2001.

[182] V. B. Braginsky, S. E. Strigin, and S. P. Vyatchanin. Analysis of parametric oscillatory instability in power recycled LIGO interferometer. *Physics Letters A*, 305:111–124, December 2002.

[183] L. Ju, S. Gras, C. Zhao, J. Degallaix, and D. G. Blair. Multiple modes contributions to parametric instabilities in advanced laser interferometer gravitational wave detectors. *Physics Letters A*, 354:360–365, June 2006.

[184] A. G. Gurkovsky, S. E. Strigin, and S. P. Vyatchanin. Analysis of parametric oscillatory instability in signal recycled LIGO interferometer. *Physics Letters A*, 362:91–99, February 2007.

[185] S. E. Strigin and S. P. Vyatchanin. Analysis of parametric oscillatory instability in signal recycled LIGO interferometer with different arms. *Physics Letters A*, 365:10–16, May 2007.

[186] A. G. Gurkovsky and S. P. Vyatchanin. Parametric instability in GEO 600 interferometer. *Physics Letters A*, 370:177–183, October 2007.

[187] M. Evans, L. Barsotti, and P. Fritschel. A general approach to optomechanical parametric instabilities. *Physics Letters A*, 374:665–671, January 2010.

[188] M. Regehr. *Signal Extraction and Control for an Interferometric Gravitational Wave Detector*. PhD thesis, California Institute of Technology, 1995.

[189] P. Fritschel, R. Bork, G. Gonzalez, N. Mavalvala, D. Ouimette, H. Rong, D. Sigg, and M. Zucker. Readout and Control of a Power-Recycled Interferometric Gravitational-Wave Antenna. *App. Opt.*, 40:4988–4998, October 2001.

[190] J. Degallaix, C. Zhao, L. Ju, and D. Blair. Thermal tuning of optical cavities for parametric instability control. *Journal of the Optical Society of America B Optical Physics*, 24:1336–1343, June 2007.

[191] Z. Zhang, Zhao C., L. Ju, and D. G. Blair. Enhancement and suppression of optoacoustic parametric interactions using optical feedback. submitted to Phys. Rev. A, 2008. `http://www.gravity.uwa.edu.au/docs/PIFeedback.pdf`.

[192] N. Antler. Passive Damping of a LIGO Mirror, 2009. Senior Thesis, Massachusetts Institute of Technology.

[193] S. Gras, D. G. Blair, and L. Ju. Test mass ring dampers with minimum thermal noise. *Physics Letters A*, 372:1348–1356, February 2008.

[194] H. Lück, A. Freise, S. Goßler, S. Hild, K. Kawabe, and K. Danzmann. Thermal correction of the radii of curvature of mirrors for GEO 600. *Classical and Quantum Gravity*, 21:985, March 2004.

[195] P. Willems, A. Brooks, M. Smith, and K. Mailand. Advanced LIGO Thermal Compensation System Preliminary Design. Technical Report LIGO-T0900304-v2, LIGO Laboratory, 2009.

[196] C. Zhao, L. Ju, J. Degallaix, S. Gras, and D. G. Blair. Parametric Instabilities and Their Control in Advanced Interferometer Gravitational-Wave Detectors. *Physical Review Letters*, 94(12):121102, April 2005.

[197] L. Merrill. Testing the suppression of parametric instability by optical interference of transverse modes. Technical Report LIGO-G0900720-v1, Amaldi 8 Conference, 2009.

[198] K. Numata. *Direct Measurement of Mirror Thermal Noise*. PhD thesis, University of Tokyo, 2002.

[199] R. DeSalvo. Gravitational Wave Detectors - The Challenge of Low Frequency G.W. Detection. Technical Report LIGO-G050521-00, LIGO Laboratory, 2005.

[200] S. Gras, D. G. Blair, and C. Zhao. Suppression of parametric instabilities in future gravitational wave detectors using damping rings. *Classical and Quantum Gravity*, 26(13):135012, July 2009.

[201] N. W. Hagood and A. von Flotow. Damping of structural vibrations with piezoelectric materials and passive electrical networks. *Journal of Sound Vibration*, 146:243–268, April 1991.

[202] D. Coyne. Private conversation.

[203] S. Kawamura, J. Hazel, and F. Raab. Suspension Preliminary Design. Technical Report LIGO-T960074-07-D, LIGO Laboratory, California Institute of Technology, 1996. `http://www.ligo.caltech.edu/docs/T/T960074-07.pdf`.

[204] F. Acernese, P. Amico, M. Alshourbagy, S. Aoudia, S. Avino, D. Babusci, G. Ballardin, F. Barone, L. Barsotti, M. Barsuglia, F. Beauville, S. Birindelli, M. A. Bizouard, C. Boccara, F. Bondu, L. Bosi, C. Bradaschia, S. Braccini, A. Brillet, V. Brisson, L. Brocco, D. Buskulic, E. Calloni, E. Campagna, F. Cavalier, R. Cavalieri, G. Cella, E. Chassande-Mottin, C. Corda, A.-C. Clapson, F. Cleva, J.-P. Coulon, E. Cuoco, V. Dattilo, M. Davier, R. DeRosa, L. Di Fiore, A. Di Virgilio, B. Dujardin, A. Eleuteri, D. Enard, I. Ferrante, F. Fidecaro, I. Fiori, R. Flaminio, J.-D. Fournier, O. Francois, S. Frasca, F. Frasconi, A. Freise, L. Gammaitoni, A. Gennai, A. Giazotto, G. Giordano, L. Giordano, R. Gouaty, D. Grosjean, G. Guidi, S. Hebri, H. Heitmann, P. Hello, L. Holloway, S. Karkar, S. Kreckelbergh, P. La Penna, N. Letendre, M. Lorenzini, V. Loriette, M. Loupias, G. Losurdo, J.-M. Mackowski, E. Majorana, C. N. Man, M. Mantovani, F. Marchesoni, F. Marion, J. Marque, F. Martelli, A. Masserot, M. Mazzoni, L. Milano, C. Moins, J. Moreau, N. Morgado, B. Mours, A. Pai, C. Palomba, F. Paoletti, S. Pardi, A. Pasqualetti, R. Passaquieti, D. Passuello, B. Perniola, F. Piergiovanni, L. Pinard, R. Poggiani, M. Punturo, P. Puppo, K. Qipiani, P. Rapagnani, V. Reita, A. Remillieux, F. Ricci, I. Ricciardi, P. Ruggi, G. Russo, S. Solimeno, A. Spallicci, R. Stanga, R. Taddei, M. Tonelli, A. Toncelli, E. Tournefier, F. Travasso, G. Vajente, D. Verkindt, F. Vetrano, A. Viceré, J.-Y. Vinet, H. Vocca, M. Yvert, and Z. Zhang. Environmental noise studies in Virgo. *Journal of Physics Conference Series*, 32:80–88, March 2006.

[205] G. Manson and G. Hoffmann de Visme. The frequency spectrum of Barkhausen noise. *Journal of Physics D Applied Physics*, 5:1389–1395, August 1972.

[206] P. Amico, L. Bosi, L. Carbone, L. Gammaitoni, M. Punturo, F. Travasso, and H. Vocca. Mechanical quality factor of mirror substrates for VIRGO. *Classical and Quantum Gravity*, 19:1663–1668, April 2002.

[207] S. Kawamura, M. Fine, and J. Hazel. Dumbbell-type standoff for magnet/standoff assembly. Technical Report LIGO-T970096-00, LIGO Laboratory, 1997.

[208] J. Carri. Magnet induced losses in LIGO large optics. Technical Report LIGO-T960166, LIGO Laboratory, 1996.

[209] P. Willems. Magnet induced losses in LIGO large optics II: indium bonding. Technical Report LIGO-T980081-01, LIGO Laboratory, 1998.

[210] D. Sigg and the LIGO Scientific Collaboration. Status of the LIGO detectors. *Classical and Quantum Gravity*, 25(11):114041, June 2008.

[211] S. Waldman and R. Weiss. Understanding Initial LIGO and Possible Influences on Enhanced LIGO. Technical Report LIGO-G080068-00, LIGO Laboratory, 2008.

[212] R. Weiss. Notes on Barkhausen Noise, 2008. `http://lhocds.ligo-wa.caltech.edu:8000/mLIGO/Magnet_Swap?action=AttachFile&do=get&target=force_scaling.pdf`.

[213] P. J. Cote and L. V. Meisel. Self-organized criticality and the Barkhausen effect. *Physical Review Letters*, 67:1334–1337, September 1991.

[214] R. Adhikari. Barkhausen test. Livingston detector log, 2008. `http://ilog.ligo-la.caltech.edu/ilog/pub/ilog.cgi?group=detector&task=view&date_to_view=12/16/2008&anchor_to_scroll_to=2008:12:16:03:30:20-rana`.

[215] L. Merrill. A Study of Thermal Noise for Enhanced LIGO, 2008. Senior Thesis, Simmons College, `http://www.ligo.caltech.edu/docs/P/P080083-00/P080083-00.pdf`,.

[216] P. Fritschel. Considerations regarding magnet strengths for the Advanced LIGO test mass quadruple suspensions. Technical Report LIGO-T050271-00-D, LIGO Laboratory, 2005.

[217] R. Schofield. Environmental Coupling During S5. Technical Report LIGO-G080209-00-Z, LIGO Hanford, 2008.

[218] M. Barton. Suspension modelling page, 2006. Linked from `http://www.ligo.caltech.edu/~e2e/`.

[219] B. Shapiro. Private conversation.

[220] M. Hewitson, H. Grote, G. Heinzel, K. A. Strain, H. Ward, and U. Weiland. Calibration of GEO 600 for the S1 science run. *Classical and Quantum Gravity*, 20:885, September 2003.

[221] M. Hewitson, K. Danzmann, H. Grote, S. Hild, J. Hough, H. Lück, S. Rowan, J. R. Smith, K. A. Strain, and B. Willke. Charge measurement and mitigation for the main test masses of the GEO 600 gravitational wave observatory. *Classical and Quantum Gravity*, 24:6379–6391, December 2007.

[222] V. P. Mitrofanov, N. A. Styazhkina, and K. V. Tokmakov. Damping of the test mass oscillations caused by multistrip electrostatic actuator. *Physics Letters A*, 278:25–29, December 2000.

[223] V. P. Mitrofanov, N. A. Styazhkina, and K. V. Tokmakov. Test mass damping associated with electrostatic actuator. *Classical and Quantum Gravity*, 19:2039–2043, April 2002.

[224] K. Morton. *Numerical Solution of Partial Differential Equations*. Cambridge University Press, Cambridge, 1994.

[225] A. Mitchell. *The Finite Element Method in Partial Differential Equations*. Wiley, New York, 1977.

[226] J. Butcher. *Numerical Methods for Ordinary Differential Equations*. J. Wiley, London, 2003.

[227] COMSOL website. `http://www.comsol.com/`.

[228] ANSYS website. `http://www.ansys.com/`.

[229] J. Franklin. *Classical Electromagnetism*, chapter 9, page 258. Pearson Addison-Wesley, Boston, 2005.

[230] B. Shapiro and J. O'Dell. Private conversation.

[231] B. O'Reilly. S5/S6 Calibration Status. Technical Report LIGO-G0900225-v3, LIGO Livingston, 2009.

[232] K. Mossavi, M. Hewitson, S. Hild, F. Seifert, U. Weiland, J.R. Smith, H. Lück, H. Grote, B. Willke, and K. Danzmann. A photon pressure calibrator for the GEO 600 gravitational wave detector. *Physics Letters A*, 353(1):1 – 3, 2006.

[233] S. Hild. Photon pressure calibration: A safe and reliable method? LVC Calibration Face to Face, Annecy, 2006. `http://www.aei.mpg.de/~sthild/presentations/PPD_sthild_ann_f2f.pdf`.

[234] J. Giaime, P. Saha, D. Shoemaker, and L. Sievers. A passive vibration isolation stack for LIGO: Design, modeling, and testing. *Review of Scientific Instruments*, 67:208–214, January 1996.

[235] N. A. Robertson, B. Abbott, R. Abbott, R. Adhikari, G. S. Allen, H. Armandula, S. M. Aston, A. Baglino, M. Barton, B. Bland, R. Bork, J. Bogenstahl, G. Cagnoli, C. Campbell, C. A. Cantley, K. Carter, D. Cook, D. Coyne, D. R. Crooks, E. J. Daw, D. B. DeBra, E. Elliffe, J. Faludi, P. Fritschel, A. Ganguli, J. A. Giaime, S. Gossler, A. Grant, J. Greenhalgh, M. Hammond, J. Hanson, C. Hardham, G. M. Harry, A. Heptonstall, J. Heefner, J. Hough, D. Hoyland, W. Hua, L. Jones, R. Jones, J. E. Kern, J. LaCour, B. T. Lantz, K. Lilienkamp, N. Lockerbie, H. Lück, M. MacInnis, K. Mailand, K. Mason, R. Mittleman, S. A. Nayfeh, J. Nichol, D. J. Ottaway, H. Overmier, M. Perreur-Lloyd, J. Phinney, M. V. Plissi, W. Rankin, D. I. Robertson, J. Romie, S. Rowan, R. Scheffler, D. H. Shoemaker, P. Sarin, P. H. Sneddon, C. C. Speake, O. Spjeld, G. Stapfer, K. A. Strain, C. I. Torrie, G. Traylor, J. van Niekerk, A. Vecchio, S. Wen, P. Willems, I. Wilmut, H. Ward, M. Zucker, and L. Zuo. Seismic isolation and suspension systems for Advanced LIGO. In J. Hough and G. H. Sanders, editors, *Society of Photo-Optical Instrumentation Engineers (SPIE) Conference Series*, volume

5500 of *Society of Photo-Optical Instrumentation Engineers (SPIE) Conference Series*, pages 81–91, September 2004.

[236] C. Hardham et al. Quiet Hydraulic Actuators for LIGO. Technical Report LIGO-P060028-00-Z, LIGO Laboratory, California Institute of Technology, 2006.

[237] B. Lantz. Advanced LIGO Single Stage HAM Vibration Isolation Table. Technical Report LIGO-G070156-00, High Precision Devices/ LIGO, 2009.

[238] B. Abbott et al. Advanced LIGO Preliminary Design Review of the BSC ISI System. Technical Report LIGO-L0900118-v7, LIGO Laboratory, 2009.

[239] M. V. Plissi, C. I. Torrie, M. E. Husman, N. A. Robertson, K. A. Strain, H. Ward, H. Lück, and J. Hough. GEO 600 triple pendulum suspension system: Seismic isolation and control. *Review of Scientific Instruments*, 71:2539–2545, June 2000.

[240] N. A. Robertson, G. Cagnoli, D. R. M. Crooks, E. Elliffe, J. E. Faller, P. Fritschel, S. Goßler, A. Grant, A. Heptonstall, J. Hough, H. Lück, R. Mittleman, M. Perreur-Lloyd, M. V. Plissi, S. Rowan, D. H. Shoemaker, P. H. Sneddon, K. A. Strain, C. I. Torrie, H. Ward, and P. Willems. Quadruple suspension design for Advanced LIGO. *Classical and Quantum Gravity*, 19:4043–4058, August 2002.

[241] I. A. Bilenko and N. Yu. Lyaskovskaya. The investigation of thermal and non-thermal noises in fused silica fibers for Advanced LIGO suspension. *Physics Letters A*, 339(3-5):181 – 187, 2005.

[242] A. Heptonstall, G. Cagnoli, J. Hough, and S. Rowan. Characterisation of mechanical loss in synthetic fused silica ribbons. *Physics Letters A*, 354(5-6):353 – 359, 2006.

[243] N. A. Robertson et al. HAM Small and Large Triple Suspensions - Preliminary Design. Technical Report LIGO-T080187-00-R, LIGO Laboratory, 2009.

[244] L. Ruet. *Active Control and Sensor Noise Filtering Duality Application to Advanced LIGO Suspensions*. PhD thesis, L'Instut National des Sciences Appliquées de Lyon, 2007.

[245] JDSU website. http://www.jdsu.com/.

[246] MEDM website. http://www.aps.anl.gov/epics/extensions/medm/index.php.

[247] D. I. Robertson, R. Pallester, and K. A. Strain. Electrostatic drive amplifier for controls prototype tests. Technical Report LIGO-E040109-00-K, Advanced LIGO UK, 2004.

[248] A. P. French. *Vibrations and Waves*. Norton, New York, 1971.

[249] SRS650. Stanford Research Systems website, http://www.thinksrs.com/.

[250] J. E. Logan, N. A. Robertson, and J. Hough. An investigation of limitations to quality factor measurements of suspended masses due to resonances in the suspension wires. *Physics Letters A*, 170(5):352 – 358, 1992.

[251] S. Rapoport. Towards detecting gravitational waves from the crab pulsar, 2009. Senior Thesis, Massachusetts Institute of Technology.

[252] B. Widrow. *Least-Mean-Square Adaptive Filters*. Wiley-Interscience, New York, 2003.

[253] R. Bork and D. Barker. CDS Data Acquisition System Conceptual Design. Technical Report LIGO-T960010, LIGO Laboratory, 1996.